Contribution to the numerical simulation of turbulent shock-induced separated flows : Application to supersonic over-expanded nozzles flows

Afaque Shams

THESE

pour l'obtention du Grade de

DOCTEUR DE L'ECOLE NATIONALE SUPERIEURE DE MECANIQUE ET D'AEROTECHNIQUE

(Diplôme National - Arrêté du 7 août 2006)

Ecole Doctorale : Sciences et Ingénierie en Matériaux, Mécanique, Energétique et Aéronautique

Secteur de Recherche : Mécanique des milieux fluides

Présentée par :

AFAQUE SHAMS

* *

CONTRIBUTION A LA SIMULATION NUMERIQUE DES DECOLLEMENTS D'ECOULEMENTS TURBULENTS INDUITS PAR CHOC :

APPLICATION A L'ECOULEMENT SUR-DETENDU DE TUYERE SUPERSONIQUE

\- - - - - - - - - - - - - - - - - -

CONTRIBUTION TO THE NUMERICAL SIMULATION OF TURBULENT SHOCK-INDUCED SEPARATED FLOWS :

APPLICATION TO SUPERSONIC OVER-EXPANDED NOZZLE FLOW

* *

Directeur de thèse : **Pierre COMTE**

Co-Direction : **Guillaume LEHNASCH**

Soutenue le 9 juillet 2010

devant la Comission d'Examen

JURY

J.-P. DUSSAUGE	Directeur de Recherche au CNRS-IUSTI, Marseille	Rapporteur
B. AUPOIX	Directeur de Recherche ONERA, Toulouse	Rapporteur
A. KOURTA	Professeur au Polytech' Orléans	Examinateur
S. DECK	Chargé de Recherche ONERA, HDR	Examinateur
P. REIJASSE	Chargé de Recherche ONERA	Examinateur
P. COMTE	Professeur ENSMA	Examinateur
G. LEHNASCH	Maître de Conférence ENSMA	Examinateur

Dedication

To my parents

Acknowledgments

”If I have seen farther than the others, it is because I was standing on the shoulders of giants.”

(Isaac Newton)

First of all I would like to acknowledge the support of the ”Higher Education Commission” (HEC), Government of Pakistan.

I want to express my deepest regards to my mentor Professor Pierre Comte, who was a constant source of guidance and encouragement during this research work. I am highly indebted to him for constantly encouraging me by giving his critics on my work. I am also grateful to my co-director Guillaume Lehnasch for his help and support.

My sincere thanks to all the jury members, specially the reviewers M. Jean Paul Dussauge and M. Bertrand Aupoix to honour me by accepting this thesis. I would like to express my deep sense of gratitude to all the invited members : T. Alziary de Roquefort, S. Palerm, D. Saucereau, C. Tenaud and H. Deniau.

In addition, I would like to acknowledge the invaluable help and support provided by ONERA and CNES partners during the course of this research work.

I acknowledge the support of my colleagues for many discussions and help to sort out the difficulties that I went through during my research tenure at L’institut Pprime, particularly S. Girard, T. B. Gatski, M. F. Shahab, G. Browaeys, A. Benyahia and A. Lebedev. I would also like to appreciate the help and the gentle behaviour of all personnel of CEAT/LEA/ENSMA, Poitiers.

Last but not the least my family whose love and prayers gather me everywhere.

RESUME

Les décollements d'écoulements induits par choc et leur éventuel réattachement sur paroi sont observés dans de nombreuses configurations d'intérêt pratique, incluant les entrées d'air, les profils transsoniques ou les tuyères de lanceurs spatiaux. Ces phénomènes mettent en jeu des interactions complexes entre couches limites et ondes de choc ou de détente conduisant à des instationnarités à basse fréquence dont l'origine reste aujourd'hui à élucider. Cette étude vise à proposer une stratégie numérique permettant de prévoir plus précisément ces phénomènes de décollement et à identifier les principaux mécanismes physiques qui pilotent l'évolution de leur structure globale. L'étude porte plus particulièrement sur les configurations de décollements libres ou séparés apparaissant en tuyère optimisée en poussée opérant en régime surdétendu. La stratégie numérique repose sur la combinaison de schémas d'ordre élevé (WENO 5), d'algorithmes d'intégration implicite en temps et d'une approche Detached Eddy Simulation (DES) incluant des corrections de réalisabilité pour la modélisation de la turbulence. Une large plage de niveaux de surdétente et des temps longs de simulation sont considérés, à la fois en condition d'entrée stabilisée et transitoire, afin de clarifier les conditions d'existence des différents régimes de décollements libres et restreints, ainsi que l'évolution temporelle de la morphologie globale de l'écoulement transitant entre ces deux régimes. L'évolution instationnaire de l'écoulement est simulée sur des temps suffisamment longs pour permettre une analyse spectrale des contributions des premiers modes azimutaux à la dynamique basse fréquence du champ de pression pariétale.

Mots clés : Choc, tuyère, décollement, supersonique, DES (Detached-Eddy Simulation), charge latérales.

ABSTRACT

Shock-induced flow separation and its subsequent reattachment are encountered in many configurations, such as supersonic inlets, transonic airfoils or rocket nozzles. These phenomena involve complex interactions of boundary layers with compression or expansion waves and exhibit a low-frequency unsteady behaviour which still requires a clear explanation. This study aims at better identifying the physical mechanisms which drive the global structure of these flows and suggesting improved numerical tools in order to predict these more accurately. The appearance of free and restricted separations in supersonic separated jets occuring in thrust optimized contour nozzles operating in over-expanded conditions is more particularly investigated while various hypothesis are tested to explain the evolution of the associated unsteady asymmetric wall pressure field in function of the nozzle pressure ratio. The numerical strategy proposed relies on a realizable extension of the Detached Eddy Simulation, combined with high order shock capturing schemes and an implicit time integration algorithm. This methodology is applied for a wide range of both constant or transient inflow conditions and leads to identify more accurately the appearance of free and restricted separations and the time-varying morphology of the flow during the transition process. For both flow regimes, the simulations are carried out for long-enough time to perform reliable statistical analysis and azimuthal expansion of the wall pressure field and thus investigate extensively the possible origins of the side-load activities.

Key works : Shock, nozzle, separation, supersonic, DES (Detached-Eddy Simulation), sideloads.

Table des matières

Table des figures

Liste des tableaux

Chapitre 1

Synthèse de l'étude

Contexte et objectifs

Les décollements d'écoulements induits par choc et leurs éventuels réattachements sur paroi sont observés dans de nombreuses configurations aéronautiques, telles que les entrées d'air supersoniques, les profils transsoniques d'avions en régime de croisière ou les divergents de tuyères de lanceurs spatiaux lors des phases d'allumage ou d'extinction. Ces phénomènes mettent en jeu des interactions complexes entre couches limites et ondes de choc ou de détente qui conduisent à des oscillations instationnaires à basses fréquences. Ces oscillations induisent des charges aérodynamiques et thermiques pouvant mettre en défaut l'intégrité des systèmes aéronautiques concernés. Leur origine reste encore aujourd'hui à élucider et leur prévision représente un enjeu aéronautique majeur qui alimente une activité de recherche particulièrement importante depuis le milieu des années 90.

Les travaux rapportés dans ce mémoire concernent plus particulièrement les écoulements sur-détendus de tuyère optimisée en poussée. Ces écoulements sont typiquement observés lors de la mise en route du moteur Vulcain du lanceur spatial Ariane lorsque la pression dans la chambre n'est pas encore suffisante pour assurer un écoulement supersonique dans toute la tuyère. La pression chute dans le divergent de la tuyère du fait de la détente des gaz et s'adapte aux conditions atmosphériques via la formation d'un système d'ondes de choc. Celui-ci interagit avec la couche limite et induit divers types de décollements. Les instabilités associées entraînent alors une perte d'axisymétrie et soumettent la tuyère à des efforts transverses conduisant à un risque potentiel d'endommagement.

Des études expérimentales menées précédemment au LEA (Laboratoire d'Etudes Aérodynamiques) à Poitiers ont permis d'identifier l'existence de deux principaux régimes d'écoulement pour ce type de tuyère : i/ un régime de séparation libre apparaissant à basse pression de chambre et correspondant à la présence d'un écoulement complètement détaché en aval du choc de séparation (régime FSS pour "Free Shock Separation") et ii/ un régime de séparation restreinte pour de plus hautes pressions génératrices, pour lequel le décollement se restreint à une ou deux zones d'étendue limitée près de la paroi (régime RSS pour "Restricted Shock Separation").

La mise en oeuvre de simulation numérique directe ou de simulation des grandes échelles reste encore inenvisageable à moyen terme sur ce type de configurations tandis que les modèles de turbulence classiques de type RANS sont mis en défaut à cause du fort déséquilibre de la turbulence, non pris en compte, à la traversée des ondes de choc en présence. L'objectif de

cette étude vise donc à proposer une stratégie numérique alternative permettant de prévoir plus précisément ces phénomènes de décollement et pouvoir ainsi analyser les principaux mécanismes physiques qui pilotent leur évolution instationnaire.

Le présent manuscript est organisé de la façon suivante. Le premier chapitre développe plus largement la problématique des décollements d'écoulements en tuyère, et développe plus précisément les objectifs visés par l'étude. Le second chapitre synthétise la phénoménologie des décollements d'écoulements induits par choc, allant d'un bref rappel de l'état de l'art sur l'interaction choc/couche limite en configuration bidimensionnelle jusqu'à la classification des différents régimes d'écoulements de tuyère sur-détendus. Les méthodes numériques et modèles de turbulence effectivement utilisés ou développés au cours de ces travaux sont ensuite présentés dans le troisième chapitre. L'approche de la simulation de tourbillon détaché (DES) y est notamment décrite avec les spécificités de la formulation proposée dans la présente étude pour remédier aux problèmes liés à la présence des chocs. Les résultats de l'étude numérique sont ensuite présentés. Le chapitre 4 traite de l'identification de l'évolution de la morphologie de l'écoulement en fonction du rapport de pression génératrice sur pression ambiante et décrit les états successivement rencontrés lors de la transition entre les régimes FSS et RSS. Les chapitres 5 et 6 développent ensuite plus en détails la caractérisation de l'instationnarité observée pour chacun de ces régimes respectivement. Une synthèse de ces résultats et quelques perspectives originales de ces travaux sont finalement proposées dans le dernier chapitre.

Phénoménologie des décollements d'écoulements induits par choc

Ce chapitre est consacré à la description phénoménologique classique des décollements d'écoulement induits par choc en configuration plane. Sont successivement abordées les spécificités des écoulements de rampe supersonique, de l'impact de choc oblique, du cas du choc droit en profil transsonique et finalement du cas de la structure de l'écoulement en présence d'un choc d'adaptation, typiquement rencontrée en tuyère fonctionnant en régime surdétendu. Il se termine par l'énumération des principales sources d'instationnarité évoquées dans la littérature pour expliquer le phénomène de charges latérales.

La formation de la structure de choc dans de tels cas d'interaction choc/couche limite peut être basiquement décrite de la façon suivante. La déflexion des lignes de courant suivant la nouvelle direction imposée par la paroi en aval de la zone d'interaction conduit à la focalisation d'ondes de compression et ainsi à la formation du choc de compression. L'information du gradient de pression adverse ainsi imposé se propage en amont via la zone subsonique de la couche limite. La décélération de l'écoulement en proche paroi conduit à l'épaissement progressif de la couche limite au fur et à mesure que l'intensité de l'interaction augmente, jusqu'à la séparation de l'écoulement en léger amont du point d'interaction (inviscide théorique) des chocs avec la paroi. Cette séparation de l'écoulement provoque une focalisation des ondes de compression en amont de cette zone d'impact (ou du coin de la rampe) et est suivie d'une zone de détente associée au nouveau changement de courbure des lignes de courant dans la recirculation ainsi formée. Dans la zone de réattachement, un nouveau choc apparaît suivant le même mécanisme de changement d'orientation des lignes de courant. Il en résulte une structure globale de choc en forme de lambda. Différents modèles ont été proposés dans la littérature pour rendre compte de l'instationnarité de cette interaction, mettant en jeu soit une influence amont prédominante

(tourbillons à grande échelle au sein de la couche limite en amont de l'interaction), soit une influence aval prédominante (mécanisme de rétroaction acoustique au sein de la zone subsonique de la zone de recirculation).

Dans le cas des écoulements de tuyères fonctionnant en régime sur-détendu, la structure de l'écoulement décollé dépend du rapport de la pression chambre sur la pression ambiante (NPR pour "Nozzle Pressure Ratio". La présente étude se concentre plus particulièrement sur le cas d'une tuyère TOC (Thrust Optimized Contour) étudiée expérimentalement au LEA (Laboratoire d'Etudes Aérodynamiques) à Poitiers. Cette tuyère présente un élargissement brusque en aval du col qui implique la formation d'un choc interne émanant de celui-ci. Pour de faibles NPRs, le régime de séparation par choc libre (FSS pour "Free Shock Separation") est observé. La structure globale de l'écoulement observé est présentée sur la figure 1.1 (gauche). L'écoulement surdétendu soumet la couche limite à un gradient de pression adverse qui induit une séparation massive à l'intérieur de la buse. L'écoulement extérieur est alors aspiré dans la tuyère le long de la paroi avant de se mélanger au jet qui reste confiné dans la partie centrale de la tuyère. Le choc oblique de séparation, qui apparaît au niveau du point de séparation, interagit faiblement avec le choc interne. Le choc de séparation se réfléchit ensuite irrégulièrement au niveau de l'axe, formant un choc droit, très large, au niveau de la partie centrale de la tuyère et un choc réfléchi. L'intersection de ce choc de séparation, du choc droit (le disque de Mach) et du choc réfléchi forme un point triple duquel une couche de cisaillement émane, séparant une zone subsonique, en aval du disque de Mach, de la zone supersonique externe. En aval de cette structure de choc amont, l'écoulement se présente donc sous la forme d'une couche de mélange annulaire supersonique soumis à des faisceaux de compression/décélération et détente/accélération se réfléchissant entre la zone de séparation externe et le coeur subsonique. Pour cette configuration d'écoulement, la pression pariétale moyenne chute progressivement depuis le col jusqu'au point de séparation. Elle subit alors une brusque élévation jusqu'à un niveau "quasi-plateau", ne réaugmentant alors plus que progressivement jusqu'au niveau de la pression extérieure.

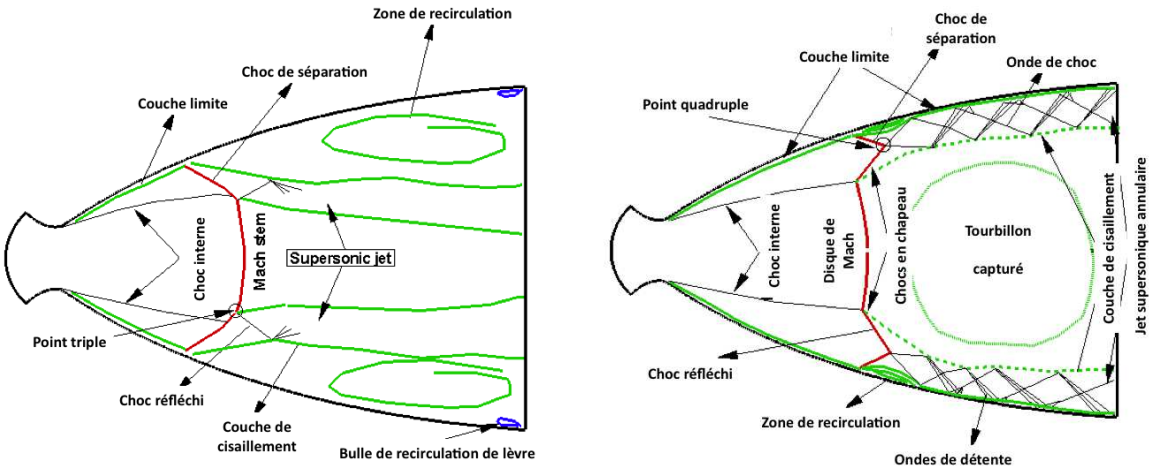

FIGURE 1.1 – Structure de l'écoulement de tuyère LEATOC : (gauche) séparation libre (Free Shock Separation (FSS)), (droite) séparation restreinte (Restricted Shock Separation (RSS)).

Pour des NPRs plus importants, un régime de séparation restreinte est observé (RSS pour "Restricted Shock Separation"). La structure de cet écoulement est schématisée sur la figure 1.1 (droite). Dans ce cas, le choc interne interagit directement avec le choc droit central. Le choc réfléchi interagit alors avec le choc de séparation, formant une structure dite de choc en

chapeau (”cap shock”). La zone de recirculation primaire présente une extension limitée et se rattache à la paroi de la tuyère. Le changement de courbure du choc droit et la différence de pression totale induite entre la zone supersonique près de la paroi et la zone subsonique centrale induisent l'apparition d'une large zone de recirculation subsonique en aval du disque de Mach. Les niveaux moyens de pression pariétale varient selon la position des faisceaux d'ondes de compression/détente se réfléchissant en aval de la structure de choc en chapeau entre la couche limite et la couche de cisaillement. Tant que le NPR reste limité, la présence d'un second choc au sein de cette zone supersonique est associée à une séparation secondaire de l'écoulement en proche paroi. Tandis que le NPR augmente, la structure de choc recule globalement vers l'aval et la recirculation secondaire s'ouvre éventuellement à l'atmosphère ambiante. Pour une gamme restreinte de NPR plus élevé, la recirculation primaire elle-même finit par s'ouvrir à l'atmosphère. Le régime où cette dernière configuration d'écoulement est observée est dénommée ”End Effect”.

Les caractéristiques instationnaires de l'écoulement évolue corrélativement à cette structure moyenne et donc au NPR. Trois principaux pics de charges latérales ont été expérimentalement identifiés. Le premier pic correspond à la plage de NPR où l'écoulement évolue du régime FSS au régime RSS. Les deux pics ensuite observés en régime RSS correspondent aux cas où la recirculation initialement restreinte atteint le plan de sortie de la tuyère et s'ouvre à l'atmosphère.

Les deux principales problématiques identifiées dans la littérature pour cette gamme d'écoulements sont d'une part, l'origine des mécanismes pilotant la transition entre les deux régimes identifiés, et d'autre part la description des phénomènes physiques pilotant les différents régimes d'instationnarité de l'écoulement. Parmi les différents ingrédients mis en jeu, on notera la possible distortion globale de la ligne de séparation (en forme de toit de tipi, notamment dans le cas où celle-ci se situe proche du plan de sortie de la tuyère. Notons néanmoins qu'une telle déformation globale de la ligne de séparation n'a à ce jour été associée qu'à des effets de gaz chauds et n'a jamais été clairement observée en gaz froid. Les zones de recirculation primaire ou secondaire correspondent à des poches fluides à pression statique plus basse que la pression atmosphérique ambiante. L'augmentation du niveau global d'instationnarité dans le cas où ces zones de recirculation s'ouvrent à l'atmosphère a donc naturellement été reliée à un probable mécanisme global de rééquilibrage des forces de pression à travers la zone tourbillonnaire subsonique centrale, provoquant un réajustement instationnaire de la position de la structure de choc en amont. Une autre hypothèse mise en avant pour expliquer le premier pic de charges latérales est le basculement global de la structure de choc amont, pouvant éventuellement laisser coexister à différents instants dans la direction azimutale les deux régimes d'écoulement (à détachement libre ou restreint). Notons finalement le rôle probablement non-négligeable des couplages aéro-élastiques et des aspects impulsionnels (instationnarités liées à l'évolution transitoire du régime de l'écoulement soumis à une montée en pression).

Description des outils numériques

Ce chapitre est consacré à la présentation de la stratégie numérique retenue, implémentée dans le code TGNS3D (volumes finis, multiblocs structurés) développé au sein de la branche Fluide de l'institut Pprime (ex-LEA).

De façon à assurer le compromis coût/précision adéquat permettant d'envisager la simulation de nombreux cas de simulation (à la fois de plusieurs régimes établis d'écoulement, établis ou transitoire), des schémas MPWENO (Monotonicity Preserving Weighted Essentielly Non-

Oscillating) à l'ordre 5 et une intégration implicite en temps ont été retenus. La présentation de ces éléments est essentiellement reportée dans l'annexe *A*.

Les principaux éléments de modélisation permettant l'établissement des équations aérothermiques décrivant l'équilibre des champs moyens des variables physiques sont ensuite rappelés. La capture par simulation numérique directe ou simulation des grandes échelles des composantes basses fréquences de l'évolution instationnaire de la structure globale d'un tel écoulement de tuyère requiert des moyens de calcul inenvisageables à l'heure actuelle. Néanmoins les approches URANS (Unsteady Reynolds Averaged Navier Stokes) ont clairement démontré leur incapacité à capturer ne serait-ce parfois que qualitativement la structure du champ de pression pariétale. La modélisation de la turbulence retenue repose donc sur une approche hybride URANS/LES de type DDES (Delayed Dettached Eddy Simulation). Cette approche consiste à se contenter de la capture du champ moyen dans les zones proche paroi (les plus coûteuses) de la couche limite tant que celle-ci reste attachée et à basculer en mode de résolution par simulation des grandes échelles uniquement dans les zones décollées de l'écoulement où les grandes échelles dynamiquement actives et responsables de l'instationnarité à basse fréquence sont présentes. Des corrections de réalisabilité ont par ailleurs été ajoutées de façon à palier autant que possible les limitations des modèles de type RANS en présence de choc (production artificielle d'énergie cinétique turbulente).

L'approche RANS (Reynolds Average Navier Stokes) consiste basiquement à décomposer les variables physique en partie moyenne (pondérée ou non par la masse volumique moyenne) et partie fluctuante, puis à moyenner temporellement les équations de transport pour cette décomposition des variables. Dans ce cas, les termes de contraintes dites turbulentes, impliquant des moyennes de produit de fluctuation, apparaissent de part la non-linéarité de la moyenne du terme de transport convectif avec la moyenne des champs de vitesse. L'approche classique retenue ici pour fermer ces termes repose sur l'hypothèse de Boussinesq qui associe ces contraintes turbulentes au gradient moyen du tenseur de déformation. L'influence de la turbulence dans ces zones est ainsi représentée par l'ajout d'une viscosité additionnelle. Le modèle à deux équations de transport $k-\omega$ standard a finalement été retenu pour cette étude. La viscosité turbulente est ainsi évaluée via le transport de l'énergie cinétique turbulente k et de de son taux de dissipation spécifique ω. Cette approche RANS permet en pratique de simuler de façon satisfaisante l'évolution du champ moyen au sein de couche limite attachée, et a été retenu, parmi l'ensemble des modèles RANS élémentaires testés, pour son meilleur comportement en présence de fort gradient de pression.

La simulation des grandes échelles repose classiquement sur une approche de décomposition en champ résolu à l'échelle du maillage et champ de sous-maille. Les équations de transport considérées correspondent cette fois-ci en toute rigueur à la convolution des équations de Navier Stokes avec un filtre spatial. Les termes additionnels de contraintes de sous-maille qui apparaissent dans cette formulation peuvent alors être fermés en suivant une approche fonctionnelle par la détermination d'une viscosité de sous-maille équivalente, permettant ainsi de relier directement ces termes de transferts sous-maille aux gradients des champs de vitesse résolue. Les équations de transport utilisées en LES sont ainsi formellement proches de celles utilisées en formulation URANS.

Dans l'approche DES ici suivie, un basculement du mode de résolution RANS au mode LES est en fait obtenu via la réévaluation, à chaque instant, des échelles de longueur caractéristiques en présence : échelle RANS évaluée par le modèle RANS d'une part, et échelle locale donnée par les caractéristiques locales du maillage d'autre part pour l'approche LES. Il

s'agit concrètement alors de modifier dans la formulation du modèle URANS, en chaque point de l'écoulement, l'échelle de longueur turbulente effectivement prise en compte en fonction à la fois du niveau de turbulence et de la capacité du maillage à la résoudre. Deux approches ont été testées au cours de cette étude. La première consiste à modifier uniquement cette échelle caractéristique dans l'expression du terme de dissipation du transport de l'énergie cinétique turbulente. La seconde consiste à appliquer cette modification également dans l'expression de la viscosité turbulente.

Les problèmes classiquement rencontrés avec une telle approche sont essentiellement reliés à la possible réduction des contraintes par le modèle (Model Stress Depletion), voir la séparation induite par le maillage (Grid Induced Separation). En effet, il est possible par mauvais ajustement du raffinement local du maillage de basculer artificiellement d'un mode de résolution à l'autre au sein de la couche limite où se retrouver dans des zones dites ambigües où le mode RANS conduit à sous-estimer les niveaux des contraintes tandis que la LES opérant dans une zone sous-résolue ne permet pas de reconstruire l'ensemble des échelles dynamiquement actives. Dans un tel cas, en présence d'un gradient de pression adverse, un décollement artificiel peut se produire et conduire à des solutions complètement erronées. De façon à éviter de tels problèmes de basculement artificiel d'un mode de résolution à l'autre, une fonction dite "bouclier" (simplement basée sur l'évaluation de la distance aux parois) est utilisée pour forcer le mode de résolution URANS en proche paroi.

Finalement, de façon à éviter la production artificielle d'énergie cinétique turbulente près des zones de choc, une correction dite de réalisabilité a été implantée. Cette réalisabilité de la turbulence consiste ici à s'assurer que le tenseur des contraintes turbulentes conserve en tout point de l'écoulement une structure compatible avec une distribution réaliste des contraintes turbulentes. Il s'agit a minima de s'assurer que les corrélations croisées vérifient les inégalités de Schwartz et que la variance de chaque composante de vitesse reste positive. Une telle contrainte s'obtient concrètement en pondérant l'expression de la viscosité turbulente en fonction des taux de déformation et de rotationnel. Une telle correction peut ainsi être vue comme un limiteur évolué de production de l'énergie cinétique turbulente.

Validation de la stratégie numérique

Ce chapitre résume les principaux tests mis en oeuvre de façon à valider la stratégie numérique effectivement retenue pour simuler les écoulements de tuyère.

Le cas test de convection d'une onde de vorticité sur un domaine périodique (cf. figure 1.2) a tout d'abord été utilisé de façon à calibrer la plage du nombre de CFL (Courant Friedrich Lax) compatible avec le maintien d'une précision satisfaisante au cours de l'intégration implicite en temps. Il est montré que pour $CFL < 25$ la dissipation induite par la méthode d'implicitation (DDADI) reste limitée et que la précision obtenue pour la capture du développement des grosses structures cohérentes est satisfaisante.

La différence de comportement des schémas au second ordre (plus largement utilisés jusqu'à présent d'après la littérature pour simuler ces écoulements) et des schémas WENO à l'ordre 5 est ensuite illustrée via la simulation d'un écoulement de tuyère. De façon attendue, les schémas au second ordre conduisent à la production d'une dissipation et d'une vorticité numérique excessive qui peut conduire au décallage artificiel de la position de la structure de choc amont, ainsi que des positions des zones de compression et détente en aval. L'utilisation d'un niveau de précision aussi modéré peut donc rendre particulièrement délicate la prévision de la structure

globale de l'écoulement dans le cas où les points de réflexion de ces ondes de choc ou de détente se situent proche de la sortie. La figure 1.3 illustre par ailleurs la possible apparition d'une seconde zone de recirculation, purement artificielle, en aval de la structure de choc lorsque les schémas au second ordre sont utilisés sur des maillages trop grossiers. Même en ne recourant qu'à des niveaux modérés de résolution, les schémas WENO5 permettent de s'affranchir de ces problèmes et d'accéder pour un coût raisonnable à la précision nécéssaire à la capture correcte des interactions complexes de chocs en présence.

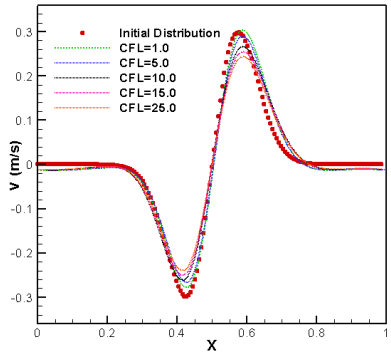

FIGURE 1.2 – Cas test de la convection périodique d'une onde de vorticité : influence du nombre de CFL sur la dissipation numérique induite.

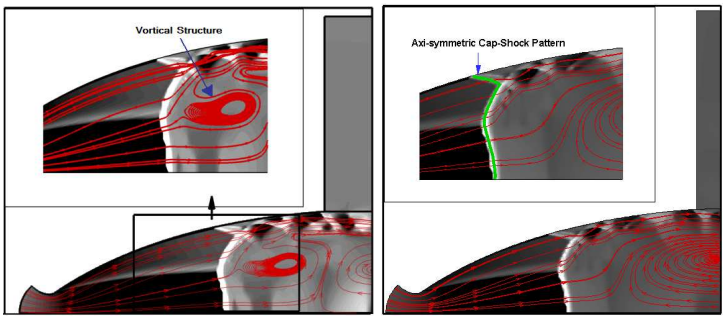

FIGURE 1.3 – Recirculation artificielle apparaissant en présence d'un excès de dissipation numérique ou de production de k : second ordre MUSCL (gauche), schémas WENO 5 (droite).

Le comportement de quelques modèles RANS classiques ($k-\varepsilon$, $k-\omega$, $k-\omega$ SST) en présence de choc a ensuite été étudié. De façon attendue, ces modèles testés souffrent de deux limitations principales : production excessive d'énergie cinétique turbulente à travers les discontinuités de choc et dépendance relativement importante de la structure de la couche limite prédite à la gestion des conditions aux limites utilisées en paroi ou à l'entrée du domaine de calcul. Il est à noter que la production excessive de k à travers les chocs augmente par ailleurs avec le niveau de résolution du maillage. La nécessité vitale de recourir à une correction adhoc permettant de limiter cette production est notamment illustrée par les résultats d'une simulation à $NPR = 15,5$ avec ou sans limitation, où l'on peut observer, dans le cas où aucune limitation n'est utilisée, la bifurcation artificielle de la structure de l'écoulement en régime RSS à une valeur relativement basse du NPR (15,5) pour laquelle le régime FSS est normalement observé. Il est par ailleurs ici démontré que l'utilisation de corrections de réalisabilité (pondération de la viscosité turbulente en fonction de l'évolution locale de l'invariant de contrainte adimensionnée, fonction de la déformation et la rotation locale de l'écoulement) conduit à une nette amélioration de la prévision des zones de décollement et du niveau du plateau de pression pariétale, par rapport au cas où des limiteurs de production plus classiques sont utilisés (simple limitation de la production quand le rapport production sur dissipation devient trop important et donc susceptible d'être non-physique). La figure 1.4 illustre l'intérêt de la prise en compte de telles corrections, pour les deux régimes d'écoulement considérés FSS et RSS, en comparant les évolutions longitudinales de la pression pariétale obtenues d'une part avec des limiteurs classiques et d'autre part avec la correction de réalisabilité.

Finalement, dans ce chapitre est démontré l'apport de la modification de l'échelle turbulente prise en compte dans le modèle pour reconstruire le terme de viscosité turbulente (formulation

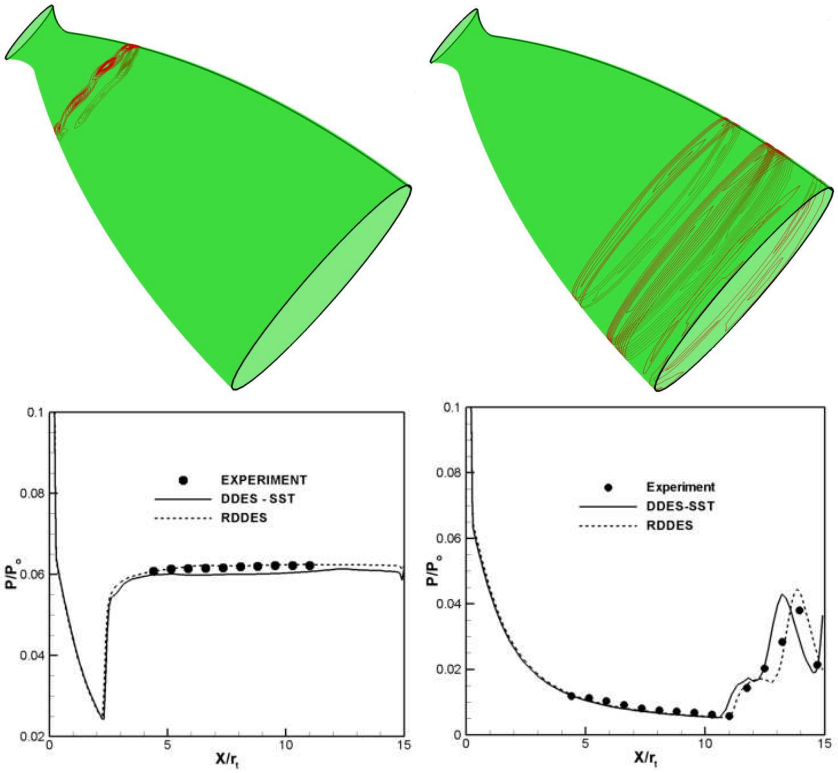

FIGURE 1.4 – Apport des corrections de réalisabilité : détection des zones de violation des conditions de réalisabilité (en rouge) en $R/\delta = 0,67$ à $NPR = 15,5$ (haut gauche) et $NPR = 38$ (haut droit) ; distribution de pression pariétale moyenne en régime FSS à $NPR = 15,5$ (bas gauche) et régime RSS à $NPR = 41,6$ (bas droite).

RDDES2) en plus de la modification déjà effectuée au sein du terme de dissipation dans le transport de k (formulation RDDES1). Il est montré que cette approche permet de diminuer le niveau de viscosité introduit sans nuire à la stabilité du calcul, et de ne pas inhiber le développement d'instabilités à grande échelle au sein des couches de cisaillement. Les figures 1.5 et 1.6 illustrent par exemple la différence de comportement observée entre les deux modèles à la fois sur le cas de la simulation d'un écoulement de jet vectorisé (soufflage vers l'amont à 45° de la direction longitudinale au niveau de la lèvre supérieure) en configuration bidimensionnelle et sur le cas d'un écoulement de tuyère LEATOC à NPR=15,5. Le champ moyen prédit par le modèle reste très similaire pour les deux modèles. Les clichés instantanés de l'écoulement démontrent néanmoins que le premier modèle conduit à une viscosité turbulente trop importante qui inhibe le développement des instabilités à grande échelle qui se développent au sein des couches de cisaillement et qui participent au battement instationnaire du jet. Pour le cas du jet vectorisé, on constate notamment que le modèle RDDES2 permet non seulement de capturer le développement des instabilités au sein de la couche de cisaillement issue de la lèvre inférieure, mais aussi de capturer l'émission acoustique attendue au niveau de la lèvre supérieure (fortement perturbée par la présence du soufflage), ce que le modèle RDDES1 ne permet pas. Pour le cas de l'écoulement de tuyère LEATOC en régime FSS, on constate par ailleurs que ce second modèle RDDES2 permet de capturer naturellement une distortion azimutale des macrostructures cohérentes qui se développent au sein de la couche de cisaillement séparant la zone de recirculation en proche paroi de la zone subsonique près de l'axe. Etant donné que la capture de telles instabilités peut jouer un rôle fondamental dans la prévision des modes d'oscillations privilégiés du jet, seule cette seconde modélisation a été retenue pour l'ensemble de l'étude ci-après rapportée.

A vu des résultats obtenus au cours de cette étude préliminaire de validation, il apparaît que l'intérêt de la stratégie numérique retenue repose sur la combinaison de schémas à capture de

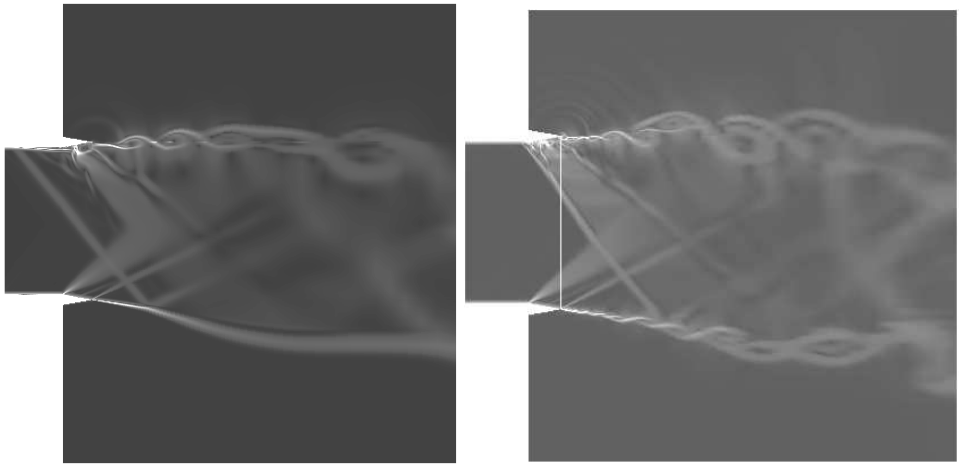

FIGURE 1.5 – Etude de l'influence du modèle RDDES1 (gauche) ; RDDES2 (droite) : visualisations instantanées pseudo-Schlieren d'un écoulement de jet vectorisé.

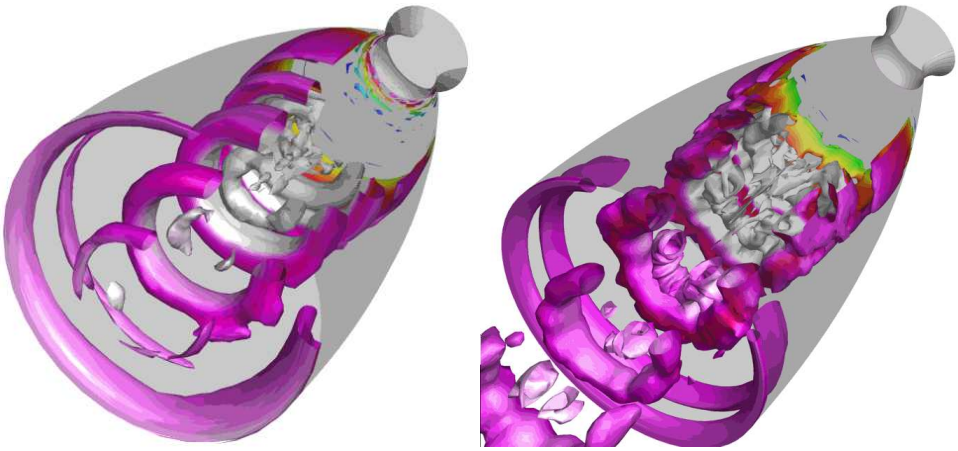

FIGURE 1.6 – Etude de l'influence du modèle RDDES1 (gauche) ; RDDES2 (droite) : visualisations instantanées d'isosurfaces du critère Q colorées par la pression statique en écoulement de tuyère LEATOC (NPR=15,5).

choc d'ordre élevé (WENO 5), d'algorithmes d'intégration implicite en temps (DDADI) et de la modélisation hybride de la turbulence précédemment décrite, qui étend l'approche DES via l'ajout de corrections de réalisabilité et la pondération des échelles turbulentes prise en compte à la fois pour l'expression de la dissipation de l'énergie cinétique turbulente et la viscosité turbulente.

Evolution de la structure globale de l'écoulement de tuyère et transition entre régimes FSS et RSS

Ce chapitre rapporte les résultats relatifs à la caractérisation de l'évolution de la structure globale de l'écoulement décollé en tuyère LEATOC en régime pseudo-transitoire représentatif d'une phase d'allumage ou d'extinction. Les caractéristiques géométriques de la tuyère LEATOC sont tout d'abord rappelées et le domaine de calcul effectivement utilisé pour simuler l'écoulement au sein de cette tuyère est défini. Le domaine modélisé inclu la fin de la partie convergente de la tuyère, l'ensemble du divergent de la tuyère TOC et s'étend sur une distance en aval et dans la direction radiale équivalent à 8 fois et 3 fois le diamètre de la section de sortie de la tuyère respectivement. La résolution et la distribution des points sont également précisées pour les différents maillages utilisés pour l'étude de sensibilité. Le meilleur coût/précision réalisé de façon à pouvoir envisager des simulations sur des temps physiques typiquement de l'ordre de $0,5$ à $0,8$ secondes, est obtenu avec un maillage contenant 200×120 points au sein de la tuyère et 200×180 points dans la zone extérieure en aval de la tuyère. L'utilisation de 72 points dans la direction azimutale a par ailleurs été jugée satisfaisante pour les cas de simulation tridimensionnelle rapportée dans les chapitres suivants (l'utilisation de 144 points ne conduisant qu'à une variation jugée trop peu significative de la structure du champ moyen). A noter que l'analyse des résultats a démontré a posteriori que le positionnement du premier point de calcul en proche paroi ($y^+ < 1$) et le nombre de points utilisé dans la couche limite était satisfaisant.

Cette première simulation en condition transitoire a été réalisée en ne retenant que l'approche URANS en configuration axisymétrique de façon d'une part à minimiser les temps de calcul requis, et d'autre part à mettre en exergue le rôle des mécanismes purement axisymétriques sur l'évolution de la structure de l'écoulement. Une loi de croissance en pallier de la pression génératrice est imposée en entrée du domaine de calcul de façon à parcourir la plage de NPR $[14-25]$. La longueur de simulation relative à chaque pallier à NPR constant a été choisi de façon à correspondre à au moins 10 fois le temps requis pour convecter les structures turbulentes à travers l'ensemble du domaine de calcul. Cette phase transitoire correspond ainsi à un temps physique relativement long de l'ordre de $0,5$ s. La même plage de NPR a été parcourue ensuite selon le même procédé en sens inverse de façon à caractériser le phénomène d'hysteresis observé expérimentalement (existence possible de chaque configuration FSS ou RSS en fonction de la condition initiale).

Le premier résultat fondamental obtenu est la prédiction correcte des valeurs seuil expérimentalement observées pour les NPR correspondant à la bifurcation de l'écoulement d'un régime à l'autre. L'écoulement dans la tuyère bascule ainsi du mode FSS au mode RSS à $NPR = 24$ lors d'une montée progressive en pression génératrice et à $NPR = 14$ lors d'une décroissance de ce rapport de pression. Dans chaque cas, il a été observé que le temps relatif à la bifurcation de l'écoulement d'une configuration à l'autre à NPR constant était relativement court par rapport au temps de la phase transitoire (typiquement de l'ordre de 5 à 6 ms). En configuration FSS, tandis que le choc interne, issu de la région du col de la tuyère conserve une position relativement constante au cours de la phase d'augmentation du NPR, le point de décollement et donc le choc de décollement reculent en aval. Le choc incident interagit ainsi avec le choc de décollement en une position de plus en plus éloignée de la paroi et de plus en plus proche du disque de Mach au fur et à mesure que le NPR augmente. Il a été trouvé que la valeur seuil du NPR où le basculement de régime est observé correspond à une configuration particulière de l'écoulement (dénomée FTQP pour Flow Triple Quadruple Point dans ce

mémoire) où le choc incident, le choc de décollement et le disque de Mach interagissent simultanément, formant un point quadruple. La figure 1.7 illustre la structure caractéristique de l'écoulement ainsi observée et deux étapes de son évolution au cours de la transition qui s'opère à NPR constant.

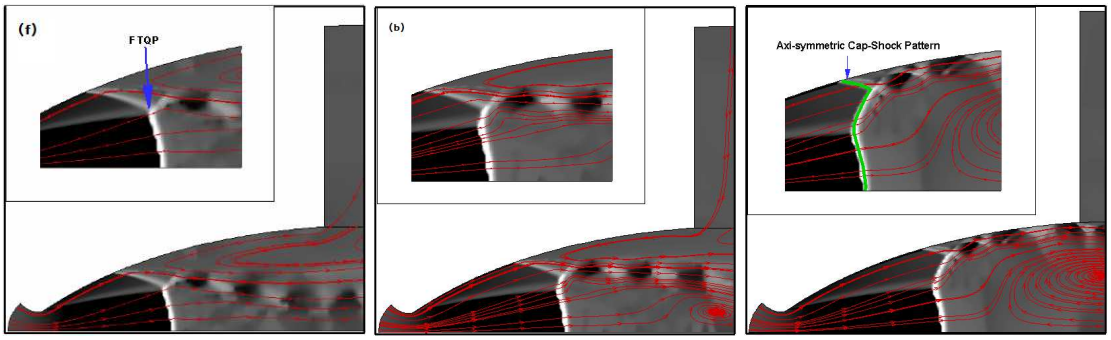

FIGURE 1.7 – Structure caractéristique FTQP (Flow Triple Quadruple Point) obtenue juste avant la transition FSS/RSS (gauche) ; structure intermédiaire montrant la formation de la recirculation centrale et le début du plaquage de la zone décollée vers la paroi (centre) ; régime RSS après la transition FSS/RSS.

Dès que cette configuration particulière est obtenue, la structure évolue radicalement. Le point quadruple se scinde en deux points triple, formant un petit disque de Mach intermédiaire entre le disque de Mach principal près de l'axe et le choc de décollement. Ce petit choc droit bascule alors rapidement en choc oblique tandis que le point de décollement et le choc de décollement recule très rapidement en aval, passant d'une position en amont du disque de Mach à une position en aval de celui-ci. Il a été vérifié que ce changement de la structure de l'écoulement était corrélé par ailleurs à une brusque modification de la distribution radiale de la quantité de mouvement pouvant expliquer la formation de la recirculation en aval du disque de Mach, également caractéristique de la configuration RSS. En simulant la phase pseudo-transitoire de décroissance du NPR, il a non seulement été observé que la nouvelle valeur seuil de NPR=14 correspond également à l'apparition de cette configuration limite FTQP, après basculement, mais aussi que les mêmes étapes de la transformation de l'écoulement sont parcourues, en sens inverse.

Etude du régime de séparation libre

Ce chapitre synthétise les résultats de l'analyse de l'instationnarité d'un jet de tuyère LEA-TOC simulé en configuration tridimensionnalle en régime FSS établi (NPR constant), pour deux niveaux de rapport de pression $NPR = 15,5$ et $NPR = 19$, correspondant à des niveaux de charges latérales croissants.

La confrontation des résultats numériques et expérimentaux disponibles a tout d'abord été réalisée et est illustrée sur la figure 1.8. Elle a permis de vérifier que la modélisation retenue permettait de reproduire de façon satisfaisante, non seulement la distribution pariétale de la pression statique moyenne et de sa variance, mais aussi la distribution de probabilité (quasi-gaussienne) de ces fluctuations de pression. L'analyse spectrale des fluctuations de pression pariétales corroborent également les tendances observées expérimentalement. Tandis que les

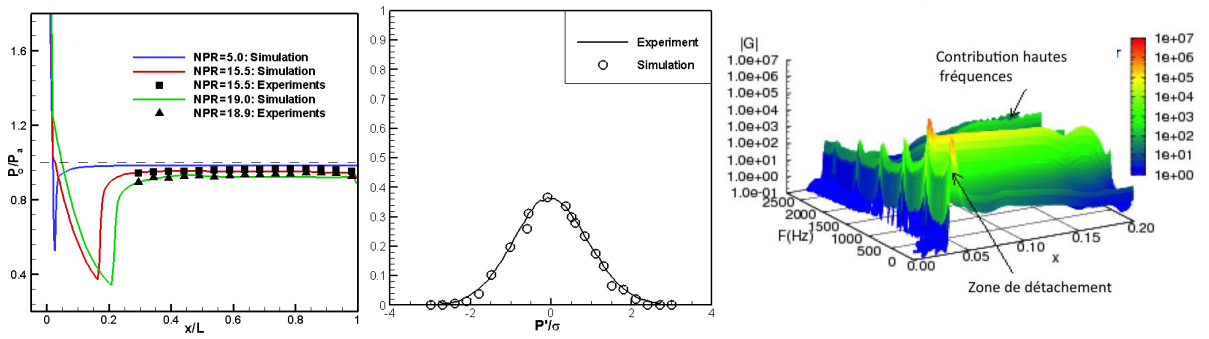

FIGURE 1.8 – Distribution de pression pariétale moyenne (gauche), distribution de la densité de probabilité des fluctuations de pression en $X/L = 0,73$ (milieu) et spectres des fluctuations (gauche) pour le cas à NPR=15,5.

fluctuations restent de très faible amplitude dans toute la partie initiale de la tuyère, elles présentent un pic au niveau du point de séparation et sont dominées par les basses fréquences ($< 1kHz$) qui restent dominantes sur l'ensemble de la peau de la tuyère. Cette gamme fréquentielle correspond au battement du choc de séparation. Tandis que la contribution des hautes fréquences est initialement négligeable, elle augmente progressivement au fur et à mesure que l'on progresse à travers la zone détachée vers la section de sortie. L'amplitude et la valeur centrale de la plage de fréquences dominantes augmentent avec le NPR en accord avec les observations expérimentales (passant typiquement de 20 Hz à 50 Hz au niveau du point de séparation pour NPR=15,5 et 19 respectivement). Les macro-structures observées en aval de la tuyère présentent une distortion importante, quasi-périodique dans la direction azimutale. Cette morphologie, précédemment illustrée sur la figure 1.6, reste en relativement bon accord avec des observations expérimentales réalisées sur des couches de mélanges axisymétriques à des nombres de Mach convectif similaires. On notera néanmoins que la résolution reste limitée dans cette zone de l'écoulement. L'interprétation du caractère physique de ces structures cohérentes reste discutable et n'est pas en accord avec l'ensemble des observations faites pour des conditions similaire de nombre de Mach convectif élevé (de l'ordre de 0,8 typiquement) qui tendent à penser uniquement à l'existence de structures cohérentes plus petites que celles ici observées. La présence de telles structures apparaît ici néanmoins être associée au battement aléatoire du jet à grande échelle qui constitue un ingrédient nécessaire à la boucle de rétroaction pilotant l'instationnarité globale de l'écoulement. Un résultat original obtenu au cours de cette étude est l'observation d'un changement relativement important de la morphologie de ces structures cohérentes et de leur dynamique avec l'augmentation du NPR. La figure 1.9 illustre par exemple que ces macrostructures présentent un aspect essentiellement axisymétrique simplement déformé azimutalement à NPR modéré (NPR=15,5) tandis que des modes obliques beaucoup plus marqués apparaissent à NPR plus élevé (NPR=19). Dans ce dernier cas, la propagation d'instabilités en amont est facilitée. Ce changement de comportement est ainsi consistant avec le fait que le niveau de charges latérales augmente avec le NPR dans ce régime FSS. Ces résultats suggèrent donc un rôle prépondérant de la dynamique tourbillonnaire (fonction du nombre de Reynolds et du Mach convectif qui augmentent avec le NPR) au sein des couches cisaillées pour expliquer la forte variation du niveau d'instabilité au sein de la tuyère en fonction du NPR.

Un autre résultat original est l'observation d'une déformation azimutale de la ligne de séparation (en amont du point triple), illustrée sur la figure 1.10. Elle produit des ondulations

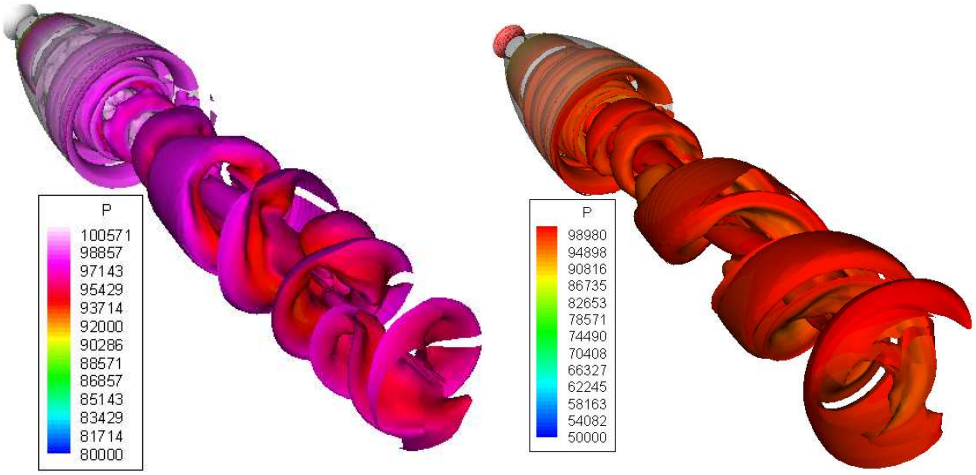

FIGURE 1.9 – Evolution de la morphologie des macrostructures dans les jets de tuyère LEATOC en régime FSS : isosurface du critère Q colorées par la pression statique à $NPR = 15,5$ (gauche), $NPR = 19$ (droite).

atypiques, quasi-périodiques, (en forme de tipi), qui se déplacent en bloc de façon aléatoire dans la direction azimutale. L'observation de ce phénomène n'a précédemment été rapportée que sur des expériences de gaz chauds. Notons que cette forme caractéristique devient néanmoins moins marquée et que les longueurs d'ondes spatiales caractéristiques associées changent sensiblement lors d'un accroissement de la résolution azimutale utilisée pour la simulation. Seuls des calculs à plus haute résolution permettraient de conclure définitivement sur la topologie exacte de cette déformation de la ligne de séparation et sur sa dynamique. Néanmoins, il est à noter que cette ligne de séparation est située suffisamment en amont du disque de Mach et le développement d'instatabilités de type Kelvin-Helmotz s'avère suffisamment rapide pour que les structures tourbillonnaires interagissent directement avec le choc réfléchi issu du point triple. Ainsi, cette déformation azimutale de la ligne de séparation apparaît-elle corrélée avec la déformation prononcée des structures en rouleau observées plus en aval dans la zone de jet libre.

Finalement, les charges latérales obtenues par intégration du champ numérique de pression pariétale fluctuant présentent les caractéristiques qualitatives attendues. Les composantes transverses sont décorrélées, tandis que la distribution de probabilité de l'amplitude de la fluctuation de charge suit une loi de Rayleigh. La décomposition en mode de Fourier azimutaux, reportée sur la figure 1.11 pour le cas à $NPR = 19$, indique que l'ensemble des modes agissent au niveau du point de séparation mais que seul le mode 0 (axi-symétrique) conserve une influence importante à travers la zone de recirculation. Ce mode 0 est par ailleurs dominé par les contributions basses fréquences ($< 50Hz$).

D'après cette analyse du comportement de l'écoulement de la tuyère LEATOC en régime FSS, l'augmentation du niveau de charges latérales avec le NPR apparaît être principalement reliée à, d'une part une perte d'axisymétrie de plus en plus prononcée de la ligne de séparation, dont la longueur augmente progressivement du fait du recul de sa position vers l'aval de la tuyère, d'autre part une modification des modes d'instabilités se développant dans le jet en aval au fur et à mesure que le NPR augmente.

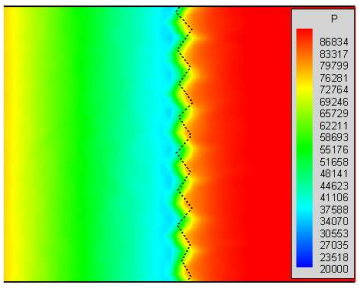

FIGURE 1.10 – Déformation de la ligne de séparation en forme de tipi : distribution de pression pariétale autour de la ligne de séparation en régime FSS à $NPR = 15,5$ à l'instant $T = 47,8 L_d/U_t$ (position initiale de la ligne de séparation indiquée en pointillés).

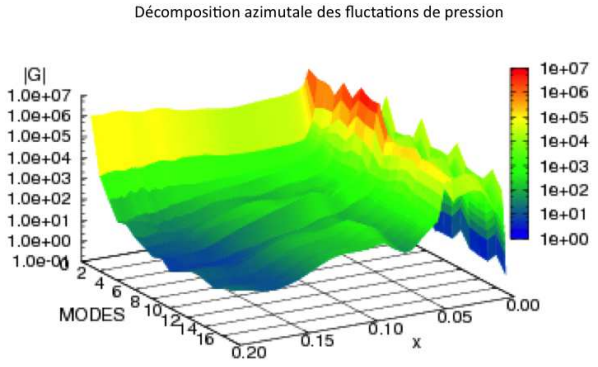

FIGURE 1.11 – Décomposition azimutale des fluctuations de pression pour le cas $NPR = 19$.

Etude du régime de séparation restreinte

Cette section synthétise dans un premier temps les résultats de l'analyse effectuée en configuration tridimensionnelle de l'écoulement pendant la phase pseudo-transitoire de montée en pression génératrice sur la plage $NPR = [12-25]$. Cette analyse a permis de confirmer les observations faites en configuration axisymétrique sur les mécanismes pilotant la transition FSS/RSS (obtention de la configuration FTCS précédemment décrite). Il est à noter qu'aucune coexistence des configurations FSS et RSS n'a pu être observée au cours de cette simulation, mettant ainsi en défaut l'hypothèse selon laquelle cette coexistence pourrait être une cause du premier pic de charges latérales observées avant la transition FSS/RSS. Les niveaux rms de charges latérales obtenus sur l'ensemble de la plage de NPR parcourue sont par ailleurs en bon accord avec les données expérimentales, bien que les temps caractéristiques de montée en pression soit différents dans les deux cas. Ces résultats semblent donc confirmer que le type de transitoire n'a une influence significative que s'il opère sur des temps relativement courts.

Une classification des différents sous-régimes observables en régime RSS est ensuite proposée, en fonction du niveau de charges latérales (faible ou fort) associé. La suite de ce chapitre se consacre ainsi à la présentation des résultats relatifs à ces différents sous-régimes RSS simulés en configuration d'écoulement établi. Le premier sous-régime (simulé pour NPR=25,5, 30 et 41,6) correspond à des écoulements présentant de faibles niveaux de charges latérales. Les pics de charges latérales en régime RSS sont observés pour les second et troisième sous-régimes (analysé pour NPR=38 et NPR=46 respectivement) et correspondent respectivement à des situations où soit la recirculation secondaire, soit la recirculation primaire s'ouvre à l'atmosphère ambiante. Dans l'ensemble des cas simulés, les résultats statistiques (champ moyen et rms) obtenus sont en bon accord avec les données expérimentales (voir exemple sur figure 1.13), de même que le spectre des fluctuations de pression. L'évolution qualitative de la nature des oscillations de pression pariétale a pu être analysée. Le signal de pression au niveau de la ligne de séparation présente des pics caractéristiques du passage du choc, tandis que des oscillations aléatoires de plus faible amplitude s'ajoutent progressivement au fur et à mesure que l'on progresse à travers la zone détachée le long de la paroi.

Pour la classe d'écoulement correspondant au premier sous-régime, une tridimensionnalisa-

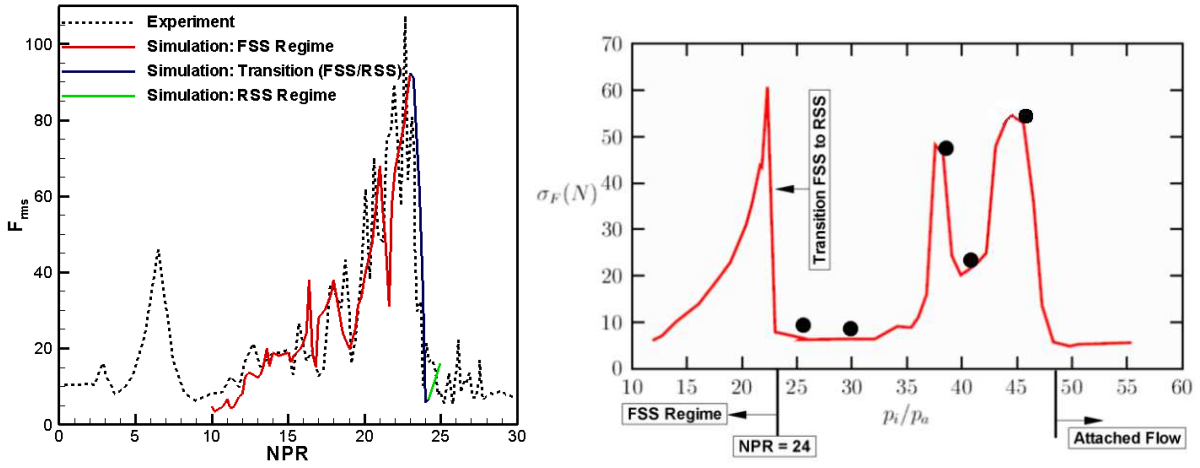

FIGURE 1.12 – Evolution des charges latérales : régime transitoire en phase d'amorçage de tuyère (gauche), régime stabilisé (ligne rouge : données expérimentales, points noirs : données de la simulation) (droite).

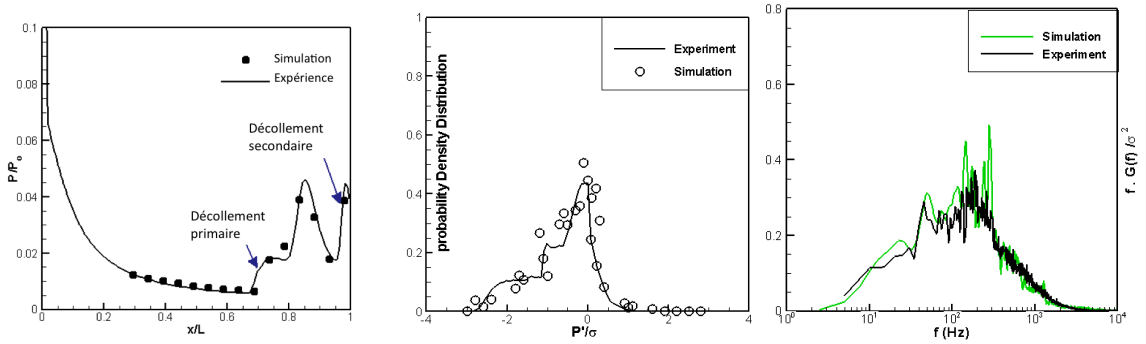

FIGURE 1.13 – Distribution de pression pariétale moyenne à $NPR = 38$ (gauche), densité de probabilité des fluctuations en $x/L = 0,98$ à $NPR = 25,5$ (milieu) et densité spectrale de puissance en $X/L = 0,93$ à $NPR = 25,5$.

tion très prononcée de la zone de recirculation en aval du système de chocs en chapeau est déjà observée et est illustrée sur la figure 1.14. L'augmentation de l'activité des charges latérales en fonction du NPR a été associée principalement à l'augmentation de la probabilité d'ouverture des bulles de recirculation secondaire ou primaire (end effect) à l'atmosphère ambiante. Dans un tel cas, l'ouverture de la zone de recirculation, à plus faible pression statique que la pression ambiante, induit une brusque oscillation de la couche supersonique et une brusque remontée d'information d'une telle augmentation de pression à travers la zone de recirculation centrale subsonique, et donc un brusque réajustement de la position du disque de Mach. Dans ce cas, l'étendue de la zone d'excursion de la structure de choc augmente fortement tandis que la dissymétrisation se traduit par un fort basculement du choc comme l'illustre la figure 1.15.

Comme pour le régime FSS, seul le premier mode de la décomposition azimutale des fluctuations de pression présente une contribution véritablement significative aux charges latérales en régime RSS. L'analyse spectrale permet en fait d'interpréter le mouvement instationnaire de la structure de l'écoulement comme un basculement aléatoire de l'ensemble de la structure de choc en chapeau superposé à une pulsation axisymétrique dans la direction longitudinale de l'écoulement séparé.

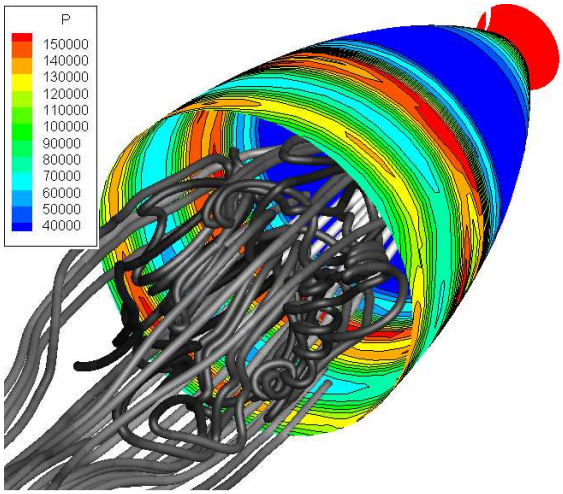

FIGURE 1.14 – Tridimensionnalisation de la bulle de recirculation en aval du disque de Mach (distribution de pression pariétale et lignes de courant instantanées à $T = 47,4 L_d/U_t$ à $NPR = 25,5$).

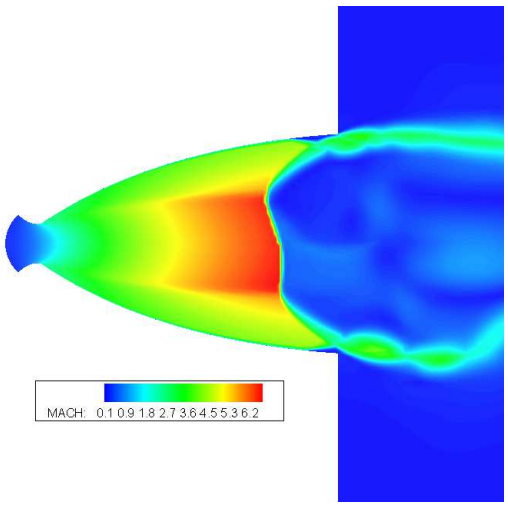

FIGURE 1.15 – Accentuation de la dissymétrisation de la structure (basculement de choc) en régime "end effect" en $T = 2,52 L_d/U_t$ à $NPR = 46$.

Notons finalement qu'en décomposant les charges latérales en contribution longitudinale, il a été trouvé que, tant que l'écoulement reste attaché, le faible niveau de charges latérale peut être associé à une quasi-compensation entre contributions positives et négative moyennes obtenues successivement le long de la tuyère. A chaque position longitudinale, cette charge moyenne correspond à un léger déphasage du signal de pression enregistré à différents points de la couronne azimutale correspondant à cette position. A l'inverse, dans le cas où une poche de recirculation s'approche de la sortie de la tuyère, elle induit un pic d'activité qui ne s'équilibre plus avec l'ensemble des contributions moyennes trouvées en amont. Ce processus d'équilibre ou de déséquilibre, synthétisé sur la figure 1.16 dépend de la position relative de la sortie de la buse par rapport à la distribution moyenne de pression résultant de la succession de réflexion d'ondes de compression et de détente entre la paroi de la tuyère et le tourbillon central subsonique.

Synthèse et perspectives

Le dernier chapitre de ce mémoire présente les principales conclusions de l'analyse des résultats de simulation des écoulements détachés de tuyère LEATOC. Le compromis coût/précision réalisé a permis de réaliser la simulation des écoulements pour une large plage de niveaux de surdétente, à la fois représentatifs de temps physiques suffisamment longs pour identifier clairement les basses fréquences en condition d'entrée stabilisée et en conditions représentatives d'une évolution transitoire de l'écoulement soumis à une variation des conditions d'entrée.

Les résultats obtenus sont en bon accord avec les données expérimentales disponibles, tant sur les niveaux moyens et les fluctuations de pression pariétale que sur les niveaux rms de charges latérales. L'évolution temporelle de la morphologie globale de l'écoulement transitant entre les deux régimes et le phénomène d'hysteresis ont pu être observés numériquement. La configuration critique correspondant au basculement entre les deux régimes correspond à l'interaction du choc incident naissant au niveau du col de la tuyère avec le point triple reliant le

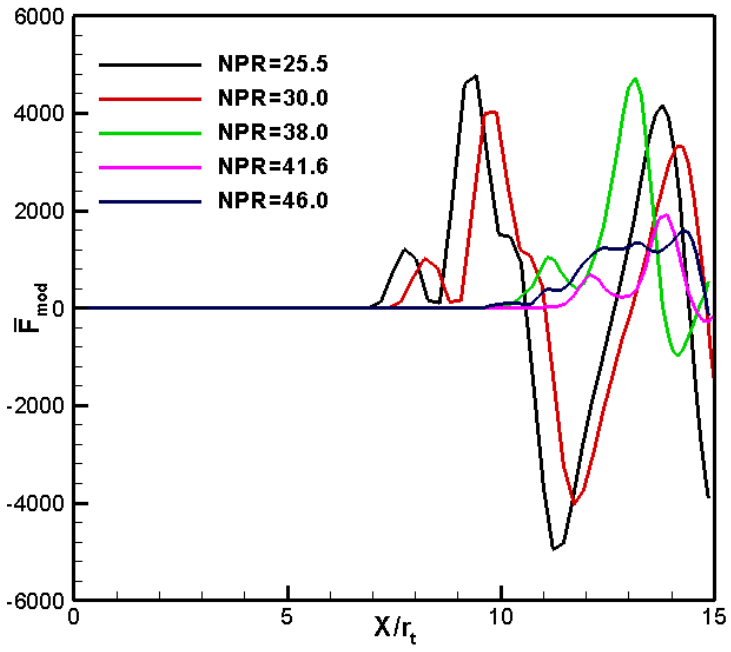

FIGURE 1.16 – Décomposition des contributions de charges latérales dans la direction longitudinale en fonction du NPR.

choc de décollement, le disque de Mach et le choc réfléchi.

L'hypothèse de la coexistence des deux régimes a par ailleurs été mise en défaut pour expliquer le premier pic de charges latérales apparaissant lorsque le rapport de pression augmente avant la bifurcation du régime de décollement libre à restreint. Les résultats obtenus conduisent à associer en fait ce pic à une augmentation progressive de l'asymétrie et de l'instabilité de la ligne de décollement en régime de décollement libre (déformation en forme de tipi), couplée à une modification des principaux modes d'instabilité dans la couche de cisaillement en aval de la structure de choc. Les charges aérodynamiques associées résultent essentiellement de la contribution des basses fréquences du premier mode azimutal.

En régime de décollement restreint, les pics de charges latérales apparaissent être liés à l'aspect fortement tridimensionnel de la recirculation subsonique en aval du disque de Mach et de l'ouverture de la seconde ou de la première zone de décollement à l'atmosphère. Par rééquilibrage violent de leur niveau de pression avec le niveau de pression atmosphérique, transféré via cette recirculation subsonique, un mouvement d'inclinaison et de précession aléatoire de la structure est induit.

Le rapport coût/précision qu'offre la mise en oeuvre du modèle proposé offre de nombreuses perspectives à court terme de ce travail de thèse. Celles-ci recouvrent à la fois des aspects fondamentaux (étude de la dynamique d'ordre bas de l'écoulement, caractérisation des modes d'instabilités privilégiés en fonction du NPR) que des aspects appliqués (étude de l'influence du type d'amorçage transitoire sur l'évolution des charges, mise en oeuvre de stratégie de contrôle des charges latérales par soufflage au niveau de la lèvre de buse...).

Chapitre 2

Introduction

Framework of the Study

The study reported in this manuscript is a contribution to the numerical simulation of turbulent shock-induced separated flows in a thrust optimized contour nozzle operating under over-expanded conditions.

Shock Wave / Boundary Layer Interaction

The characteristics of a supersonic turbulent boundary layer are drastically altered in the presence of an adverse pressure gradient. It adapts to the higher-pressure level by means of a shock-wave system. Flow separation occurs when the turbulent boundary layer cannot negotiate the adverse gradient imposed by the inviscid outer flow and involves complex shock wave-boundary layer interactions. In high speed turbulent flow regime, the phenomenon of shock-wave and turbulent boundary layer interactions is frequently encountered in many internal and external aerodynamic configurations and has been a subject of research interest on a broad scale. The large amount of experimental results on shock wave/boundary layer interaction in two-dimensional flows has allowed a clear identification of the role played by the main parameters involved in the interaction process. The situation is not so satisfactory in 3D flows because of the difficulty to establish a clear physical description of the flow organisation.

The various two-dimensional flow configurations which involve shock wave and boundary layer interaction can be typically categorized in four basic interactions : (i) the ramp flow (Fig. 3.2), (ii) the impinging-reflection shock (Fig. 3.5), (iii) the normal shock (turbomachine cascades, air intakes (channel), supersonic diffusers, shock tubes and transonic profiles) and (iv) the pressure jump as in over-expanded nozzle (Fig. 3.6-3.7). These interactions can lead to high pressure rise and heat loads, as well as regions of separated flow. The motion of shock-system is moderate when there is no separation, but can be very important in the presence of separation zones. In addition, it has been found that shock waves are subjected to motions yielding frequencies much lower than the characteristic frequencies of the incoming boundary layer. In many aeronautical situations, this low-frequency unsteadiness may generate large fluctuating forces that can be of severe magnitude and has therefore been the main topic of many studies. A particular example of low-frequency unsteadiness has been reported for shock-induced separated flows in rocket nozzle operating at ground level. The resulting high level fluctuating loads, i.e. side-loads, are undesirable and may sometimes lead to structural damage. Several attempts in the past have been made to understand these separated flows and side-loads problems ; however, the key physical mechanism remains unclear.

Towards Rocket Nozzles

The performance of **rocket engines** depends strongly on the design of the expansion nozzle. In order to increase the vacuum performance, it is desirable to achieve high expansion rates. However, during the start-up / shut-down or at low altitude operation, the ratio of the chamber pressure to the ambient pressure may be insufficient to insure full flowing at the nozzle exit. Turbulent boundary layer separation may then occur along the nozzle wall. The nozzle of the first stage rocket engine of present launchers is usually designed in order to achieve full flowing at sea level for the nominal chamber pressure. For a given pressure, the corresponding nozzle area ratio may be estimated by using classical separation criteria such as Schmucker's [131] with some safety margin. However, the engine will inevitably encounter flow separation during transient start-up and shut-down. The separated flow usually exhibits, in some pressure ratio range, a strong unsteadiness and sometimes a loss of symmetry which generates lateral forces, called side loads. Practically, the upper limit of the area ratio is defined by the acceptable level of the side-loads when operating in these off-design conditions. One needs therefore to master the flow separation and side load problems. The first stage engine of modern launch vehicles usually involves a **thrust optimized contour (TOC) nozzle** which offers the advantage of a high thrust/mass factor.

A Brief Survey of Previous Studies in TOC Nozzle

The flow in such a TOC nozzle is characterized by the existence of an internal shock emanating from a region close to the throat. Flow separation and side-load activities in thrust-optimized contour nozzle have been the subject of several experimental and numerical studies in the past [4], [5], [11], [21], [25]-[28], [40], [53]-[55], [58], [59], [62], [63], [67], [73], [93], [94], [96]-[106], [108]-[111], [121]-[123], [131], [134], [140], [143], [152]. The work of Nave and Coffey [98] on the J-2S TOC nozzle demonstrated clearly the existence of two different flow regimes namely the Free Shock Separation (FSS) where the boundary layer separates from the nozzle wall and never reattaches back to the wall, and the Restricted Shock Separation (RSS) characterized by a recirculation bubble with reattachment on the nozzle wall (see Fig. 3.6-3.7). During the transient start-up phase, the separated flow is first governed by the FSS structure which is then replaced by the RSS structure when the chamber pressure exceeds a certain critical value of the nozzle pressure ratio (NPR), i.e. total chamber pressure / ambient pressure P_o/P_a. This NPR highly depends upon the nozzle contour. The hysteresis of the FSS to RSS transition was also clearly identified. In 1998, the paper of Frey and Hagemann [53] puts emphasis on the distinction between FSS and RSS flows and on the RSS flow structure recovered by numerical simulations. This RSS flow regime involves a special shock pattern called cap-shock followed by a trapped vortex surrounded by an annular supersonic jet (see Fig. 3.7). The existence of a reverse flow (trapped vortex) in the plume of thrust-optimized contour nozzles was first reported by Chen et al. [21]. However, no explanation regarding the generation of this reverse flow was provided. Later on, Nasuti and Onofri [96], [97], [102] & [103] stressed the role of the centreline vortex trapped behind the central normal shock and suggested that the flow upstream of the Mach stem is not uniform so that the shock cannot be straight and its strength varies along the shock profile. Hence, a rotational flow appears downstream of the Mach stem with velocity and entropy gradients. Frey and Hagemann [55] & [62] proposed to interpret the cap-shock pattern as an inverse Mach reflection of the weak internal shock at the centreline. The resulting curvature of the Mach stem in inverse Mach reflection phenomenon induces vorticity according

to Crocco theorem. Furthermore, they proposed that this cap-shock pattern is the key driver for transition from FSS to RSS flow configuration [55], [62] & [63]. Later on, Moríñigo et al. [94] reported that transition from FSS to RSS occurs upon the fulfilment of two flow conditions : the axis of the separated jet should be deflected towards the wall ; and the jet boundary must intercept it. This latter explanation for transition process seems to be the consequence of cap-shock pattern. Recently, Nasuti and Onofri [97] emphasized that the importance of the internal shock is more on a quantitative rather than on a qualitative level and concluded that the occurrence of flow reattachment at the wall depends more on the upstream pressure gradient rather than simply on the existence or not of an internal shock. In view of such different phenomenological interpretations, **a better understanding of this complex transition process (FSS to RSS) still requires more consideration**. The critical nozzle pressure ratio (CNPR) at which this transition takes place highly depend upon the nozzle contour. However, all TOC nozzle contours exhibit RSS flow regime for NPR $\geq$ CNPR. Starting from the pioneering work of Nave and Coffey [98], it is known that both separated flow regimes, in some particular pressure ratio range, exhibit strong unsteadiness and sometimes a loss of symmetry which eventually generate side-loads. The measurements of side-loads, performed on either sub-scale or full-scale thrust-optimized nozzles, show several peaks when plotted with respect to NPR [54], [63], [98], [101] & [106]. Although some explanations have been given, the origins of these peaks are still unclear. Östlund [106] reported that the side-load peaks are characterised by their high level and impulsive occurrence and are radically different for different nozzle contours. Frey et al. [54] suggested that **a dissymmetric transition FSS to RSS**could be a possible explanation for an increased level of side-loads. However, further experimental and numerical investigations are still required to validate this hypothesis. In an extensive experimental investigation by Nguyen et al. [101], the physical origins of side loads in thrust-optimized nozzle were highlighted by the analysis of wall pressure fluctuations. They reported that **"the high level of side-loads at the end of the FSS regime are attributed to a high unsteadiness of the separation line rather than an oscillation between the FSS and RSS regimes, which seems impossible due to the strong hysteresis of FSS to RSS transitions [101]"** (see Fig. 2.1). Various experimental studies [54], [63], [98], [101] & [106] have also demonstrated that, soon after the transition process, the RSS flow regime is characterized by a relatively low level of side-load activities. A similar behaviour has also been observed in the numerical simulations of RSS flow regime performed by Deck [25] (see also [27]). More recently, Wang [152] reported that in the NPR range, soon after the transition, the recirculation bubble attached to the nozzle wall stabilizes the RSS flow regime and the resulting reattachment line is observed to be more or less symmetric. It should be noted that the side-load activities computed by Wang [152] were based on transient flow conditions, re-producing more or less the start-up behaviour of a real engine. The drawback of such an approach is that it precludes a classical analysis of the flow unsteadiness considered as the fluctuations superimposed on a steady mean flow. Thus, **no clear explanation regarding the unsteady behaviour of RSS flow regime and the corresponding low level of side-loads has clearly been reported till now**. In the RSS regime, the multiple reflections of compression and expansion waves trapped in the supersonic region between the nozzle wall and the central annular vortex may induce a second recirculation bubble whose existence was demonstrated experimentally by wall streamlines visualizations [100]. Furthermore, Nguyen [100] (see also Nguyen et al. [101]) reported that when the pressure ratio increases, this system of two recirculation bubbles moves downstream towards the nozzle exit, and results in two peaks in the side-load activities, as shown in Fig. 2.1. The first peak is attributed to the random opening/closing of the

second recirculation bubble when the secondary reattachment line reaches the nozzle lip. However, **this flow regime still requires more investigation to better understand the physical mechanisms which effectively cause this strong global unsteadiness**. Following the evacuation of the secondary bubble, when the reattachment line corresponding to the main/primary recirculation zone reaches the nozzle lip, the recirculation bubble opens randomly to the ambient atmosphere. The resulting flow regime is known as **end-effect regime**. This flow regime was initially observed and reported by Nave and Coffey [98] on J-2S TOC nozzle. Nguyen et al. [101] demonstrated that this end-effect regime is characterized by a global quasi-axial pulsation which induces a very high level of fluctuations. In this case, the side loads seem to be induced by small pressure difference superimposed upon a large amplitude axi-symmetric global unsteadiness. From a three-dimensional URANS simulation Moríñigo and Salva [93] have observed such a large amplitude self-sustained oscillation in a study of the J-2S TOC nozzle. More recently, Deck [28] has also performed a DDES simulation of the strong global unsteadiness which occurs in this end-effect regime in LEATOC nozzle. This pulsatory regime was also reproduced by the axi-symmetric URANS simulation of Nebbache and Pilinski [99].

Motivation

The aforementioned brief survey of shock-induced separated flow in rocket nozzle indicates that despite of several experimental and numerical studies, the flow physics is not completely known and requires further investigation. The present work addresses the above mentioned highlighted issues in the framework of Computational Fluid Dynamics (CFD). These points have been the main motivation of this research work and are summarized hereafter :

1. The cause of flow transition from FSS to RSS regime and its reverse process ? To answer this, a wide range of NPR (11-25) has been considered on a thrust optimized contour (LEATOC) nozzle. The flow field and momentum balance has been analysed to investigate the hysteresis process and is reported in Chapter 6.
2. The key physical mechanism responsible for the increasing unsteadiness/side-loads in FSS flow regime (before the transition process) ? This is addressed by investigating more deeply the flow regime at three particular NPR values in the FSS range which are reported on the side-load chart of LEATOC nozzle in Fig. 2.1. For these cases, the unsteady wall pressure field is analysed to determine the physical origin of the resulting side-load activities (see Chapter 7).
3. Appearance of flow dissymmetry (if any) and side-load activities during transition process ? The transient transition from FSS to RSS has been reproduced in the NPR range 10-25, by increasing progressively the inlet stagnation pressure. Evolution of the computed side-loads activities can thus be put in correspondence with the global flow behaviour during the transition process and is given in Chapter 8.
4. Flow unsteadiness and variation of side-load activities in RSS flow configuration ? An extensive investigation of the flow at five NPR along the broad range of RSS flow has been performed (see points reported on the side-load chart of LEATOC nozzle in Fig. 2.1). The examination of the unsteady wall pressure field lead to the better identification of mechanisms leading to the appearance of side loads (see Chapter 8).

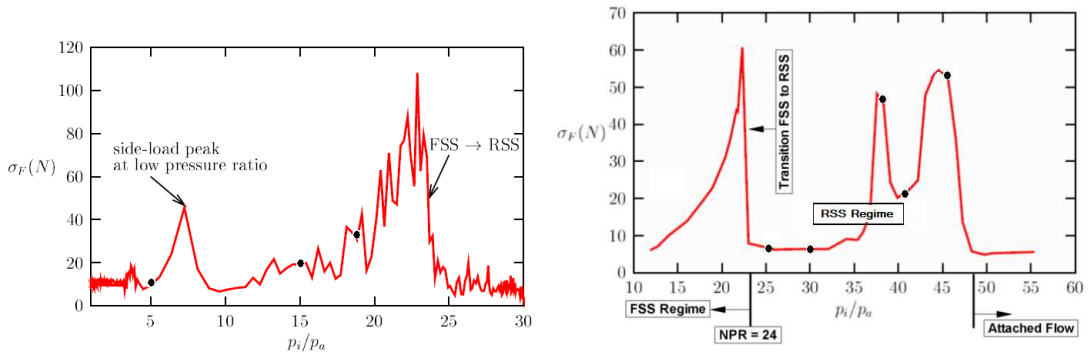

FIGURE 2.1 – Evolution of RMS (σ_F) side-loads with respect to the nozzle pressure ratio, during start-up of LEATOC nozzle with (Left) transient & (Right) stabilized inflow conditions, respectively [101].

Selection of Numerical Tools

This research work aims at investigating globally various aspects of shock-induced separated nozzle flows which occur in a wide range of NPR in LEATOC nozzle. This is a thrust optimized contour (TOC) nozzle and has been experimentally investigated at the Laboratoire d'Etudes Aérodynamiques (LEA), Poitiers, France [101]. These shock-induced separated flows exhibit high Reynolds number and involve low frequency large scale unsteadiness and therefore require sufficiently long integration time (time samples) in order to perform a reliable statistical analysis. Direct Numerical Simulation (DNS) and Large Eddy Simulation (LES) of such complex flows carried out in a wide range of NPR was obviously not possible. Traditional Reynolds Averaged Navier-Stokes (RANS) approaches do not attempt to resolve any turbulent flow structures, but model the effect of turbulence on the mean flow in terms of representative mean turbulence scales. As a result, all spectral effects are lost in the time averaging process. The unsteady variant of this, URANS, although managing to resolve non-stationary mean flows, still does not appear to be sufficiently suitable for a representative resolution of turbulence. Accordingly, it seems viable to use hybrid methods, such as Detached Eddy simulation (DES), to capture large scale motion of these massively separated flow configurations. Such separated flows exhibit strong shock-boundary layer and shock-turbulence interactions at high Reynolds number. In such conditions, turbulence models based on one- or two-equations may loose the realizability property. In order to cope with this problem, a new version of Detached Eddy Simulation (DES) based on the two-equation $k-\omega$ model with realizability corrections is proposed in this research work. In addition, a fifth order monotonicity preserving weighted essentially non-oscillatory (MP-WENO) numerical scheme is used to achieve high accuracy results and overcome the lack of efficieny of too dissipative lower order schemes. Finally, a second order implicit scheme for time discretization has been used to achieve a long time of integration. Of course, in DES, we are also restricted by the severe limit of grid resolution required in particular in the azimuthal direction in order to switch into the LES mode of DES. In fact the use of these alternative type of modelling rigorously requires enough spatial resolution to fulfil the LES requirements ideally. Deck [25], in his pioneering DES for LEATOC nozzle used only 72 grid points in the azimuthal direction, whereas in his recent DDES of end-effect, 144 grid point were used [28]. For that study, at best, the time integration was performed up to 0.2 s only. In fact, Deck [28] estimated that in the case of LEATOC nozzle, 7200 grid points are required to satisfy the criterion of LES

resolution in the azimuthal direction. In practice, because of a limited computational power, we need to make the compromise to switch the DES into a hybrid method with less number of grid points in the azimuthal direction in order to address the wide range of NPR and the longest times of integration as possible. For this study, the minimal satisfying resolution which gives the opportunity to capture the main unsteady features of the flow-field was found to be 72 points in the azimuthal direction. It allowed us to reach sufficiently long integration time (up to 0.8 s) for each NPR considered to carry out a representative characterization of the unsteadiness.

Organization of This Thesis

This dissertation is organized as follows :

1. **Shock-induced separated flows**
   This chapter contains a bibliographic review of different shock-induced separated flow configurations, with a special attention on over-expanded rocket nozzle flow regimes. This includes the advances addressed in the literature in order to understand these complex flow regimes.
2. **Numerical Methods and Turbulence Modelling**
   This part of the dissertation presents the description of numerical tools used to perform the simulations. The various numerical schemes and turbulence modelling techniques, including the proposed DES approach, which have been implemented in the code TGNS3D, are presented in this chapter.
3. **Validation of Numerical Tools**
   In this chapter, a wide range of tests cases including a vortex advection, shock-induced separated flows in axi-symmetric and rectangular nozzles are performed to validate the numerical schemes and turbulence models that are implemented in code TGNS3D. Different issues and problems related to these numerical tools are discussed in the framework of shock-induced separated flow configurations.
4. **Evolution of Flow Structure in Over-Expanded Rocket Nozzle**
   The detailed characteristics of LEATOC nozzle, its mesh generation, computational domain and the prescribed boundary conditions are documented in this chapter. This is followed by an overall analysis of the flow structure appearing in the case of FSS and RSS flow regimes, and of its evolution during the forward and reverse transition processes between these flow regimes.
5. **Free Shock-Induced Separated Flows**
   The unsteady behaviour of free shock separated flow regime is investigated and reported in this part of the thesis. In particular a comparative study at three different NPR values has been made to characterize the flow unsteadiness and investigate the origin of the resulting side-load activities.
6. **Towards Restricted Shock Separated Flow Regime**
   This chapter is divided into two major parts, (i) the flow transition process from FSS to RSS with transient inflow conditions and (ii) restricted shock separation. The section focuses on the differences of behaviour of side-load activities and flow unsteadiness appearing during the flow transition process and more specifically in RSS configuration.

7. **Conclusions**
   This section summarizes the main conclusions drawn from the numerical investigation of shock-induced separated flows in rocket nozzle operating under over-expanded conditions.

Chapitre 3

Phenomenology of Shock-Induced Separated Flows

Appearance of shock-waves is almost inevitable in transonic or supersonic flows. They are provoked by a change in the flow direction (as at the compression ramps of a supersonic air intake or at a control surface), an increase of the downstream pressure as on a transonic wing, a pressure jump as in a rocket nozzle operating under over-expanded conditions, or a brutal deceleration as in front of the nose of a re-entry vehicle. In addition, these interactions with the boundary layers may lead to flow separation with possible occurrence of large scale unsteadiness. The temperature rise across the shock-waves most often affects the thermodynamics properties of gas, and is the origin of high level of heat transfer [31]. The large amount of experimental results on shock wave/boundary layer interaction in 2D flows has allowed a clear identification of the role played by the main parameters involved in the interaction process. The situation is not so satisfactory in 3D flows because of the difficulty to establish a clear physical description of the flow organisation.

Basic Interactions : (Oblique) Shock-Wave & Boundary Layer

One can categorize them in four basic interactions [33] : the ramp flow (Fig. 3.2), the impinging reflecting shock (Fig. 3.5), the normal shock case (e.g. transonic profile) and the pressure discontinuity resulting from adaptation to a higher downstream pressure level, as in over-expanded rocket nozzles (Fig. 3.6 & 3.7). The first two categories are the most studied configurations and a brief overview of the main characteristics of these flows is given in the following sections.

3.1 Shock Wave and Boundary Layer Interaction in Compression Ramp and Flat Plate Case

3.1.1 Compression Ramp Flow (2D)

In the case of two-dimensional ramp / compression corner, when a high speed flow turbulent boundary layer approaches to the inclined wall (compression corner), a shock system is generated as a result of the flow deflection. When the angle of ramp (let say α) is relatively small, the overall flow structure is not much affected by the interaction of the shock with the incoming

boundary layer at the origin of compression corner. The main difference is the spreading of the wall pressure distribution. The step function type pressure distribution of the inviscid solution is being replaced by a progressive rise between the upstream pressure level (p_1) and the final pressure value (p_2) corresponding to oblique shock equations [6] (see Fig. 3.1). This spreading of the wall pressure distribution indicates the mechanism of upstream influence through which the pressure downstream of the shock is felt upstream of its origin in a perfect fluid. In Fig. 3.2, it is shown that the upstream propagation is due to the existence of their subsonic layer (region) in the boundary layer through which any information (signal) is propagated : both in upstream and downstream direction. The shock formation causes a progressive dilation of the subsonic region, a deflection of the flow, and thus a focalization of the supersonic contiguous part of the flow compression waves at a certain distance away from the wall. The subsonic layer is extensively thin in turbulent boundary layer at relatively high Mach and Reynolds numbers flow. In such conditions, the shock originates from a region very close to the wall and propagates in a boundary layer where it is bent due to the Mach number variation [6], [30] & [32]. In these situations, two types of shock waves form. The first one is associated with the flow separation upstream of the ramp. The second shock originates from the reattachment region and interacts with the separation shock at a short distance from the wall. Both flow separation and reattachment are progressive and the inclined compression waves coalesce into shocks at some distance away from the wall. With the increase in Mach number, this coalescence of compression shocks is so rapid that the separation and reattachment shocks form within the boundary layer and seem to originate from the wall as shown in Fig. 3.3. A centered expansion emanates from triple point ('I' in Fig. 3.3), when Mach number of the incoming flow is greater than 2.

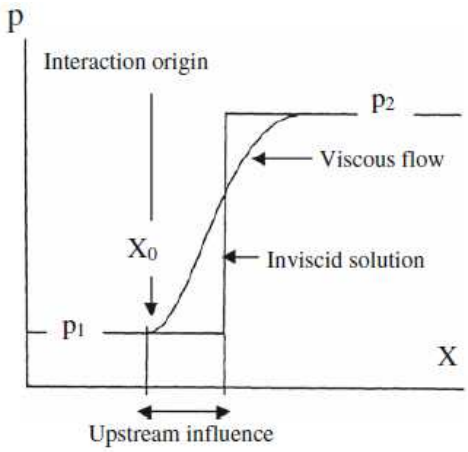

FIGURE 3.1 – Pressure distribution across shock for viscous and inviscid solution, (from Délery & Dussauge [33]).

Based on series of experiments, Zheltovodov [161], [163], [164] & [165] described the principal elements of the flow field structure and turbulence transformation in the compression corner / ramp (see Fig. 3.4). These are (1) the amplification of the turbulence by shock waves in the boundary layer (2) and external flow (3) suppression of turbulence by the expansion fan (4) formation of a new layer in the near wall part of the attaching flow (5) formation of Taylor-Görtler vortices and (6) reverse transition in the separation region due to the favourable pressure gradient and decrease of the local Reynolds number in the reverse flow caused by the decrease of the velocity in the direction of the separation point. The unsteady behaviour of the shocks

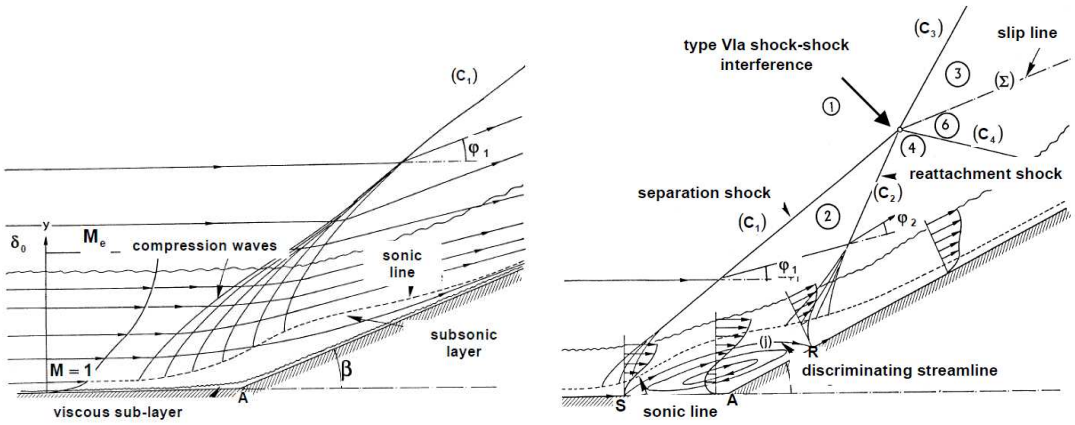

FIGURE 3.2 – The structure of a ramp flow (Left) without and (Right) with boundary layer separation, (from Arnal & Délery [6]).

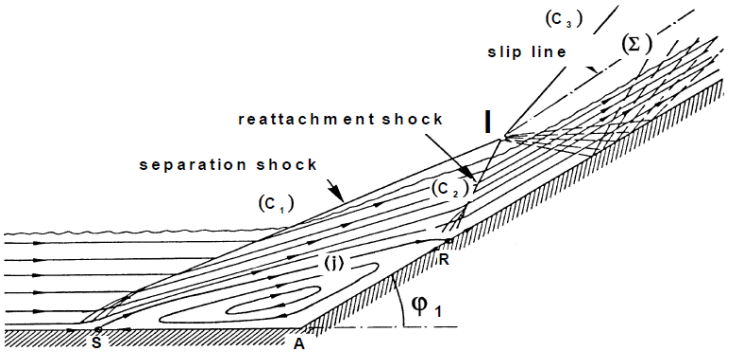

FIGURE 3.3 – Ramp flow with boundary layer separation at high Mach number, (from Arnal & Délery [6]).

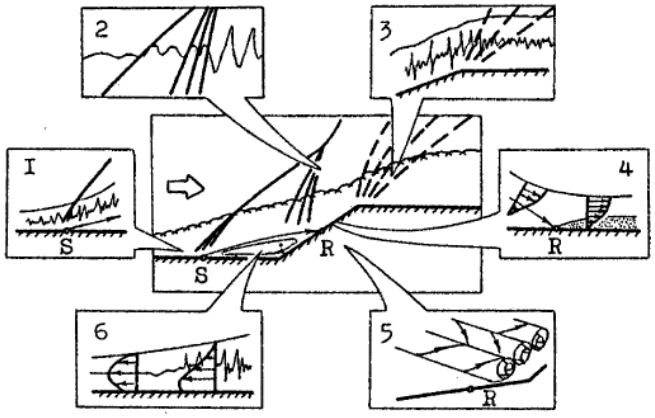

FIGURE 3.4 – Turbulence structure in 2D compression corner, (from Knight et al. [68]).

system and separated flow in the compression corner / ramp is an important aspect which could be found in the detailed reviews have been prepared by Adams [1], Dolling [38], [39] & Smits and Dussauge [135]. Analyses of this very phenomenon performed by several researchers have shown that the appearance of separation and accompanying large-scale eddies (in the separated shear layer) for high ramp angle (e.g. 25° & 45°) at high Mach number (M≥2) stimulate relatively high level of fluctuations of mass flow, velocity and temperature (in comparison with the case of low ramp angle e.g. $\alpha = 8°$, without flow separation) in attached viscous and external flow [68]. Dolling and Murphy [34] and Dolling and Or [35], in their detailed studies addressing the unsteadiness of the shock system in the case of compression corner, observed that frequencies related to the separation shock motion are below the order of frequency of the energy containing eddies in the incoming boundary layer. Moreover, the study of Andreopoulos and Muck [2] have shown that the frequency of separation shock unsteadiness is approximately of the same order as the bursting frequency of the upstream boundary layer. However, Erengil and Dolling [45], [46] identified both small- and large-scale fluctuations of the separation shock motion. Later on, physical interpretation of shock system unsteadiness variation in the vicinity of the compression corner at different stages of separation development during its interaction with large eddies is proposed by Glotov [60]. By using high speed shadowgraphy in addition to the measurements of the surface pressure fluctuations Glotov [60] concluded that (i) for small-scale separation the large eddies in the external part of the boundary layer periodically supplant the separation (reverse flow) zone and prevent the penetration of disturbances from downstream to upstream. Furthermore, this process stimulates large deformations of the shock-wave similar to the interaction of a shock-wave with a vortex ring. (ii) for large-scale separation, such eddies are displaced downstream of the separation shock-wave above the surface together with the separated shear layer, and the disturbances penetrating upstream from the attachment region play the main role in stimulating low-frequency shock-wave fluctuations, with high-frequency fluctuations stimulated by the former mechanism superimposed upon these. This latter interpretation is in good agreement with conclusions made by Bibko et al. [10].

3.1.2 Impinging-Reflecting Oblique Shock

In this case, the penetration of incident oblique shock into the boundary layer generates a very complex wave pattern resulting from its refraction through the rotational and supersonic part (which is nearly a parallel flow) of the boundary layer. This is similar to the previous mentioned case of 2D compression corner without flow separation, and the existence of a subsonic inner layer allows the upstream propagation of the shock influence. When this incident shock is strong enough to separate the boundary layer, the resulting separation shock meets the incident shock at some distance from the wall as shown in Fig. 3.5. The resulting structure of the inviscid outer stream strongly depends on the boundary layer development in the interaction region. The dramatic change in the shock pattern leads to several difficulties in the modelling of this interaction. However, a better prediction requires an accurate capture of these flow discontinuities. Furthermore, in hyper-enthalpy flows, the sensitivity of the shock system to the gas thermodynamics may have large impact on the interacting flow [6].

Several of these studies have been reviewed by Green [61], Charwat [20], Stanewsky [139], Délery and Marvin [29]. In a series of experiments performed at high Mach number 2.6-2.85, Kuehn [70] proposes a criteria for incipient separation based on the appearance of an inflection point in the mean wall pressure distribution and the observed unsteady behaviour of the shock

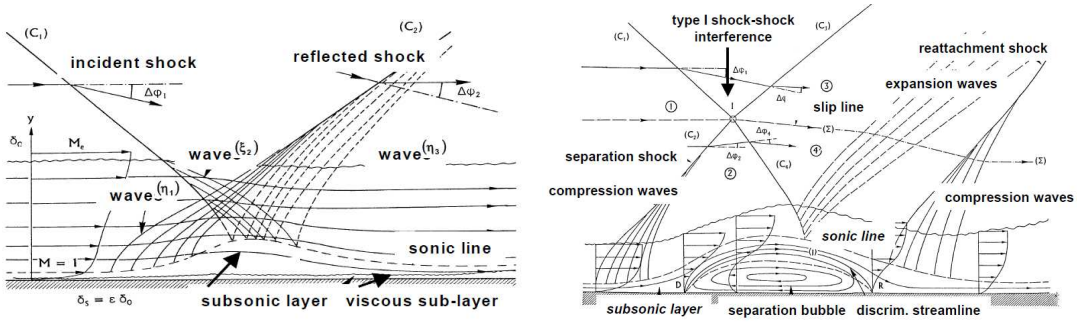

FIGURE 3.5 – Impinging-reflecting shock (Left) without & (Right) with separation, (from Arnal & Délery [6])

system. Three-dimensional effects were observed by Reda and Murphy [120] due to the effect of side-wall boundary layer on the incipient separation and interaction size. An optical visualization of Görtler-type vortices was performed by Brazhko [14] was showed that they result into the periodic variation of heat transfer at high Mach number i.e. 5 & 6 for separated flows of laminar and turbulent boundary layers. A connection between downstream vortical structures and the low frequency shock motion was found by J.-P. Dussauge & J.-F. Debiève [41] in their shock-reflection experiments. Erengil & Dolling [45] suggested that a frequency scaling based on the separation length and on the upstream external velocity is likely to be the proper scaling for this flow configuration. Furthermore, Dolling [39] pointed out that the experimental setup might have an artificial influence on the large-scale shock motion. The Görtler vortices which develop in the nozzle of the wind tunnel may introduce some possible temporal variations in the incoming boundary layer, which may cause large-scale shock motion (LSSM). Streamwise vortices affect the turbulence structure and the properties of the mean flow significantly ([14], [51], [66], [84], [160] & [162]). More detailed information regarding the mean flow and turbulence measurements are provided for example by Rose and Johnson [128], Mikulla and Horstman [90], Modarress and Johnson [91], and Meyer et al. [89]. They demonstrated the increase of fluctuations of mass flow and velocity, turbulence intensity, Reynolds shear stress and turbulent kinetic energy downstream of the interaction. Furthermore, the strength of impingement oblique shock has a significant effect on the flow properties downstream of the interaction. A possible candidate for explaining the low frequencies of the shock motions may be the very large scale eddies (VLSE) characterised in subsonic boundary layers and put in evidence by the Ganapathisubramani et al. [57]. The importance of the meandering of the VLSE in such interactions and their effect on shock motion is discussed by Dussauge [42], [43], as well as the influence of upstream perturbations of vorticity is considered. Pirozzoli and Grasso [116] performed a DNS of this case and proposed a mechanism whereby acoustic feedback in the separation bubble drives the shock motion. More recently Piponniau et al. [115] proposed a model explain the low frequency unsteadiness found in the shock-induced separation for the cases where the flow is reattaching downstream.

3.2 Separated Flows in Supersonic Nozzle

In today's advanced launchers, the nozzle of the first stage rocket engine has to operate from sea-level atmospheric conditions to low ambient pressure environment at high altitudes.

The performance of the propulsion system is high in vacuum owing to its design. However, at the very beginning of the flight, the wall pressure level required for an adapted attached flow can be much lower than the ambient pressure. An adverse pressure gradient of sufficient strength can cause the separation of the boundary layer. Such a condition typically occurs in a nozzle with over-expanded condition, i.e. ”n” (ratio of nozzle exit pressure to the ambient pressure) less than 1. As soon as ”n” is slightly reduced below one, an oblique shock system is formed from the trailing edge of the nozzle wall due to the induced adverse pressure gradient. When the value of n further decreases, the viscous layer cannot sustain the adverse gradient imposed by the inviscid flow and the boundary layer separates from the wall. The work of Nave and Coffey [98] on the J-2S TOC nozzle demonstrated clearly the existence of two different types of separated flow regimes namely (i) free shock separation (FSS) & (ii) restricted shock separation (RSS), as shown in Fig. 3.6 & 3.7.

No matter, whatever the nozzle contour is, FSS flow regime occurs when rocket engine runs in a strong over-expansion regime. In the free shock separation case, the over-expanded flow fully separates from the wall. The resulting streamwise wall pressure evolution is mainly governed by the physics of the shock wave/boundary layer interaction occurring in supersonic flow separation. The separation and the subsequent formation of a recirculation zone give rise to an oblique shock wave near the wall (see Fig. 3.6). This incident oblique shock (also known as separation shock) interacts with the Mach disk/stem, and a reflection shock appears from the triple point. The separated flow then continues as a free jet. The fluid outside of the nozzle gets sucked into it and separates from the nozzle lip, yielding a small recirculation bubble counter-rotating with respect to the massively recirculation zone. Due to the oblique shock, the wall pressure suddenly rises and reaches a plateau (see Fig. 3.6) with a level always slightly less than the ambient atmospheric pressure due to the loss occurring at the nozzle lip, associated with the small counter rotating vortex. The annular supersonic region appears with two mixing layers ; an internal one between the supersonic flow and the subsonic flow downstream of the Mach disk and external one between the supersonic flow and the outer fluid sucked into the nozzle. Under certain conditions, a reattachment of the flow occurs and hence a totally different flow pattern appears which is characterized by a special shock shape called cap-shock (sketched of Fig. 3.7) and by the existence of a low speed trapped vortex downstream of the Mach disk/stem. In TOC type rocket nozzles, an internal shock arises in the throat region. This internal shock interacts with the Mach disk far away from the throat. A triple point exists, where the internal shock, the normal shock and the transmitted cone-shaped oblique shock meet. The separation shock interacts with the cone-shaped oblique shock. This interaction is regular and two reflected oblique shocks form from the common interaction point, called quadruple point. The whole structure made by the separation shock, the conical shaped shock and the Mach disk/stem is called cap-shock. A free shear layer and the separated boundary layer also interact with these reflected oblique shocks and, downstream of this interaction, the separated layer is turned back towards the nozzle wall and reattaches, enclosing a small recirculation zone. The annular supersonic flow is subjected to expansion and compression waves reflected between the nozzle wall and the mixing layer separating the high speed region from the central trapped vortex. These reflected waves give an oscillatory wall pressure distribution which can lead in some case to secondary separation as shown by Nguyen [100]. Since early seventies, Nave and Coffey [98] have first shown that these flow regimes exhibit an undesirable strong unsteadiness and loss of symmetry in certain range of NPR. The resulting lateral fluctuating pressure loads, so-called side-loads, can damage nozzle or the launcher control system and thus has driven a particular

attention from the community.

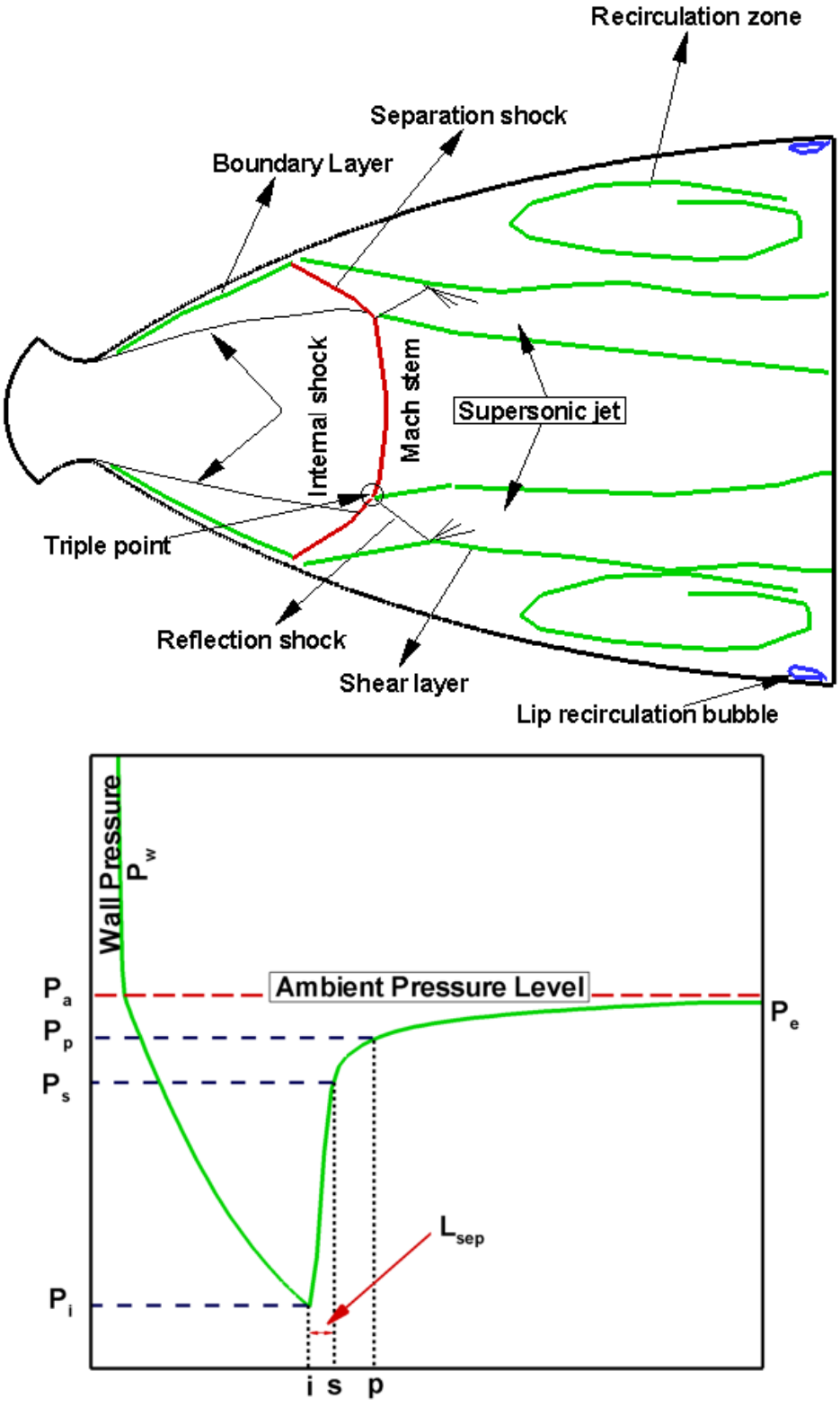

FIGURE 3.6 – (Top) Sketch of free shock separated flow in TOC nozzle, (Bottom) Evolution of pressure along nozzle wall in the case of FSS, i=incipient, p=plateau, a=atmosphere, e=exit and s=separation.

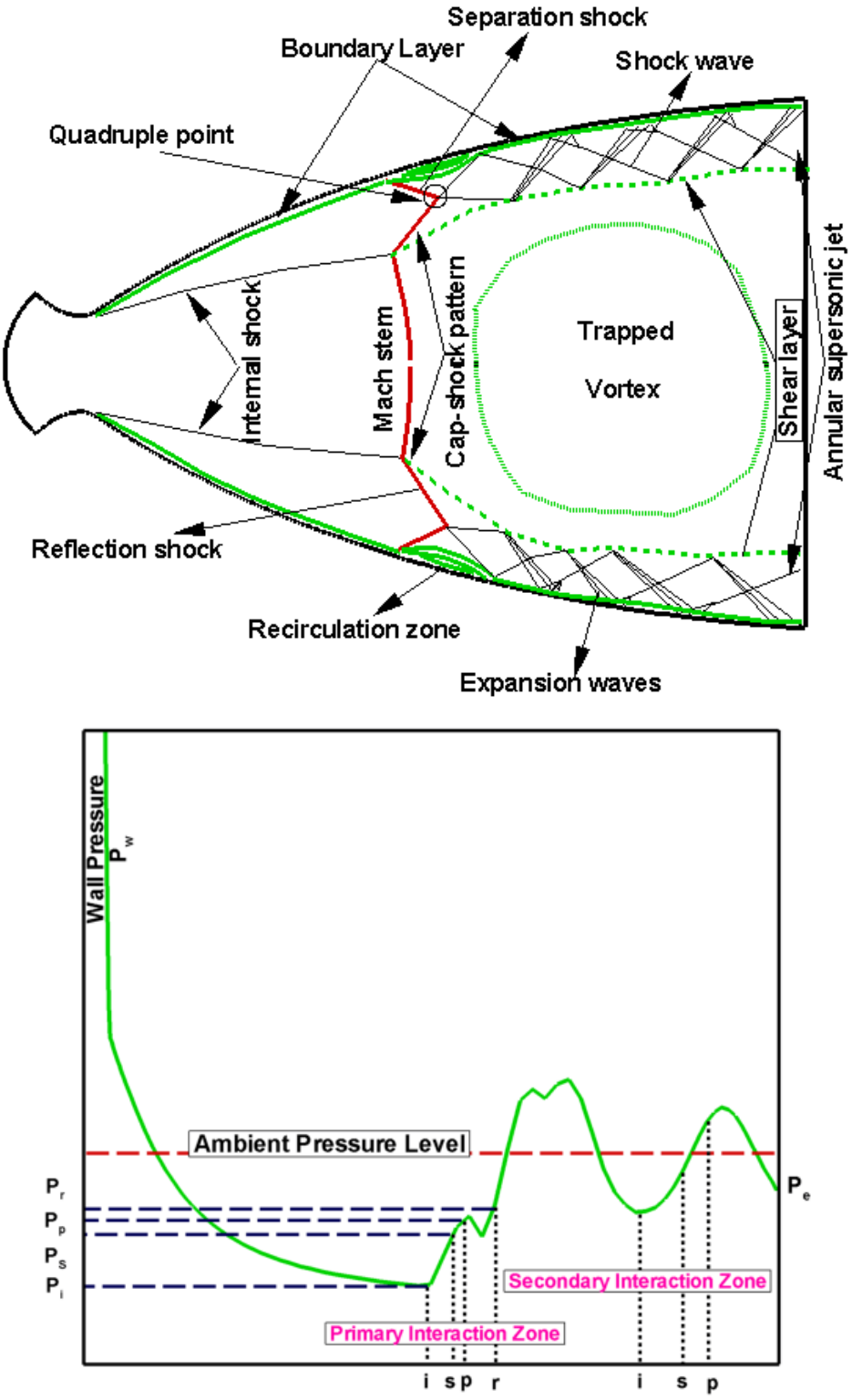

FIGURE 3.7 – (Top) Sketch of restricted shock separated flow in TOC nozzle, (Bottom) Evolution of pressure along nozzle wall for RSS configuration, i=incipient, p=plateau, a=atmosphere, e=exit, s=separation and r=reattachment.

3.2.1 Shock Structure in Over-Expanded Rocket Nozzle

In the separated flow regime, the separation line moves downstream (towards the nozzle exit) with the increasing nozzle pressure ratio (NPR). For lower NPR, when flow regime is governed by FSS configuration, the flow-field in the center portion remains supersonic at nozzle exit, but is surrounded by an annular shaped section of subsonic flow (recirculation region). There is a discontinuity at the separation location and the thrust is reduced, compared to a nozzle that would have been cut off at the separation plane. Shock waves exist outside the nozzle in the external plume. Exhaust plumes for both these operating conditions contain classical Mach disk pattern and its reflecting shock. Depending on the nozzle contour in a certain range of nozzle pressure ratio, an additional shock structure, i.e. cap-shock pattern, in the exhaust plume can be observed. Appearances of classical Mach disk and cap-shock pattern in the exhaust plume of Vulcain nozzle are shown in Fig. 3.8. This Vulcain nozzle has a parabolic contour in which an internal shock emanates near the throat of the nozzle. This internal shock is very weak and interacts with the separation shock and Mach stem. Figure 3.9 & 3.10, presents stereographic images of Mach disk and cap-shock pattern in exhaust jet from TIC and TOC, respectively, observed by Reijasse [122] at ONERA. In comparison with the Mach disk which appears in the FSS flow configuration, the cap-shock pattern is fairly complex (Fig. 3.10). Furthermore, Reijasse observed that, downstream of this complex cap-like structure, a large stabilized recirculation zone appears which is surrounded by the annular supersonic jet (see Fig. 3.11).

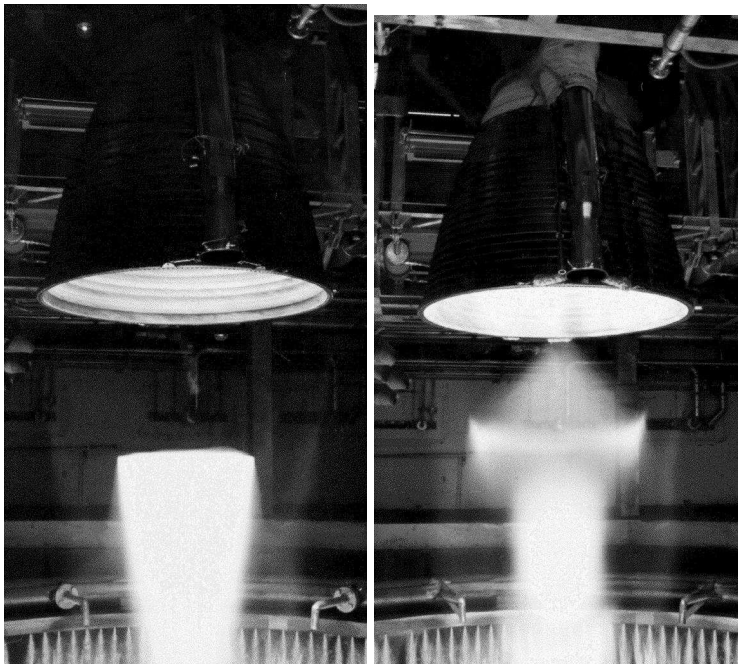

FIGURE 3.8 – Exhaust plume from Vulcain nozzle during over-expanded operation (Left) Mach disk & (Right) Cap-shock pattern (Courtesy photo : SNECMA).

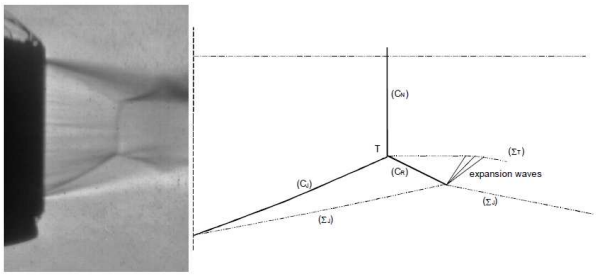

FIGURE 3.9 – Shock structure in the exhaust plume of TIC nozzle (ONERA) at NPR = 56.4, Left : Stereography & Right : Sketch, (from Reijasse [122]).

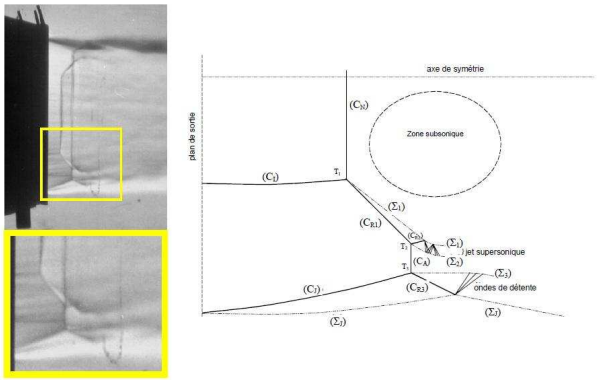

FIGURE 3.10 – Cap-shock structure in the exhaust plume of TOC nozzle (ONERA) at NPR = 62.0, Left : Stereography & Right : Sketch, (from Reijasse [122]).

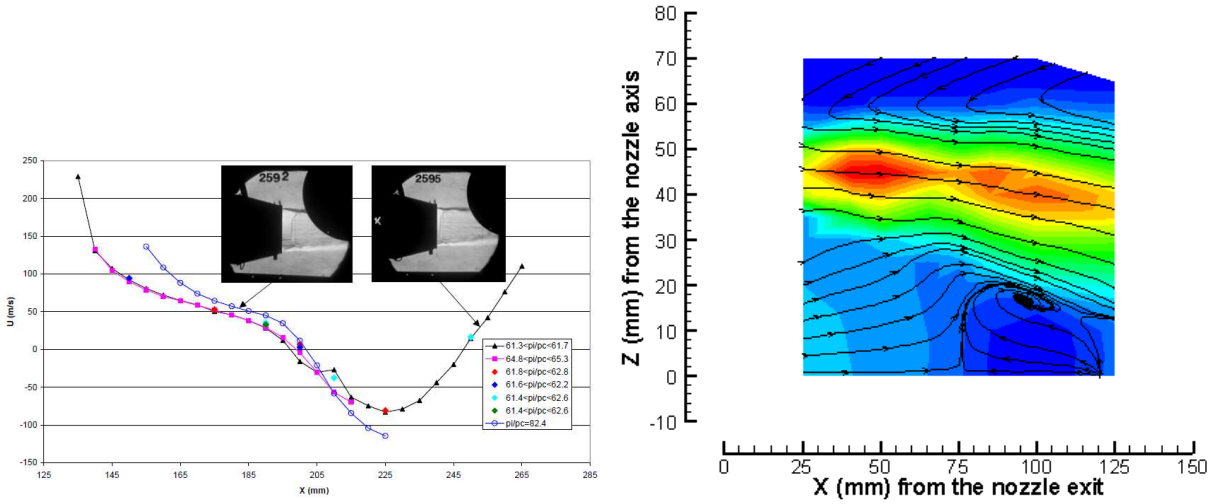

FIGURE 3.11 – (Left) LDV probing in the nozzle axis from the exit plane & (Right) streamlines & iso-velocity contours from LDV measurement (ONERA), (from Reijasse [122]).

3.2.2 Flow Transition Between FSS ⇔ RSS Flow Regimes

During the start-up process of rocket nozzle, at low NPR, free shock separation occurs. Depending on the nozzle contour, this FSS flow switches into RSS configuration. This process of flow transition was first reported by Nave and Coffey [98] in J-2S TOC nozzle. The evolution of measured side-loads during the start-up process of J-2S engine is shown in Fig. 3.12 along with the sketch of both flow regimes. These authors suggested that the first peak in the side-load activities corresponds to the critical nozzle pressure ratio (CNPR) at which the flow transition takes place. However, soon after transition, a low level of side-loads was observed in RSS flow regime. They put in evidence that the second peak of side-loads corresponds to the case the reattachment line in RSS flow moves outside the nozzle exit. This particular flow configuration was named as ”end-effects” : that is when the trapped recirculation zone is opened to the atmosphere of relatively high pressure. Furthermore an hysteresis between FSS and RSS regimes was clearly indentified and is shown in Fig. 3.12 with the help of nozzle thrust efficiency.

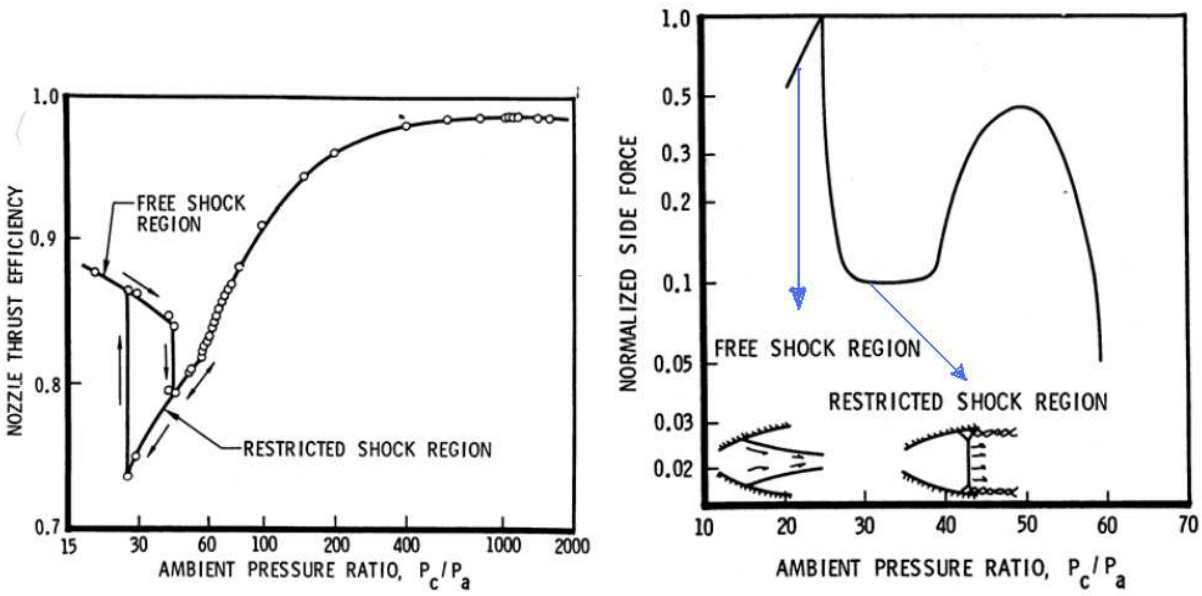

FIGURE 3.12 – Thrust efficiency and recorded side-loads during the start-up operation : J-2S TOC nozzle, (from Nave & Coffey [98]).

After the pioneering work of Nave and Coffey [98] a various studies were performed to understand the existence of these flow regimes and their effects on the nozzle geometry resulting in dangerous side-loads and thermal effects.

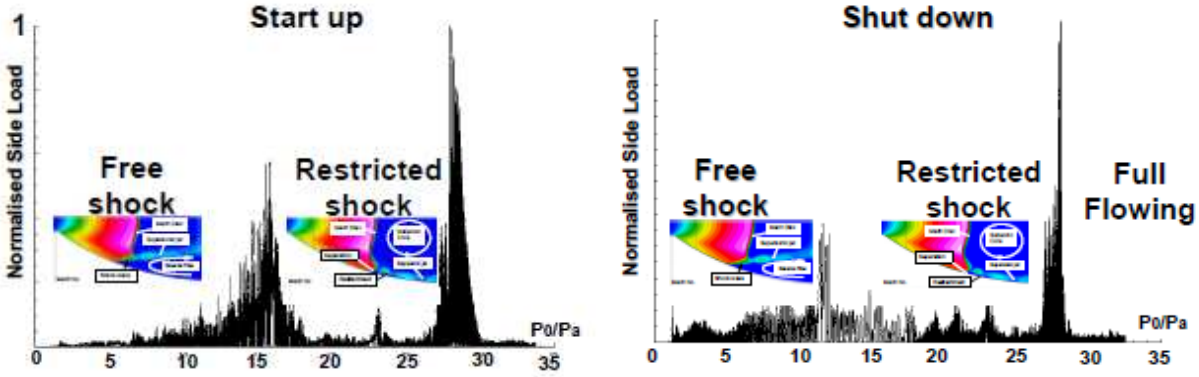

FIGURE 3.13 – Evolution of side-loads with respect to the NPR during the start-up and shut-down operation of VAC-S1 (TOC) nozzle, (from Östlund [106]).

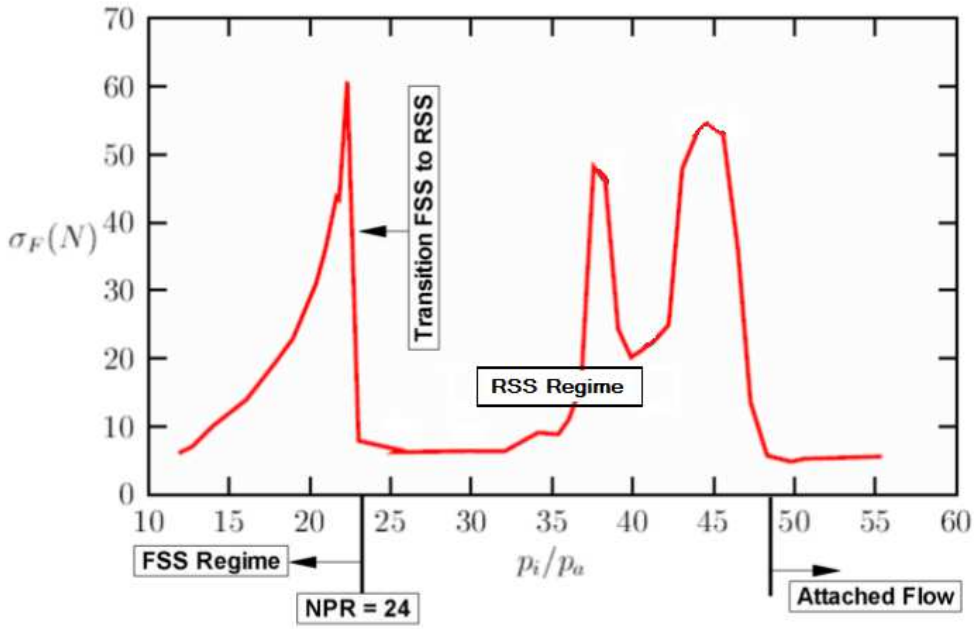

FIGURE 3.14 – RMS value of recorded side-loads during start-up operation process in LEATOC nozzle, (from Nguyen [100]).

Figure 3.13, presents the evolution of the side-loads on VAC-S1 (TOC) nozzle during the start-up and the shut-down process along with numerically obtained the Navier-Stokes axi-symmetric solution in FSS and RSS regimes [106]. Similarly in the case of J-2S nozzle (as in Fig. 3.12), two peaks of the side loads were observed during the experiments. However, the range of NPR corresponding to these peaks of side-loads is different. Östlund [106] suggested that the origin of side-load peaks is characterized by their high level and impulsive occurrence. As a consequence, the separation and side-load characteristics are radically different for different nozzle contours. In the recent past, the start-up process of thrust optimized contour nozzle has been experimentally investigated at the Laboratoire d'Etudes Aérodynamiques (LEA), Poitiers, France (and is denoted as LEATOC nozzle [100]). The root mean square (RMS) value of the side-loads is plotted against the nozzle pressure ratio in Fig. 3.14. During the start-up

phase, when the flow is in FSS regime, the side-load activities increase before the transition process. This level in side-load activities was attributed to the increasing unsteadiness of the separation line rather than to the direct effect of NPR [100]. As soon as the transition from FSS to RSS flow regime takes place (i.e. NPR=24), the highly unsteady flow becomes quasi steady due to the reattachment of the separated jet and the subsequent formation of the large stabilized trapped vortex. Although RSS flow regime seems stabilized, there exist two peaks in this very regime. The possible explanation is the intermittent opening of the separation bubbles or the small recirculation zones caused by the reattachment of the free separated jet. Different studies were carried out to understand the possible cause of this flow transition but this cause is still not fully clear. Series of studies have been performed by Hagemann and Frey [55], [62] & [63], who reported that the cap-shock pattern is the key factor which causes the flow reattachment. From an analysis based on axi-symmetric RANS calculations, they have shown that this formation of cap-shock pattern corresponds to the phenomenon of inverse Mach reflection. Following the idea that the cap-shock pattern is the key driver for the flow transition from FSS to RSS, an analytical model was developed by Dasa/DLR [54] for thrust optimized or parabolic contour nozzles (for details see [54]). Later on, Moríñigo et al. [94] reported that transition from FSS to RSS occurs when two flow conditions are fulfilled : the axis of the separated jet should be deflected towards the wall ; and the jet boundary must intercept it. This latter explanation for the transition process seems to be the consequence of the cap-shock pattern. Recently, Nasuti and Onofri [97] emphasized that the importance of the internal shock is more on a quantitative rather than on a qualitative and concluded that the occurrence of flow reattachment at the wall depends on the values and kind of upstream pressure gradient rather than simply on the existence or not of an internal shock.

3.2.3 End-Effects Regime

The RSS flow regime is usually characterized by a relatively low level of side loads. Such a behaviour of side-load activities has been reproduced by numerical simulations by Deck [25] (see also [27]) and Wang [152]). However, the nozzle wall is exposed to a rather high heat flux in the vicinity of the reattachment line [140]. The structure of the RSS configuration, as sketched in Fig. 3.7, moves downstream towards the nozzle exit, when the NPR increases. When the reattachment line reaches the nozzle lip, the recirculation bubble opens to the ambient atmosphere and the resulting operating regime is known as end-effects regime. This regime was first reported by Nave and Coffey [98]. Experimental results for thrust-optimized contour nozzles in the previous section have shown that the end-effects regime is usually characterized by high side loads with a level comparable with level of the peak observed just before the FSS $\rightarrow$ RSS transition. Frey and Hagemann [54] attributed that this high side-load level to a periodic pulsation process driven by the difference between the plateau pressure in the recirculation bubble and the ambient atmospheric pressure. However, Nguyen et al. [100] reported that wall pressure fluctuations associated with this pulsation process are characterized by a fairly broadband spectra, i.e. this pulsation process is a random process rather than a strictly periodic one. They concluded that this end-effects regime is characterized by a global quasi axial pulsation which induces a very high level of fluctuations and suggested that the side loads are in fact induced by small pressure differences superimposed upon a large amplitude axi-symmetric global unsteadiness. These large amplitude self-sustained oscillation has also been obtained by Moríñigo et al. [93] in three-dimensional URANS simulation of the J-2S TOC nozzle. More recently,

Deck [28] has performed a DDES simulation reproducing the strong global unsteadiness which occurs in the end-effect regime in LEATOC nozzle. This pulsatory regime was also reproduced by the axi-symmetric URANS simulation of Nebbache and Pilinski [99].

3.2.4 Possible Origins of Side-Loads Activities in Over-Expanded Nozzles

Due to the unsteady and non-symmetric nature of the flow separation in rocket nozzle, lateral forces act on the nozzle wall. These lateral forces are commonly known as side-loads. The first important report dealing with side-loads activities was published within the framework of the J-2S rocket nozzle, by Nave and Coffey [98]. Side-loads have been observed either in subscale or full-scale rocket nozzles during the start-up or shut-down operation with separated flow inside the nozzle.

FIGURE 3.15 – The three space shuttle main engines : SSME during the transient start-up process, showing teepee like structure of separation line (Photo : NASA)

Fig. 3.15, displays snapshot taken during the transient start-up of the Space Shuttle Main Engines, SSME, shortly prior to lift-off. The three-dimensional separation line is clearly visible due to water vapour condensation on the wall of cryogenic cooled nozzle extension. The question arises to know whether the asymmetry (which causes side-loads) is due to the perturbations coming from upstream or downstream. One possible assumption is that the asymmetry is a result of the boundary layer evolution downstream of the throat, but upstream of the separation point. The turbulent pulsations in the boundary layer show a statistical asymmetric behaviour and hence, especially the largest turbulent structures could trigger asymmetric separation. Another hypothesis is that the turbulent shear layer, which emanates from the separation point, causes pressure pulsations in the separated region, that result in a non-symmetric pressure distribution and can even influence the position of the separation through the subsonic recirculation region. In the case of RSS, downstream of the reattachment line, the flow along the wall becomes supersonic again, thereby inducing shocks and expansion waves that results in wall pressure peaks with values above the ambient pressure. With the increase in the nozzle pressure ratio, this recirculation zone moves downstream. Finally the reattachment line reaches the nozzle exit and then opens to the atmosphere at ambient condition. This is connected with the pressure increase in the recirculation zone, which makes the separation line move upstream. Thereby the recirculation zone closes again, and results in a drop in static pressure which results in a downstream movement of the separation point. This pulsation process connected with the

opening and closing of the separation zone may generate significant side-load peaks. The same phenomenon can be observed during the shut-down.

In brief, the possible origins for side-loads generated by asymmetric wall pressure evolution inside the nozzle and suggested in the literature are :

3.2.4.1 Tilted Pressure Line

The assumption of a tilted separation line in pure free shock separation flow regime is the basis of several side-load models. The principle of this basic idea is illustrated in Fig. 3.16. Several comparisons of experimental data with this approach of a tilted separation line have shown that none of the models correctly predicts the side-load behaviour of all rocket nozzles [106].

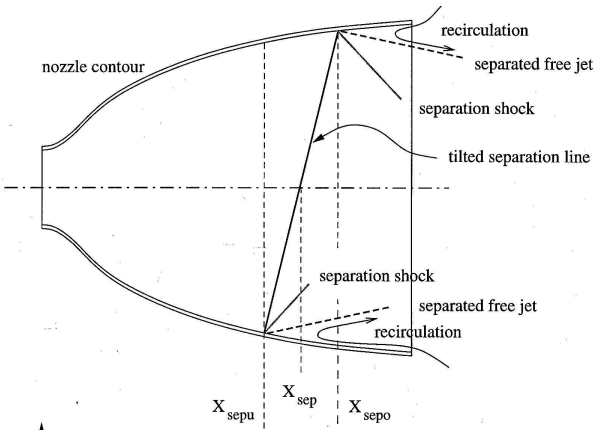

FIGURE 3.16 – Principle of the tilted separation line, (from Östlund [106]).

In fact, the models based on this assumption lead to correct predictions of side-load only for special nozzle families. As soon as one of the models is applied to a nozzle which is very different in shape, the agreement between predicted and measured forces is rather poor [106]. This suggests that the simple underlying assumption of a tilted separation line probably does not account for the true key physical mechanisms responsible for the peak of side-loads.

3.2.4.2 Side-loads due to Random Pressure Pulsation

The combination of random oscillations of the separation line and random pressure pulsations in the separated flow region is the basic idea of Dumnov side-load model [40]. This model is based on a statistical generalization of empirical data for the pulsation pressure field at the wall. The empirical data are mainly based on sub-scale cold-gas experiments with separated nozzle flows. For these experiments, only conical and truncated ideal contour nozzles were used. The application of Dumnov model to Russian rocket nozzles, like RD-0120 conical nozzle, gave a reasonable agreement between measured and predicted side-loads [106].

3.2.4.3 Side-Loads due to Aero-elastic Coupling

Slight variations in wall pressure can cause significant distortion of the nozzle contour. This distortion in turn results in a further variation in wall pressure and the system forms a closed

loop, which may result in a significant amplification of the initial load. The study of closed-loop effects of jet separation has not been attacked vigorously due to the complexities involved in generating accurate asymmetric dynamic models of the nozzle-engine support system, the jet boundary layer separation, and interaction at the boundary of the two sub-systems. However, a technique for handling these difficult coupling problems has been developed by Pekkari [108] & [109]. This model consists of two main parts, the first dealing with the equation of motions of the thrust chamber as aerodynamic loads are applied, and a second part modelling the change of the aerodynamic loads due to the distortion of the wall contour [106]. The wall pressure in the attached region is the nominal vacuum pressure profile with a pressure shift due to the displacement of the wall. This pressure shift is determined with the use of linearised supersonic flow theory. In the separated region the wall pressure is equal to the ambient pressure. The model is useful for checking whether aero-elastic instability is present in the case of separated nozzle flow and can also evaluate the corresponding aero-elastic amplification. This model was extensively validated at Volvo Aero corporation showing that side-loads can lead to the aero-elastic effects in weak nozzle structures [104] & [105].

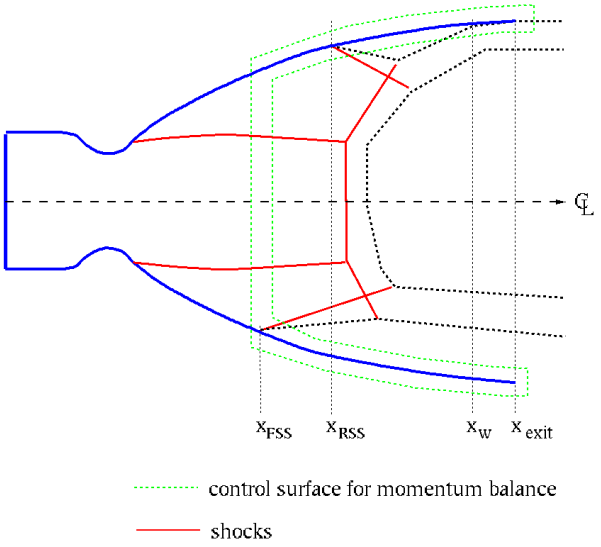

FIGURE 3.17 – Dissymmetric flow-field inside the nozzle at an instant exhibit FSS and RSS flow regimes simultaneously, (from Östlund [106]).

3.2.4.4 Side-Loads due to a Global Change of the Separated Flow Structure

Initially it was observed that in sub-scale cold gas experiments, the transition in separated flow regimes from FSS to RSS and vice-versa is the origin of two-distinct side-load peaks [21] & [98]. By assuming that the initial transition from FSS to RSS requires a certain time, an intermediate phase might exist during which one side of the nozzle experiences a free shock separation while the other one a restricted shock separation. Because the separation point is further downstream in the RSS regime and the behaviour of wall pressure are totally different between the two cases, severe lateral forces could act on the nozzle. The main characteristic of these side-load forces is their high value of impulsive occurrence. Based on the briefly described restricted shock separation models of reference [53] & [105], Dasa/DLR [145] and Volvo [105] have developed side-load models by assuming that the initial transition from free to restricted

shock separation is the key side-load driver in TOP and CTIC rocket nozzles. The basic idea behind is, that at the instant of transition a maximum side-load is expected if one half of the nozzle features FSS-, while the other half shows already RSS flow condition. For this case, the side-load calculation is squarely based on physical reasoning namely from a momentum balance across the complete nozzle surface, as illustrated in Fig. 3.17. With this model the aerodynamic side-load can be calculated. Due to the short duration of the aerodynamic side-load, the pulse excitation theory can be used when evaluating the mechanical load.

Chapitre 4

Numerical Methods & Turbulence Modelling

4.1 Brief Overview of the Code Description : TGNS3D

In this research work all simulations are performed by means of the numerical code, named TGNS3D, which is developed at Laboratoire d'Etudes Aérodynamiques, Poitiers, France. This code solves the three dimensional unsteady compressible Navier-Stokes equations on a multi-block structured grid in curvilinear coordinate system. The computational domain is discretized by using the finite volume method, which means that we are interested in the average value of the state vectors U on the control volume. The average value of the state vector on the volume control is taken equal to the value of the vector in the center of it. Two different turbulence modelling methodologies i.e. RANS modelling and Hybrid RANS/LES method have been implemented for the turbulent flow prediction. Details of these modelling techniques are given latter in this chapter. Since shock-induced separated flow contains complex flow discontinuities, a high order low dissipative shock-capturing scheme appeared to constitute a necessary ingredient. Two different type shock capturing schemes based on Roe flux method [127] for the discretization in space have been used, including second order Monotone "Upstream-Centered Schemes for Conservation Laws" (MUSCL) [75]-[79] and fifth order version of the Monotonicity Preserving Weighted Essentially Non-Oscillatory (MPWENO) scheme of Balsara and Shu [8]. A second order two-step temporal scheme with implicit linearization is used in order to achieve larger time step and consider sufficiently long time integration. A diagonally dominant alternating direction implicit (DDADI) approach is used for the inversion of a large sparse matrix system corresponding to the implicit scheme. Further details regarding to the code TGNS3D and the implemented numerical schemes are given in Annex A.

4.2 Turbulence Modelling

4.2.1 The Navier-Stokes Equations

The fluid motion can be described in a mathematical way by using Newton's second law of motion and a constitutive relation regarding the viscous forces. We assume that the continuum hypothesis is valid, i.e. that the molecules are so small and large in number that they constitute a continuum. The relation between the stresses and rates of deformation is assumed

to be linear (Newtonian fluid). Based upon these assumptions, the Navier-Stokes equations for a compressible fluid are :

– Continuity equation :

$$\frac{\partial \rho}{\partial t} + \frac{\partial \rho u_i}{\partial x_i} = 0 \tag{4.1}$$

Here ρ denotes the density, t is time and u_i is the components of the velocity vector ($i = 1,2,3$).

– Momentum Equation :

$$\frac{\partial \rho u_i}{\partial t} + \frac{\partial \rho u_i u_j}{\partial x_j} = -\frac{\partial p}{\partial x_i} + \frac{\partial \tau_{ij}}{\partial x_j} \tag{4.2}$$

Where p is the pressure, τ_{ij} represents the tensor of viscous stresses. We consider only gas flows and the volume forces are neglected.

– Energy Equation :

$$\frac{\partial \rho E}{\partial t} + \frac{\partial \rho E u_i}{\partial x_i} = -\frac{\partial p u_i}{\partial x_i} + \frac{\partial \tau_{ij} u_j}{\partial x_i} - \frac{\partial q_i}{\partial x_i} \tag{4.3}$$

E is the total energy (i.e. internal energy e and kinetic energy) and q_i represent the components of the vector of heat flux.

Considering a perfect gas, the specific heat constant is denoted $\gamma = \frac{C_p}{C_v}$, and the pressure is given by :

$$p = \rho R T \tag{4.4}$$

Where T is the temperature and R is the ratio of the universal constant of an ideal gas and the molecular mass of gas ($R = \Re/M$ with $\Re = 8.345\, J mol^{-1} K^{-1}$). The constant can be expressed as the difference of specific heat at constant pressure and volume $R = C_p - C_v$. Thus, the pressure can be expressed as a function of the internal energy $e = C_v T$ by :

$$p = \rho(\gamma - 1)e \tag{4.5}$$

For a Newtonian fluid, the viscous stress tensor τ_{ij} is given by :

$$\tau_{ij} = \mu\left(\frac{\partial u_i}{\partial x_j} + \frac{\partial u_j}{\partial x_i}\right) + \lambda \delta_{ij} \frac{\partial u_k}{\partial x_k} = 2\mu S_{ij} + \lambda \delta_{ij} \frac{\partial u_k}{\partial x_k} \tag{4.6}$$

where $S_{ij} = \frac{1}{2}\left(\frac{\partial u_i}{\partial x_j} + \frac{\partial u_j}{\partial x_i}\right)$ is the strain-rate tensor and δ_{ij} is the Kronecker delta :

$$\delta_{ij} = \begin{cases} 1 & \text{si } i = j \\ 0 & \text{sinon} \end{cases}$$

Assuming that the fluid follows the Stoke's law, $2\mu + 3\lambda = 0$, and the viscous stress tensor τ_{ij} can be written as :

$$\tau_{ij} = \mu\left(\frac{\partial u_i}{\partial x_j} + \frac{\partial u_j}{\partial x_i} - \frac{2}{3}\delta_{ij}\frac{\partial u_k}{\partial x_k}\right) = 2\mu\left(S_{ij} - \frac{1}{3}\delta_{ij}\frac{\partial u_k}{\partial x_k}\right) \tag{4.7}$$

The heat flux vector q_i is expressed in terms of temperature gradient given by the Fourier law as :

$$q_i = -\kappa\frac{\partial T}{\partial x_i} \tag{4.8}$$

Here κ denotes the coefficient of thermal conductivity. By introducing the Prandtl number, $P_r = \frac{\mu\, C_p}{\kappa}$ (≈ 0.72 for air), the heat flux becomes :

$$q_i = -\frac{\mu\, C_p}{P_r}\frac{\partial T}{\partial x_i} \tag{4.9}$$

Finally, the molecular viscosity is given by the Sutherland law :

$$\mu(T) = \mu_0\left(\frac{T}{T_0}\right)^{\frac{3}{2}}\frac{T_0 + 110.4}{T + 110.4} \tag{4.10}$$

with , $T_0 = 273.16\,K$ et $\mu_0 = 1.711\,10^{-5}\,kgm^{-1}s^{-1}$.

4.2.2 Statistical Treatment of Navier-Stokes Equations

Since the exact dynamics of turbulence cannot be fully computed for high Reynolds number. The traditional Reynolds-averaged [124] Navier-Stokes equations (RANS) is still used. Traditional closure concepts eliminate some information about the dynamics of turbulence, and the universality of the model is lost. Therefore, capabilities of the model must be determined by careful comparison with experiments. No such unified turbulence model is available at present. However, applicability of turbulence modelling has enabled computing more complex flows.

4.2.2.1 Reynolds Averaging

The first approach for the approximate treatment of turbulent flows was presented by Reynolds in 1895 [124]. The methodology is based on the decomposition of the flow variables ϕ into a mean Φ and a fluctuating part ϕ', where Φ is defined as the ensemble average, which is given as :

$$\Phi = \overline{\phi} = \lim_{k\to+\infty}\frac{1}{N}\sum_{k=1}^{N}\phi_k \tag{4.11}$$

The equations are averaged over a time period that is large compared with that of the typical time scale of the turbulent fluctuations. Reynolds-, or time-averaging is defined as :

$$\overline{\phi} = \lim_{\tau \to +\infty} \frac{1}{\tau} \int_0^{\tau} \phi \, dt \tag{4.12}$$

The Reynolds decomposition of a flow variable is :

$$\phi = \overline{\phi} + \phi' \quad with \quad \overline{\phi'} = 0 \tag{4.13}$$

4.2.2.2 Favre (mass) Averaging

In case of compressible flows, it is advisable to apply the density (mass) weighted or Favre decomposition [49] & [50] to certain quantities in Navier-Stokes equations instead of Reynolds averaging. Otherwise, the averaged governing equations would become considerably more complicated due to additional correlations involving density fluctuations. The most convenient way is to employ Reynolds averaging for density and pressure, and Favre averaging for other variables such as velocity, internal energy, enthalpy and temperature, which is given as :

$$\widetilde{\phi} = \frac{\overline{\rho \phi}}{\overline{\rho}} \tag{4.14}$$

Hence the Favre decomposition reads :

$$\phi = \widetilde{\phi} + \phi'' \tag{4.15}$$

From above relation one can note that $\overline{\rho \phi''} = 0$, but $\overline{\phi''} \neq 0$.

4.2.3 Favre- and Reynolds- Averaged Navier-Stokes Equations

In turbulence modelling, it is quite common to assume that Morkovin's hypothesis [95] is valid. It states that the turbulent structure of a boundary layer is not notably influenced by density fluctuations if $\rho' << \overline{\rho}$. Application of the Reynolds averaging to density and pressure and of the Favre averaging to the remaining flow variables in the compressible Navier-Stokes equations yields :

$$\frac{\partial \overline{\rho}}{\partial t} + \frac{\partial \overline{\rho} \widetilde{U_i}}{\partial x_i} = 0 \tag{4.16}$$

$$\frac{\partial \overline{\rho} \widetilde{U_i}}{\partial t} + \frac{\partial \overline{\rho} \widetilde{U_i} \widetilde{U_j}}{\partial x_j} = -\frac{\partial \overline{p}}{\partial x_i} + \frac{\partial}{\partial x_j} \left(\widetilde{\tau_{ij}} - \overline{\rho} \, \widetilde{u_i'' u_j''} \right) \tag{4.17}$$

$$\frac{\partial \overline{\rho}\widetilde{E}}{\partial t} + \frac{\partial \overline{\rho}\widetilde{E}\widetilde{U}_i}{\partial x_i} = -\frac{\partial \overline{p}\widetilde{U}_i}{\partial x_i} + \frac{\partial \tilde{\tau}_{ij}\widetilde{U}_i}{\partial x_i} - \frac{\partial}{\partial x_i}\left(\tilde{q}_i - \overline{\rho}\widetilde{E''u_i''}\right) \tag{4.18}$$

$$\tilde{q}_i = -\overline{\kappa}\frac{\partial \widetilde{T}}{\partial x_i} - C_p\overline{\rho}\widetilde{T''u_i''} \tag{4.19}$$

$$\overline{p} = \overline{\rho} r \widetilde{T} \tag{4.20}$$

Where $\tau_{ij}^R = -\overline{\rho}\widetilde{u_i''u_j''}$ is called the Reynolds stress tensor and $q_i^t = \overline{\rho}\widetilde{E''u_i''}$ is the turbulent heat flux. These are the only terms which are not computable from the mean flow, and whch must be modelled to close the system of equations.

4.2.3.1 Eddy Viscosity (Linear Closure) Model

In laminar flows, the energy dissipation and the transport of momentum normal to the streamlines is mediated by the viscosity, so it is natural to assume that the effects of turbulence on the mean flow can be represented as an increased viscosity. One of the most significant contributions to turbulence modelling was presented in 1877 by Boussinesq [12] & [13]. His idea is based on the observation that the momentum transfer in a turbulent flow is dominated by the mixing caused by large energetic turbulent eddies. The Boussinesq hypothesis assumes that the turbulent shear stress is related linearly to mean rate of strain, as in a laminar flow. The proportionality factor is the eddy viscosity.

The Boussinesq hypothesis for Reynolds averaged incompressible flow can be written as :

$$\overline{\tau_{ij}^R} = -\rho\overline{u_i'u_j'} = 2\mu_t\overline{S}_{ij} - \frac{2}{3}\rho k\delta_{ij} \tag{4.21}$$

where $\overline{S}_{ij}$ denotes the Reynolds-averaged strain-rate tensor, k is the turbulent kinetic energy ($k = \frac{1}{2}\overline{u_i'u_i'}$), and μ_t stands for the turbulent eddy viscosity. Unlike molecular eddy-viscosity, μ_t represents no physical characteristic of the fluid, but it is a function of the local flow conditions. Additionally, μ_t is also strongly affected by flow history effects.

For the case of compressible Favre- and Reynolds-averaged Navier-Stokes equations, the Boussinesq eddy-viscosity hypothesis is given by :

$$\overline{\tau_{ij}^F} = -\rho\widetilde{u_i''u_j''} = 2\mu_t\tilde{S}_{ij} - \frac{2\mu_t}{3}\frac{\partial \tilde{u}_k}{\partial x_k}\delta_{ij}\frac{2}{3}\overline{\rho}\tilde{k}\delta_{ij} \tag{4.22}$$

4.2.4 Presentation of Turbulence Model $k-\omega$

In this section, the turbulence models based on RANS approach are presented. It is important to remind here that the main hub of the present research work is based detached eddy simulation (DES), which is discussed in detail later in this chapter. For such type of shock-induced separated flow regimes various RANS models, which are also the possible choices for hybrid RANS/LES methods are discussed here (for details readers are requested to see their corresponding references). For the sake of simplicity, the symbols for Reynolds and Favre averages are dropped in the following.

4.2.4.1 Spalart-Allmaras Model (SA)

The Spalart-Allmaras model is a relatively simple one-equation model that solves a modelled transport equation for the kinematic turbulent eddy viscosity [136]. This embodies a relatively new class of one-equation model in which it is not necessary to calculate a length scale related to the local shear layer thickness. The transport equation for Spalart Allmaras model reads :

$$\frac{\partial \rho\widetilde{\nu}}{\partial t} + \frac{\partial}{\partial x_j}(\rho\widetilde{\nu}U_j) = c_{b_1}(1-f_{t_2})\rho\widetilde{S}\widetilde{\nu} + \frac{1}{\sigma}\left[\frac{\partial}{\partial x_j}\left(\rho(\nu+\widetilde{\nu})\frac{\partial\widetilde{\nu}}{\partial x_j}\right) + c_{b_2}\rho\frac{\partial\widetilde{\nu}}{\partial x_j}\frac{\partial\widetilde{\nu}}{\partial x_j}\right] - \left[c_{w_1}f_w - \frac{c_{b_1}}{\kappa^2}f_{t_2}\right]\rho\left[\frac{\widetilde{\nu}}{d}\right] \tag{4.23}$$

with,

$$\nu_t = \widetilde{\nu}f_{v_1} \tag{4.24}$$

The functions are derived from :

$$\chi = \frac{\widetilde{\nu}}{\nu} \quad f_{v_1} = \frac{\chi^3}{\chi^3 + c_{v_1}^3} \quad f_{v_2} = 1 - \frac{\chi}{1+\chi f_{v_1}} \quad f_{t_2} = c_{t_3}e^{-c_{t_4}\chi^2}$$

$$f_w = g\left[\frac{1+c_{w_3}^6}{g^6+c_{w_3}^6}\right]^{\frac{1}{6}} \quad g = r + c_{w_2}(r^6 - r) \quad r = \frac{\widetilde{\nu}}{\widetilde{S}\kappa^2 d^2}$$

$$\widetilde{S} = S + \frac{\widetilde{\nu}}{\kappa^2 d^2}f_{v_2} \quad S = (2\Omega_{ij}\Omega_{ij})^{\frac{1}{2}} \quad \Omega_{ij} = \frac{1}{2}\left(\frac{\partial U_i}{\partial x_j} - \frac{\partial U_j}{\partial x_i}\right)$$

The constants are :

$$c_{b_1} = 0.1355 \quad c_{b_2} = 0.622 \quad \sigma = \frac{2}{3} \quad \kappa = 0.42 \quad c_{w_1} = \frac{c_{b_1}}{\kappa^2} + \frac{1+c_{b_2}}{\sigma}$$

$$c_{w_2} = 0.3 \quad c_{w_3} = 2 \quad c_{v_1} = 7.1 \quad c_{t_3} = 1.1 \quad c_{t_4} = 2$$

4.2.4.2 $k-\varepsilon$ Model : Chien

It is a two-equation model, which includes two extra transport equations to represent the turbulent properties of the flow [22]. This allows a two-equation model to account for history effects like convection and diffusion of turbulent kinetic energy. The first transported variable is turbulent kinetic energy 'k' and the second transported variable is the turbulent dissipation 'ε'. It is the variable that determines the scale of the turbulence, whereas the first variable k determines the energy in the turbulence.

These transport equations for the $k-\varepsilon$ model of Chien reads :

$$\frac{\partial \rho k}{\partial t} + \frac{\partial}{\partial x_j}(\rho k U_j) = P - \rho\varepsilon - \rho D + \frac{\partial}{\partial x_j}\left((\mu + \frac{\mu_t}{\sigma_k})\frac{\partial k}{\partial x_j}\right) \tag{4.25}$$

$$\frac{\partial \rho\varepsilon}{\partial t} + \frac{\partial}{\partial x_j}(\rho\varepsilon U_j) = c_{\varepsilon_1}f_1\frac{\varepsilon}{k}P - \rho c_{\varepsilon_2}f_2\frac{\varepsilon^2}{k} + \frac{\partial}{\partial x_j}\left((\mu + \frac{\mu_t}{\sigma_\varepsilon})\frac{\partial\varepsilon}{\partial x_j}\right) + \rho E \tag{4.26}$$

with,

$$\mu_t = \rho c_\mu f_\mu \frac{k^2}{\varepsilon} \tag{4.27}$$

and,

$$P = -\overline{u_i u_k}\left(\frac{\partial U_j}{\partial x_k}\right)^2 \tag{4.28}$$

Where $C_{\varepsilon 1}$, $C_{\varepsilon 2}$, C_μ, σ_k, and σ_ε are the model constants. The damping functions f_μ, f_1 and f_2 and the extra source terms D and E are only active close to the solid walls and makes it possible to solve k and ε down to the viscous sub-layer. The constants, damping functions and the boundary conditions are given below :

$$\sigma_k = 1; \quad \sigma_\varepsilon = 1.3; \quad c_{\varepsilon_1} = 1.35; \quad c_{\varepsilon_2} = 1.8; \quad D = 2\nu\frac{k}{x_j^2}$$

$$E = \frac{2\mu\varepsilon}{y^2}e^{-0.5y^+}; \quad f_\mu = 1 - e^{-0.0115y^+}; \quad f_1 = 1; \quad f_2 = 1 - 0.22e^{-(\frac{R_t}{6})^2}$$

4.2.4.3 $k-\omega$ Models : Wilcox & Menter's SST

- **Wilcox $k-\omega$ Model**

The $k-\omega$ model is one of the most common turbulence models [155]. It is a two-equation model in which first transported term is the turbulent kinetic energy k and the second transported variable is the specific dissipation ω, which is defined as :

$$\omega = \frac{\varepsilon}{\beta^* k} \tag{4.29}$$

The transport equation for Wilcox $k-\omega$ model are given below, for details about this model see [155] :

$$\frac{\partial \rho k}{\partial t} + \frac{\partial}{\partial x_j}(\rho k U_j) = P - \beta^* \rho k \omega + \frac{\partial}{\partial x_j}\left((\mu + \sigma^* \mu_t)\frac{\partial k}{\partial x_j}\right) \tag{4.30}$$

$$\tag{4.31}$$

$$\frac{\partial \rho \omega}{\partial t} + \frac{\partial}{\partial x_j}(\rho \omega U_j) = \alpha\frac{\omega}{k}P - \beta\rho\omega^2 + \frac{\partial}{\partial x_j}\left((\mu + \sigma\mu_t)\frac{\partial \omega}{\partial x_j}\right) \tag{4.32}$$

with,

$$\mu_t = \frac{\rho k}{\omega} \tag{4.33}$$

Finally the standard constants of the model are effectively used in this study and are given below (the details about the calibration of these constant is given in [156])

$$\alpha = \frac{5}{9} \quad \beta = \frac{3}{40} \quad \beta^* = c_\mu = 0.09 \quad \sigma = \sigma^* = 0.5$$

• **Menter's SST $k-\omega$ Model**

The SST $k-\omega$ model was proposed by Menter in 1993 [86]. The SST formulation combines the best of the two models i.e. the use of the $k-\omega$ formulation in the inner parts of the boundary layer : which makes the model directly usable all the way down to the wall through the viscous sub-layer, hence the SST $k-\omega$ model can be used as a 'Low-Re turbulence model' without any extra damping functions. The SST formulation also switches to a $k-\varepsilon$ behaviour in the free-stream and thereby avoids the common $k-\omega$ problem that the model is too sensitive to the inlet free-stream turbulence properties. This model shows good behaviour in adverse pressure gradient and separated flows.

The transport equations for SST $k-\omega$ reads :

$$\frac{\partial \rho k}{\partial t}+\frac{\partial}{\partial x_j}(\rho k U_j)=P-\beta^*\rho k\omega+\frac{\partial}{\partial x_j}\left((\mu+\sigma_k\mu_t)\frac{\partial k}{\partial x_j}\right. \tag{4.34}$$

$$\frac{\partial \rho\omega}{\partial t}+\frac{\partial}{\partial x_j}(\rho\omega U_j)=\rho\frac{\gamma}{\mu_t}P-\beta\rho\omega^2+\frac{\partial}{\partial x_j}\left((\mu+\sigma_\omega\mu_t)\frac{\partial\omega}{\partial x_j}\right) +2(1-F_1)\rho\sigma_{\omega_2}\frac{1}{\omega}\frac{\partial k}{\partial x_j}\frac{\partial\omega}{\partial x_j} \tag{4.35}$$

with,

$$\mu_t=\frac{\rho k/\omega}{max\left(1,\frac{\Omega F_2}{a_1\omega}\right)} \tag{4.36}$$

The function F_1, switch the Wilcox model near the wall ($F_1=1$), and $k-\varepsilon$ model away from the wall ($F_1=0$) and the function F_2 limits the value of turbulent viscosity, are given by :

$$F_1=tanh(arg_1^4) \quad \text{with} \quad arg_1=min\left[max\left(\frac{\sqrt{k}}{0.09\omega y},\frac{500\nu}{y^2\omega}\right),\frac{4\rho\sigma_{\omega_2}k}{CD_{k\omega}y^2}\right]$$

$$\text{et} \quad CD_{k\omega}=min\left(2\rho\sigma_{\omega_2}\frac{1}{\omega}\frac{\partial k}{\partial x_j}\frac{\partial\omega}{\partial x_j},10^{-20}\right)$$

$$F_2=tanh(arg_2^4) \quad \text{with} \quad arg_2=max\left(2\frac{\sqrt{k}}{0.09\omega y},\frac{500\nu}{y^2\omega}\right)$$

The constants appears in this model are calculated as follows : Let ϕ be the constant used in SST model and ϕ_1 and ϕ_2 are the constants used $k-\omega$ and $k-\varepsilon$ model respectively, then :

$$\phi=F_1\phi_1+(1-F_1)\phi_2 \quad \text{where} \quad \phi=(\sigma_k,\sigma_\omega,\beta,\gamma)$$

$$k-\omega \quad \text{Model} \quad \sigma_{k_1}=0.85 \quad \sigma_{\omega_1}=0.5 \quad \beta_1=0.075 \quad \gamma_1=\frac{\beta_1}{\beta^\star}-\frac{\sigma_{\omega_1}\kappa^2}{\sqrt{\beta^\star}}$$

$$k-\varepsilon \quad \text{Model} \quad \sigma_{k_2}=1.0 \quad \sigma_{\omega_2}=0.856 \quad \beta_2=0.0828 \quad \gamma_1=\frac{\beta_2}{\beta^\star}-\frac{\sigma_{\omega_2}\kappa^2}{\sqrt{\beta^\star}}$$

4.2.5 Simulation of Supersonic Separated Flows

The numerical study of turbulence in compressible flows in presence of shock-waves is a difficult problem especially because of its multi-scale character. Indeed, this problem shows three characteristic scales : Δx, λ^2_{choc}, η_k, which represent spatial grid size, the thickness of the shock and the smallest scale dynamically active of the velocity field respectively. In addition, the flow undergoes very rapid changes that are difficult for the simulation. More precisely, the turbulent kinetic energy is amplified behind the shock, the turbulence becomes anisotropic and the largest wave numbers are the most amplifies. It can be shown that the thickness of the shock, λ_{choc}, is of the order of mean free path $\overline{\lambda}$. For standard conditions of temperature and pressure, λ_{choc}= 5.10^{-8}m, for air [80]. The decrease in the cost of computer power over the last few years has increased the impact of computational fluid dynamics. Numerical simulations of fluid flows, which until a few decades ago were confined to the research environment, are now successfully used for the development and design of engineering devices. Despite the advances in computer speed and in algorithmic developments, the numerical simulation of turbulent flows has not yet reached a mature stage : none of the techniques currently available can reliably be applied to all problems of scientific or technological interest.

The solution of the Reynolds-averaged Navier-Stokes equations (RANS) is the tool that is most commonly applied, especially in engineering applications, to the turbulent flow problems. The RANS equations are obtained by time- or ensemble-averaging the Navier-Stokes equations to yield a set of transport equations for the averaged momentum. The effect of all the scales of motion is modelled. Models for the RANS equations have been the object of much study over the last 30 years, but no model has emerged that gives accurate results in all flows without ad hoc adjustments of the model constants (see [157]). This may be due to the fact that the large, energy-carrying eddies are much affected by the boundary conditions, and universal models that account for their dynamics may be impossible to develop.

In direct numerical simulations (DNS), on the other hand, all the scales of motion are resolved accurately, and no modelling is used. DNS is the most accurate numerical method available at present but is limited by its cost. Because all scales of motion must be resolved, the number of grid points in each direction is proportional to the ratio between the largest and the smallest eddy in the flow. This ratio is proportional to $Re_L^{3/4}$ (where Re_L is the Reynolds number based on an integral scale of the flow). Thus, the number of points in three dimensions is $N_x N_y N_z \propto Re_L^{3/4}$. Present computer resources limit the application of DNS to flows with $Re_L = O(10^4)$, and the $Re_L^{3/4}$ dependence of the number of grid points makes it unrealistic to expect that DNS can be used for high-R_e engineering applications in the near future.

Large-eddy simulation is a technique intermediate between the solution of the RANS equations and DNS. In large-eddy simulation (LES) the large, energy carrying eddies are computed, whereas only the small, subgrid scales of motion are modelled. LES can be more accurate than the RANS approach because the small scales tend to be more isotropic and homogeneous than the large ones, and thus more amenable to universal modelling. Furthermore, the modelled subgrid scale (SGS) stresses only contribute to a small fraction of the total turbulent stresses. Compared with DNS, LES does not suffer from the same strict resolution requirements of DNS. LES has received increased attention in recent years, as a tool to study the physics of turbulence in flows at higher Reynolds number or in more complex geometries than DNS. Its most successful applications, however, have still been for moderate Reynolds numbers ; examples include the flow inside an internal combustion engine [148] or the sound emission from the trailing edge of

a hydrofoil at $Re_c = 2.0 \times 10^6$ (Wang & Moin [150]). In a wide range of flows in the geophysical sciences (especially in meteorology and oceanography) and engineering (for instance, in ship hydrodynamics or in aircraft aerodynamics), however, the Reynolds number is very high, of the order of tens or hundreds of millions. The extension of LES that resolves the wall-layer structures (henceforth called "resolved LES") to such flows has been less successful owing to the increased cost of the calculations when a solid boundary is present.

The first complete analysis of grid-resolution requirements for LES of turbulent boundary layers can be found in the landmark paper by Chapman [19]. The flow in a flat-plate boundary layer or plane channel is generally divided into an inner layer in which the effects of viscosity are important and an outer one in which the direct effects of the viscosity on the mean velocity are negligible. Chapman [19] examined the resolution requirements for inner and outer layers separately. In the outer layer in which the important eddies scale like the boundary-layer thickness or the channel half-height δ, he obtained an estimate for the outer-layer resolution by integrating Pao's [107] energy spectrum and showed that the number of points in the wall-normal direction required to resolve a given fraction of the turbulent kinetic energy is essentially independent of R_e.

Assuming that the grid size in the streamwise and spanwise directions are fixed fractions of the boundary-layer thickness (which varies approximately like $Re^{0.2}$) his estimate results in a total number of grid points proportional to $Re^{0.4}$. Chapman estimated that only 2500 points are required to resolve a volume δ of the flow, where $\overline{\delta}$ is an average boundary-layer thickness. In actual calculations, a wide range of resolutions is found : In calculations of plane channel flow, for instance, Schumann [132] used between 128 and 4096 points to resolve a volume δ^3 (here δ is the channel half-height), whereas Piomelli et al. [112] used 1000 points. The resolution of the inner layer is much more demanding : Its dynamics are dominated by quasi-streamwise vortices (see [126]) whose dimensions are constant in wall units (i.e., when normalized with the kinematic viscosity ν and the friction velocity $u_\tau = (\tau_w/\rho)^{1/2}$, where τ_w is the wall stress and ρ the fluid density). If the inner-layer eddies are resolved, a constant grid spacing in wall units must be used.

In a boundary layer or channel flow, this requirement results in streamwise and spanwise grid sizes $\Delta x^+ = 100$, $\Delta z^+ = 20$ (where wall units are defined as $x_i^+ = x_i u_\tau/\nu$). As the outer flow is approached, however, larger grid spacing can be used. An optimal computation, therefore, would use nested grids, with Δx^+ and Δz^+ increasing as one moves away from the wall. Under these conditions, Chapman [19] estimated that the number of points required to resolve the viscous sub layer is

$$(N_x N_y N_z)_{vs} \propto C_f Re_L^2$$

where $C_f \propto Re_L^{-0.2}$, gives

$$(N_x N_y N_z)_{vs} \propto Re_L^{1.8}$$

In plane channel flow (an important test case for numerical simulations) Chapman's [19] estimate for the cost of the outer layer needs to be modified. The size of the largest eddies is determined by the channel height and is not a function of the Reynolds number, whereas the cost of resolving the inner layer is the same for channels and boundary layers. Grid-resolution estimates for more complex flows cannot be derived a priori. To estimate the cost of the calculation, one must consider that the equations of motion must be integrated for a time proportional

to the integral timescale of the flow, with a time step limited by the need to resolve the life of the smallest eddy. Reynolds [125] estimates the cost by assuming that the operation count scales like the number of points and that the time step can be determined by the time-scale of the smallest eddy, which is inversely proportional to its length scale and, therefore, to the grid size. This gives a number of time steps proportional to $(NxNyNz)^{1/3}$ and a total cost that is proportional to $(NxNyNz)^{4/3}$. This estimate gives a cost that scales like $Re^{0.5}$ for the outer layer, and $Re^{2.4}$ for the inner one. This estimate disregards the viscous stability conditions and is strictly valid only for calculations in which at least the diffusion is treated implicitly, or neglected.

The only economical way to perform LES of high Reynolds-number attached flows, therefore, is by computing the outer layer only. The grid size can, under these conditions, be determined by the outer-flow eddies, and the cost of the calculation becomes only weakly dependent on the Reynolds number. Because the grid is too coarse to resolve the inner-layer structures, the effect of the wall layer must be modelled. In particular, the momentum flux at the wall (i.e., the wall stress) cannot be evaluated by discrete differentiation because the grid cannot resolve either the sharp velocity gradients in the inner layer or the quasi-streamwise and hairpin vortices that transfer momentum in this region of the flow. Therefore, some phenomenological relation must be found to relate the wall stress to the outer-layer flow. This requirement spurred the development of models for the wall layer, also known as approximate boundary-conditions. Wall-layer models were initially developed along parallel lines by geophysical scientists and engineers. The principal difference between the two fields is the presence of stratification, which is important in meteorological flows but usually not in engineering ones.

The limitations of LES, when applied to wall-bounded flows, were recognized in the very early stages of the development of the technique : In the ground-breaking LES of plane channels and annuli by Deardorff [24] and Schumann [132], respectively, approximate wall-boundary conditions were introduced to model the effect of the wall layer, which could not be resolved with the computer power available at that time even at moderate Reynolds numbers. In the methodology they proposed, information from the outer flow is used to determine the local wall stress, which is then fed back to the outer LES in the form of the proper momentum flux at the wall due to normal diffusion. The no-transpiration condition was used on the wall-normal velocity component. Today this general approach is still in use in various forms. The cost of these calculations is due to the outer-layer computation only and is proportional to $Re^{0.5}$ for spatially developing flows. The results obtained by Deardorff [24] for the turbulent channel flow at infinite Reynolds number do not compare well with the experimental data of Laufer [72].

The wall model, however, most likely has a small contribution to these errors, which are mainly due to the resolution in the outer layer that was not sufficient to resolve the large energy-carrying structures. A total of 6720 grid nodes were used, which corresponds to approximately 400 points to resolve a volume δ^3 ; this is six times less than the number of required points estimated by Chapman [19]. One main obstacle to the application of large-eddy simulations (LES) to industrial applications is the CPU time required to perform resolved LES of wall-bounded flows. In wall-bounded flows the integral scale, away from walls, is proportional to the boundary-layer thickness, δ. A reasonable estimate of the grid spacing in each direction is then $\Delta x_i = \delta/25 - \delta/15$. If one considers a cube of side δ and volume δ^3 as the basic unit, its resolution will require about 400 grid points. In order to simulate a computational domain of dimensions $Lx \times Ly \times Lz$ one needs $N_{c,x} \times N_{c,y} \times N_{c,z}$ unit cubes, with $N_{c,x} = L_x/\delta$ and so on. The number of grid points can then be estimated by multiplying the number of δ^3 cubes by the

number of points per cube (400).

As the Reynolds number Re (based on the boundary-layer thickness) is increased, θ decreases, and the number of cubes required to cover the area $Lx \times Lz$ increases (it may be assumed that, in the direction normal to the wall, only a few (2 or 3) boundary-layer thicknesses need to be resolved : in the inviscid region the grid can be coarsened rapidly, so that the number of points required to resolve the potential region is negligible). For boundary-layer flows, in which $\delta \propto Re^{0.2}$, this results in a number of cubes proportional to $Re^{0.4}$ so that the number of grid points required to resolve the outer layer is

$$NxNyNz \propto Re^{0.4}$$

In the near-wall region, the Re-dependence of the resolution is much steeper, since the near-wall eddies that need to be resolved scale with wall units. As the Reynolds number is increased, the physical dimensions of these eddies decrease much more rapidly than the boundary-layer thickness, resulting in more stringent grid requirements. To obtain the cost of a calculation one must also consider that the equations of motion must be advanced for several integral time-scales of the flow in order to obtain converged statistics. The time-step is generally determined by a CFL condition, which gives $\Delta t \propto \Delta x/U$ (in attached flows the streamwise direction is the most restrictive from this point of view).

Thus, the number of time steps required to perform a simulation is proportional to the number of grid points in one direction, $N_t \propto Re^{0.2}$ for the outer layer, while $N_t \propto Re^{0.6}$ for the inner layer. The total cost of a calculation, therefore, scales like $Re^{0.6}$ for the outer layer, and like $Re^{2.4}$ if the inner layer is to be resolved. As a consequence of this unfavourable scaling, wall-resolved LES are limited to very moderate Reynolds numbers. Only if massive computational resources (clusters with thousands of processors) are available, calculations at Reynolds numbers of marginal engineering interest ($Re = 10^5$) are possible.

4.2.6 Towards Hybrid LES-RANS Techniques

Each simulation of a turbulent flow is performed for a particular purpose. The minimum goal presumably is to determine the mean flow with acceptable precision. Further levels are the computation of higher moments or the determination of instantaneous unsteady features. Reynolds-Averaged Navier-Stokes (RANS) models provide results for mean quantities with engineering accuracy at moderate cost for a wide range of flows [17]. In other situations, dominated by large-scale anisotropic vortical structures like wakes of bluff bodies, the average quantities are often less satisfactory when a RANS model is employed. Then Large Eddy Simulation (LES) performs generally better and bears less modelling uncertainties. Furthermore, LES by construction provides unsteady data that are indispensable in many cases : determination of unsteady forces, fluid-structure coupling, identification of aerodynamic sources of sound, and phase-resolved multiphase flow, to name but a few issues. Unfortunately, LES is by a factor of 10 to 100 more costly than RANS computations [15] : LES requires a finer grid, cannot benefit from symmetries of the flow in space, and provides mean values only by averaging the unsteady flow field computed with small time-step over a long sampling time. Hence, it seems natural to attempt a combination of both turbulence modelling approaches and to perform LES only where it is needed while using RANS in regions where it is reliable and efficient. Close to walls, the LES philosophy of resolving the locally most energetic vortical structures requires to substantially reduce the step size of the grid since the dominating structures become very small in this

region. Furthermore, when increasing the Reynolds number, the scaling of the computational effort is similar to that of a DNS in its dependence on R_e just with a smaller constant [19]. That makes the approach unfeasible for wall-bounded flows at high R_e, such as the flow over a wing [137]. As a remedy, some sort of wall model can be introduced to bridge the near-wall part of the boundary layer and to make the scaling of the required number of grid points independent of R_e. Near-wall models in the form of wall functions relying on the logarithmic law of the wall have been used since the very first LES [24], [132]. Slightly rephrased, statistical information is used in place of higher resolution. Since then, this approach has been extended in different directions. Other scaling and wall laws can be used [150], [151] & [154] as well as boundary layer equations in the wall adjacent cell [7], [16]. Details are given in reviews on LES, such as [56], [113], & [130]. In this perspective it is natural to enhance the approach by considering a full RANS model in the near-wall region and to combine it with an LES for computation of the outer flow. Hence, detached eddy simulation (DES) has been considered for this present study to perform the numerical simulations and is given in the following section.

4.2.7 Realizable Delayed Detached Eddy Simulation (RDDES)

Supersonic separated flow configurations in rocket nozzles yield strong shock-boundary layer and shock-shock interactions. A common two-equation model typically violates the realizability under these circumstances [146] and has not been found in good agreement with the experimental data [105]. To deal with such type of flow configurations, a new version of DES has been proposed in this research study and is referenced as Realizable Delayed Detached Eddy Simulation (RDDES).

This RDDES formulation is based on $k-\omega$ model due to its well known capability of separation point prediction, especially in strong adverse pressure gradient flows. In much more complicated flow configurations when we deal with supersonic separated flows these two-equation linear models based on Boussinesq assumption violates the realizability constraints. This also affects the capability of these standard RANS models to predict the separation point. Hence to deal with these complex flow regimes, this new version of DES based on $k-\omega$ model is used along with realizability correction. Formulation of RDDES includes the extension of two equations $k-\omega$ model, which has already been reported in section (4.2.4), and is given below :

4.2.7.1 (U) RANS Mode : Realizability Constraint

Schumann [133] and Lumely [85] defined the weak version of realizability : the variances of the fluctuating velocity components must be positive and the cross-correlations should be bounded by Schwartz inequality.

$$\overline{uv}^2 \leq \overline{u^2v^2},\ \ \overline{uw}^2 \leq \overline{u^2w^2},\ \ \overline{vw}^2 \leq \overline{v^2w^2} \tag{4.37}$$

$$\overline{uv}^2 \leq \overline{u^2v^2},\ \ \overline{uw}^2 \leq \overline{u^2w^2},\ \ \overline{vw}^2 \leq \overline{v^2w^2} \tag{4.38}$$

These constraints are not fulfilled by the linear models based on Boussinesq assumption, and they can be infringed in the presence of strong shock wave and boundary layer interactions (shock induced separation). In order to avoid these unrealistic results, Moore & Moore [92] proposed correction based on realizability constraints. The general idea of this correction is based

on observation that, realizability can be ensured by properly decreasing the level of turbulent eddy viscosity, and is given as :

$$\mu_t = \alpha_\nu C_\mu \rho k/\omega \tag{4.39}$$

where

$$\alpha_\nu = min(1, \overline{\alpha}_\nu) \quad \& \quad \frac{1}{\overline{\alpha}_\nu C_\mu} = A_o + A_s(s^2 + A_r\overline{\omega}^2)^{1/2}$$

Here s is the dimensionless mean strain rate S/ω with $S^2 = 2S_{ij}S_{ij} - \frac{1}{2}S_{kk}^2$, and $\overline{\omega}$ is the dimensionless vorticity invariant $\sqrt{2\Omega_{ij}\Omega_{ij}}/\omega$.

$$S_{ij} = \frac{1}{2}\left(\frac{\partial U_i}{\partial x_j} + \frac{\partial U_j}{\partial x_i}\right); \quad \Omega_{ij} = \frac{1}{2}\left(\frac{\partial U_i}{\partial x_j} - \frac{\partial U_j}{\partial x_i}\right) \tag{4.40}$$

$A_o = 2.85$; $A_s = 1.77$; $A_r = 1$

4.2.7.2 DES Extension

4.2.7.3 RDDES1

In 2005, Yan et al. [158] have investigated different length scales substitutions in DES based on Wilcox standard $k-\omega$ model. Following this, we propose the implementation of DES based on the Wilcox $k-\omega$ model with realizability correction. In order to understand the expression of the modifications, equations (4.31) and (4.39) are rewritten as follows :

$$\frac{\partial \rho k}{\partial t} + \frac{\partial}{\partial x_j}(\rho k U_j) = P_k - \frac{\rho k^{3/2}}{L_k}\omega + \frac{\partial}{\partial x_j}\left((\mu + \frac{\mu_t}{\sigma_k})\frac{\partial k}{\partial x_j}\right) \tag{4.41}$$

$$\nu_t = \frac{\mu_t}{\overline{\rho}} = C_\mu L_\nu k^{1/2} \tag{4.42}$$

Here, L_k and L_ν have no independent meaning, but denote the turbulent length scale L_t in equations 4.41 and 4.42, respectively. This is defined as

$$L_t = \frac{k^{1/2}}{C_\mu \omega} \tag{4.43}$$

Defined classical DES length scale is given as :

$$L_{DES} = min(L_t, C_{DES}\Delta) \tag{4.44}$$

Where C_{DES} is 0.7 [158] and $\Delta = max(\Delta_x, \Delta_y, \Delta_z)$ is the computational mesh size. L_{DES} is a continuous function, given by the minimum of the two length scales. For DES implementation, the turbulent length scale L_t in the dissipation term of k transport equation is replaced by the DES length scale L_{DES}, so that :

$$L_k = L_{DES}, \quad L_\nu = L_t \tag{4.45}$$

This substitution leads to calculate the eddy viscosity like in the standard RANS model with the realizability correction as discussed earlier.

DDES Part

Menter and Kuntz [87] use shielding functions F_1 & F_2 of the SST model to protect the "RANS mode" in the boundary layer from early switching to "LES mode". Later on this switching function in generalized form was given by Spalart et al. [138] and the resulting DES formulation was named as 'Delayed Detached Eddy Simulation (DDES)'. In the framework of this study, we have used the F_1 function and the modified DDES length scale for the present DES is given by :

$$L_{DDES} = L_t - f_{DDES} \times max(0, L_t - C_{DES}\Delta) \tag{4.46}$$

Where $f_{DDES} = 1 - F_1$, when this function is 0 : RANS mode activate near wall region and turns into LES mode when it is equal to 1.

4.2.7.4 RDDES2

Recently it has been found that, with a classical DDES, the introduction of the DES length scale only in the dissipation term, may cause a delay in the development of the resolved shear layer. This development of shear can be accelerated in fact by introducing the DES length scale in the turbulent viscosity term, as also been done in the case of X-LES [69]. This has been done for this RDDES approach too, only by changing both the turbulence length scales L_k and L_ν (given above) by DES length scale (L_{DES}).

$$L_k = L_{DDES}, \quad L_\nu = L_{DDES} \tag{4.47}$$

In the boundary layer region, this RDDES2 remains identical to the Wilcox $k-\omega$ model with the realizability correction. In the LES mode (resolved region), for the dissipation term, it remains the same as RDDES1. In addition, the modified eddy viscosity term is :

$$\nu_t = C_\mu C_{DES} \Delta k^{1/2} \tag{4.48}$$

Here the constant $C_{DES} = 0.95$, as used by Yan et al. [158]. Again in order to shield the boundary layer the same switching function, as for RDDES1, has been applied.

Chapitre 5

Validation of Numerical Tools

The numerical prediction of shock-induced separated flows encounters a number of problems regarding the numerical schemes and turbulence modelling. A better prediction of these flow regimes requires improved numerical schemes (spatial and temporal) and has been a challenge for the existing RANS models and their respective extension to hybrid methods. Different numerical strategies have been implemented during this research work to improve the available tools. This chapter addresses the preliminary comparative studies carried out to validate the choice of implemented numerical methods and/or turbulence models, which are used to investigate supersonic separated flows in over-expanded nozzle.

5.1 Choice of Numerical Schemes

In this section, a comparative study of second order MUSCL and fifth order MPWENO schemes (for space discretization) is reported. The validation of their combination with the second order implicit scheme for temporal discretization is then addressed.

5.1.1 Advection of a Vortex

The main goal of the present test case is to evaluate the diffusive or dispersive properties of the aforementioned shock-capturing scheme in the framework of implicit time integration. The similar type of test case was also performed by Tenaud et al. [144] for the evaluation of higher order shock-capturing schemes. It simply consists in advecting a vortex in a uniform 2D flow.

Flow Configuration

The computational domain is a square [0,1] [0,1] with grid 200 $\times$ 200. An isolated Taylor vortex is initially superimposed to a uniform flow at a Mach number $M = 0.8$. The tangential velocity is given by :

$$V_\theta(r) = C_1 r.e^{-C_2 r^2} \tag{5.1}$$

with

$$C_1=\frac{U_c}{r_c}e^{1/2}, \qquad C_2=\frac{1}{2r_c^2}, \qquad r=\sqrt{(x-x_o)^2+(y-y_o)^2}$$

We set $r_c = 0.075$ and $U_c = 0.3$. Following these values, the radius of the viscous core is $\frac{1}{2}$. The inital position of the vortex center is $x_o = \frac{1}{2}, y_o = \frac{1}{2}$. Periodic boundary conditions are applied in both directions (x, y). Different tests have been performed at different CFL numbers and are discussed below.

Results

The simulations are performed during five periods of convection through the domain. The conservative quantities are recorded at fifth length scale $T5$ where the center of the vortex coincides with the center of the domain. Owing to the effect of the numerical diffusion, the radius of the viscous core is a growing function of time. This is illustrated in the Fig. 5.1 & 5.2, where the distribution of the vertical velocity component $V(m/s)$ along the centerline of the domain $(y = \frac{1}{2})$ is compared to the initial distribution. The comparison is made between fifth order MPWENO, the second order MUSCL (with minmod limiter) scheme and the initial distribution of the vortex (see Fig. 5.1). As expected, the second-order MUSCL scheme appears to be far more dissipative than fifth order MPWENO scheme. Even at only CFL=5.0, the peak value of the tangential velocity has decreased by about 30 % in the first case, whereas, the error is less than 5 % for the second case. The individual comparison of MPWENO scheme is then done for $1.0 \leq \text{CFL} \leq 25.0$ (see Fig. 5.2). At relatively low CFL, only a very small amount of dissipation is induced by the scheme. However, this numerical dissipation increases as a function of the CFL number. Even at CFL=25.0, the presented scheme lead to results in good agreement with the initial vortex distribution. Even if this test remains basic, it constitutes a relevant tool to calibrate the CFL number, not only from the stability standpoint, but also from the perspective of maintaining a sufficient level of accuracy.

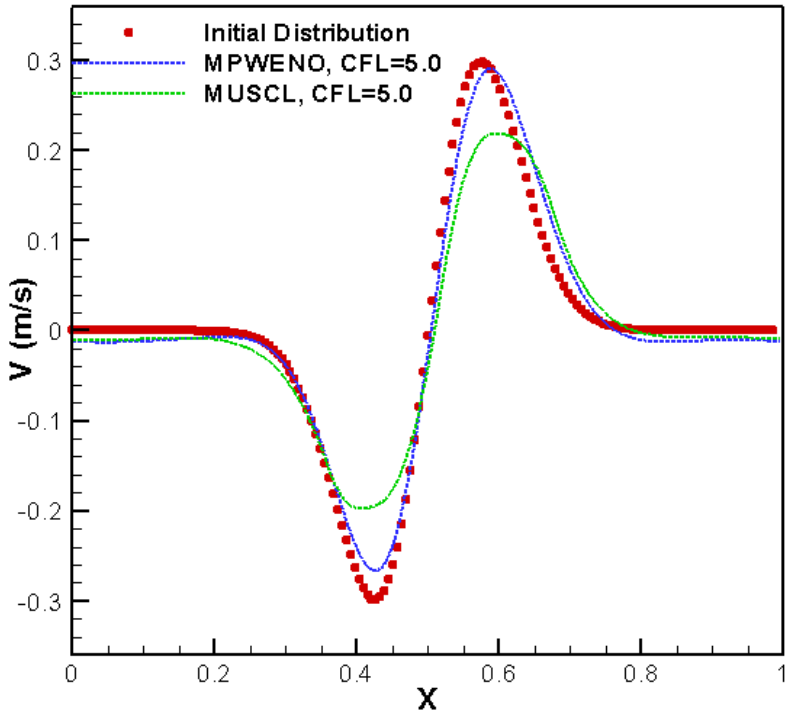

FIGURE 5.1 – Streamwise distribution of vertical velocity (V) on line y=0.5 showing the influence of numerical scheme on advection of a vortex (Mach=0.8 and after 5 periods of advection).

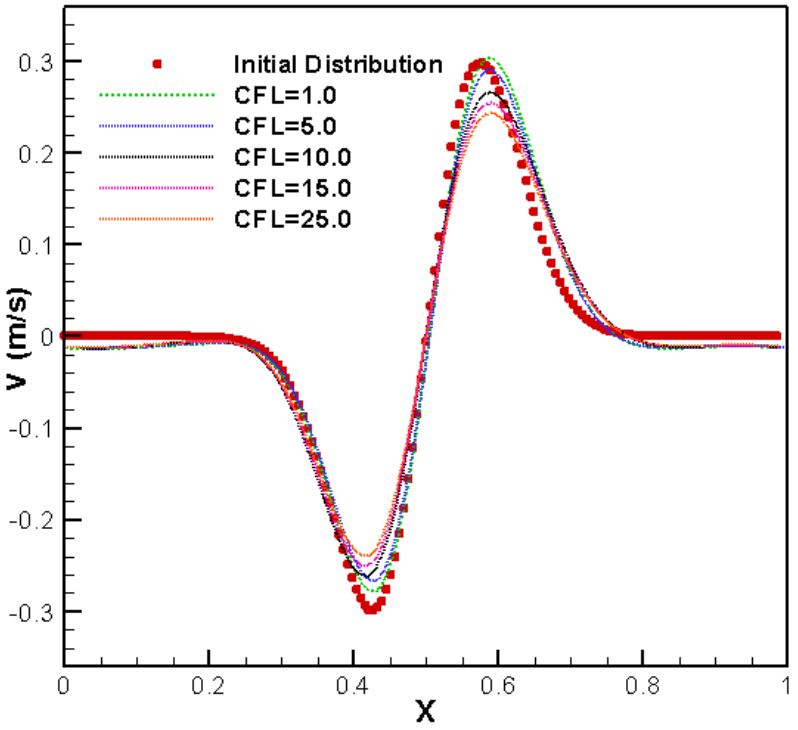

FIGURE 5.2 – Streamwise distribution of vertical velocity (V) on line y=0.5 : MPWENO scheme, indicating the influence of numerical scheme on advection of a vortex (Mach=0.8 and after 5 periods of advection).

5.1.2 Influence of Numerical Schemes on Shock-Induced Separated Flows

Since the flows in FSS and RSS flow contain flow discontinuities, selecting the lowest dissipative numerical schemes is important to obtain a correct numerical solution. The case of free shock separation has been selected here to perform the comparison of numerical schemes (i.e. second order MUSCL and fifth order MPWENO) and to assess their influence on the numerical solution. Three dimensional numerical solutions are obtained by using $k-\omega$ model with realizability corrections for a grid containing 4.32 million points (details regarding to the influence of turbulence models for such flow configurations will be discussed latter in this chapter). The results show that the axial location of Mach disk, with respect to the nozzle throat, is only slightly over-estimated by MUSCL in comparison with MPWENO scheme. The most significant difference in terms of numerical dissipation appears in fact in the vorticity production across the flow discontinuities.

Figure 5.3, presents the evolution of the shock function ($f(x) = \frac{U}{c} \cdot \frac{gradp}{|gradp|}$) and the magnitude of vorticity along the nozzle axis, respectively. One can notice that the second order MUSCL scheme seems to be dissipative in comparison with MPWENO, as we have already observed in vortex advection test case. However, the important point to note here is that, downstream of Mach disk (along the nozzle axis), MUSCL scheme leads to an artificially high level of vorticity production, which seems mainly related only to a too high numerical diffusion. This type of non-physical behaviour has also been observed during the axi-symmetric URANS (k-ω model with realizability correction) calculations for flow transition from FSS to RSS configuration, as shown in Fig. 5.4-5.5. Here the purpose is not to explain transition process, but the objective is to highlight the appearance of vortical structure (in addition to the large trapped vortex) downstream of the cone-shaped shock for the numerical solution obtained by using MUSCL scheme. Such type of vortices has also been reported by Moríñigo et al. [94] during the axi-symmetric RANS calculation (by using second order discretization in space) on J-2S TOC nozzle to reproduce forward (FSS to RSS) flow transition process. However, in the solution obtained by using fifth order MPWENO scheme, such vortical structures are not observed. One may conclude that the formation of these vortices, other than trapped vortex, downstream of the cap-shock pattern, are not physical and result from an excess of numerical dissipation. Accordingly, in order to limit as far as possible the occurrence of any numerical artifact, all simulations in this research are performed by using fifth order MPWENO scheme.

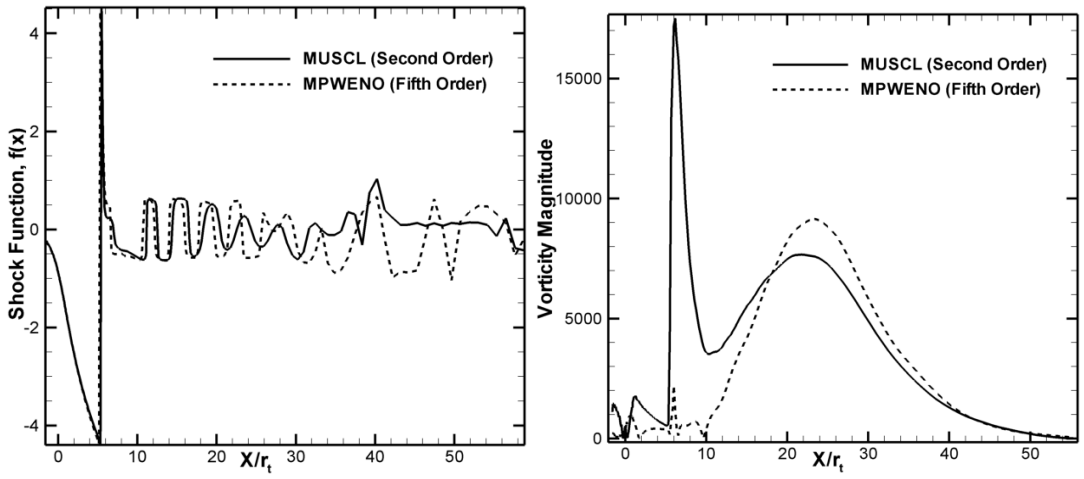

FIGURE 5.3 – Influence of numerical schemes on the axial evolution of the shock-function ($f(x) = \frac{U}{c}\frac{grad\ p}{|grad\ p|}$, c=speed of sound) & vorticity magnitude along the nozzle axis in a simulation of FSS flow configuration (NPR=15.5).

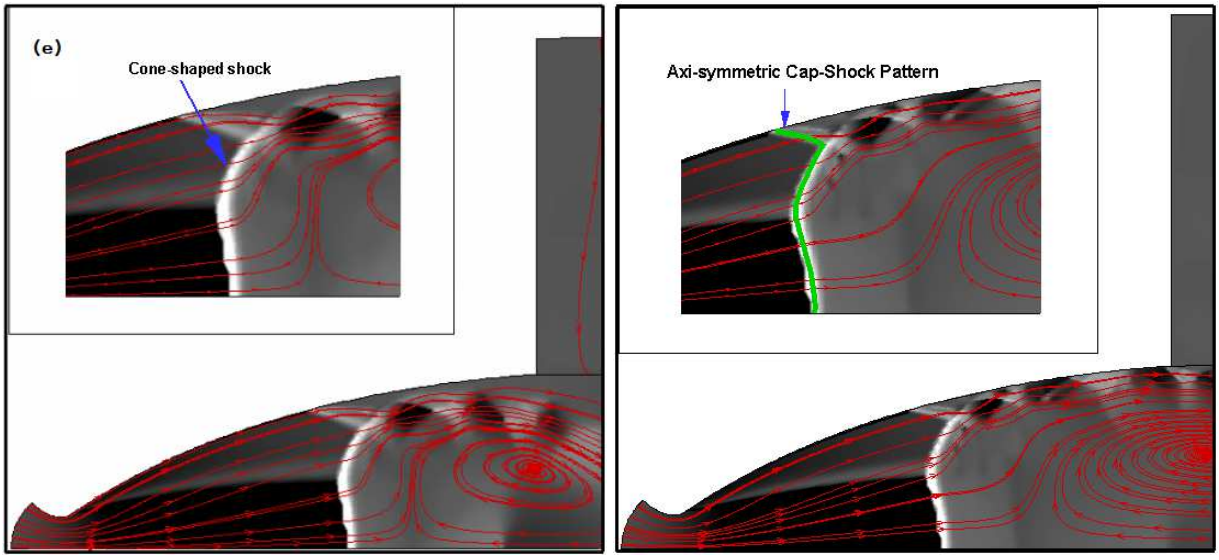

FIGURE 5.4 – Influence of the numerical scheme on the evolution of the flow topology during the flow transition process at two different instants (NPR=24.0 & fifth order MPWENO scheme).

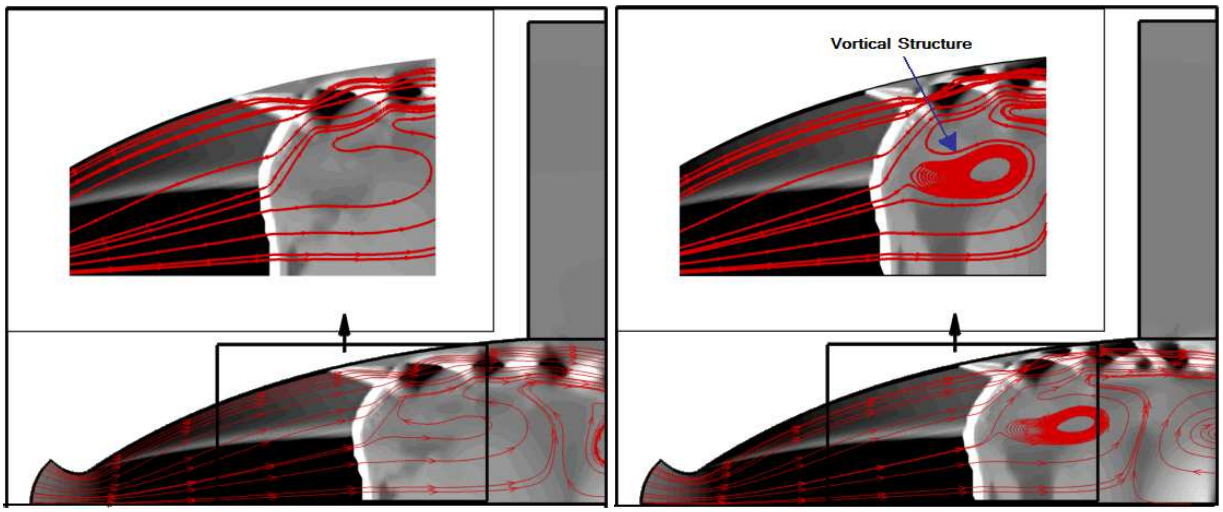

FIGURE 5.5 – Influence of the numerical scheme on the evolution of the flow topology during the flow transition process at two different instants (NPR=24.0 & second order MUSCL scheme), showing the non-physical appearance of vortical structures downstream of the shock system.

5.2 Choice of the Turbulence Model for the Simulation of Supersonic Separated Flow

The numerical prediction of these supersonic separated flows, which lead to high pressure and heat loads, has been a challenge for the existing RANS models and their respective hybrid LES/RANS extension. Accurate prediction of turbulent flows with adverse pressure gradient and separation has been an area of interest over decades. Significant disagreement with the experimental data has been observed, especially in the presence of strong shock-waves and their interaction with the turbulence (boundary layers) [146].

Various turbulence models have been used to study these flow regimes [21], [110], [26] & [105]. Such type of shock-induced separated flows contains different flow discontinuities and the use of turbulence models based on linear approximation across the shock produces some non-physical behaviour and sometimes completely changes the flow physics. Several modifications have been proposed to improve the prediction capabilities of these models e.g. realizability constraint, compressibility correction, length scale modification, rapid compression correction [23], [82] & [92]. A few of them are used and discussed here. In this section we have focused our attention on the numerical prediction of free shock separated flows in LEATOC nozzle. The free shock separation exhibits relatively strong shock-wave / turbulent boundary layer interaction followed by a massive separation. A number of numerical studies by different researchers have been performed for such complex flow regimes [21]-[105] and few of them have been accepted. Among them two-equation $k-\omega$ model has shown some improved results due to their known ability to predict pressure gradient flows. Various RANS turbulence models, implemented in code TGNS3D, have been tested in the framework of axi-symmetric calculations in order to ascertain the sensitivity of the solution to the RANS turbulence model. They correspond to :

– Spalart Allmaras (SA) Model [136].

– k-ε model with Chien correction [22].
– Wilcox k-ω model [155].
– SST k-ω model [86].
– k-ω model with realizability correction [92].

Series of experiments performed by Nguyen [100] on LEATOC nozzle have found that during the start-up process, only free shock separation occurs for NPR $\leq$ 24. When NPR reaches that limit, this free separated jet reattaches back to the nozzle wall and restricted shock separation takes place. The present numerical study of the sensitivity of the simulated flow-field to the turbulence model is performed for NPR's in the range less than 24. During the numerical prediction of FSS flow regimes, we have encountered several issues related to the aforementioned RANS models, which are discussed in the following sections.

5.2.1 Behaviour of RANS Model Across the Shocks

In eddy-viscosity models, the Reynolds stresses are linearly related to the mean strain rates via eddy viscosity. These model works well in certain cases where the turbulent time scale is of the same order in magnitude of the mean strain. However, the present flow configuration exhibits strong shock-wave / boundary layer interaction (i.e. highly non-equilibrium flow) and the time scale of the mean distortion is significantly smaller than the turbulence time scale. As a result, the equilibrium concept assumed by using an eddy viscosity breaks down and the models yields unrealistically high values of the production of turbulent kinetic energy (TKE). Figure 5.6 shows the numerical solution obtained for SA and k-ε model with Chien correction at NPR=15.5 and 20 respectively. According to the experimental study [101], during the start-up at this NPR in LEATOC nozzle only FSS flow regime appears. However, the high unrealistic turbulence predicted by these models across the shock causes the free annular supersonic jet to reattach back to the nozzle wall. Several modifications, such as realizability constraint, compressibility correction and production limiters have been proposed to overcome this problem. For example, SST k-ω model limits this production with respect to the dissipation term according to :

$$P_k = min(P_k, 20.D_k) \text{ [86]} \tag{5.2}$$

A similar kind of limiter is proposed by Wallin [149] :

$$P_k = min(P_k^{model}, P_k^{lim}) \tag{5.3}$$

where $P_k^{lim} = \rho K \sqrt{P_k^{model}/\mu_t}$. This limiter is not active for $P_k^{model} < \varepsilon/C_\mu$. Recently Pilinski et al. [111] limited the ratio of μ/μ_t to 90000, for such type of separated flows in thrust ideal contour (TIC) nozzle. These types of modifications enable the model to successfully reproduce FSS flow configuration at NPR=15.5 as depicted in Fig. 5.7. Comparisons of iso-contours of turbulent kinetic energy are also given in Fig. 5.8. They illustrate the level of decrease in turbulent eddy-viscosity and kinetic energy value by using these limiters. One can effectively ascertain that along the nozzle axis, downstream of the shock, an artificially high level of turbulence is produced when the linear eddy-viscosity model is used. This turbulence produces a sufficient amount of artificial radial momentum away from the nozzle axis sufficient enough for the flow reattachment.

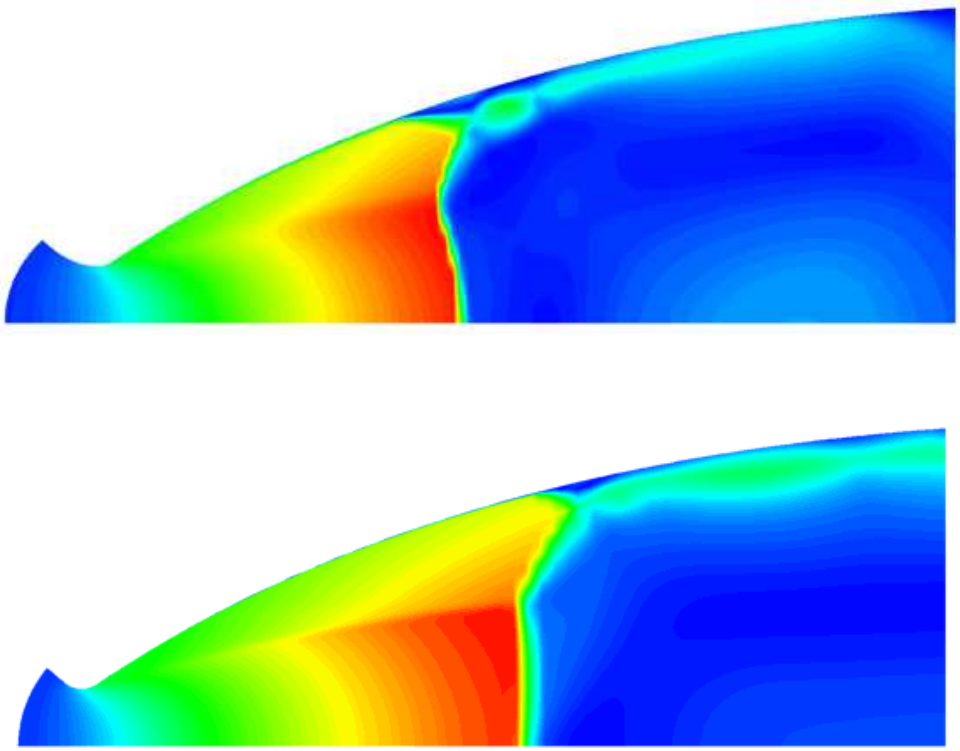

FIGURE 5.6 – Numerical solution (iso-Mach contours) obtained by (Top) S-A model at NPR=15 and (Bottom) $k-\varepsilon$ model at NPR=20, display RSS flow regimes, respectively (mesh : 200*120 (nozzle) & 200*180 (exterior domain)).

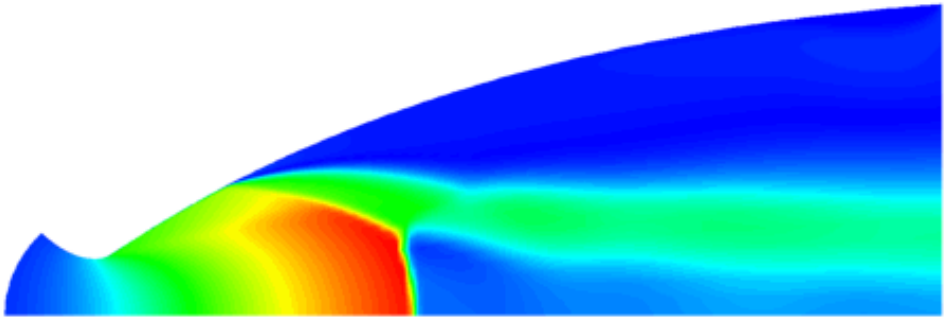

FIGURE 5.7 – Influence of turbulence model on the numerical solution showing FSS configuration at NPR=15.5 : iso-Mach contour, $k-\omega$ with production limiter, mesh : 200*120 (nozzle) & 200*180 (exterior domain).

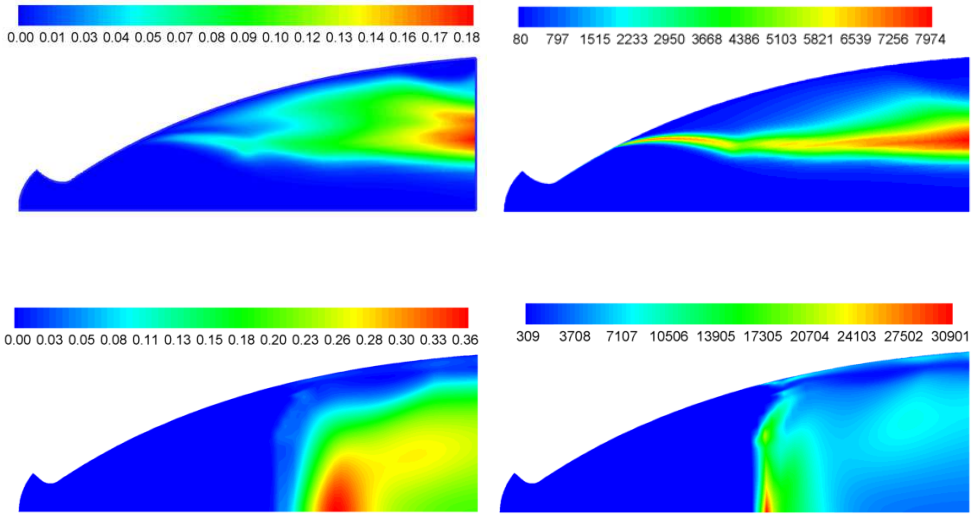

FIGURE 5.8 – Influence of the production limiter, (Top) with & (Bottom) without limiter, on the overall flow topology appear in the numerical solution produced by RANS model at NPR=15.5 (mesh : 200*120 (nozzle) & 200*180 (exterior domain)), (Left) turbulent viscosity (μ_t) & (Right) turbulent kinetic energy.

5.2.2 Grid Sensitivity in the Shock Region

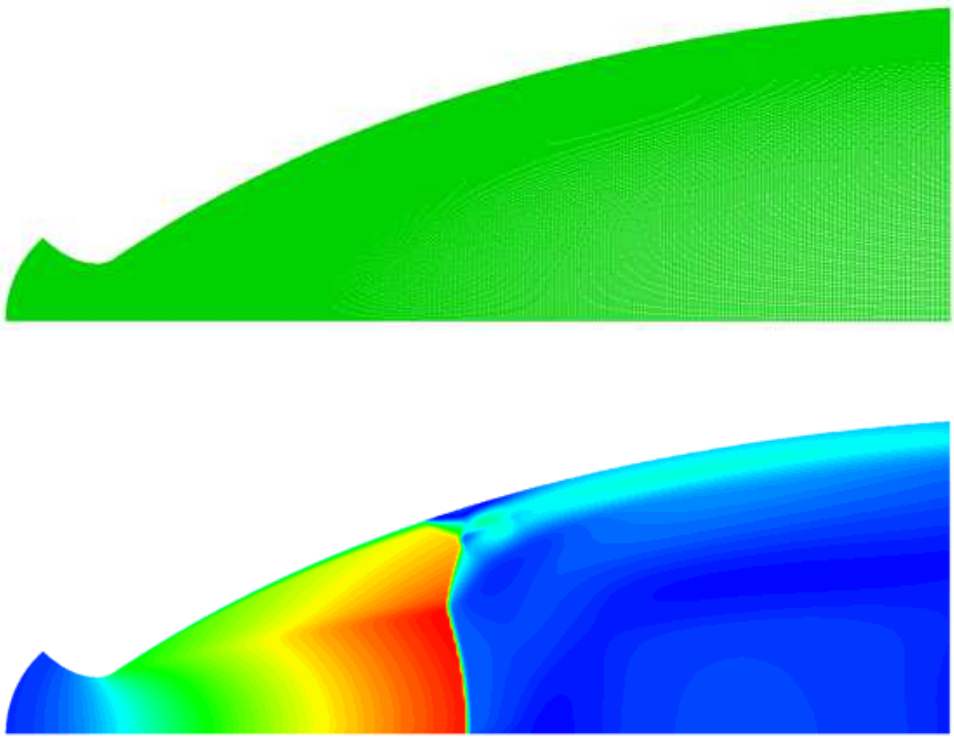

FIGURE 5.9 – Mesh (500*200) inside the nozzle (Top) and respective obtained solution (Bottom) showing RSS flow regime at NPR=15.5.

The second issue of the turbulence models is related to their sensitivity, through the shock

region, to grid refinement. These supersonic separated flows exhibit several discontinuities and require fairly refined grid. Across the shock, an eddy-viscosity model gives a high amplification of TKE. The production term typically varies as a function of $\propto 1/\delta^2$, where δ is the shock thickness.

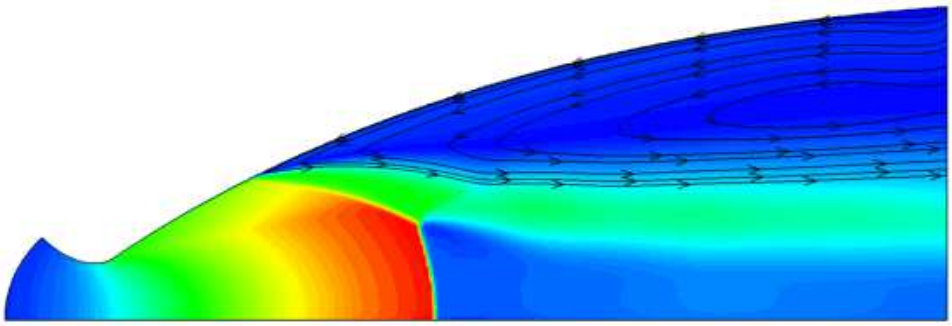

FIGURE 5.10 – Numerical solution on fine mesh (500*200), display correctly predicted FSS configuration at NPR=15.5 : $k-\omega$ with realizability correction.

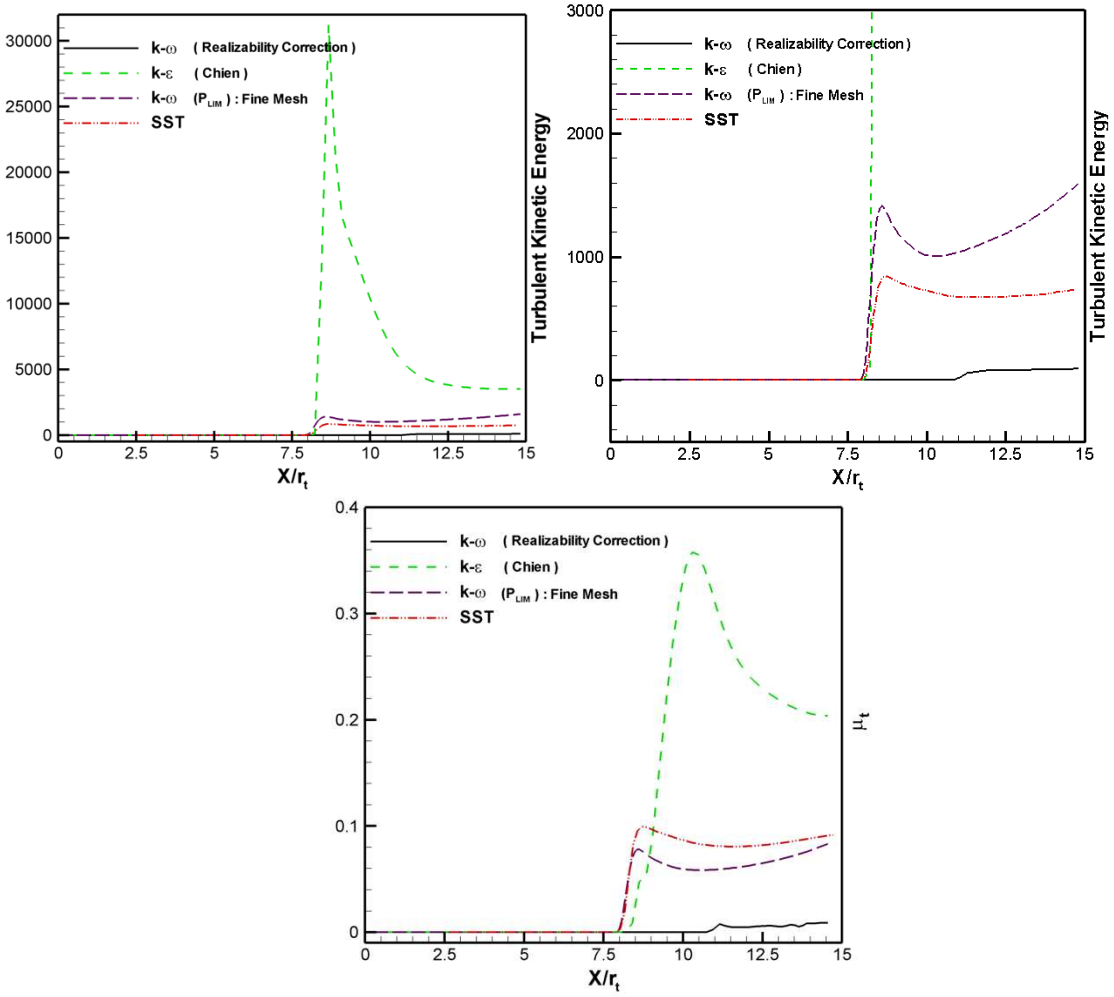

FIGURE 5.11 – Evolution of (Top) TKE (m^2/s^2)& (Bottom) μ_t ($kg/m.s$) along the nozzle axis (across the shock : Mach stem), r_t=throat radius=0.01362 m.

Let suppose that Δx is the mesh size where the shock wave occurs. The production term varies in fact as the inverse of Δx. This suggests that the more you refine the grid, the more non-physical behaviour of eddy-viscosity model is likely to occur across the shock. Such an example can be seen in Fig. 5.9 with very refined mesh of 500×200 (Δx inside the nozzle is of the order of the boundary layer thickness in this case). Figure 5.9 (right), shows the solution obtained by the Wilcox $k-\omega$ model, which yields an unexpected numerical solution at NPR=15.5. Conversely, the numerical solution obtained by Wilcox $k-\omega$ model with this realizability correction on the same fine mesh is presented in Fig. 5.10. One can notice a successfully reproduced FSS flow regime. Hence, grid convergence is also possible.

In Fig. 5.11, the evolution of turbulent kinetic energy and eddy-viscosity along the shock (Mach disk) are plotted for the discussed RANS models. The eddy viscosity model (k-ε with Chien correction) yields a very high level of turbulence downstream of the shock. Even if this unrealistic level of turbulence is quite well controlled by using the production limiters, the model become sensitive to the mesh refinement and produces non-physical results. Here again, the realizability correction removes this grid sensitivity problem, as well as the associated unrealistic production of turbulence.

5.2.3 Epilogue

A preliminary numerical investigation of a free shock separated flow has been carried out on a thrust optimized contoured (LEATOC) nozzle. A comparative study of the aforementioned models has shown that standard turbulence models based on Boussinesq assumption yield unrealistic high values of turbulence kinetic energy across the strong shock which can sometimes radically change the flow structure. By using a production limiter seems to give comparatively better results. However, even in such a case, the production of TKE varies inversely with the shock thickness and also restricts us to achieve grid convergence in these scenarios. This problem is solved when models are modified based on a realizability constraint.

5.3 Use of Hybrid RANS/LES Methods

Hybrid modelling methods, combining RANS and LES techniques, have been an area of great interest since the last decade. Various hybrid techniques have been proposed in this regard for the better prediction of complex turbulent flows. The idea of Detached Eddy Simulation was first proposed by Spalart et al. [137] in order to overcome the deficiencies of RANS models for predicting massively separated flows. This technique has recently received an increasing attention to fill up the gap between (U)RANS and LES. This original DES formulation is based on a modification of the Spalart-Allmaras RANS model [136] such that the model reduces to a RANS formulation near solid surfaces and to a sub-grid scale (SGS) like model away from the wall. Later on, a DES implementation based on two-equation model was proposed by Travin et al. [147] for Menter-SST model. Currently DES is used in combination with the Spalart-Allmaras (SA) [136], $k-\omega$ [155] model and their popular variants. The main reason why these models have been selected as the underlying RANS models lies in there improved separation prediction capability. However, under certain conditions, these models over-predict the extent of separation [88]. This issue of separation point prediction becomes much more

severe when we deal with shock-induced separated flows. In the previous section, we have noticed the influence of turbulence models to obtain numerical solution for FSS flow regime in LEATOC nozzle. As a results two new variants of DES are proposed in this research work, i.e. RDDES-I and RDDES-II (see Chapter 4). In the present section a detailed comparative study of different hybrid techniques is reported and is used for the numerical prediction of FSS and RSS flow regime in LEATOC nozzle. The following issues are more particularly addressed in the framework of hybrid RANS-LES Methods :

- Development of shear layer.
- Modelled stress depletion and grid-induced separation.
- Realizability issue.
- Model sensitivity for the prediction of separation point and flow structure.

5.3.1 Development of Shear Layer

The first issue that has been considered here is the development of shear layer in free shock separated flow regime in LEATOC nozzle and the shock-induced separated flow in a square nozzle configuration.

5.3.1.1 Free Shock Separation in LEATOC nozzle

Figure 5.12, presents the flow structures found within and downstream of the nozzle obtained by RDDES-I and RDDES-II. One can notice that for RDDES-I (which is based on the classical DES approach), replacing the turbulence length scale with the DES length scale in the dissipation term, the convection of eddy viscosity from the separated boundary layer into the shear layer dampens the development of resolved turbulent structures. By introducing the DES length scale into turbulent viscosity term in addition to the dissipation term, this development of shear layer is accelerated (see Fig. 5.12). Accordingly, in order to improve our predictive capacity to observe the early development of large turbulent structures, the second formulation is retained to carry out the numerical study presented in the following chapters.

The motion of shock in shock wave / boundary layer interaction is moderate when there is no separation, but can be important in presence of massively separated zones : like in the present case considered. These separated zones have their own dynamics, mainly dominated by the presence of a reverse flow, producing eddies of scales which are larger than the boundary layer scales. In the case of a curved oblique shock formation and the subsequent formation of a recirculation region, the shock motion is rather insensitive to the upstream conditions. This suggests that the pressure fluctuation produced in the separated region of the nozzle wall by these large turbulent structures of the jet downstream of the nozzle are linked with the unsteadiness of the separated shock [100].

In Fig. 5.13, two-point correlation maps of pressure signals in the separated region computed for RDDES-I and RDDES-II (starting from their respectively predicted separation point locations) are shown. This map is symmetric with a unitary diagonal : the pressure signal is auto-correlated. One can notice that for a particular location, the value of the correlation coefficient decreases as the distance between these two sensors increases. Moreover, the pressure signal probes located in the fully separated zone are strongly correlated. Obviously, the correlations between points in the inlet or the throat region are not significant due to the very small

level of fluctuations in these regions, and are not shown here.

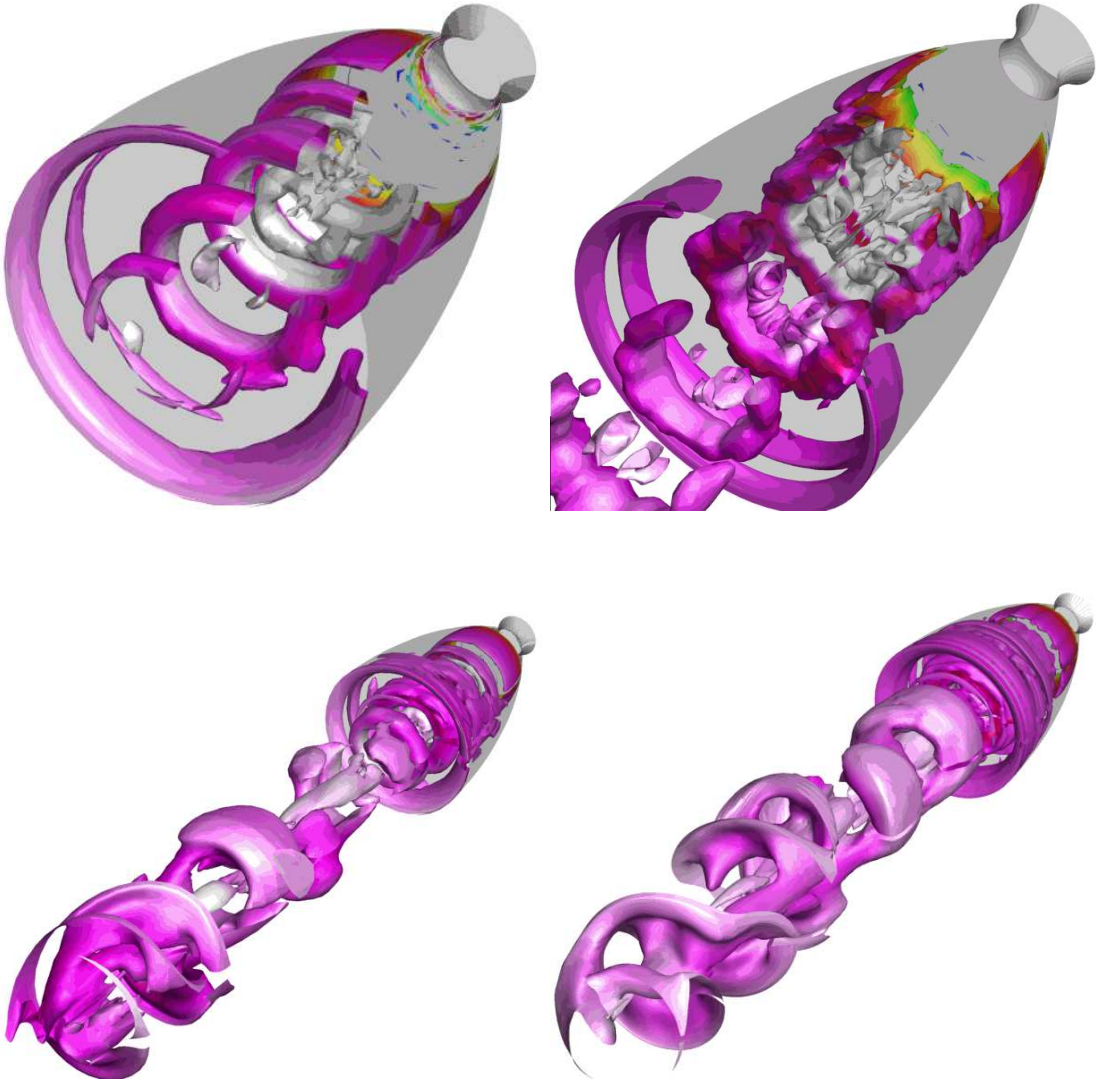

FIGURE 5.12 – Resolved large-scale turbulent structures inside and downstream of the nozzle for free shock separated flow (Left) RDDES-I & (Right) RDDES-II : Iso-surfaces of Q-criterion coloured with static pressure (NPR=15.5).

RDDES-I shows mainly positive correlation due to the global pressure oscillations produced by the quasi axi-symmetric turbulence structure inside the nozzle. In addition, correlation between the beginning of the separation region and the nozzle exit is very low (almost zero). This is due to the fact that the delay in the development of resolved turbulent structures also dampens the levels of pressure fluctuations close to the nozzle lip.

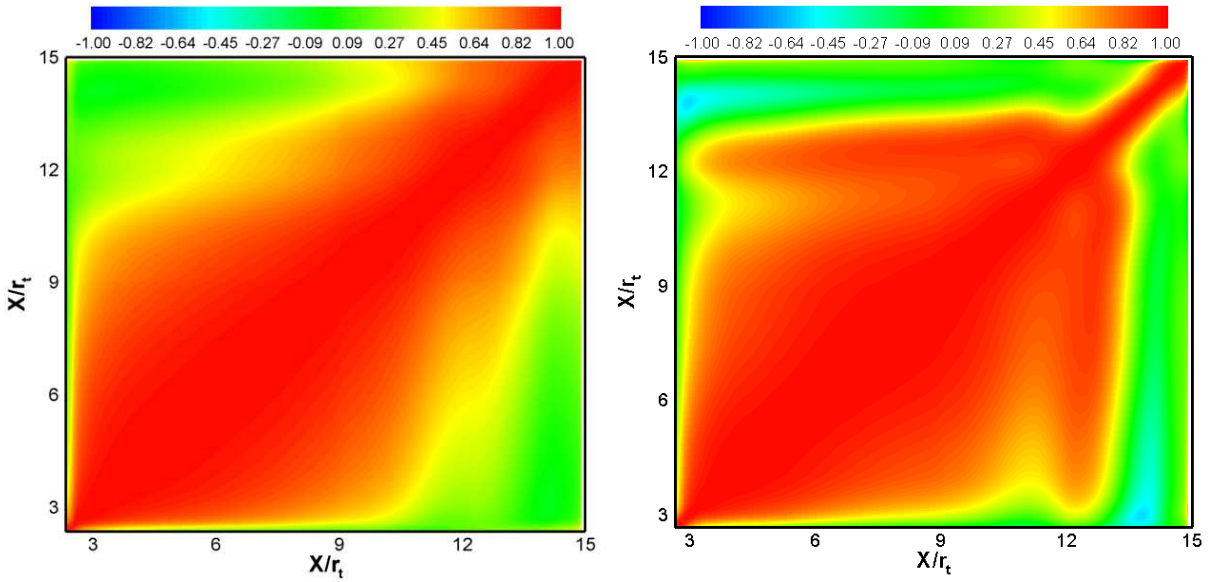

FIGURE 5.13 – Computed cross correlations of the pressure signal for the case of FSS regime : (left) RDDES-I & (right) RDDES-II (NPR=15.5), where r_t=0.01362 m is the throat radius.

5.3.1.2 The Case of Rectangular Nozzle

Another interesting case considered here is a rectangular nozzle, experimentally studied at Laboratoire d'Etudes Aérodynamiques [101]. A cross flow jet actuator (fluidic control) is used on the smallest dimension of the exhaust of the rectangular nozzle (see Fig. 5.14). This cross flow jet causes the main stream to separate and creates asymmetry. This results in a vectorization of the main flow. The nozzle dimensions and the computational domain are explicitly given in Fig. 5.14. The numerical solutions obtained from RDDES-I and RDDES-II in quite similar conditions of fluidic injections, are presented in Fig. 5.15. A fifth order low dissipative MPWENO has been used for this case.

The comparison between RDDES-I and RDDES-II is made here, although there is a slight difference between these two test configurations with respect to the percent injection, which is higher in the case of RDDES-I. We can notice that the use of the RDDES-I results in a flow separation located upstream of the one obtained when RDDES-II is used. From Fig. 5.15, one can notice that the use of RDDES-II has expedited the development of shear layer on the upper and lower wall of the nozzle. Whereas this development of shear layer is observed only on the upper wall of the nozzle in the case of RDDES-I, where cross flow jet actuator is used.

The similar kind of problem is also reported by Kok et al. [69]. Thus by introducing the DES length scale into the turbulent viscosity term in addition to the dissipation term, this development of shear layer is accelerated (see Fig. 5.15). Finally by using RDDES-II we can observe the development of large turbulent structures earlier then RDDES-I.

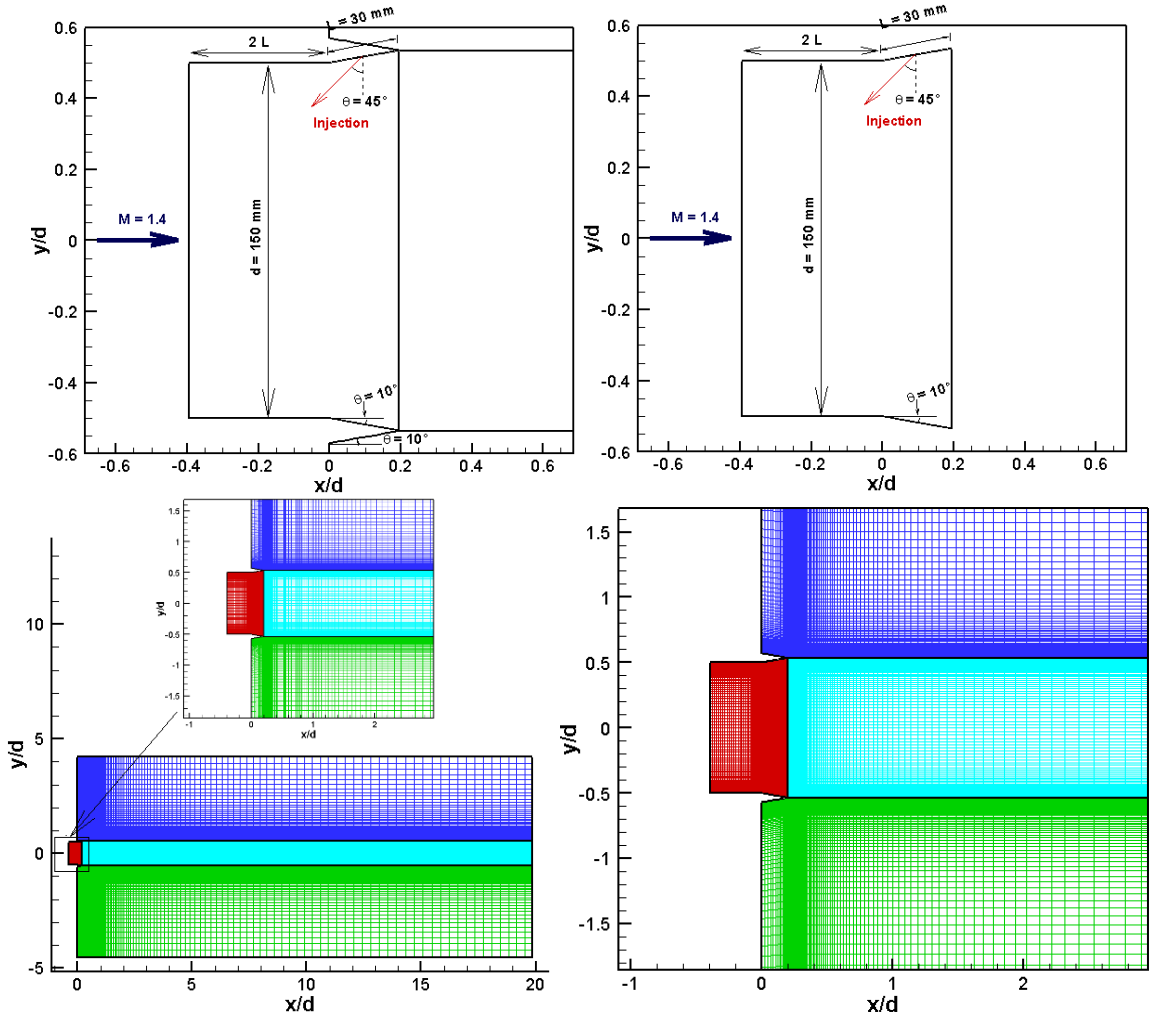

FIGURE 5.14 – Rectangular nozzle geometry (Top) and computational domain (Bottom).

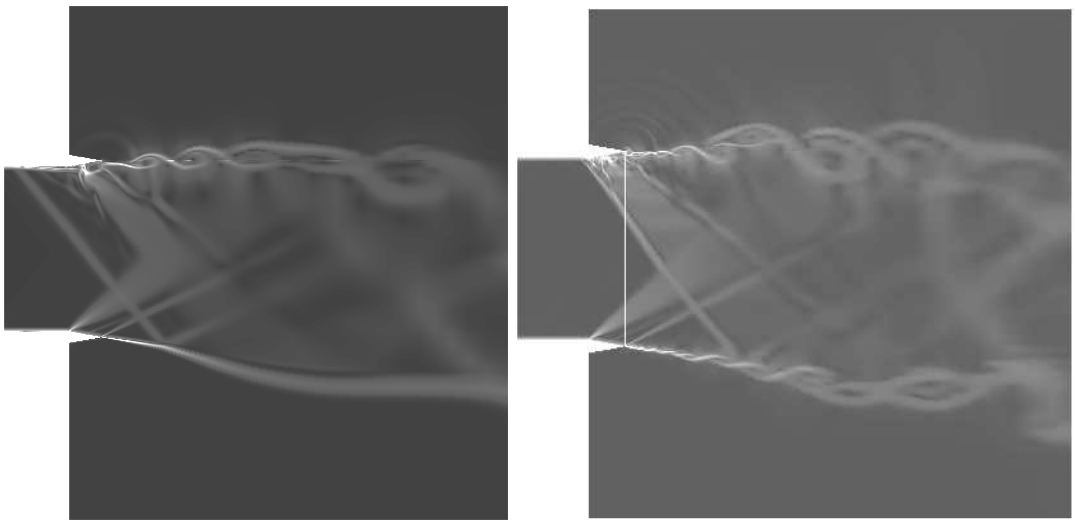

FIGURE 5.15 – Iso-contours of density gradient showing the development of shear layer in the case of rectangular nozzle (Left) RDDES-I & (Right) RDDES-II.

5.3.2 Modelled Stress Depletion and Grid-Induced Separation

As a result of numerous studies of the original DES method, several key shortcomings were identified : for grids with fine wall-tangential resolution, the grid-dependent switch between RANS and LES mode may encroach inside the boundary layer, resulting in a depletion of the modelled stresses and in a subsequent strong under-production of the skin friction. In strong cases, this may cause a spurious prediction of the skin friction and to an artificial separation. This phenomenon is known as grid-induced separation [87]. In order to avoid this problem, the DDES shield function is used for the present study. The evolution of this shielding function in the divergent part of the nozzle is shown in Fig. 5.16. It shows that, along the nozzle wall, the RANS mode is forced. The comparison of the results obtained with $k-\omega$ model and RDDES for a grid spacing of about 1/30th of the boundary layer thickness are reported in Fig. 5.16. We can notice that the velocity and turbulent viscosity profile for RDDES inside the boundary layer correspond well to the one obtained by the RANS model, and f_{DDES} safely rises from 0 at the wall to 1 in the outer part of the boundary layer.

The early switching into LES mode inside the boundary layer may lead to the problem of "Modelled Stress Depletion (MSD)". Numerically obtained (at NPR=15.5 : FSS flow regime) shear stresses along the nozzle wall are plotted in Fig. 5.17. A comparison is made between $k-\omega$, RDDES and Limited Numerical Scales (LNS) [9] models (see also Annex A.9). No shielding function is used with LNS so that an ambiguous mesh distribution near the wall region leads to the early switching into the LES mode. However, close to the near wall, the mesh is not fine enough to resolve the shear stresses. As a result, the depletion in the level of wall shear stresses is observed in comparison with the RDDES and k-ω model. As depicted from Fig. 5.17, this depletion in shear stress level also leads to an onset separation for LNS model, which may sometimes give misleading results. Figure. 5.18 shows the LNS solution obtained for NPR=41.6. In LEATOC nozzle, as it was mentioned earlier, at this much higher NPR, the flow regime turns into RSS configuration. Surprisingly, LNS does not lead to predict this configuration because of the onset prediction separation point.

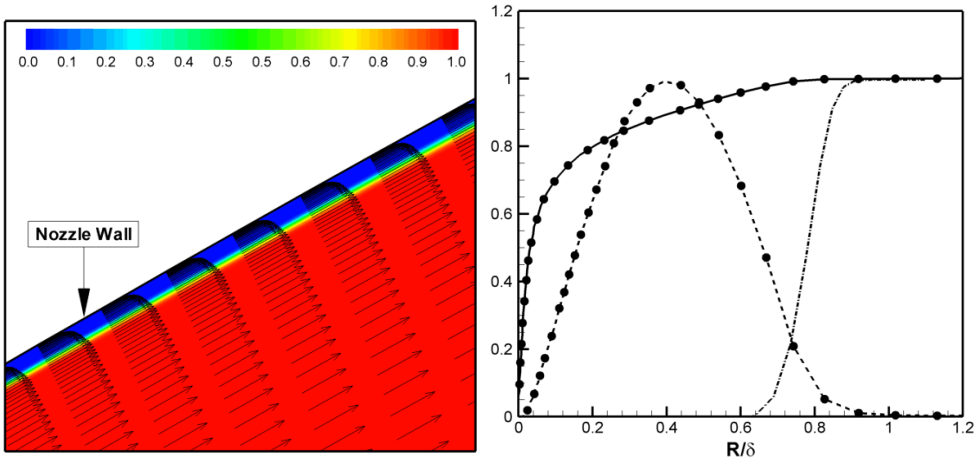

FIGURE 5.16 – (Left) Iso-contours of DDES shielding function and velocity vectors for the attached flow in the divergent part of LEATOC nozzle & (Right) Comparison of velocity and eddy viscosity profiles for RDDES and k-ω model : $-\cdot-$, f_{DDES} ; RANS : —, U/U_∞, - - -, 0.017 μ_t/μ ; •, RDDES (mesh, (200*120 (nozzle) +200*180 (exterior))*72, NPR=15.5).

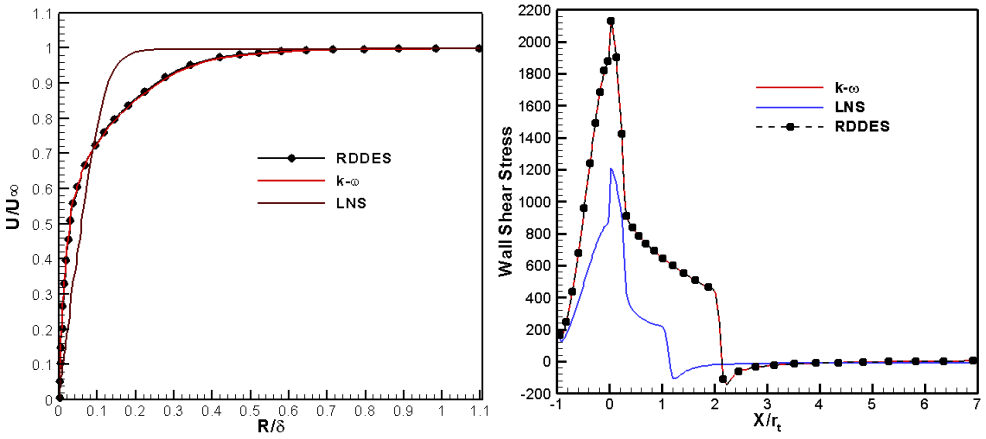

FIGURE 5.17 – (Left) boundary layer velocity profile & (Right) wall shear stresses along the nozzle wall for FSS flow regime, indicating the effect of modelled stress depletion.

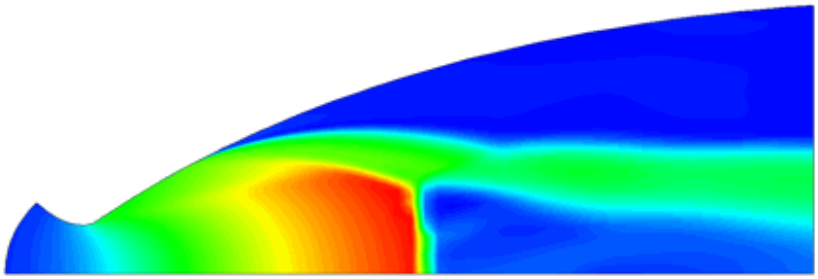

FIGURE 5.18 – Numerical solution obtained by LNS : Iso-Mach contours (mesh, 200*120 (nozzle) +200*180 (exterior), NPR=41.6).

5.3.3 Realizability Issue

In this section, the importance of using a realizability correction is highlighted. The weak version of the realizability has been defined by Schumann and Lumely [85] & [133], which states that the variances of the fluctuating velocity components must be positive and the cross-correlations bounded by the Schwartz inequality, that is :

$$\overline{u^2} \geq 0, \ \overline{v^2} \geq 0, \ \overline{w^2} \geq 0 \tag{5.4}$$

$$\overline{uv}^2 \leq \overline{u^2 v^2}, \ \overline{uw}^2 \leq \overline{u^2 w^2}, \ \overline{vw}^2 \leq \overline{v^2 w^2} \tag{5.5}$$

Strictly speaking, the above mentioned relations hold only for the statistical average ; with mass-averaging, the density fluctuations should be taken into account. Nevertheless, their effects are expected to be negligible. Since the above constraints are not automatically fulfilled by linear models based on the Boussinesq assumption, they can be infringed in various circumstances, and especially in the presence of strong adverse pressure gradients, as in the present cases. In such turbulent models, the turbulent stresses are linear with respect to the strain rate S_{ij}

$$\frac{\widetilde{u_i u_j}}{k} = -2\frac{\nu_t}{k}S_{ij} + \frac{2}{3}\delta_{ij} \tag{5.6}$$

and the turbulent viscosity ν_t is related to the turbulent kinetic energy (TKE) k and dissipation ε by :

$$\nu_t = C_\mu \frac{k^2}{\varepsilon} \tag{5.7}$$

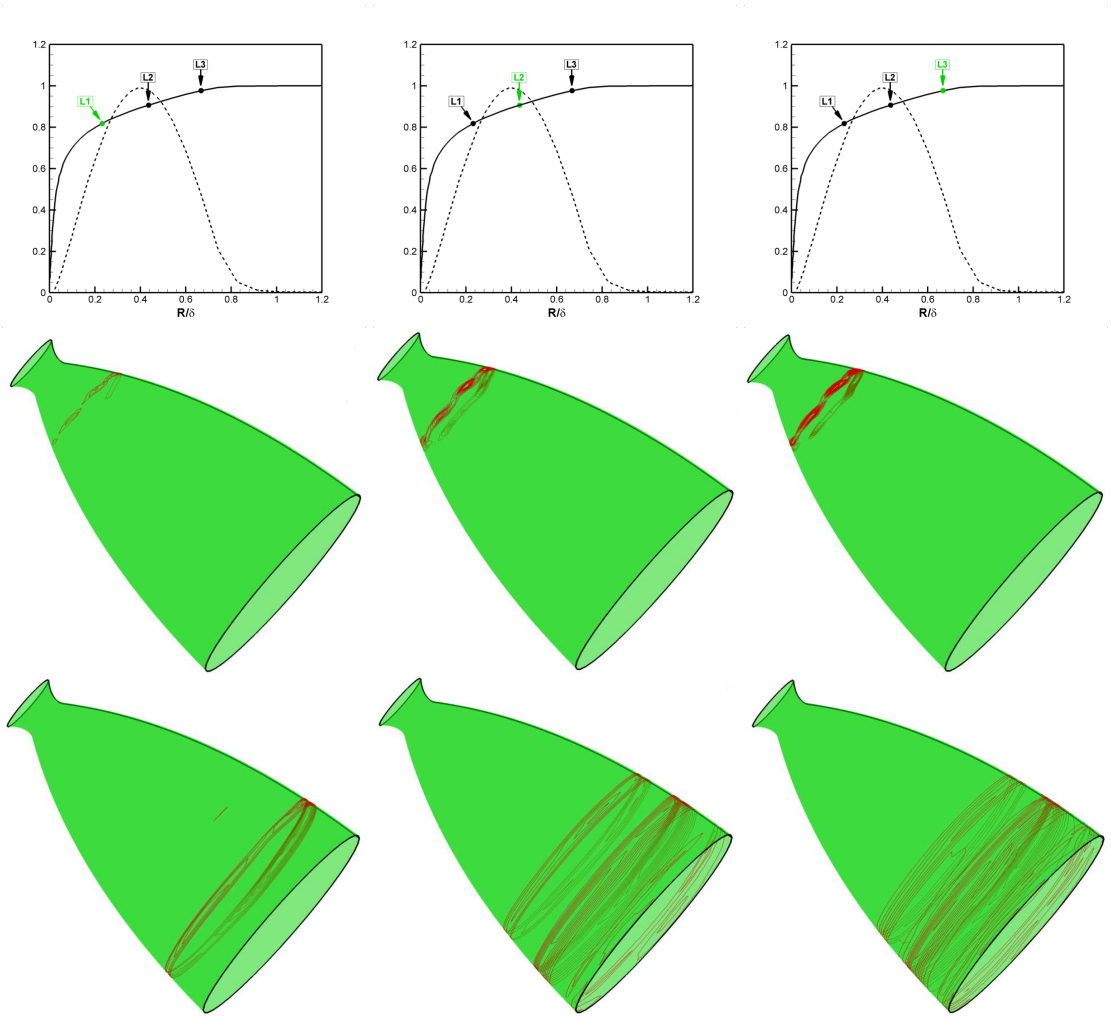

FIGURE 5.19 – Traces of $s \geq \frac{2}{3C_\mu}$ at R/δ = 0.23, 0.44 & 0.67, highlighting the realizability infringement (Top ; Left to Right) for (Middle) FSS : NPR=15.5 & (Bottom) RSS : NPR=38 ; mesh, (200*120 (nozzle) +200*180 (exterior))*72.

The structural parameter $\widetilde{uv}/k$ is known to be constant in a large part of the boundary layer and almost with any pressure gradient. The constant value $C_\mu^c = 0.09$ is usually chosen to reproduce this behaviour in the logarithmic region with no pressure gradient. In order to understand the infringement of the realizability constraint, dimensionless strain invariant s is introduced :

$$s = \frac{k}{\varepsilon}S \;\; with \;\; S = \sqrt{2S_{ij}S_{ij}} \tag{5.8}$$

By using these relations for the present flow configurations, the realizability constraints become equivalent to :

$$s \leq \frac{2}{3C_\mu} \tag{5.9}$$

This shows that how large value of s (i.e. strong velocity gradients) leads to an infringement of the realizability constraints (as shown in Fig. 5.19). The numerical solution obtained by using $k-\omega$ based DDES is shown in Fig. 5.19 for FSS and RSS flow regimes. Starting from $y/\delta = 0.23$, one can notice that some traces of realizability infringement ($s \geq \frac{2}{3C_\mu}$) are noticeable in the region of shock-wave / boundary layer interaction. When we move further in the outer region of boundary layer, this zone enlarges. This realizability issue is more delicate in RSS flow regime. In RSS configuration, the free separated jet reattaches back to the nozzle wall, and, due to the successive shock and expansion waves interaction, a secondary separation occurs. This also leads to a realizability violation in these mentioned regions. The introduction of realizability correction enables to overcome this problem and no trace of realizability infringement is observed in such a case. Finally, the turbulent kinetic energy production P_k is given as :

$$\frac{P_k}{\rho\varepsilon} = C_\mu s^2 - \frac{2}{3}\frac{k}{\varepsilon}S_{kk} \tag{5.10}$$

5.3.4 Model Sensitivity for the Prediction of Separation Point

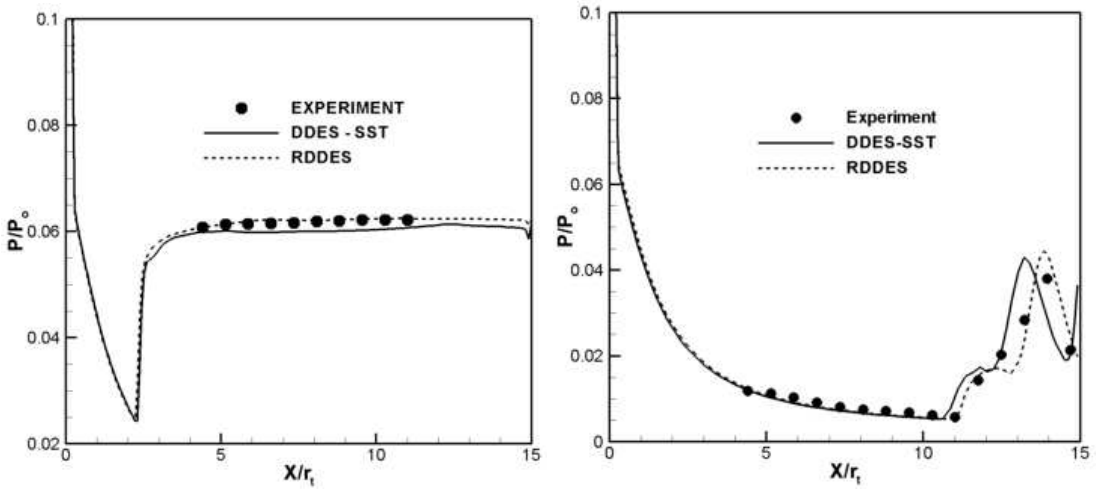

FIGURE 5.20 – Evolution of mean wall pressure along nozzle wall at (Left) NPR=15.5 & (Right) 41.6.

The SST model uses a production limiter to avoid a non-physical increase in the production of TKE. In Fig. 5.20, a comparison between the experimental data and the mean wall pressure of numerically obtained is given. At relatively low NPR (NPR=15.5 : FSS regime), both RDDES and DDES-SST show good agreement with the experiment. In the case of DDES-SST, a small disagreement in the separation point location and the pressure downstream of it is due to the prediction of a higher level of turbulence through the shock-wave / boundary interaction.

Conversely, RDDES proves it superiority in its capacity to better predict the location of this separation line, and the resulting wall pressure evolution.

The data obtained from various experimental studies for free shock separated flow configuration [5], [11], [40], [48], [67] & [73] are plotted in Fig. 5.21. These correspond to a variety of nozzle geometries, both in full scale/sub-scale models and hot/cold fire conditions. It is worth to mention here that the working fluid for all these experiments is air, except for Bloomer hot fire measurements for which $\gamma = 1.2$: rocket fuel and liquid oxygen are used. The present results of RDDES for various NPR in this range of free shock separation regime are also compared with the free interaction model and with the model proposed by Keanini et al. [67]. The separation pressure ratio in figure indicates that RDDES leads to a satisfactory prediction in comparison with the experimental data in a wide range of incipient Mach number (M_i).

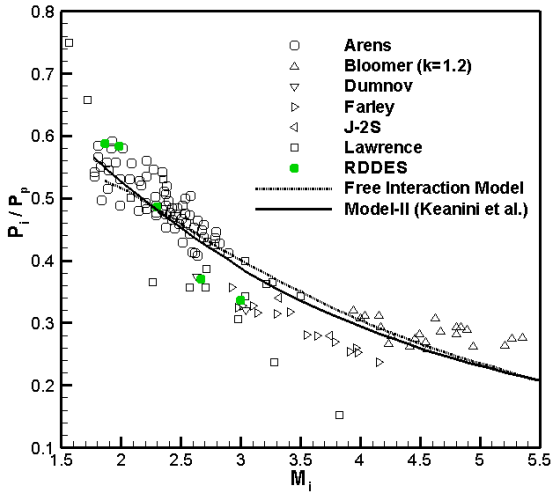

FIGURE 5.21 – Comparison of RDDES with separation measurements in rocket nozzles and analytical models

In the case of restricted shock separation, there appear multiple compression and expansion waves which interact with the boundary layer. As a result, the zone of realizability infringement (in the outer parts part of the boundary layer) is larger than in the case of FSS configuration. Moore et al. [92] pointed out that, when we go from two to three dimensions, Menter has substituted $\sqrt{S^2+\Omega^2}$ to $\frac{\partial U}{\partial y}$ instead of Ω. Only this point is missing to ensure that the SST model is realizable. The turbulence level in a boundary layer directly affects the flow separation in adverse pressure gradient. From Fig. 5.20, we can see that at high NPR (i.e. 41.6) DDES-SST under-predicts the mean separation point location. This in turns seems to be the reason for incorrect flow recovery prediction downstream of the reattachment. This under-prediction of the separation point also leads to a secondary separation caused by the interaction of shock and expansion waves in the annular supersonic jet. On other hand, the separation point location is well predicted by RDDES, only leads to a slight disagreement for flow reattachment and downstream pressure.

It should be noted that, at high NPR, condensation of oxygen occurs in the experiments which induces two effects :

– An increase of the inviscid static pressure upstream of the separation : this can be interpreted as a higher equivalent NPR.
– A decrease of the inviscid Mach number upstream of the shocks.

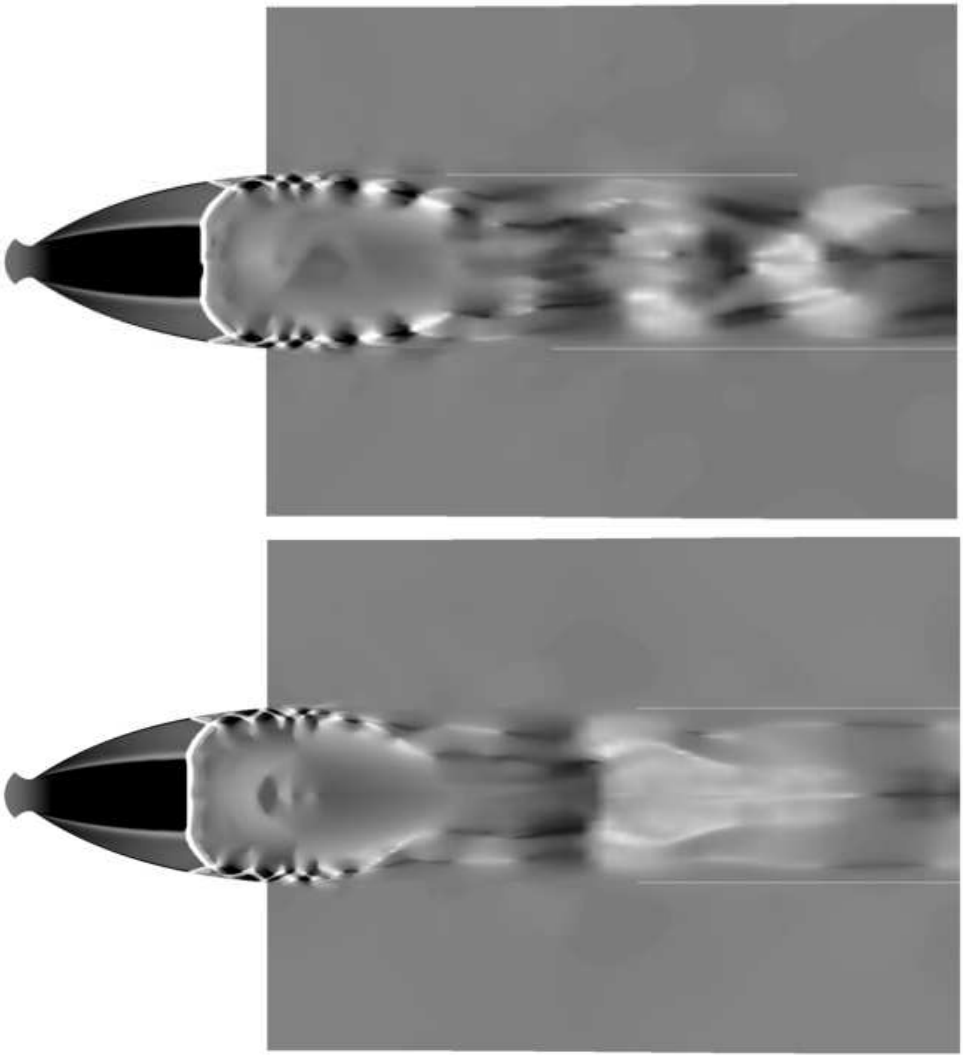

FIGURE 5.22 – 2D slices at $\theta = 0^o \& 180^o$, iso-contours of shock function at NPR=41.6 for (Top) RDDES & (Bottom) DDES-SST (mesh, (200*120 (nozzle) +200*180 (exterior))*72).

This can be interpreted as higher equivalent NPR upstream of the separation, as shown in Fig. 5.20. The numerical solutions obtained by RDDES and DDES-SST are shown in Fig. 5.22. These results highlight the fact that even a small under-prediction of the separation point location can lead to a significant modification of the resulting flow structure (secondary separation) and associated level of unsteadiness, for details see Chapter 8.

5.4 Conclusions

Various tests have been performed to validate the implemented numerical schemes and turbulence models in order to investigate shock-induced separated flow regimes in an over-expanded nozzle. Comparisons between second order MUSCL and fifth order MPWENO schemes suggest that low order dissipative schemes are not sufficient enough for such type of flow configurations. Due to its high numerical diffusion across the shock, MUSCL leads to artificial vortical structures and sometimes may results in misleading solutions. Conversely, MPWENO

scheme is comparatively less dissipative, while representing a good compromise in terms of computational cost. Flow in over-expanded nozzle involves low frequency random fluctuations. Therefore, integration during a sufficiently long time is required to be able to perform some statistical analysis of the results. This justifies the choice of an implicit scheme for the time integration, which has been implemented. On the condition that moderate CFD (< 25) are used, it has been shown that the resulting numerical diffusion remains moderate. A comparative study of RANS models has shown that standard RANS models based on Boussinesq assumption yields unrealistic high values of TKE across the shock, which sometimes changes the flow physics. In order to overcome this problem, production limiter and realizability corrections have been added to these models. Accordingly, the new variants of DES proposed in this research work, are based on the realizability correction added to the Wilcox k-ω model, i.e. RDDES-I & RDDES-II. In RDDES, a shielding function is used to avoid the MSD problem. Furthermore, the introduction of additional DES length scale in turbulent eddy viscosity term (for RDDES-II), has been shown to accelerate the development of resolved turbulence, and shows superiority over RDDES-I. As a conclusion, the following simulations of shock-induced separated flows in rocket nozzles are based on the RDDES-II formulation in combination of fifth order MPWEO and second order implicit linearization for the time integration (with CFL < 25.0).

Chapitre 6

Evolution of Flow Structure in Over-Expanded Rocket Nozzle

This chapter addresses the analysis of the flow structure appearing in the free shock separated (FSS) and restricted shock separated (RSS) flow regimes and the hysteresis process between these two configurations. For this purpose, simulations are performed in a thrust optimized contoured (TOC) nozzle, whose general characteristics are given first.

6.1 General Characteristics of LEATOC Nozzle

In order to investigate the aforementioned different shock-induced separated flow configurations in convergent-divergent rocket nozzles, the LEATOC nozzle has been considered in this research work. This LEATOC nozzle is a thrust optimized contoured nozzle which is approximated by a parabola following Rao's method [119] and which has been experimentally investigated at Laboratoire d'Etudes Aérodynamiques (LEA), Poitiers, France [101], (see Fig. 6.1). Figure 6.2 shows the contour of LEATOC nozzle nondimensionalized by the throat radius in the axial and radial direction. Furthermore, Table. 6.1, summarizes its main characteristics.

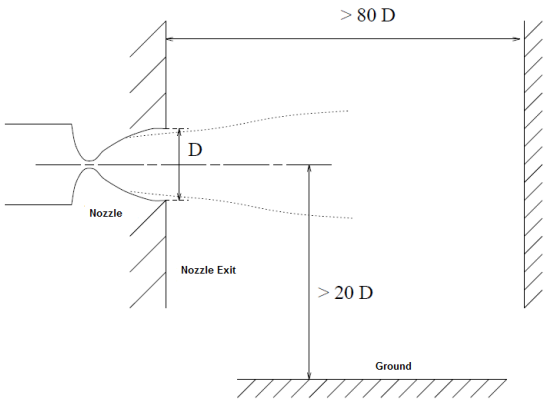

FIGURE 6.1 – Geometric configuration of LEATOC nozzle [100].

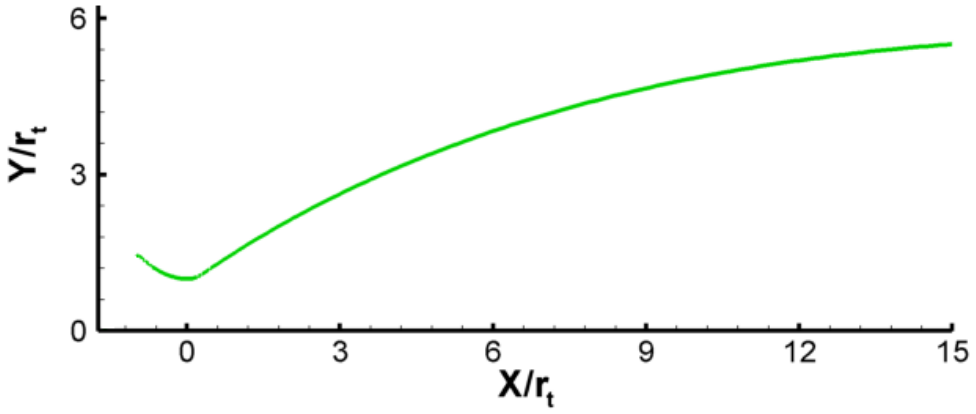

FIGURE 6.2 – Contour of LEATOC.

Parameters	
Throat Radius r_t (m)	0.01362
Maximum Half-Angle β_m (^{o})	34
Half-Angle at Nozzle Exit β_e (^{o})	4
Divergent Length L (m)	0.2043 (15*r_t)
Area Ratio ε	30.32

TABLE 6.1 – Parameters of LEATOC nozzle.

6.1.1 Experimental Setup : [101]

The experimental study of this LEATOC nozzle was carried out on a sub-scale nozzle using a specific test facility at Laboratoire d'Etudes Aérodynamiques (LEA). The exit section of the nozzle is located in the external plane of the wall (of the hall) where the test facility was built. The ground is located at more than 20 nozzle exit diameters along the nozzle axis. The air supply system and the settling chamber were designed carefully with several screens in order to decease as far as possible upstream perturbations.

6.1.2 Dimensionless Analysis

Starting from very low nozzle pressure ratios during the start-up up to the full-flowing regime (i.e. no flow separation occurs inside the nozzle) the Reynolds number of this particular flow does not remain constant, and is a function of NPR. A dimensionless analysis of the LEATOC nozzle is performed here to express this Reynolds number (R_e) dependency to the NPR. By definition, we know that R_e is based on the characteristic length of the geometry and the stagnation conditions. Let us consider D_{ref} as the characteristic length for the nozzle, and P_o & T_o as the stagnation pressure and temperature of the combustion chamber (i.e. inlet conditions for the nozzle inlet). Hence $R_e(D_{ref}, P_o, T_o)$ is given as :

$$R_e = \frac{D_{ref}.U.\rho}{\mu(T)} \tag{6.1}$$

$\mu(T)$ is the viscosity and is given by the Sutherland law :

$$\mu(T) = \mu_o(\frac{T}{T_o})^{3/2}.\frac{T_o+110.4}{T+110.4} \tag{6.2}$$

Here the value of μ_o corresponds to the total temperature ($T_o = 300.0K$) and is 1.844×10^{-5} $kg.m^{-1}.s^{-1}$, ρ and U are the density and velocity of the flow respectively. By using the following isentropic relation one can substitute ρ and U in the form of dimensionless Mach number (M) and the stagnation pressure (P_o).

$$\rho U^2 = \gamma M^2 p = \gamma M^2 \frac{P_o}{(1+\frac{\gamma-1}{2}M^2)^{\frac{\gamma}{\gamma-1}}} \tag{6.3}$$

By using this relation, the expression for the Reynolds number becomes :

$$R_e(D_{ref}, P_o, T_o) = \frac{D_{ref}}{\mu(T)}\sqrt{\frac{\gamma}{R}}(1+\frac{\gamma-1}{2}M^2)^{\frac{1+\gamma}{2(1-\gamma)}}M\frac{P_o}{T_o} \tag{6.4}$$

Where R represents universal gas constant. In this research work we are dealing with chocked nozzle conditions, and we know that whatever the NPR is, Mach number at the nozzle throat is unity (i.e. 1). In order to simplify the Reynolds number expression for a wide range of nozzle pressure ratios, it is better to write it in terms of NPR and chocked throat conditions. By using this, we get :

$$M_t = 1$$

$$D_{ref} = D_t$$

$$T_t = \frac{2}{\gamma+1}T_o$$

Finally, the Reynolds number at the throat of LEATOC nozzle is given by :

$$R_{e_t} = \frac{D_t}{\mu(T_t)}\sqrt{\frac{\gamma}{R}}(1+\frac{\gamma-1}{2})^{\frac{1+\gamma}{2(1-\gamma)}} \tag{6.5}$$

An approximated direct and simple relationship between R_e and NPR (P_o/p_a) : where p_a is the ambient pressure) can be made by substituting the value of constants and the other variables.

$$R_{e_t} \approx 0.45 \times NPR \times 10^5 \tag{6.6}$$

6.1.3 Evolution of Side-Load Activities in LEATOC Nozzle

Figure 6.3 & 6.4 display the measured RMS value of side-loads obtained in LEATOC during the start-up process. This side-load evolution as a function of NPR typically displays four peaks. Apparently, the first two seem to appear when the nozzle operates under FSS configuration. The very first one is at relatively low NPR, i.e. 7.5. When the NPR increases (in FSS flow regime) the flow is highly unsteady and non-symmetric and the level of side-loads becomes more important in the range of NPR=24, than it is at lower NPR. This global unsteady behaviour suddenly becomes quasi-stationary when the supersonic separated jet reattaches back to the nozzle wall

i.e. when the flow transition from FSS to RSS occurs. Figure 6.4 displays two side-load peaks when the nozzle operates in restricted shock separated (RSS) flow regime. The first peak in RSS regime corresponds to the flow state for which the secondary separation bubble opens to the atmosphere, and produces global unsteadiness. This behaviour seems to be similar to the case of end-effect, which corresponds to the second peak of side-loads in the RSS regime.

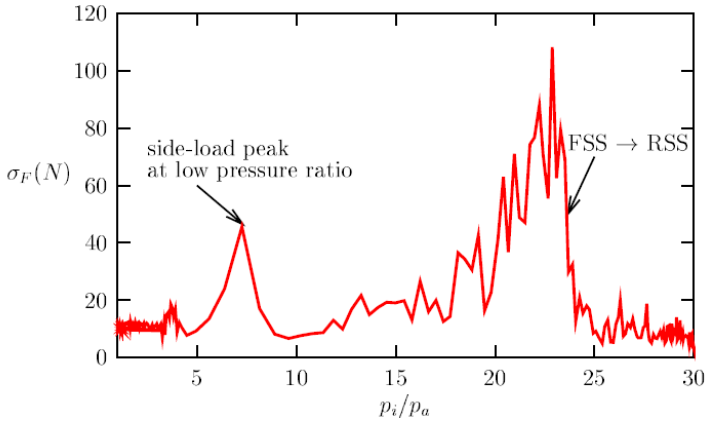

FIGURE 6.3 – RMS side-loads (σ_F) evolution with respect to the nozzle pressure ratio during the start-up of LEATOC nozzle : Experiments performed for transition (FSS to RSS) regime with transient inflow conditions [100].

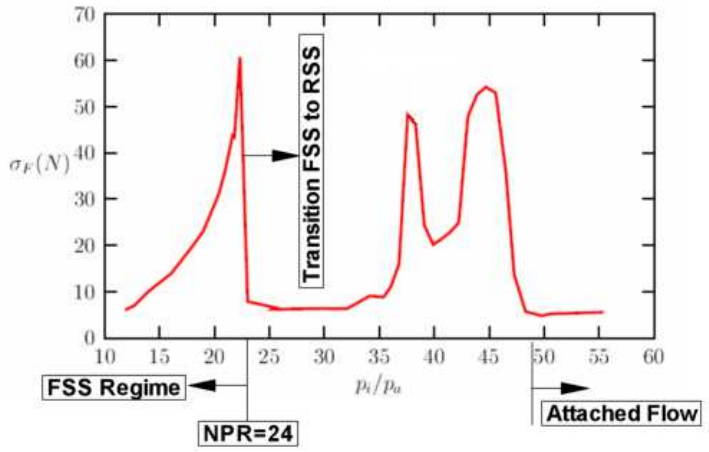

FIGURE 6.4 – RMS side-loads (σ_F) during the start-up of LEATOC nozzle, with stabilized inflow conditions [100].

6.2 Computational Domain and Mesh Description

The computational domain used to perform numerical simulations is set according to the experimental set-up. It is composed of two zones i.e. (i) nozzle and (ii) exterior. Figure. 6.5 presents these two zones of the computational domain in the meridian plane. Starting from the low NPR flow regime, at which separation point locations are very near from the nozzle throat, to the end-effect flow configuration or full-flowing configuration where no separation takes

place inside the nozzle. The numerical simulations reported in the following are all performed on the same type of extended computational domain. The mesh generation is based on two steps (i) 2D grid generation of the nozzle followed by the exterior domain and (ii) extrusion of this 2D grid in the azimuthal direction.

FIGURE 6.5 – Computational domain : meridian plane.

6.2.1 Two-Dimensional Mesh Description

The flow separation takes place in the rocket nozzle when it operates under over-expanded conditions and results a counter-current mixing layer forms around the principle separated jet. The essential difference of this mixing layer with respect to the co-current mixing layer is that it supports the absolute instability [100]. Accordingly, we might assume that the influence of the inflow turbulence conditions becomes less important. Based on this assumption, the simulations are performed by imposing arbitrary stagnation conditions at the inlet with 1% turbulence level. However, the flow attached to the nozzle wall (before separation) is viscous and the central core (upstream of the Mach stem) is assumed to be inviscid, as shown in Fig. 6.7, for both FSS and RSS regimes. The thickness of the attached boundary layer evolves in the range of 0.1-0.3 mm, from the throat to the (LEATOC) nozzle exit, respectively.

Three sets of mesh in the axi-symmetric configuration have been tested order to check the grid sensitivity. Their characteristics are given in Table. 6.2. The first one, i.e. mesh type A (see Fig. 6.6), contains 160 $\times$ 100 grid points inside the nozzle and yields a minimum grid space (first grid point) normal to the nozzle wall equal to $10^{-6}m$. The value of r^+ based on RANS (Wilcox k-ω) model calculations was found to be less than 2 for this case. This study of grid sensitivity was done on free shock separated flow regime at NPR=16.5. The results obtained show no subtantional difference with regard to the global flow structure inside the nozzle, except a better capture of thin boundary layer profiles for the meshes type B & C with the value of $r^+ < 1$. Nevertheless, from the three dimensional simulations (with RDDES method) based on mesh type B (by its extrusion in the azimuthal direction) it has been observed that value of r^+ remains less than 1, which appears sufficient to capture correctly the wall shear stresses (see section 6.2.2).

Nozzle	Exterior	Total	Type
160*100	160*180	44800	A
200*120	200*180	60000	B
300*180	200*240	102000	C

TABLE 6.2 – Types of Meshes used for the grid sensitivity analysis.

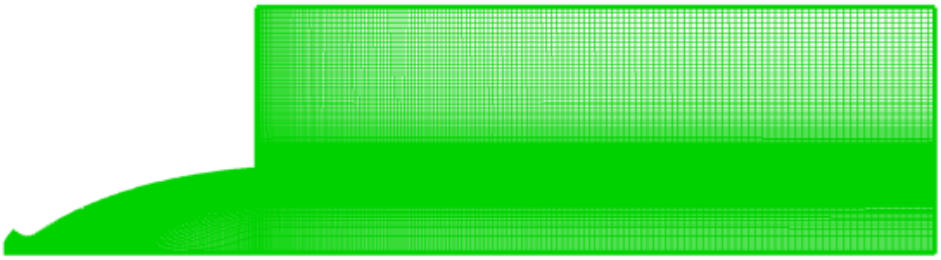

FIGURE 6.6 – Mesh of the computational domain (meridian plane : Mesh type B).

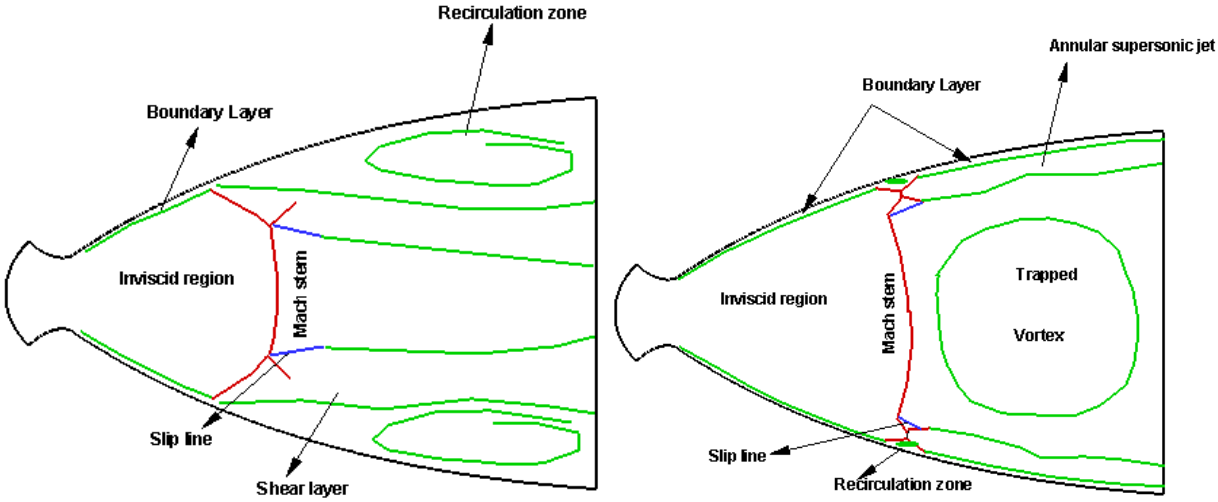

FIGURE 6.7 – Sketches of FSS and RSS flow configurations.

6.2.2 Three-Dimensional Mesh Description

A satisfactory analysis of such type of unsteady and non-symmetric flows requires a sufficiently long amount integration time so that the flow-field is statistically axi-symmetric. Hence, several three dimensional grid configurations in the azimuthal direction i.e. 36, 72 & 144, have been considered in this research work in order to check the grid requirements. The three dimensional mesh generation has been achieved by extruding the aforementioned 2D mesh in the azimuthal direction, see Table. 6.3.

Azimuthal Direction	Type
36	D
72	E
144	F

TABLE 6.3 – Types of Meshes used for the extrusion of computational domain in the azimuthal direction

The grid configuration B (axi-symmetric) in combination with grid resolution 72 (in azimuthal direction) allows us to perform time integration up to 0.8 s (for a wide range of NPR's)

and thus to better evaluate the low-frequency components of the unsteady flow. The resulting fluctuating loads caused by these low frequencies calculated by using this mesh are found to be in satisfactory agreement with the experiments [100].

Figure. 6.8 displays the combination of 2D B-grid and 3D E-grid, respectively. The resulting mesh is called BE-grid. A three-dimensional view of the nozzle along with the 2D slices in the meridian plane is given.

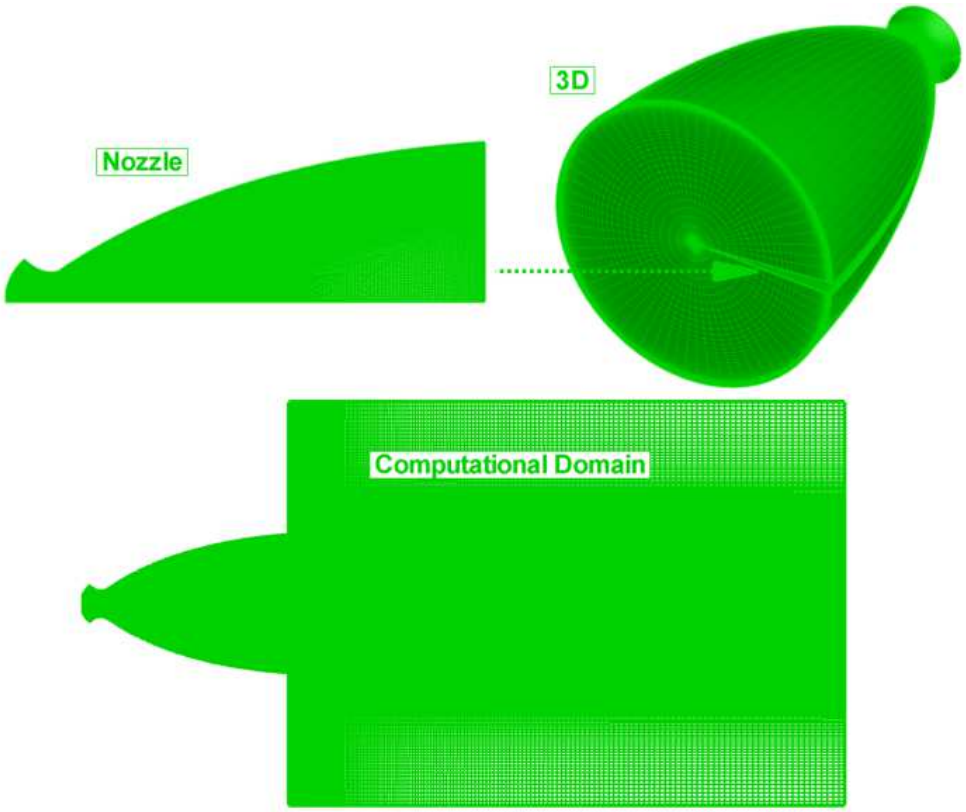

FIGURE 6.8 – BE type grid configuration of 3D computational domain.

The dimensionless distance r^+, which is a Reynolds number based on the friction velocity u_τ, is given as

$$r^+ = (\sqrt{\rho_w|\tau_w|}/\mu_w)r = (ru_\tau/\nu_w) \tag{6.7}$$

The value of r^+ at the first mesh point on the nozzle wall for both flow configurations (FSS and RSS) is calculated (by two-equation Wilcox $k-\omega$ model) and remains less than 1.0, which is satisfactory for the correct calculation of the viscous stresses (see Fig. 6.9). This mesh configuration (Mesh type BE) contains around 10 to 30 grid points inside the boundary layer and the first mesh point is located at 1×10^{-7}m from the nozzle wall. Based on RANS modelling technique (Wilcox $k-\omega$ model) the calculated streamwise distribution of r^+, density and shear stresses along the nozzle wall are given in Fig. 6.9.

The mesh distribution inside the nozzle in terms of Δx along the nozzle axis and wall is given in Fig. 6.10 : Right, and the distribution of Δr from the outer part of the boundary layer to the nozzle axis at three different streamwise locations inside the nozzle are given in Fig. 6.10 : Left. In Fig. 6.10 : Left, r=0 represents the nozzle axis and radial distribution evolves according to the local nozzle radius. In the azimuthal direction, the mesh distribution is constant

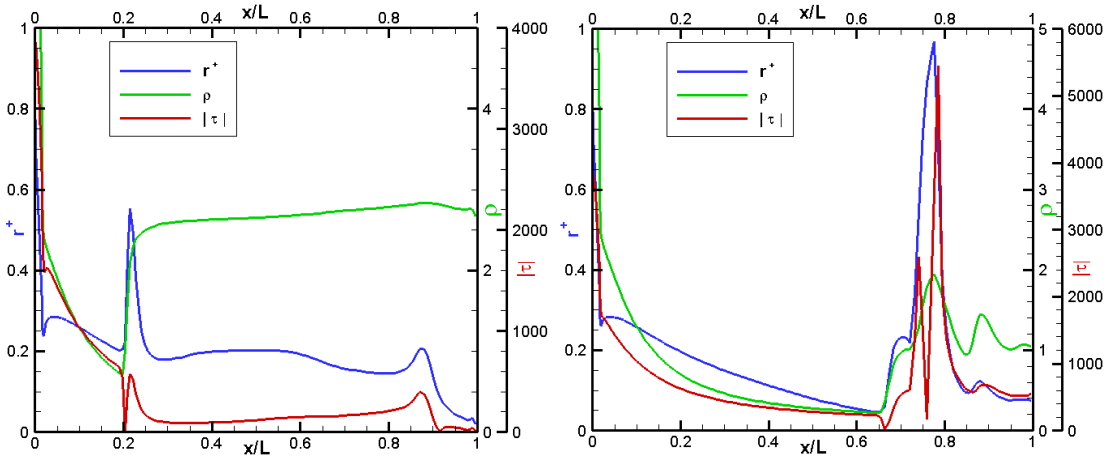

FIGURE 6.9 – Evolution of r^+ at first mesh point along the nozzle contour (Mesh type BE), (Left) FSS : NPR=16.5 & (Right) RSS : NPR=38.0.

but varies along the evolution of nozzle radius with respect to the number of grid points in that direction. For mesh configuration E, i.e. 72 points in z direction, Δz ($\approx$ r$\Delta\theta$, where θ is in radian) from throat (r_t=13.62 mm) to the nozzle exit (r_t=75.0 mm) is in the range of 1.2-6.5 mm, respectively. As expected, even with 144 points distribution (i.e., Δz_t-$\Delta z_e \approx$ 0.6-3.3 mm) in the azimuthal direction, the mesh is not sufficiently resolved to fulfil the LES resolution requirements. Nevertheless, the mesh configuration of type G (i.e. 72 grid points in azimuthal direction) represents a satisfactory compromise to perform sufficiently long time integration. The side-loads and the unsteady behaviour of low-frequency shock motion obtained in this case, which is of prime importance in this research work, is found to be in good agreement with the available experimental data (for details see chapter 7), and is then considered for the most part of the presented study. Accordingly, the mentioned DES technique seems to switch into a hybrid method with less eddy viscosity (outside the boundary layer) rather than large eddy simulation, without inhibiting a relevant analysis of the most important large-scale phenomena.

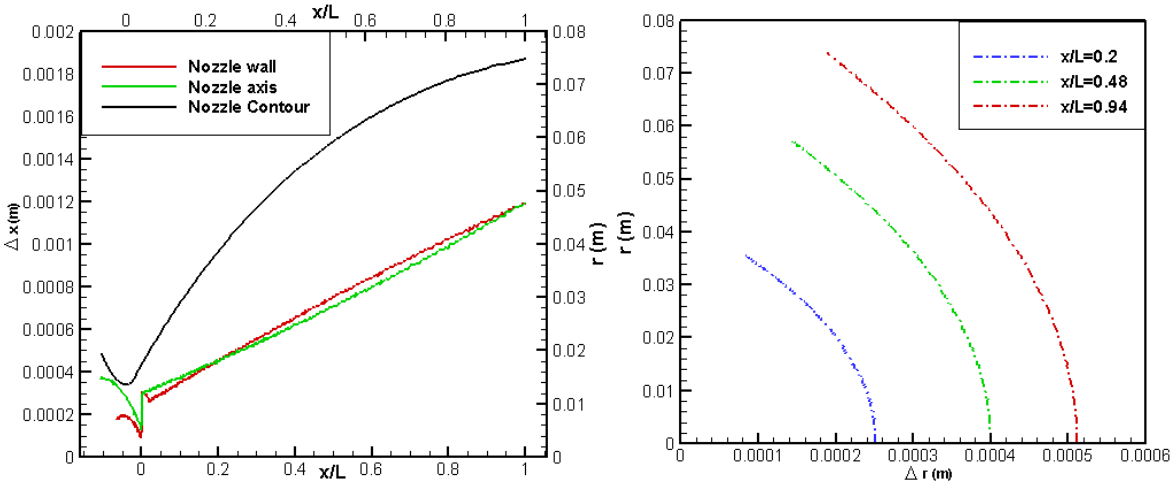

FIGURE 6.10 – Evolution of δx (left) and δr (right) for BE type mesh configuration.

6.2.3 Boundary Conditions

The nozzle throat, and the nozzle exit are at x/r_t=0 & 15.0, respectively, nondimensionalized by the radius of nozzle throat (see Fig. 6.2). The computational domain is limited by the nozzle wall (and the symmetric axis for an axi-symmetric simulation). A subsonic inflow boundary is prescribed in a cross-section located in the convergent part at a small distance upstream of the throat ; a solid wall is used in the outer part of the nozzle exit plane and some freely chosen external and downstream boundaries are prescribed. By assuming that the upcoming flow is free from any perturbations, the nozzle inlet can therefore be considered as steady (except of course within the incoming turbulent boundary layer at the nozzle wall). A cold driving gas is prescribed at the nozzle inlet. This nozzle inlet boundary is divided into two segments :

- An inviscid segment with subsonic inflow on which 5 quantities are prescribed : the stagnation pressure and temperature (T_t =300K), the direction of the velocity $tan^{-1}(V/U)$ orthogonal to the boundary, the turbulent kinetic energy $k = 10^{-2}m^2/s^2$ and the specific dissipation $\omega = 500s^{-1}$.
- A boundary layer segment of thickness 0.1 mm on which only non-dimensional profiles of velocity u/u_∞, temperature $(T - T_{wall})/(T_\infty - T_{wall})$, turbulent kinetic energy k/u_∞^2 and dissipation $\varepsilon\mu/(\rho u_\infty^4)$

The ratio of chamber total pressure p_c on ambient pressure p_a varies from 5.0-46.0. At the walls, a non-slip adiabatic condition is set and prescribed wall temperature is $T_{wall} = 300K$. For external boundary conditions, LODI (Locally One Dimensional Inviscid) method, introduced by Poinsot and Lele [117], is used. This reduces the cost of the three-dimensional simulations by taking relatively smaller computational domain. In order to reduce the reflection of pressure waves at the downstream boundary where the static pressure is imposed, an approach proposed by Rudy and Strikwerda [129] has been used, in which the amplitude of the incoming wave is linked to the difference between the local pressure P and the atmospheric pressure P_a.

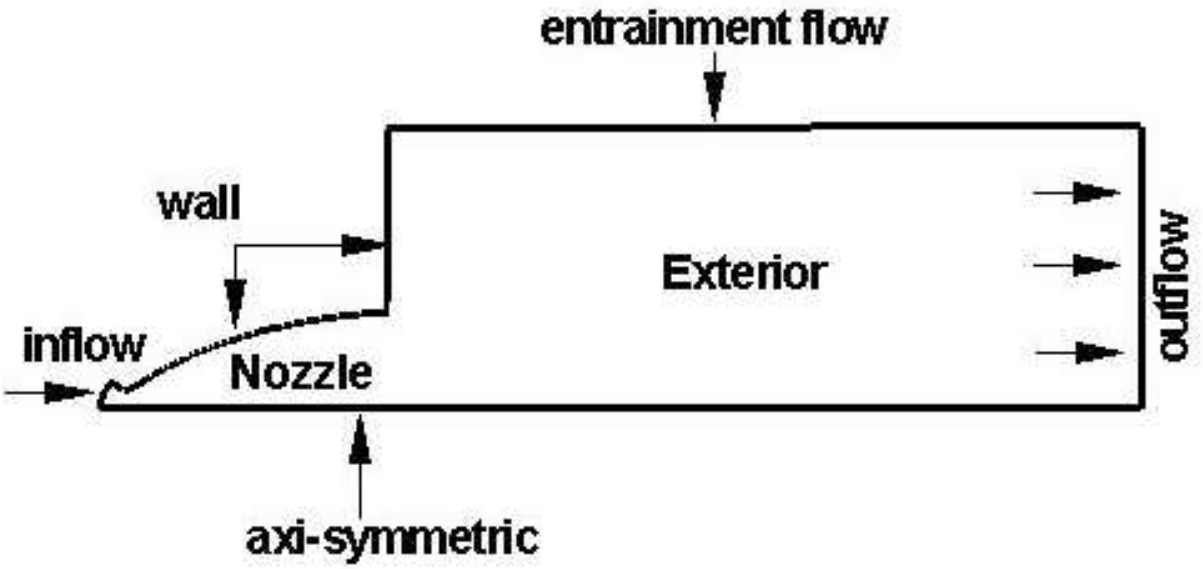

FIGURE 6.11 – Meridian section of the computational domain with prescribed boundary conditions.

An entrainment inflow, i.e. flow entering into the computational domain, is imposed by five quantities, the stagnation pressure and temperature (T_t =300K), the direction of velocity normal to the boundary, ambient turbulent kinetic energy level $k = 10^{-4}m^2/s^2$ and specific dissipation $\omega = 500s^{-1}$. The chamber temperature (300K) was set equal to the ambient temperature. The computation starts with either an impulsive or a sequential start-up / shut-down process. For the impulsive start-up process, the initial condition is quiescent everywhere, except that the chamber condition is prescribed up to nozzle inlet. For sequential start-up or shutdown process, the initial flow field is the flow field previously computed along with the new prescribed chamber pressure at the inflow location.

The time step is set according to the results obtained for the test case of a vortex convection (see Chapter 4). According to this test, the transient flow solution remains accurate as long as the Courant-Friedrichs-Lewy (CFL) number is less than 25. Therefore, a CFL of 25 or less is used in all simulations reported here.

6.3 Flow Structures Observed in LEATOC Nozzle

In this section, a brief description of numerically investigated shock-induced separated flows which appear in a LEATOC nozzle is given. These results are obtained by using the RDDES approach in combination with fifth order MPWENO scheme.

6.3.1 FSS Flow Regime

Figure 6.12 displays the predicted free shock separated flow regime which yields the correct expected qualitative features. It is characterized by the flow separation with no subsequent flow reattachment. A low speed flow, from outside the nozzle, is sucked into the nozzle and results in the formation of a small recirculation bubble near the nozzle exit. This small recirculation zone is counter-rotating with respect to the large separation zone. The separation shock interacts with the Mach stem and forms a triple point with the reflecting oblique shock. A slip line emanates from this triple point and is directed towards the nozzle axis. Hence, the flow is globally diverted towards the nozzle axis downstream of this Mach reflection. The shear layer between the free jet and the recirculation bubble interacts with the reflected oblique shock and makes the supersonic annular jet with the slip line emanates from the triple point. This shock/shear layer interaction produces large scale instabilities which are convected and finally form large coherent flow structures which are shown in Fig. 6.13. The pressure evolution along the nozzle wall for this FSS configuration is shown in Fig. 6.14. Upstream of the flow separation, the wall pressure yields a continuous decrease followed by a sudden rise due to the shock wave / boundary layer interaction, which causes the boundary layer separation. Downstream of the separation point, the wall pressure rapidly reaches a plateau level and then slightly increases, but remains less than the ambient pressure. This pressure loss is due the presence of a small recirculation zone near the nozzle lip.

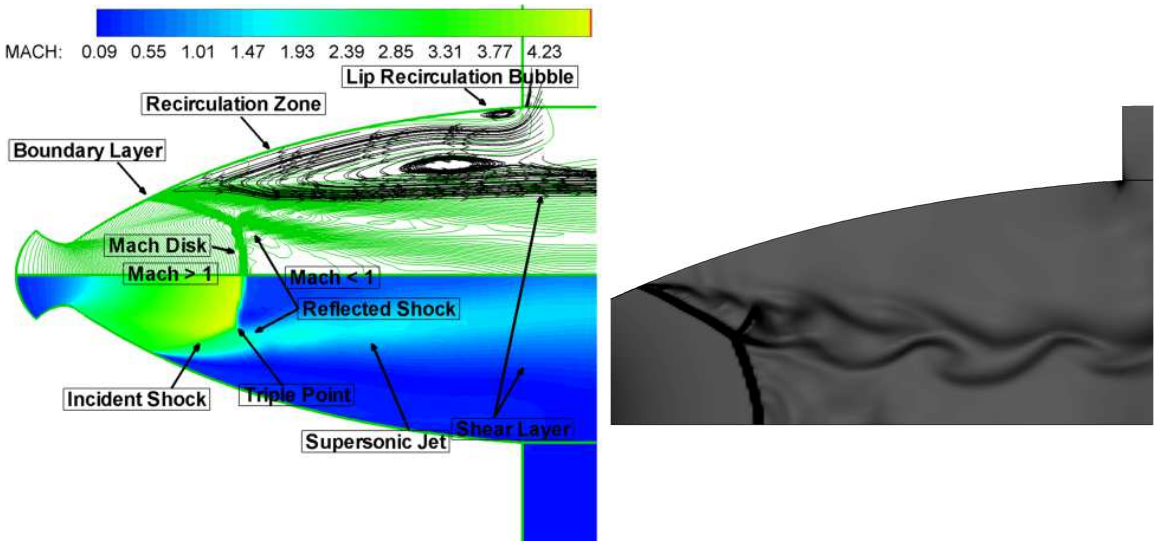

FIGURE 6.12 – Free shock separated (FSS) flow regime (Left) 2d slice at θ=0° & 180°, iso-Mach contours (RDDES, mesh type BE, NPR=15.5) & (Right) Zoom of near Mach reflection with iso-contours of density gradient (type C, NPR=15.5).

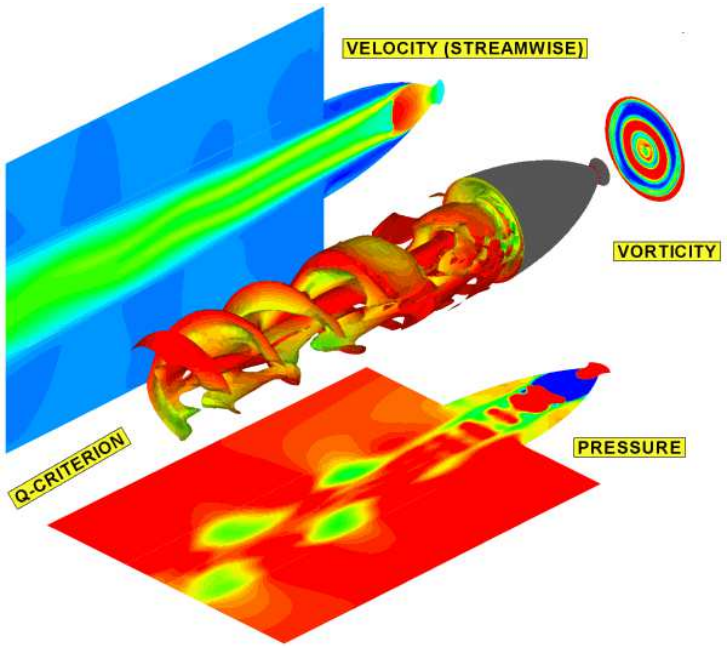

FIGURE 6.13 – Free shock separation configuration : Iso-surface of Q-criterion coloured with static pressure, and projection of iso-contours of pressure, velocity and vorticity fields (RDDES, mesh type BE, NPR=15.5).

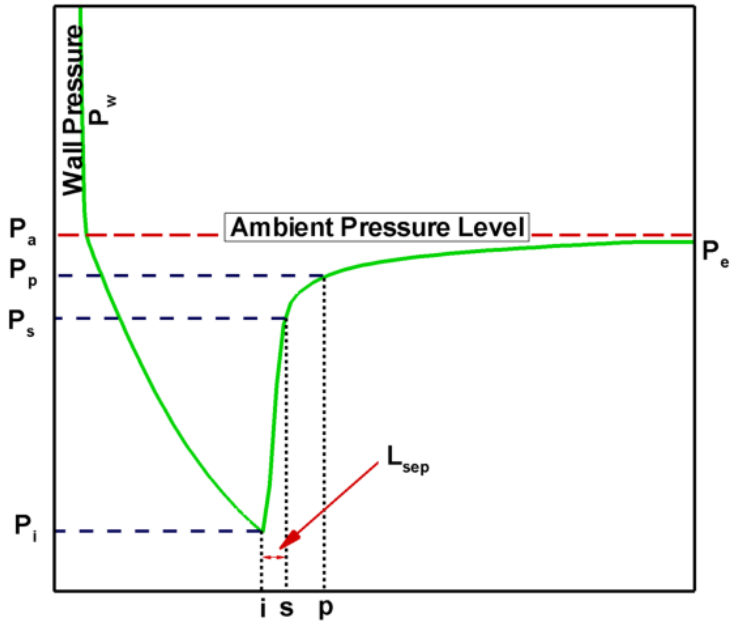

FIGURE 6.14 – Evolution of nozzle mean wall pressure in FSS flow configuration, NPR=15.5, i=incipient ; s=separation ; p=plateau ; a=ambient.

6.3.2 RSS Flow Regime

A completely different type of shock structure appears in the case of restricted shock-induced separation. Instead of the separation shock, as in FSS regime, an internal shock forms the triple point with the Mach stem and the reflected oblique shock. This reflected shock is also denoted as cone-shaped shock. The internal shock occurs near the throat region (see Fig. 6.15). In this case, the slip line which originates from the triple point is inclined away from the nozzle axis and diverts the flow towards the nozzle wall. The separation shock interacts with the reflected oblique shock. This interaction is regular and two reflected oblique shocks form from this interaction point, called quadruple point. The whole structure, including the separation shock, the cone-shaped shock (CSS) and the Mach stem (MS) is called cap-shock pattern. The free shear layer and the separated boundary layer also interact with these reflected oblique shocks. Downstream of this interaction, the separated layer reattaches back to the nozzle wall, enclosing a small recirculation zone. The annular supersonic flow is subjected to expansion and compression waves reflecting between the nozzle wall and the mixing layer which separates the high speed region from the central trapped vortex. These reflected waves lead to an oscillatory wall pressure distribution and, in some cases, to a secondary separation as shown in Fig. 6.17. Downstream of the cap-shock pattern, a large adverse pressure gradient vortex is trapped. Figure 6.16, shows the large scale structures appearing downstream of this trapped vortex.

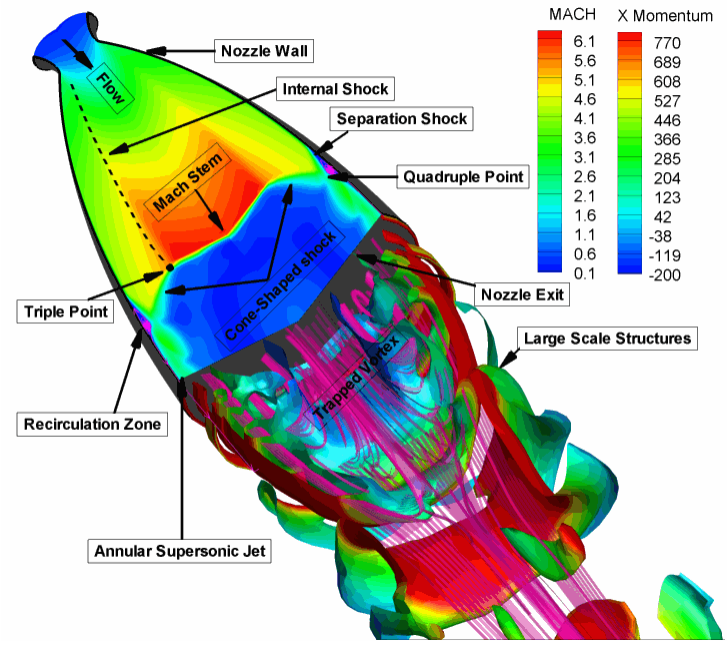

FIGURE 6.15 – Restricted shock separation flow regime (RDDES, mesh type BE, NPR=38.0).

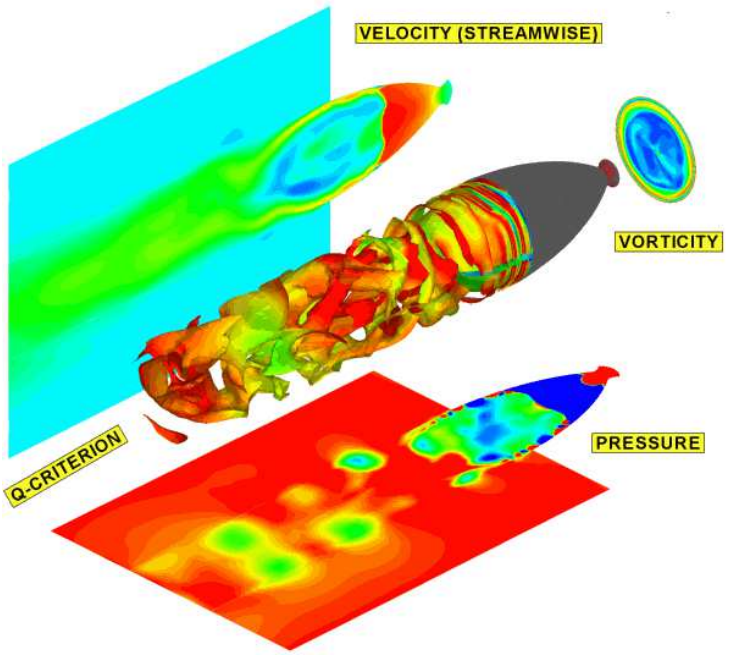

FIGURE 6.16 – Free shock separation configuration : and projection of Iso-surface of Q-criterion coloured with static pressure, iso-contours of pressure, velocity and vorticity fields (RDDES, mesh type BE, NPR=25.5).

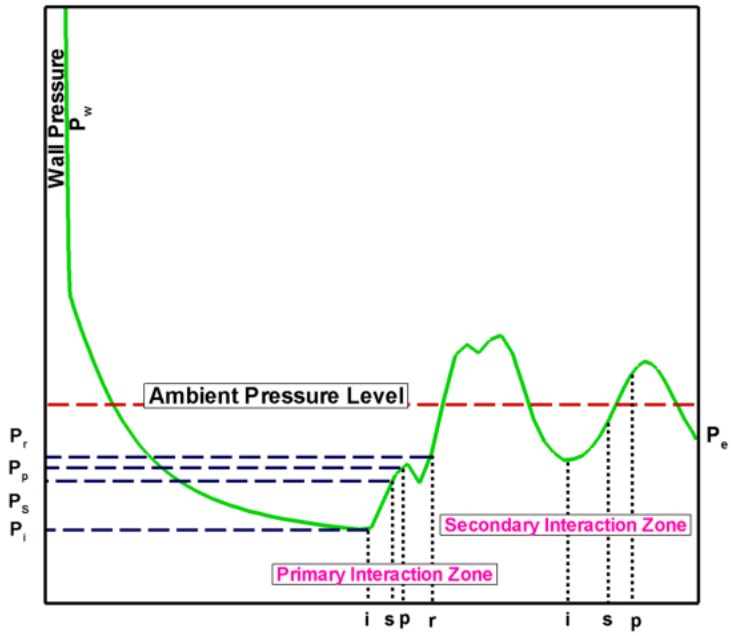

FIGURE 6.17 – Evolution of nozzle mean wall pressure in RSS flow configuration at NPR=25.5, i=incipient ; s=separation ; p=plateau ; a=ambient ; r=reattachment.

6.4 Evolution of the Flow Structure During the Transition Between FSS and RSS regimes

In a series of experiments performed on LEATOC nozzle [100], it has been found that the value of critical NPR at which FSS flow regime turns into RSS configuration, i.e. flow transition, is 24. There is a strong experimental evidence of an increasing unsteadiness and loss of symmetry in the FSS regime when approaching the critical NPR value from below for transition : the initial state for FSS $\longrightarrow$ RSS transition is clearly 3D and unsteady [101]. Due to the observed hysteresis, the FSS $\longrightarrow$ RSS transition is a one way process : oscillation between the FSS and RSS state is not possible because the reverse RSS $\longrightarrow$ FSS transition would occur at a much lower NPR than the forward FSS $\longrightarrow$ RSS transition. In the case of RSS regime, for an NPR just above the critical value, the measured side load level (see Fig. 6.3) is much lower than in the case of FSS regime just before transition. The FSS/RSS transition is a process which seems to start from a strongly 3D unsteady flow and finish in a much quieter and less 3D state.

The numerical calculation allows us to investigate the duration of the transition process provided that one uses a very low rate of increase of the NPR in order to reach a situation where the duration of the transition is independent of the rate of increase of the NPR. If the duration of the axi-symmetric transition is short, it would confirm that the FSS/RSS transition is not by itself a source of high side loads and that the total impulse communicated to the nozzle cannot be very large. Hence, axi-symmetric numerical investigation of forward and reverse flow transition, i.e. from FSS to RSS and RSS to FSS, respectively, for a wide range of NPR has been carried out. Thanks to the URANS calculation new (step increase or decrease) inflow conditions are progressively modified from the initial fields of previously obtained solution in order to reproduce forward and reverse flow transition. We might note that the flow transition FSS⇔RSS involves two essential changes in this flow :

1. A change in the mean (axi-symmetric) flow associated with an increase in the abscissa of the separation point and a completely different mean flow field.
2. A change in the amplitude and frequency of the non-symmetric unsteady perturbations superimposed on the basic axi-symmetric field.

The main aim of this axi-symmetric numerical simulation is to capture the first feature, by assuming than the second feature does not play an essential role during the transition process.

6.4.1 Forward Flow Transition FSS to RSS

In this section forward flow transition from FSS to RSS flow regime in the range of NPR (11-25) has been investigated in the framework of axi-symmetric URANS calculations based on two-equation Wilcox $k-\omega$ model [155] with realizability correction [92].

6.4.1.1 Boundary Conditions

The present calculations are performed on B-type grid (see Table. 6.2). A stagnation temperature of 300 K and a time-varying stagnation pressure (P_o) have been prescribed at the nozzle inlet. Stagnation to ambient pressure ratio P_o/P_a, i.e. NPR, is increased from 11 to 25 with unitary staircase increments $\Delta NPR = 0.5$ and the time elapsed at each ΔNPR is 20 ms until the critical nozzle pressure ratio (CNPR) is achieved. This time elapsed (i.e. 20 ms) for each constant NPR correspond to around 8 (eight) times the convective time based on U_t (velocity at nozzle throat, $\approx$ 330 m/s) and L_d (length of the computational domain, $\approx$ 0.8 m) which is sufficient enough to capture at least 10 successions of shock excursion and thus any sudden change in the flow structure that could occur during the transition process. Once we reach CNPR, calculations are performed till we observe the RSS flow regime (see Fig. 6.18). Non-slip flow and adiabaticity conditions are set at the walls.

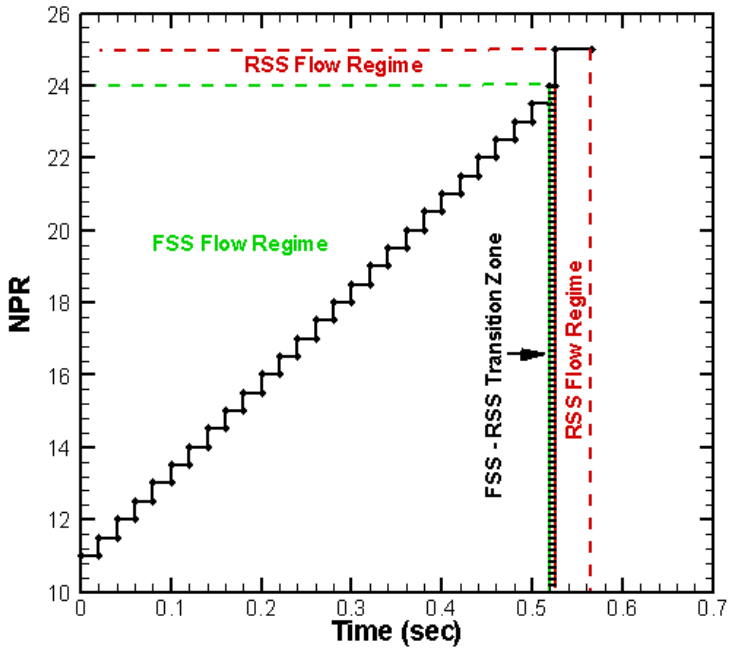

FIGURE 6.18 – NPR v/s time history of the calculations for forward flow transition process.

The first result of this numerical experiment is that the CNPR is 24.0. This is in agreement with the value experimentally observed by Nguyen et al. [100] & [101]. However, the physical time duration of this numerically observed transition (FSS to RSS) is about 5.35 ms, which seems to be smaller than the transition time reported Nguyen et al. [101] i.e. 50 ms. We should note that, for a dual bell nozzle this duration of flow transition has been reported to be less than 10 ms [123].

An additional axi-symmetric calculation based on a sudden increase of NPR from 23 to 30 has been performed in order to check the dependence of this time required for the transition process to the rate of increase of NPR. The observed time duration for transition FSS to RSS process is approximately 6.48 ms in such a case which is relatively higher than the transition case for which the NPR is kept fixed in the range of CNPR. In fact, the axial position of the separation point for the case of NPR=30.0 appears relatively downstream in comparison to the NPR=24.0 (RSS configuration), so it seems natural to observe a greater amount of time for the flow reattachment (i.e. transition process).

6.4.1.2 Analysis of Flow Structure

Although numerical results are recorded at all aforementioned NPR's but here for the convenience we have selected snapshots at few values of NPR and are given in Fig. 6.19 & 6.20. Depending upon the flow structures observed during the numerical calculations, flow regimes have been divided into three zones corresponding to their NPR, (i) FSS zone (NPR = 11-24), (ii) Transition zone (NPR = 24.0) and (iii) RSS zone (NPR= 24.0-25.0) and are presented in Fig. 6.19 & 6.20. These three separated flow regimes contain flow discontinuities ; hence a shock function is used to detect the fine flow structures and is defined by :

$$f(x) \equiv \frac{\mathbf{U}}{c} . \frac{\texttt{grad}\, p}{|\texttt{grad}\, p|} \tag{6.8}$$

This function represents the Mach number of the velocity component in the direction of the pressure gradient. A bright region indicates shocks or compression zones and a dark region highlights expansion zones. Figure 6.19 : a-f, displays the flow structure which appears in the FSS regime. Figure. 6.19 : a, displays the free shock separated flow regime successfully reproduced at NPR=16.5. An internal shock which emanates from the nozzle throat region interacts with the separation shock from the nozzle wall. This interaction causes a small deflection of this separation shock before interacting with the Mach stem at the triple point. A zoom near the triple point, internal and the separation shock depicts more clearly this deflection. From the triple point, a slip line emanates. It is inclined towards the nozzle axis and so is the flow as it is emphasized by the streamlines.

As depicted from Fig. 6.19 : a-f, the distance between the throat and the Mach stem increases as a function of NPR. Similarly, the separation point location also moves downstream along the nozzle. In the case of FSS flow regime, the relative distance between the separation point (SP) location and the Mach stem (MS) almost remains constant (as shown in Fig. 6.27). As a consequence of this relative shift of MS and SP towards the nozzle exit, the interaction point of internal shock with the separation shock moves towards the triple point. Figure 6.19 : f, presents a snapshot taken when this internal shock reaches the triple point and forms a common point of interaction for internal shock, separation shock, Mach disk and reflected oblique shock.

According to our knowledge, such type of interaction has not been reported in the literature. It is interesting to note that a clean curved separation (incident) shock now interacts directly

with the Mach disk along with the internal shock and a slight change in the angle of reflected shock is observed. This resulting angle of reflected shock is a common effect caused by the two incoming incident shock (separation and internal shock) at common interaction point at the Mach disk. By looking at the Fig. 6.20, one can notice that soon after the occurrence of this interaction FSS flow regime switches into RSS configuration, i.e. flow transition (FSS to RSS) takes place. Hence, this point of interaction (a common point for Mach stem, internal, incident and the reflected shocks) will be called "Flow Transition Quadruple Point (FTQP)". Appearance of "FTQP" is specific to the nozzle in which there exists an internal shock, for example TOC nozzle.

In the present case of LEATOC nozzle, this FTQP is observed at NPR = 24, which correspond to the experimentally observed NPR value at which flow transition was observed by Nguyen et al. [101]. One may conclude that the NPR at which this FTQP point occurs corresponds to the CNPR. This CNPR, at which flow reattachment takes place (i.e. 24.0), is considered as transition zone, see Fig. 6.19 : a-d. Once we reach the FTQP, a sudden change in the flow structure can be observed by the appearance of a small normal shock called annular Mach Disk (AMD), attached to the Mach disk (see Fig. 6.20 : a). The formation of this AMD changes the FTQP into two triple points, i.e. and upper and lower triple points. The relative distance between Mach stem and the separation point in the axial direction decreases and the observed AMD turns into an oblique shock (cone-shaped shock). Once the AMD disk turns into this oblique shock, a slip line, which is originated from the triple point is diverted away from the nozzle axis, which is depicted in Fig. 6.20 : b, with the deflection of streamlines away from the nozzle axis in the triple point region, whereas in the previous case of FSS, streamlines were reflecting back to the nozzle axis from the triple point due to the Mach reflection.

The cone-shaped reflected shock interacts with the incident shock and results into the formation of two reflected shock from the quadruple point. It is worth noticing that during this transition process (see Fig. 6.19 & 6.20), i.e. starting from the formation of FTQP (FSS regime) till this separated supersonic jet reattaches back to the nozzle wall (RSS regime), the relative distance between the Mach stem and the separation point in the streamwise direction drastically decreases (see Fig. 6.27). Moreover, the size of this oblique cone-shaped shock increases, whereas the size of the separation shock decreases, accordingly. This combined axi-symmetric structure of separation shock, Mach stem and cone-shaped shock is known as cap-shock pattern and is shown in Fig. 6.20 : f. Downstream of this axi-symmetric cap-shock pattern, a large vortex is formed which is trapped by the annular supersonic jet around it (see Fig. 6.20). The size of this vortex increases with the size of the cap-shock pattern and the separated supersonic jet finally reattaches back to the nozzle wall and traps a small recirculation zone between the separation and the reattachment point locations. This results in the appearance of restricted shock separated flow regime.

Based on axi-symmetric RANS calculations by using second order space discretization scheme in space, Moríñigo et al. [94] reported that multiple vortical structures appears downstream of the cone-shaped shock, in addition to the large trapped vortex. We should recall that such type of non-physical vortical structure has also been observed in the case second order MUSCL scheme is used (see Chapter 5, Section 5.1.2). However, in the present transition process based on fifth order MPWENO scheme such vortical structures are not observed.

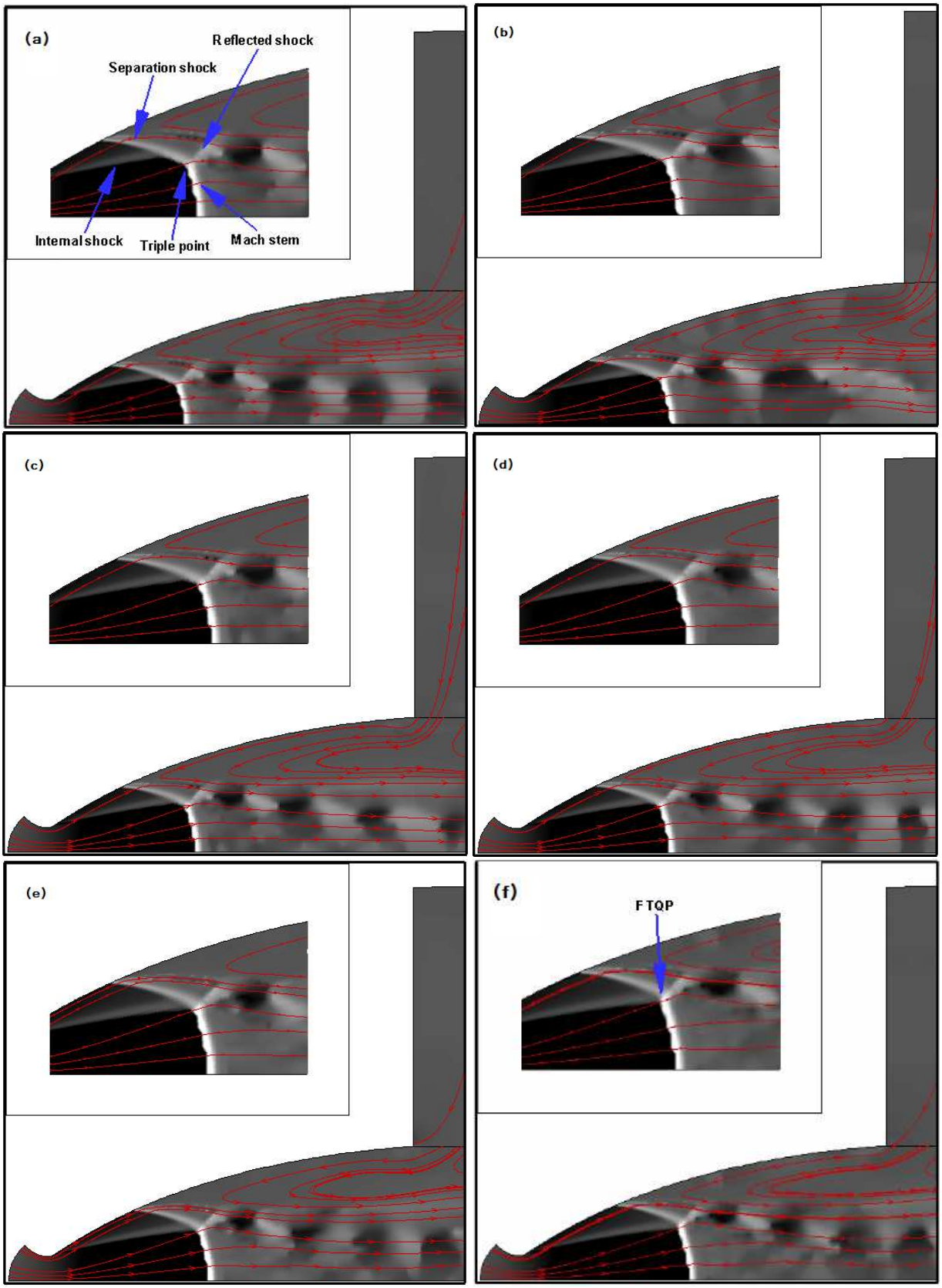

FIGURE 6.19 – Evolution of the flow structure with the increase of NPR : iso-contours of shock function along with the streamlines at NPR (a) 16.5 ; (b) 17.5 ; (c) 18.5 ; (d) 20.0 ; (e) 22.0 ; (f) 24.0 (mesh type B, MPWENO scheme), FTQP : Flow Transition Quadruple point.

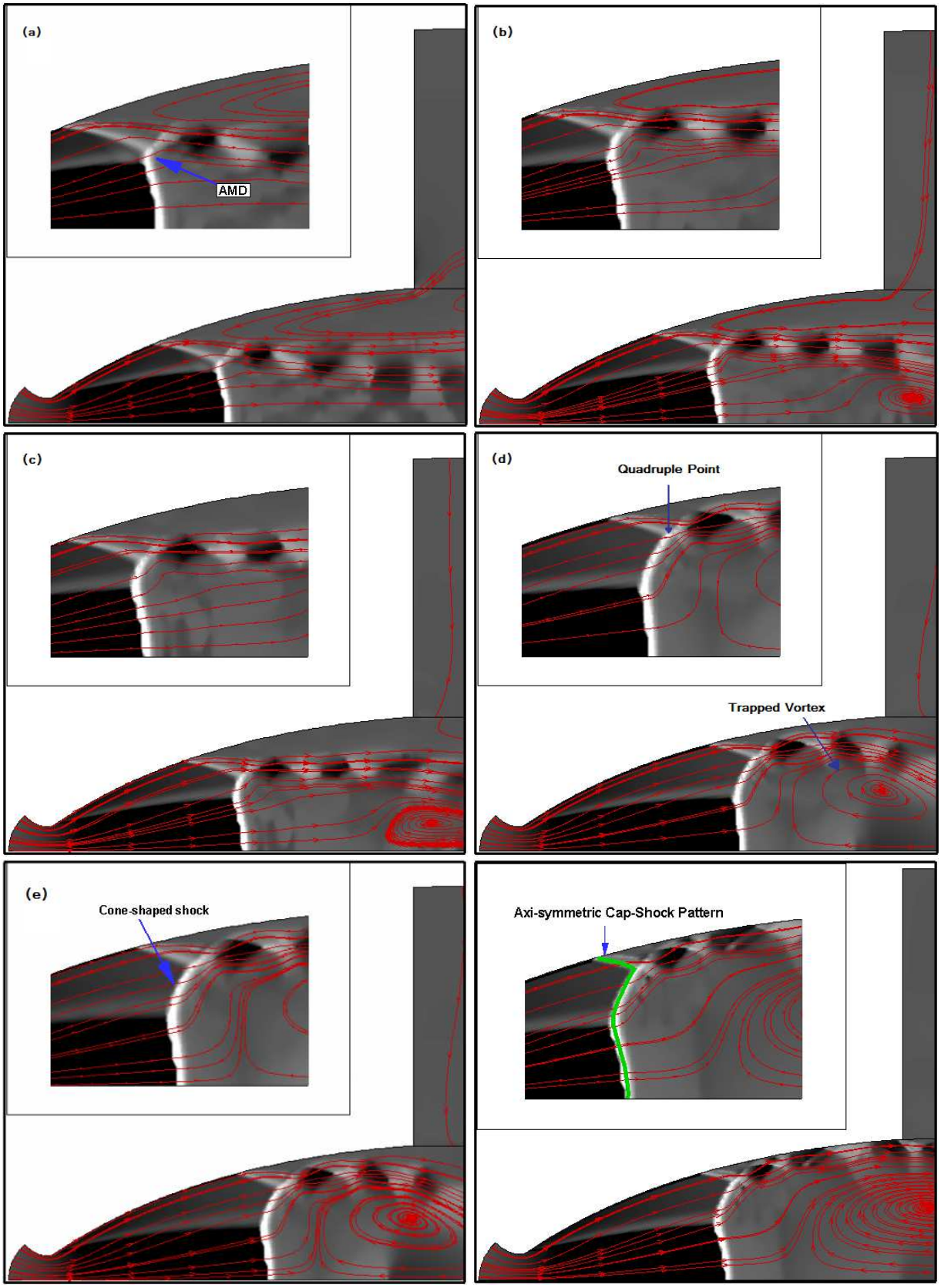

FIGURE 6.20 – Evolution of the flow structure during the FSS to RSS transition process : iso-contours of shock function along with the streamlines at NPR 24, Time (T) = T_{CNPR} + (a) 1.8 ms ; (b) 3.3 ms ; (c) 3.6 ms ; (d) 4.8 ms ; (e) 4.9 ms ; (f) 5.35 ms : flow transition FSS/RSS (mesh type B, MPWENO scheme).

In the case of free shock separation, the flow is governed by the regular reflection of a concave Mach disk/stem, when considered along with the flow direction. Furthermore, for the transition case, with the gradual increase of NPR (as in Fig. 6.20), when the flow becomes RSS, this shape of the Mach disk remains unchanged, i.e. concave. However, Frey et al. [55] reported that RSS is the result of an inverse Mach reflection of the internal shock and that the Mach disk could be convex for the case of Vulcain nozzle. Recently, Nasuti et al. [97] on J-2S nozzle, reported that the convex shape of the Mach stem is due to the balance of pressure across it, rather than to the phenomenon of inverse Mach reflection. Conversely, only a concave shape of the Mach disk is observed here. However, it is worth noting that, when the transition is performed with a high jump in the NPR increase, i.e. from 23.0 to 30.0 (see Figure 6.21), and the Mach disk becomes convex with respect to the incoming flow direction. Based on these observations, one may conclude that the shape of the Mach disk during the transition process highly depends upon the rate of change of the inlet stagnation conditions. This eventually produces a variation of the pressure jump across the Mach disk and modifies its shape accordingly near the triple point region.

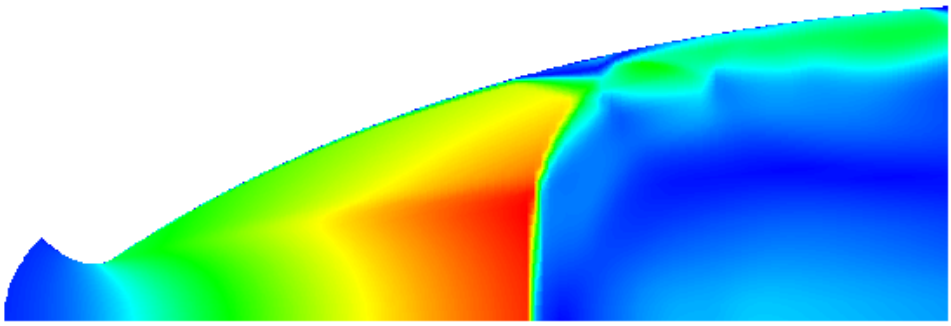

FIGURE 6.21 – Particular RSS flow structure appearing during the transition process a sudden increase in NPR value from 23.0 to 30.0

6.4.1.3 Evolution of the Mean Wall Pressure

The wall pressure numerically obtained at different NPR during this flow transition is compared with the available experimental data. Figure 6.22 shows plots of the wall pressure (normalized with the inlet stagnation pressure P_o) along the nozzle axis (normalized with the throat radius r_t). The predicted wall pressure is in good agreement with its corresponding experimental data. One can notice that for FSS flow regime, the wall pressure suddenly increases at the incipient separation point and reaches a plateau, and then gradually increases, but remains less than the ambient pressure. In the case of RSS flow regime, after reaching the plateau a sudden rise in the pressure occurs due to the reattachment of the annular supersonic jet. Further decrease and increase in the wall pressure are due to the successive interactions of shock and expansion waves in the annular supersonic jet. These successive interactions cause a secondary flow separation (see [100]).

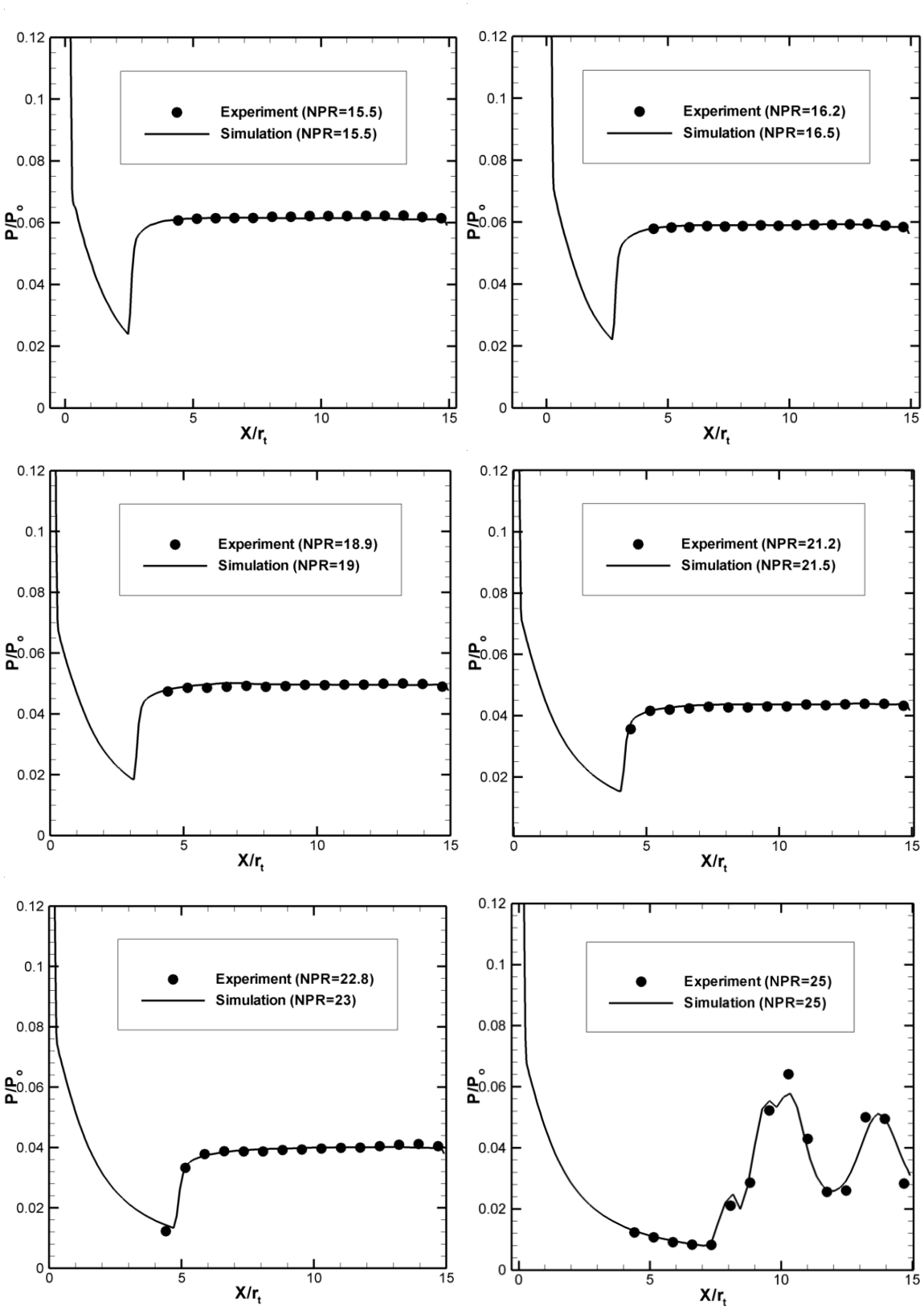

FIGURE 6.22 – Evolution of wall pressure along nozzle axis.

6.4.1.4 Axial & Radial Momentum Analysis

The evolutions of the Mach number and the axial momentum along the nozzle axis are given in Fig. 6.23 & 6.24. They correspond to snapshots in Fig. 6.19 & 6.20. Starting from NPR = 16.5 until the critical nozzle pressure ratio is reached (Fig. 6.23 : a-f), we observe a gradual increase in the level of Mach number along the nozzle axis which suddenly decreases across the Mach stem. Downstream of the Mach stem, successive increase and decrease of the Mach number can be observed, but remains less than 1. Corresponding to this evolution of Mach number a similar behaviour is observed for axial momentum distribution along the symmetry axis. However, it always remains positive. This typical behaviour of axial momentum and Mach number can be noticed (see Fig. 6.24 : a) even when AMD is present in the separated flow structure during the transition process.

As soon as AMD turns into oblique shock (cone-shaped shock) the axial momentum downstream of the Mach stem decreases and becomes negative in a certain region along the axis of symmetry, as shown in Fig. 6.24 : b. The negative axial momentum indicates the appearance of recirculation zone (see Fig. 6.20 : b). The first of the two stagnation points corresponding to the enclosed area of negative axial momentum, has an abscissa corresponding to the minimum value of Mach number along the axis. The size of this negative axial momentum, i.e. recirculation zone, increases as a function of the size of the cone-shaped shock and a large trapped vortex is finally observed downstream of the cap-shock pattern (Fig. 6.20). This negative momentum produces a force/push against the main flow in the central part of the cap-shock pattern. In the meantime, the expanded/accelerated flow surrounding the central core of the nozzle, pushes the separation point further downstream. As a result, the relative size of the cone-shaped shock increases to adjust the quadruple point corresponding to the flow regime at a particular NPR. In addition, the size of the recirculation zone downstream of the cap-shock pattern increases. In order to investigate more precisely the flow behaviour across the Mach stem throughout this transition process, radial momentum profiles, before and after the Mach stem (MS), have been reported for each corresponding snapshots shown in Fig. 6.25 & 6.26. The locations of these upstream and downstream stations have been carefully selected to take into account the effect of the cone-shaped shock. They are given by :

$$X_1 = MS - \frac{\Delta x}{r_t}$$

$$X_2 = MS + \frac{\Delta x}{r_t}$$

Here $\frac{\Delta x}{r_t} = 0.6$ and X_1 & X_2 are two upstream and downstream axial locations, respectively. By looking at the radial momentum distribution along (from symmetry axis to nozzle wall) for both mentioned stations, one can first notice a positive radial momentum starting from the nozzle axis, which is due to the flow expansion in the divergent part of the nozzle (see Fig. 6.25 : a). This positive radial momentum suddenly becomes negative. This is caused by the large recirculation followed by the free shock separation. The overall radial momentum upstream and downstream of the Mach stem is negative and high enough to divert the flow towards the nozzle axis (see Fig. 6.25 : a-e).

A slight decrease in the negative radial momentum downstream of the MS has been observed when AMD appear in the separated flow regime (see Fig. 6.26 : a). Interestingly, when this AMD turns into an oblique shock, as in Fig. 6.20 : b, a sudden change in the direction of radial

momentum, from negative to positive is observed near the triple point region (the emanating slip line is inclined away from nozzle), which afterwards shows negative distribution due to the existence of the recirculation zone near the nozzle wall. As a function of the size of cone-shaped shock, the magnitude of this positive radial momentum near the triple point region increases and maximizes the probability of the annular supersonic jet to reattach back to the nozzle wall. Figure. 6.26 : f, shows that the radial momentum distribution is positive and high enough to this cause flow reattachment. Finally, RSS flow regime is reached as shown in Fig. 6.20 : f.

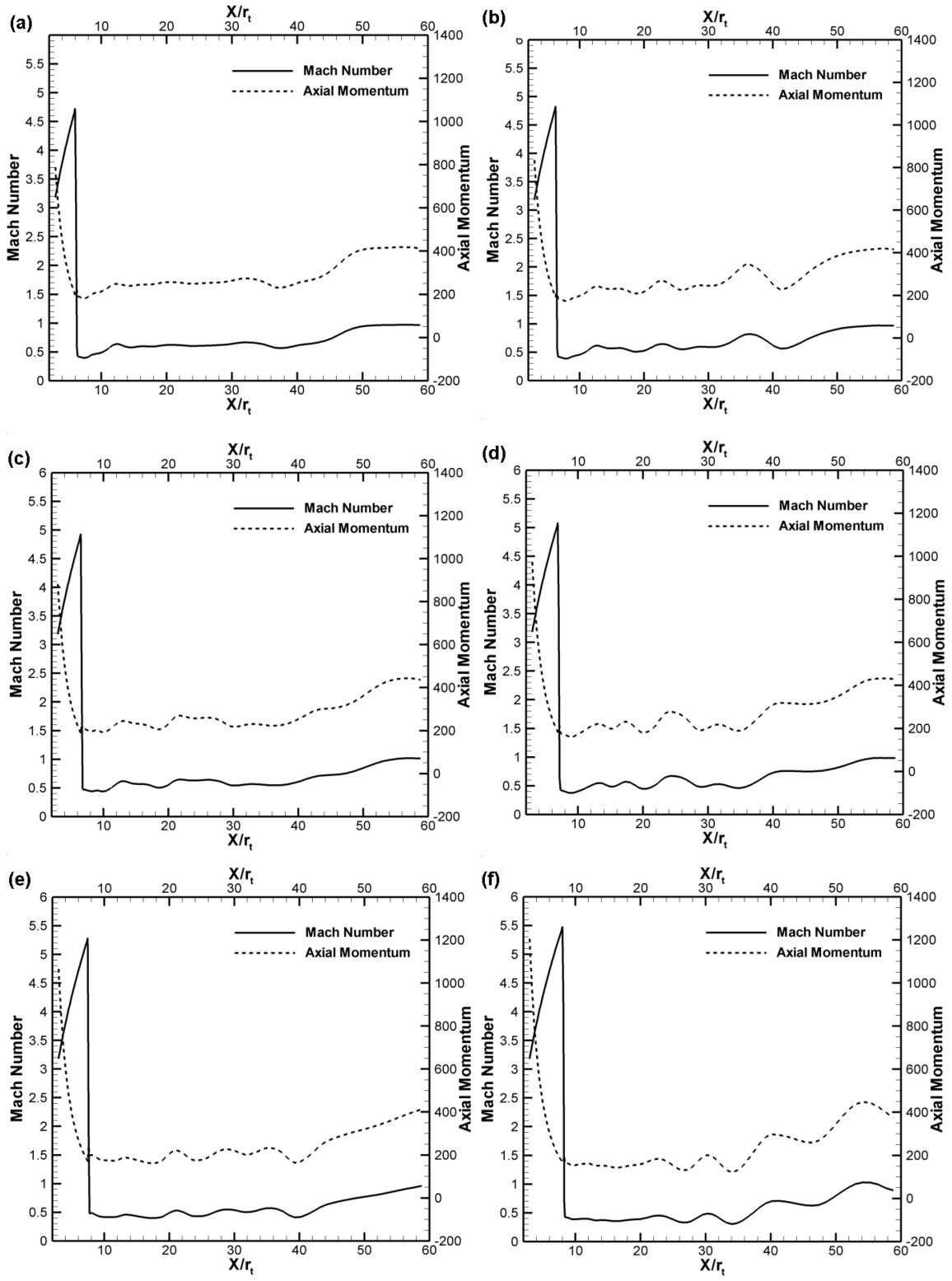

FIGURE 6.23 – Evolution of Mach number & axial momentum ($kg/m^2.s$) along the nozzle axis at NPR (a) 16.5 ; (b) 17.5 ; (c) 18.5 ; (d) 20.0 ; (e) 22.0 ; (f) 24.0, corresponding to the snap-shots shown in Fig 6.19.

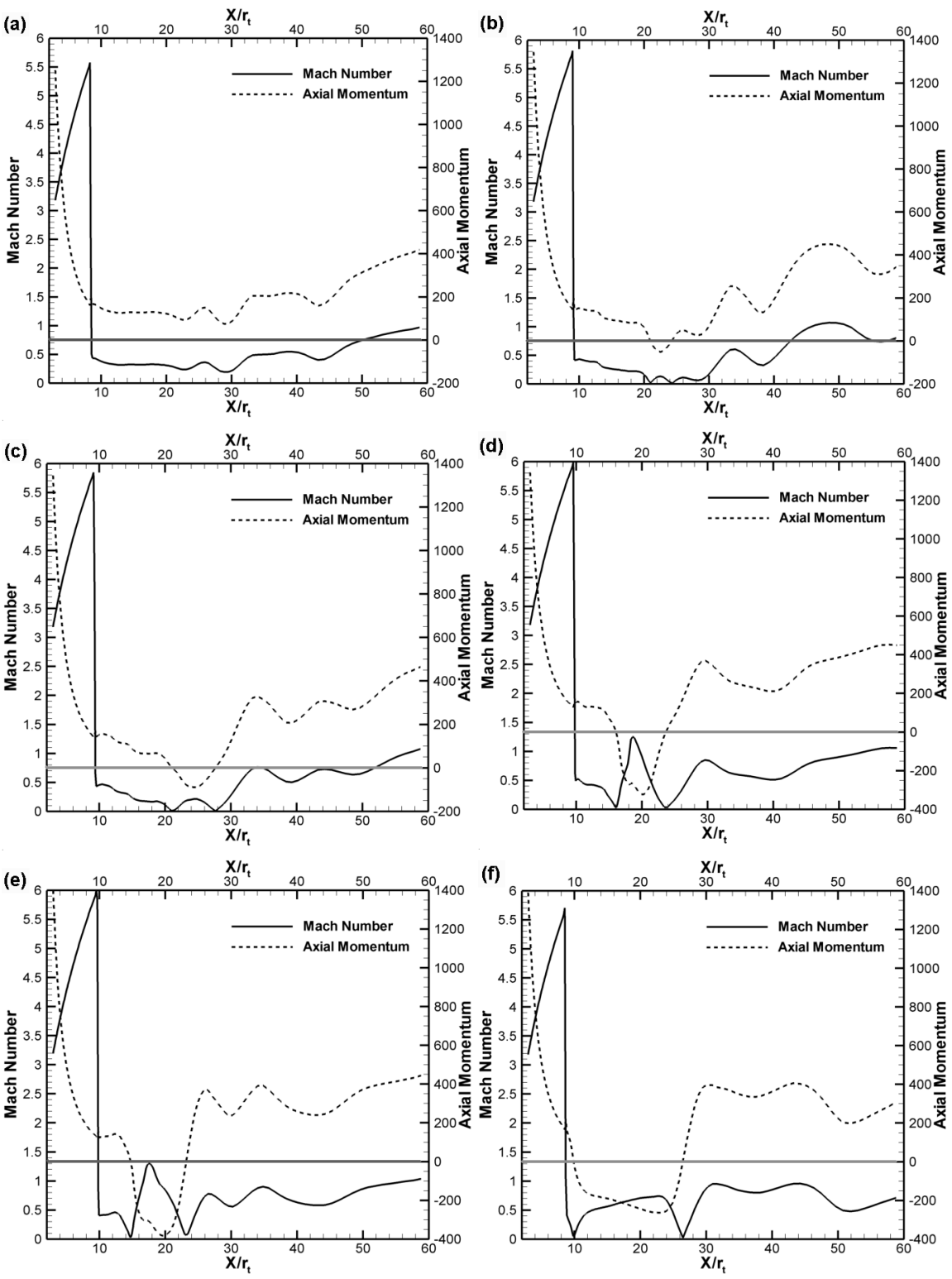

FIGURE 6.24 – Evolution of Mach number & axial momentum ($kg/m^2.s$) along the nozzle axis at NPR 24, Time (T) = T_{CNPR} + (a) 1.8 ms ; (b) 3.3 ms ; (c) 3.6 ms ; (d) 4.8 ms ; (e) 4.9 ms ; (f) 5.35 ms : flow transition FSS/RSS, corresponding to the snap-shots shown in Fig 6.20.

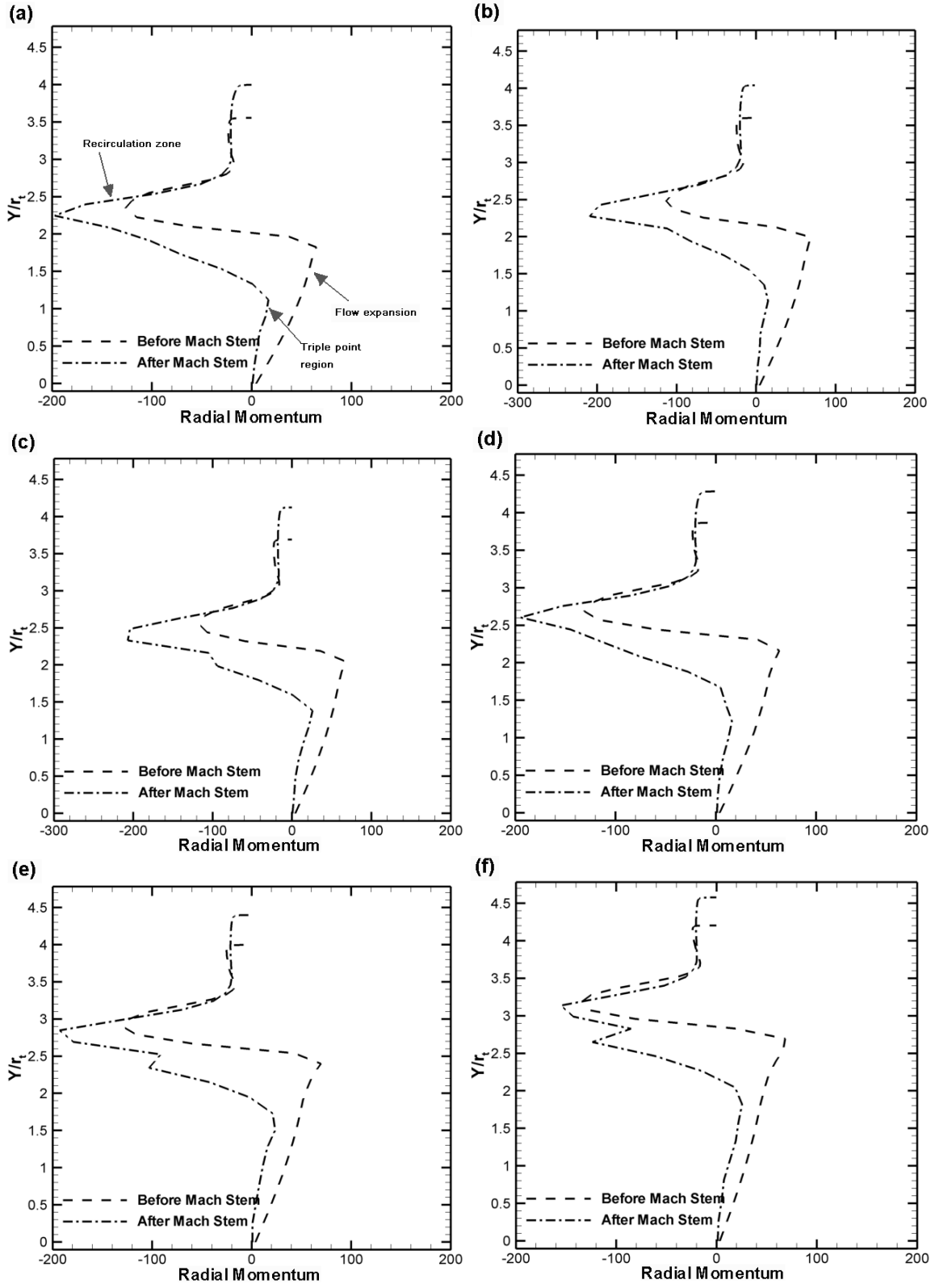

FIGURE 6.25 – Radial momentum ($kg/m^2.s$) distribution before and after Mach stem of their corresponding NPR (a) 16.5 ; (b) 17.5 ; (c) 18.5 ; (d) 20.0 ; (e) 22.0 ; (f) 24.0, corresponding to the snap-shots shown in Fig 6.19.

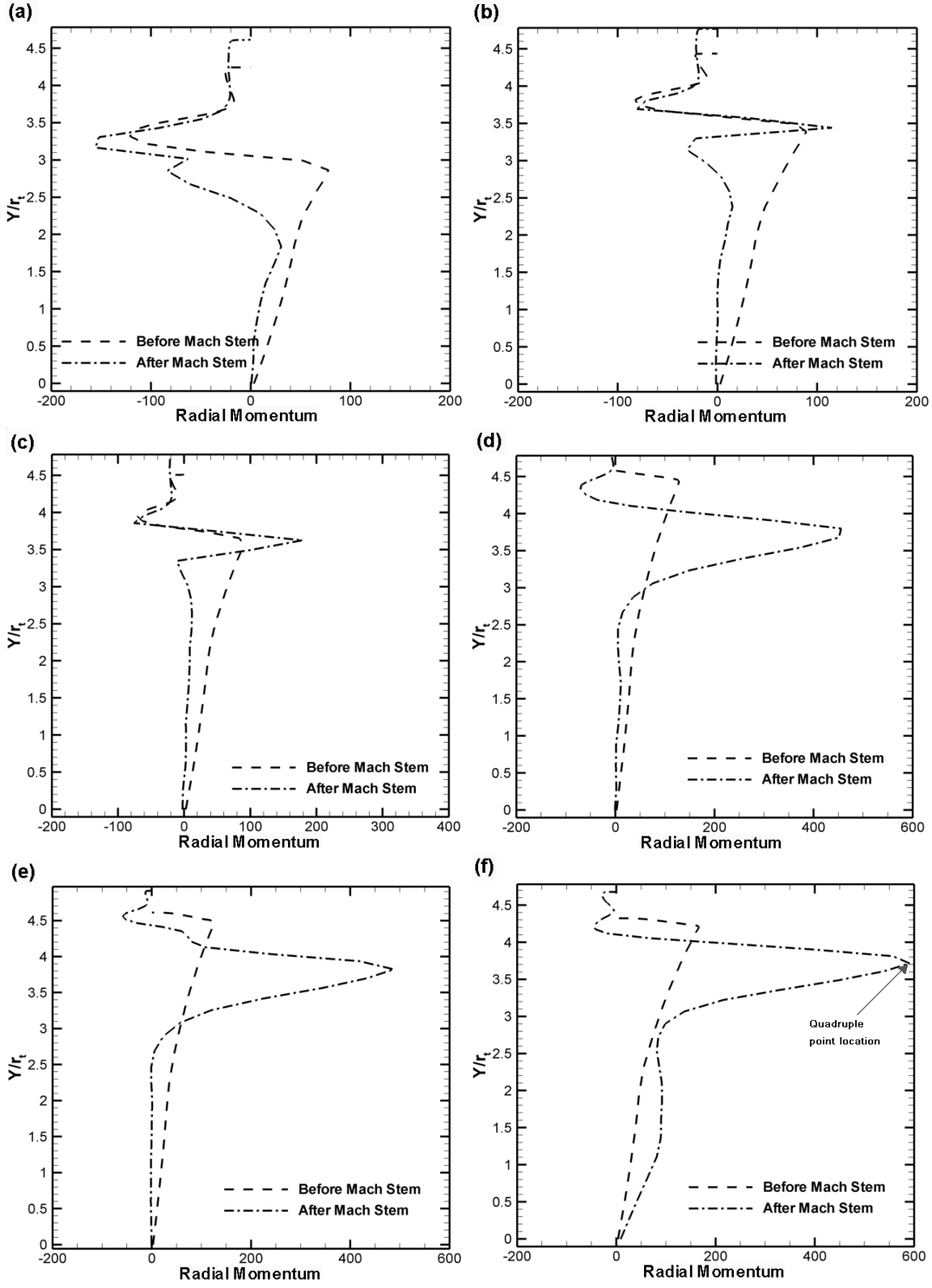

FIGURE 6.26 – Radial momentum ($kg/m^2.s$) distribution before and after Mach stem, Time (T) = T_{CNPR} + (a) 1.8 ms ; (b) 3.3 ms ; (c) 3.6 ms ; (d) 4.8 ms ; (e) 4.9 ms ; (f) 5.35 ms : flow transition FSS/RSS, corresponding to the snap-shots shown in Fig 6.20.

6.4.1.5 Mach Disk and Separation Point Locations

As discussed in the previous sections (6.4.1.2 & 6.4.1.4), the relative distance between the separation point location and the Mach stem plays an important role in flow structure change during the flow transition. Figure 6.27, displays this respective axial distance for FSS and RSS regimes at different NPR's. In the case of FSS flow regime, the relative distance between the separation point and the Mach stem is in the range of $X/r_t = 2.54 - 3.12$. However, when the flow switches from FSS to RSS flow regime, this relative distance suddenly decreases by around $X/r_t \approx 1$. From Fig. 6.27, we can notice that in RSS configuration, this relative distance further decreases when the NPR increases. In addition, this movement of separation point location in RSS regime also causes an increase in the size of the recirculation zone trapped between the separation and the reattachment of the annular supersonic jet. We can note that the size of the stabilized trapped vortex, downstream of the cap-shock pattern also increases in the RSS regime when the NPR increases. The distribution of negative axial momentum along the nozzle axis downstream of the cap-shock pattern produces a negative push (against the main flow) in the central core and is one of the possible explanation for the shift of the separation point location downstream of the Mach stem. The radial momentum across the respective quadruple points increases when NPR increases (for the case of RSS). This also confirms the aforementioned mentioned argument.

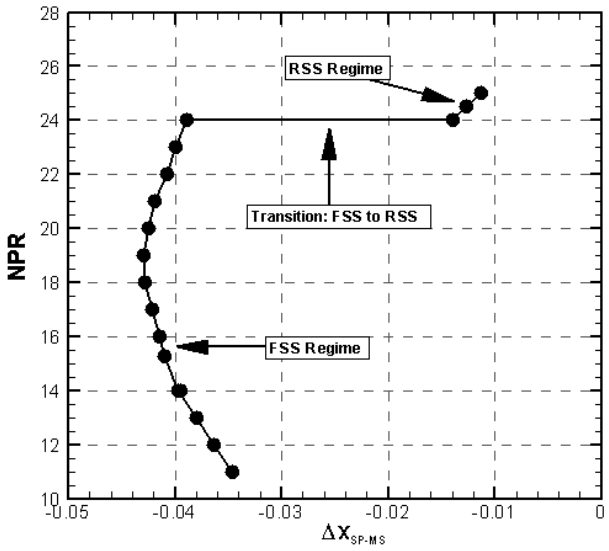

FIGURE 6.27 – Evolution of the relative distance between separation point (SP) and Mach stem (MS) locations (ΔX_{SP-MS}) along the nozzle axis with respect to the NPR during the forward transition process, FSS to RSS flow regime.

6.4.2 Reverse Transition

Experimentally, it has been observed that this flow transition process is a hysteresis cycle. Nguyen [100] have reported that during the shut-down process of LEATOC (reverse transition from RSS to RSS) the critical nozzle pressure ratio is around 14. After successfully reproducing the forward flow transition from FSS to RSS, the reverse process is numerically reproduced here. Keeping the same process of step change in the NPR value, axi-symmetric URANS calculations are performed by stepping down the NPR at the same difference of 0.5 bar. The boundary

conditions for step change in NPR for the combined start-up and shut-down processes are shown in Fig. 6.28. Present numerical calculations lead to a hysteresis cycle in the NPR range of 24-14, which is in good agreement against the experimental observation [100]. The time observed for the reverse transition process is about 5.12 ms which is smaller than the previously observed forward transition process. Series of snapshots for the reverse transition process are presented in Fig. 6.30-6.32. Only the zoom near the triple and the recirculation zone are reported here to clearly visualize the detachment of the supersonic annular jet : from RSS to FSS.

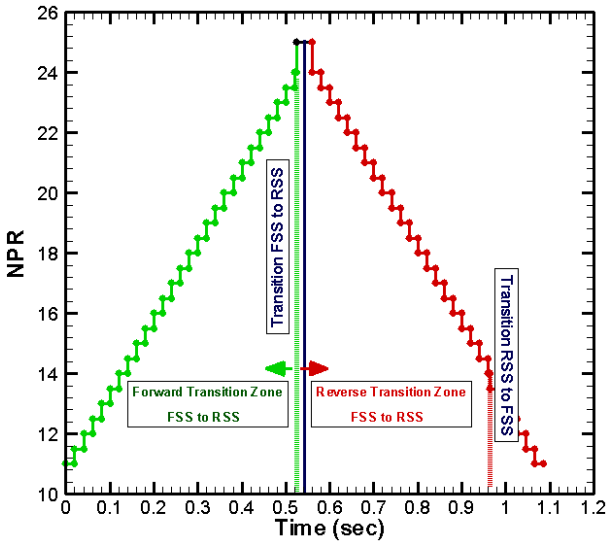

FIGURE 6.28 – NPR v/s time history of the calculations for forward and reverse transition process.

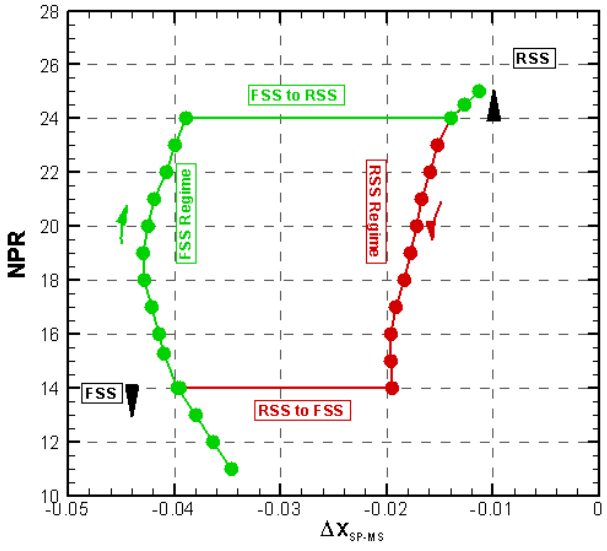

FIGURE 6.29 – Evolution of the relative distance between separation point (SP) and Mach stem (MS) location (ΔX_{SP-MS}) along the nozzle axis with respect to the NPR during the forward and reverse transition process, FSS ⇔ RSS flow regime.

In this range of NPR, from 25 to 14 (see Fig. 6.30 & 6.31), the flow remains in restricted

shock separation configuration. Figure 6.30 : e, which corresponds to NPR=14.0, we still observe an axi-symmetric cap-shock pattern and an internal shock which interacts with the Mach stem. Following the same criterion as mentioned for the forward transition, i.e. flow transition quadruple point, the supersonic annular jet detaches back from the nozzle wall. From snapshots (Fig. 6.31 - 6.32 : a) one can notice that during the time advancement, the size of the cone-shaped shock decreases and switches into an annular Mach disk. The presence of this annular Mach disk has also been observed in the forward transition process. As a consequence, the separation point location moves further upstream. This annular Mach disk then disappears and the separation shock directly interacts with the Mach stem and forms the quadruple point, i.e. FTQP. This suggests that the formation of "Flow Transition Quadruple Point" is also the limiting case for reverse transition process (switching limit from RSS to FSS). When this shock structure is reached, the supersonic jet is completely detached from the nozzle wall and the FSS flow regime takes places. A further decrease in NPR was also performed in order to check the behaviour of the internal shock. The position of this internal shock interaction with respect to the separation shock moves further upstream when we reduce the NPR. The relative distance between the separation point location and the Mach stem for the hysteresis cycle are plotted against their NPR (see Fig. 6.29). This plot indicates that the relative axial distance between the separation point location and the Mach stem for RSS configuration is comparatively small in comparison with the FSS regime. Once we reach the CNPR for reverse transition process, we observe a sudden increase of this relative distance between the separation point and the Mach stem location. Since this reverse transition occurs at NPR lower than in the case of forward flow transition, the net relative distance between the separation point and the Mach stem location is relatively small. This also indicates the fact that the time required for the reverse transition should be smaller than for the forward transition.

6.5 Epilogue

A mean flow analysis has been carried out to understand the global evolution of flow structures, in particular during the transition process from FSS to RSS and vice versa. An attempt was made in order to understand the cause of this transition process for a wide range of NPR=10$\Leftrightarrow$25, by using stabilized inflow conditions. The forward and reverse transition (hysteresis) process was reproduced and a good agreement with the experiments was found. In LEATOC (TOC type) contour nozzle, an internal shock appears near the throat region and directly interacts with the separation shock in the low NPR range (in FSS regime). This critical interaction is observed when this internal shock interacts with the existing triple point, following the increase in NPR, i.e. approaching to CNPR. This common interaction point has been reported as 'Flow Transition Quadruple Point (FTQP)' and was observed against the critical nozzle pressure ratio for forward transition process. Radial and axial momentum imbalances across this FTQP lead to the formation of the cap-shock pattern and of the subsequent flow reattachment (RSS regime), accordingly. This suggests that FTQP is the limiting case for change in flow structure from FSS to RSS. This is also the case in the reverse transition. Further studies would be required to check whether this hypothesis still holds for different nozzle contours (other than LEATOC). Finally, it has been observed that the curvature of Mach disk highly depends on the level of increase of inlet stagnation conditions, i.e. NPR. Whereas it is concave for small NPR increments, it becomes convex with respect to the incoming flow when large impulsive increase in the inlet pressure is applied.

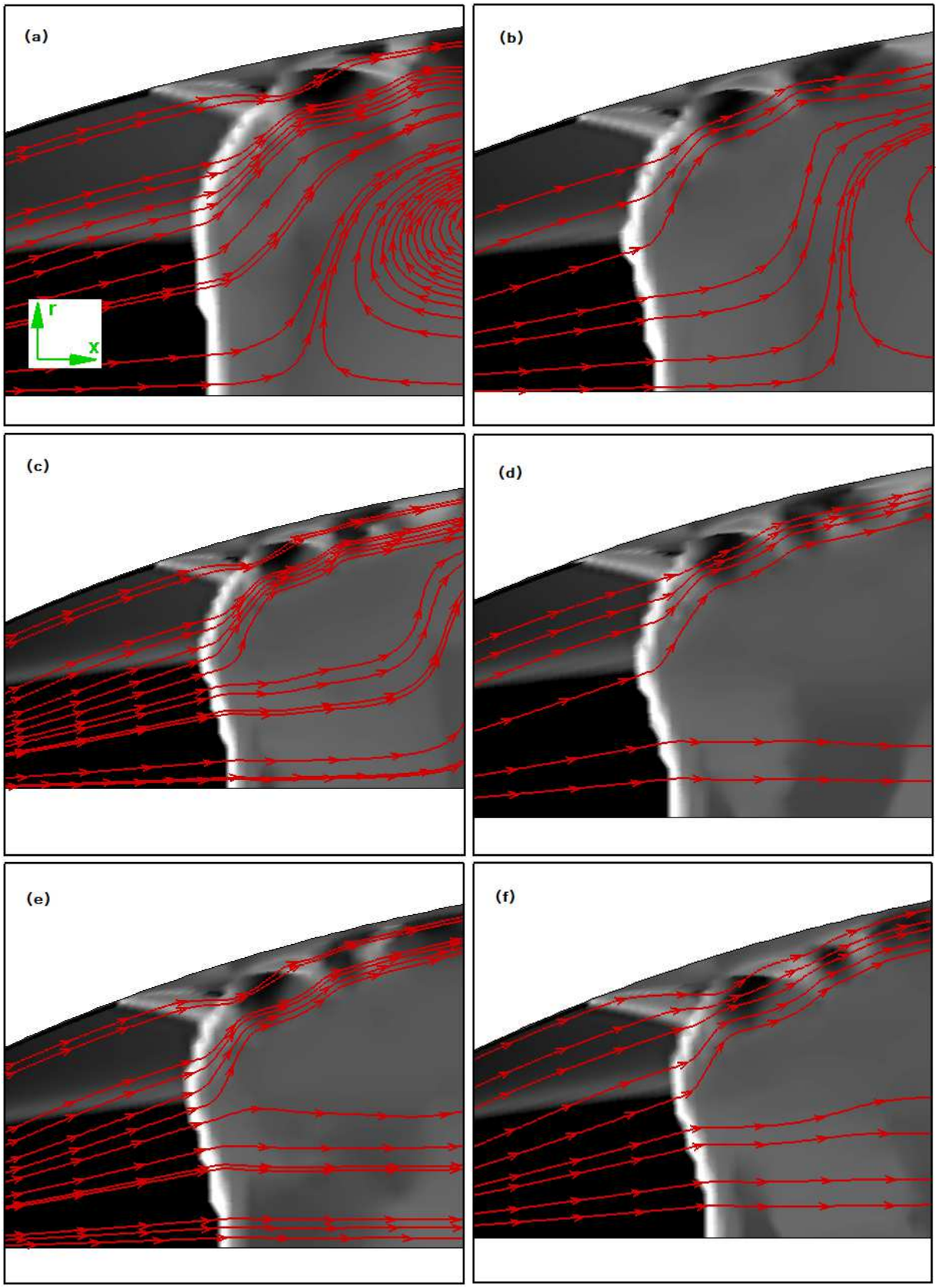

FIGURE 6.30 – Reverse transition process RSS to FSS : zoom of near separation point and Mach stem : Iso-contours of shock function (f(x)) and streamlines at NPR (a) 25.0 ; (b) 23.0 ; (c) 21.0 ; (d) 17.0 ; (e) 15.0 ; (f) 14.0 (mesh type B, MPWENO scheme).

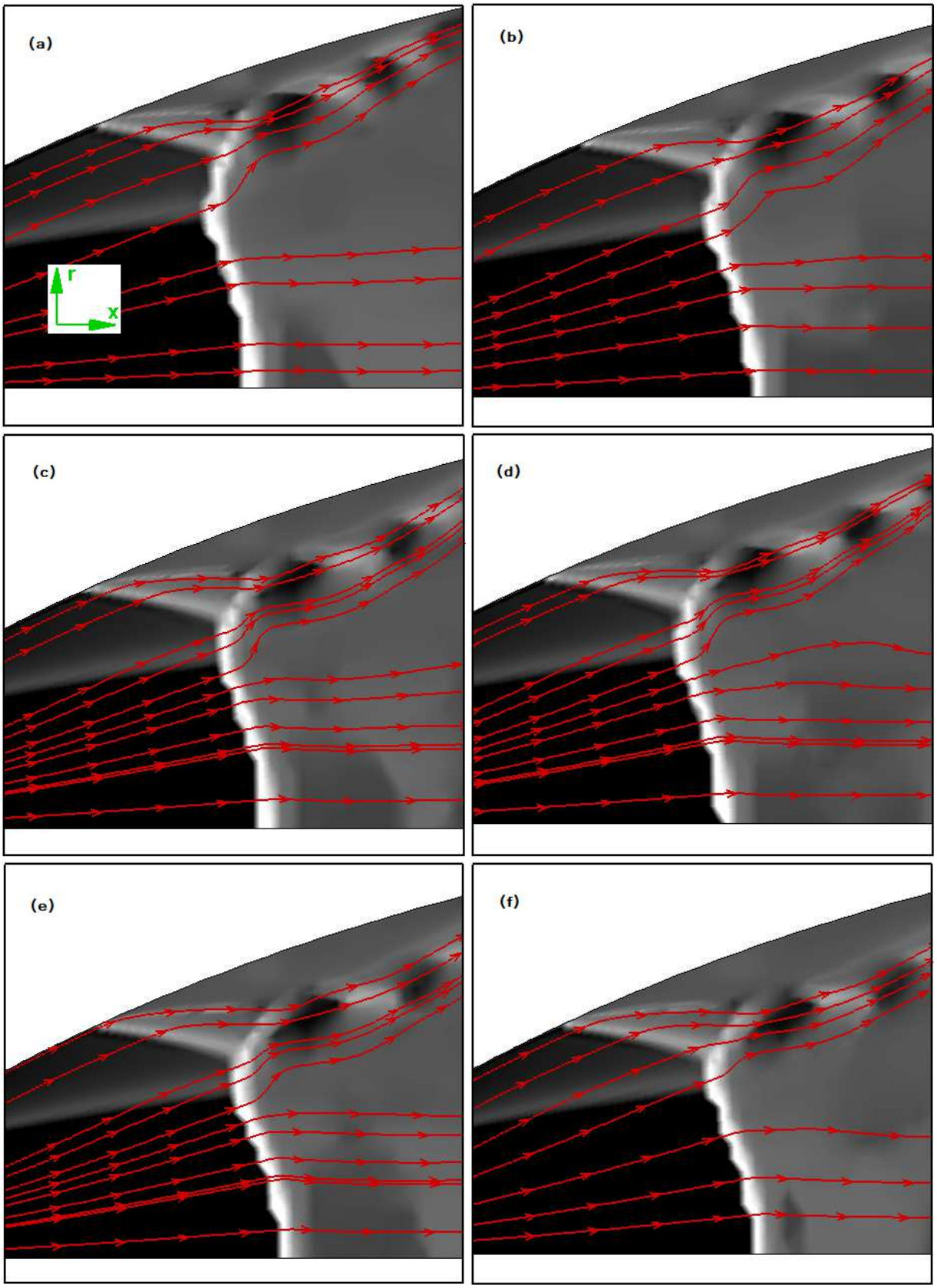

FIGURE 6.31 – Reverse transition process RSS to FSS : zoom of near separation point and Mach stem : Iso-contours of shock function (f(x)) and streamlines at NPR=14.0, Time (T) = T_{RSS} at NPR=14.0 + (a) 1.2 ms ; (b) 1.8 ms ; (c) 2.3 ms (d) 2.5 ms ; (e) 3.1 ms ; (f) 3.4 ms (mesh type B, MPWENO scheme).

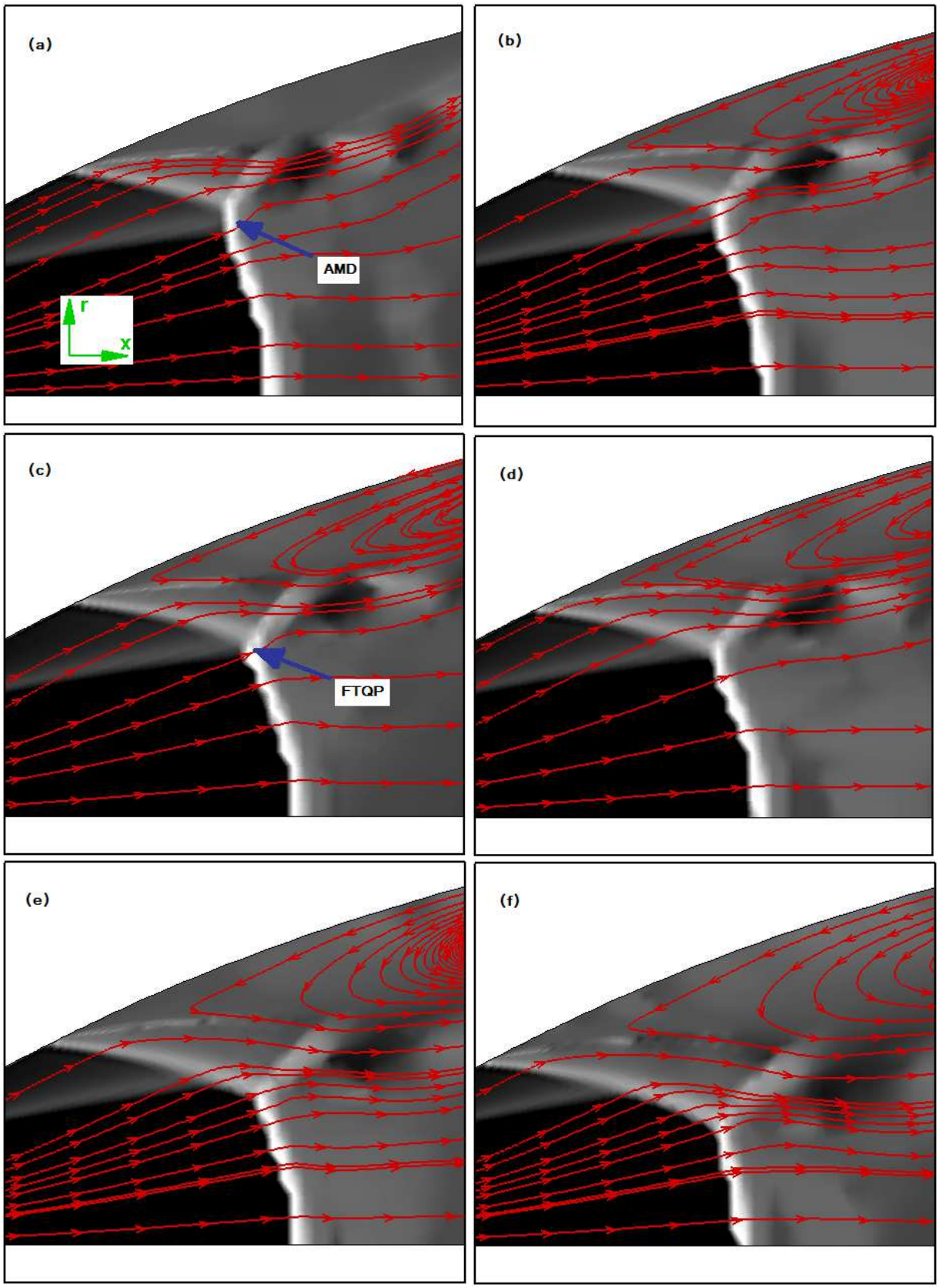

FIGURE 6.32 – Zoom of near separation point and Mach stem : Iso-contours of shock function (f(x)) and streamlines at NPR = 14.0, Time (T) = $T_{RSS}atNPR = 14.0$ + (a) 4.2 ms ; (b) 4.8 ms ; (c) 5.1 ms : reverse transition RSS/FSS process & (d) 13.5, (e) 12.5 ,(f) 11.0 (mesh type B, MPWENO scheme), AMD : annular Mach disk ; FTQP : flow transition quadruple point.

Chapitre 7

Free Shock-Induced Separated Flow Regime

7.1 Free Shock Separation

In LEATOC nozzle, at relatively low NPR, the separated flow regime is characterized by the appearance of a free shock separation. However, after certain NPR (NPR≈24.0) this flow regime is switched into RSS configuration. The occurrence of FSS below this critical limit is confirmed by several mean wall pressure plots shown in [100] and also in the previous Chapter 6. Furthermore, based on series of experiments by Nguyen [100], it has been reported that there is an increasing unsteadiness and loss of symmetry, which eventually causes an increase in the level of side-load activities, when NPR approaches to CNPR, i.e. NPR value close to FSS→RSS transition process. In order to analyse this unsteady behaviour in FSS flow configuration in LEATOC nozzle, simulations are performed at three different NPR, i.e. 5.0, 15.5 & 19.0 and are reported here. The parameters used to perform these simulations at these NPR are given in Table.7.1.

Simulation Parameters	-	-	-
NPR	5.0	15.5	19.0
Mesh Type	CE	BE	BE
Number of grid points (million)	≈ 10	4.32	4.32
$\Delta\, T_{save}$ (μ s)	20	50	50
Number of samples	8600	6400	6400
Integration time (s)	0.172	0.32	0.32
Physical sampling frequency (KHz)	50	20	20
Range of minimum possible frequency for analysis (Hz)	6	3	3

TABLE 7.1 – Simulation parameters for NPR=5.0, 15.5 & 19.0

The evolution of the predicted mean wall pressure with respect to these three pressure ratio's is compared with the available experimental data in Fig. 7.1. When the pressure ratio P_o/P_a increases, the plateau of the mean wall pressure is shifted downstream and its value decreases. At the nozzle exit, the ambient atmospheric fluid is sucked into the nozzle and then re-entrained

downstream by the main separated jet, which results in the formation of a small counter clockwise recirculation at the nozzle lip. The gap between the nozzle wall and the mixing layer that forms around the separated jet decreases when the separation line moves towards the nozzle exit. The length of this separation line increases as a function of the nozzle radius.

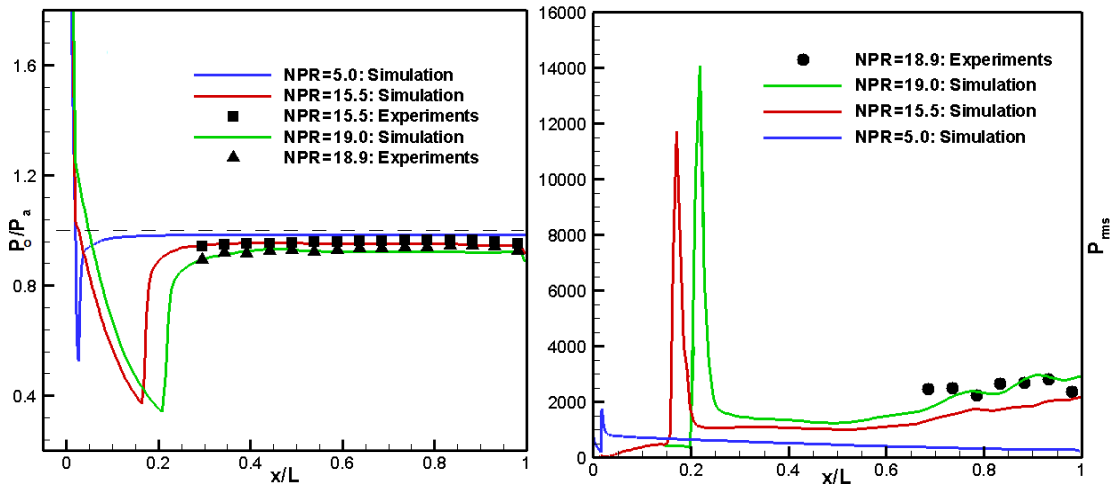

FIGURE 7.1 – Evolution of (Left) mean wall pressure non-dimensionalized by the ambient pressure and (Right) RMS of pressure fluctuations (Pa).

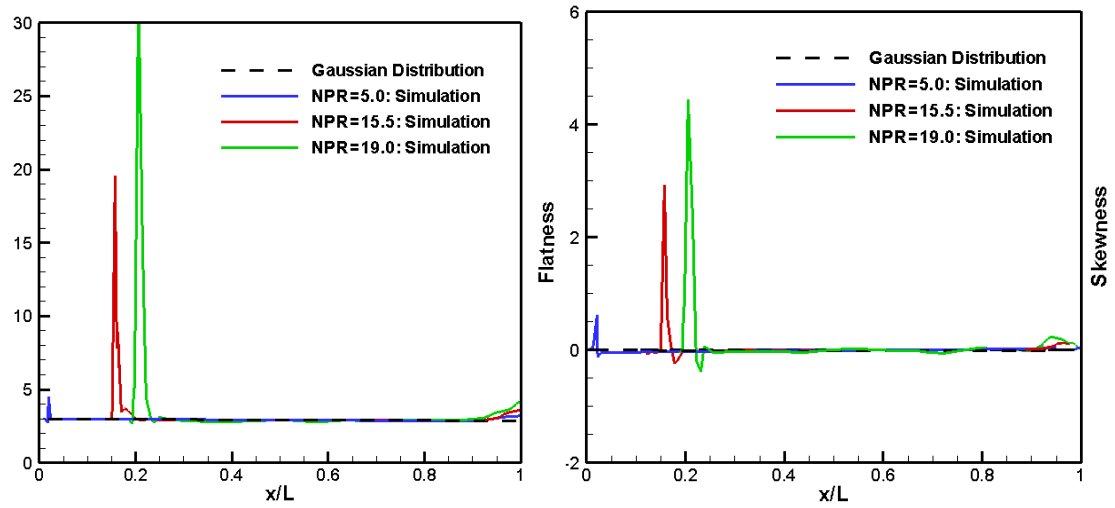

FIGURE 7.2 – Evolution of (Left) flatness and (Right) skewness of wall pressure fluctuations.

As shown by Fig. 7.1 : Right, the level of pressure fluctuations in the separated region increases with the pressure ratio. The distribution of RMS of wall pressure signals is qualitatively correct with a peak around the separation point location and a significant level in the separation region downstream of it. Given that the length of the separation line varies with the nozzle radius, this peak around the shock excursion region naturally increases for higher NPR. The overall pressure jump between the beginning of separation and the plateau only slightly increases. This suggests that this RMS level increase is not directly linked to the increase of the inlet stagnation pressure but is rather due to the increasing instability of the flow. Figure 7.2,

presents the skewness of recorded wall pressure fluctuations which also seems qualitatively correct with positive values at the beginning of the separation (occurrence of the positive pressure fluctuations when the separation is in its most upstream position) and the negative values at the beginning of the plateau (occurrence of a negative pressure fluctuations when the separation is in its most downstream position). Downstream of the shock excursion region or separation line, the computed skewness and flatness level are close to 0 and 3, respectively : level of flatness for Gaussian fluctuations. A departure from Gaussian behaviour is clearly noticeable from the peaks, indicating the increasing instability when the nozzle radius increases. In addition, a small increase in the level of skewness and flatness near the nozzle exit is noticed. This is due to the presence of a small recirculation zone near the nozzle lip.

This statistical analysis at three NPR's shows that the flow behaviour in FSS configuration remains almost the same, except regarding the level of pressure fluctuations which is directly linked with the axial location of the separation line. For the case of NPR=5.0, this separation line is located very close to the nozzle throat and is associated with a comparatively low level of unsteadiness, as indicated by the computed RMS level. On the other hand, for the case of NPR=15.5 & 19.0, the separation line is located far downstream of the throat at relatively close locations.

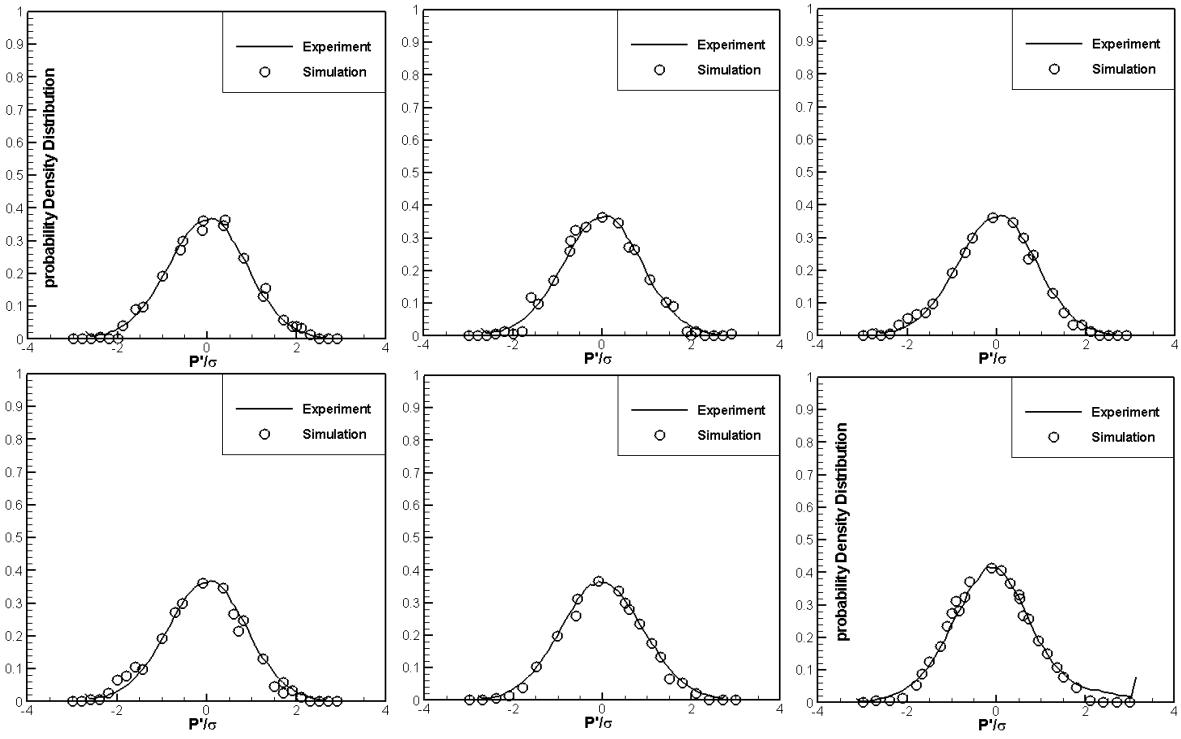

FIGURE 7.3 – Probability density function of pressure fluctuations (Left to Right - Top to Bottom) at x/L = 0.73, 0.78, 0.83, 0.88, 0.93 & 0.98 : NPR=15.5).

The probability density function of the pressure signals in the separation region has been computed and is given in Fig. 7.3. The calculated PDF's show a good agreement in comparison with the available experimental data and indicate that pressure signals display Gaussian distribution which corresponds to the zero skewness and flatness of factor 3. A slight variation in the PDF at location x/L=0.98 is observed, which is due to the appearance of small the recirculation bubble near the nozzle exit.

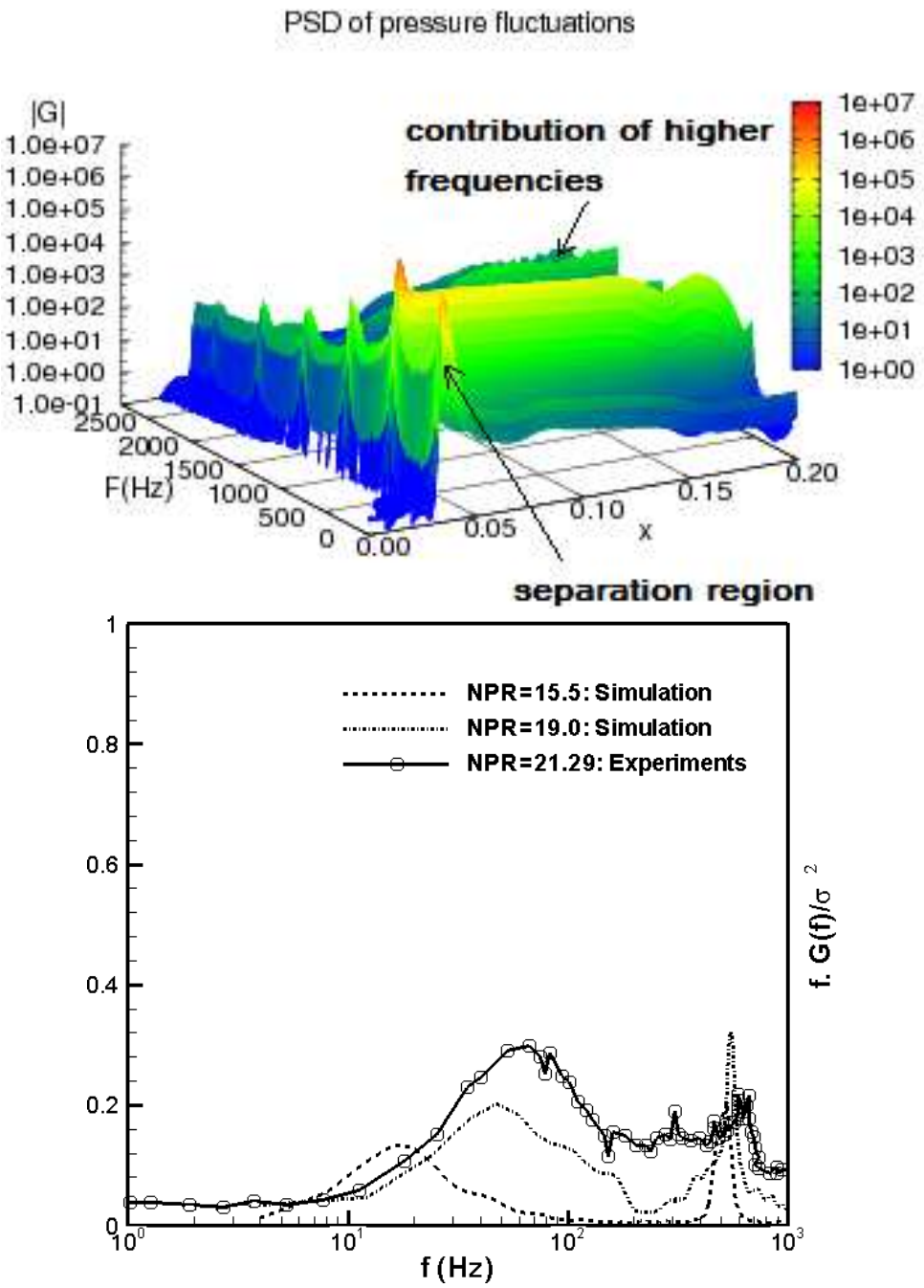

FIGURE 7.4 – Spectra of the wall pressure fluctuations : (Top) along the nozzle wall ; log(G(f)) : NPR=15.5, and (Bottom) at x/L=0.326.

Figure 7.4 presents the computed power spectral density (PSD) of the nozzle wall pressure fluctuations. PSD functions are computed using the Welch's procedure [153]. By looking at Fig. 7.4 : Top, one can notice that near the separation point location, the pressure fluctuations are dominated by the low frequencies, i.e. $< 1kHz$, which can be associated with the excursion of the separation shock. The contribution of the high frequencies increases progressively when we move away from the separation line towards the nozzle exit. However, the contribution of the low frequencies remains significant in the whole separated region. These PSD results are in agreement with the experimentally observed behaviour of wall pressure spectra for FSS

configuration in LEATOC nozzle (for details see [100]). The range of low frequencies which characterizes shock motion for NPR=15.5 and 19.0 can be more clearly understandable from the PSD plots shown in Fig. 7.4 : Bottom. A comparison with the experimental data is made at x/L=0.326, which is located close to the separation at NPR=21.23 is observed. By looking at the Fig. 7.4 : Bottom, we can notice that the contribution of low frequency ($<$ 200 Hz) fluctuations increases progressively as the pressure ratio increases. A narrow peak around 500 Hz is also observed for the computed PSD's which contributes weakly to the shock motion. We should note that the relatively higher frequency range, near 500 Hz, is not very well captured by simulations. An increase in the level of its peak is due to the fact that this particular x/L location appears further downstream in the plateau region, in comparison with the experimental case at NPR=21.23. Nevertheless, the PSD analysis indicates that in the vicinity of the separation line, the pressure fluctuations are essentially dominated by low frequencies and suggests that RMS level of pressure fluctuations as a function of NPR is due to the increase of the contribution of low frequency.

In the case of free shock separation, when the flow separates from the nozzle wall, counter-current mixing layer forms between the annular supersonic free jet and the low speed flow around it. The essential difference between this counter-current and a classical co-flowing (co-current) mixing layer is that in certain conditions, it supports the absolute instabilities. From instantaneous images of this mixing layer, we can observe that the presence of the flow around the jet leads to the formation of large scale coherent structures (see Fig. 7.7). These structures act as obstacles that can influence the wall pressure. This suggests that in these cases, the influence of upstream disturbances is less important than those one of the downstream low frequency motions. A snapshot of structures formed in the shear layers inside the nozzle are displayed in the Fig. 7.5. Their topology and behaviour appear to be in quite good qualitative agreement with these reported by Strykowski [141] for shear layer at convective Mach number (M_c) = 0.8 (see Fig. 7.6).

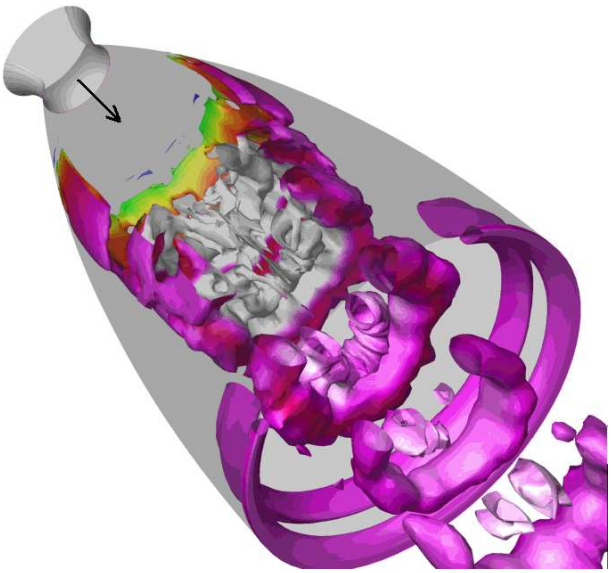

FIGURE 7.5 – Cross-section of instantaneous structures of the mixing layer appear in the case of RSS regime at NPR=15.5 : M_c=0.66

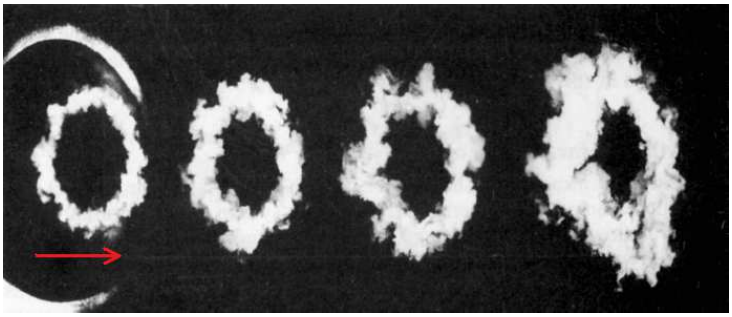

FIGURE 7.6 – Instantaneous structures of mixing layer by the laser perpendicular to the nozzle axis at M_c=0.85 [141].

This mixing layer is inviscidly unstable via the Kelvin-Helmholtz primary instability mechanism. The instability waves grow downstream up to roll up of coherent vortex rings (see Fig. 7.5). Streamwise vortex structures develop through a secondary three-dimensional instability of the thin vorticity layer (braid) between two neighbouring vortex rings. Figure 7.7 displays the instantaneous images of large scale structures which appear in this massively separated flow configuration. These structures are shown with the help of Q-criterion coloured by the iso-pressure contours at the value of $0.1 * U_t^2/(D_e)^2$, where U_t is the velocity at the nozzle throat and D_e is the throat exit diameter. The supersonic jet coming from the nozzle is in fact an annular region with two mixing layers. An internal one between the supersonic flow and the subsonic region downstream of the Mach stem and the external one between the supersonic flow and the fluid outside the nozzle. The relative Mach numbers (M_r=$\frac{2\Delta U}{c_1+c_2}$) calculated at the nozzle exit ($x/L = 1.0$, for NPR=15.5) for these inner and outer mixing layers are 0.7 & 0.78 respectively. At these relative Mach numbers, the turbulent flow undergoes only low compressibility effects [74]. Figure 7.7 : Left, illustrates the predominantly two-dimensional azimuthal nature of the rollers which bend quasi-periodically in the azimuthal direction. This behaviour is in agreement with the numerical observation made by Leep et al. [74] for low compressible mixing layers. The random behaviour of these non-stationary coherent structures in the azimuthal direction can cause the flapping of the separated jet. Let us consider a scenario in which these coherent structures positioned in a dissymmetric way in the azimuthal direction, for example at $\theta = 0°$ and not at $\theta = 180°$. In such a case, the separated jet inclines towards the side $\theta = 0°$. This inclined position of jet is not stable because the coherent structures are convected downstream and change the position in the azimuthal direction. The formation and distribution of the coherent structures vary in time (see Annex B, Fig. B.7). This can explain the flapping of the separated jet at low frequencies.

For the case of NPR=19.0, the relative Mach number at nozzle exit is higher than in the case of NPR=15.5. Iso-surfaces with the help Q-criterion coloured with pressure are shown at various instants for this particular case. One can notice large helical structures around the jet which shows that at this M_r, i.e. 0.85 at nozzle exit, the oblique disturbances now dominate, see Fig. 7.7 : Right. This inclined position of jet is not stable because the coherent structures around the jet are non-stationary and are convected towards the downstream and change the position in the azimuthal direction (see Fig. B.12). Dominant oblique disturbances in the case of NPR=19.0 suggest relative increase of the absolute instability of flow in comparison with the case at NPR=15.5.

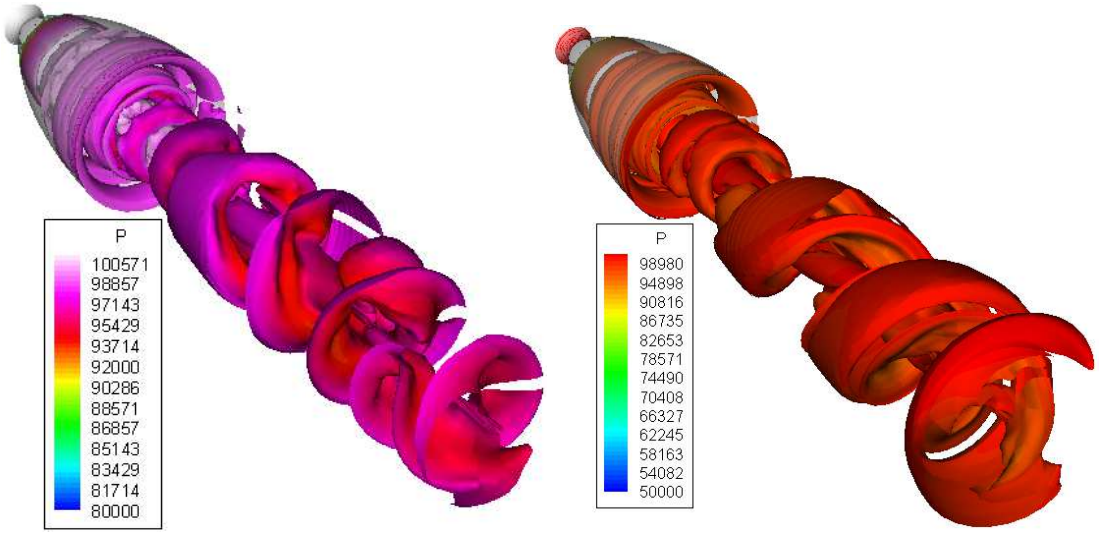

FIGURE 7.7 – Evolution of type of jet instabilities as a function of NPR : iso-surface of Q-criterion ($0.1 * U_t^2/D_e^2$) coloured with pressure (Pa) in the case of FSS configuration at (Left) T=$17.4 * L_d/U_t$ & (Right) $34.6 * L_d/U_t$ for NPR=15.5 and 19.0 (see also Fig. B.6-B.7 & B.12), respectively .

The random behaviour of these coherent structures near the nozzle exit is shown with the help of 2D slices of iso-pressure contours along with streamlines (see Fig. 7.8). Solid black lines indicate the sonic lines of the upper and lower shear layers of the annular supersonic jet. Flow across annular supersonic jet varies in time and causes distortion of the separated jets and their respective sonic lines. This asymmetric flow in the azimuthal direction is responsible for pressure variations in radial and circumferential direction and results in the asymmetric pressure distribution at the nozzle wall, which is responsible for the dangerous fluctuating loads.

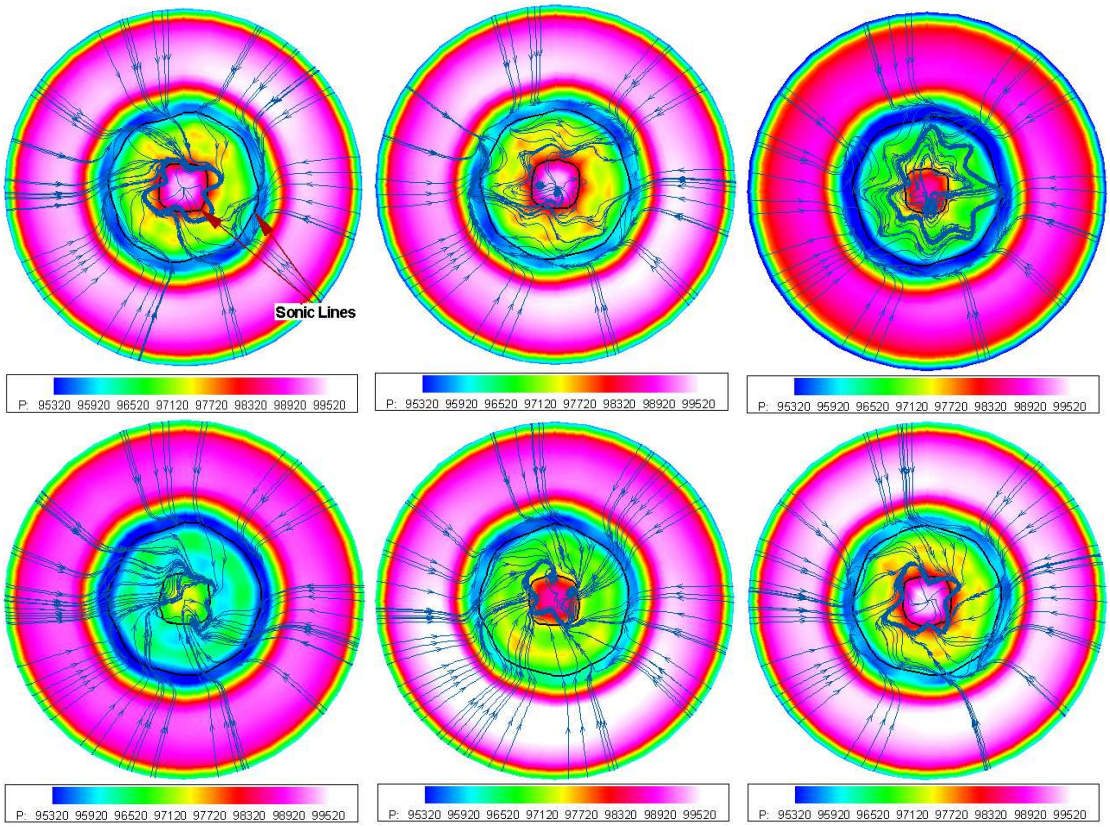

FIGURE 7.8 – Random behaviour of the flow structure at the nozzle exit (2D slice at nozzle exit) : iso-pressure contours (Pa), streamlines and sonic lines (solid black line) at T=0.4, 4.3, 8.7, 39.1, 43.5 & 47.8 $*L_d/U_t$ (Left to Right - Top to Bottom, respectively) : NPR=15.5 (see also Fig. B.8).

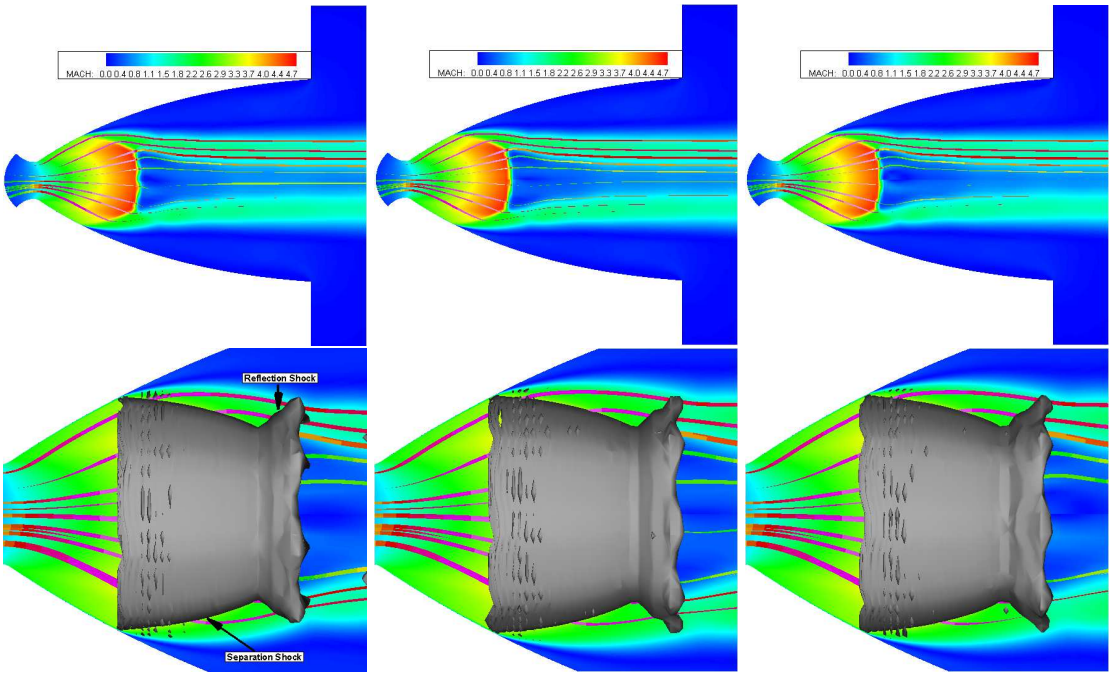

FIGURE 7.9 – (Top) Iso-contours of Mach number and streamlines & (Bottom) Zoom near the Mach reflection : iso-surface of shock function (separation line, separation shock and reflected shock) at T= 0.4, 4.3 & 8.7 $*L_d/U_t$, Left to Right, respectively : NPR=15.5 (see also Fig. B.9-B.10).

2D slices of iso-Mach contours and three dimensional iso-surfaces of the shock-function (f(x)=1 : shocks) inside the nozzle are given in Fig. 7.9 to highlight the flow behaviour near the separation line. In this flow configuration, the separation line is located relatively far upstream of the triple point. Thus the separated shear layer from the nozzle wall interacts with the reflected oblique shock. This interaction is highly unsteady and can be depicted from the wavy/uneven and random behaviour of the reflected shock (iso-shock surfaces), as shown in Fig. 7.9. This reflection shock, the separation shock and the Mack disk form a combined shock system. As a result, the shear layer and reflection shock interaction makes the whole shock system move. A similar type of wavy/uneven and unsteady behaviour can be observed at the foot of the separation shock, where the shock wave and boundary layer interaction takes place. This indicates the evolving azimuthal asymmetry of the separation line. It is worth mentioning that there is clear experimental evidence regarding the random and unsteady behaviour of the separation line in the azimuthal direction. The visualizations obtained by Nave and Coffey [98] for hot gas study show the presence of a conical shock type separation line in form of teepees, which seems to rotate circumferentially and to appear and disappear randomly because the separation line lies near to the nozzle exit. This observation was confirmed by images taken during the ground start-up phase of the engine SSME (see Fig. 3.15).

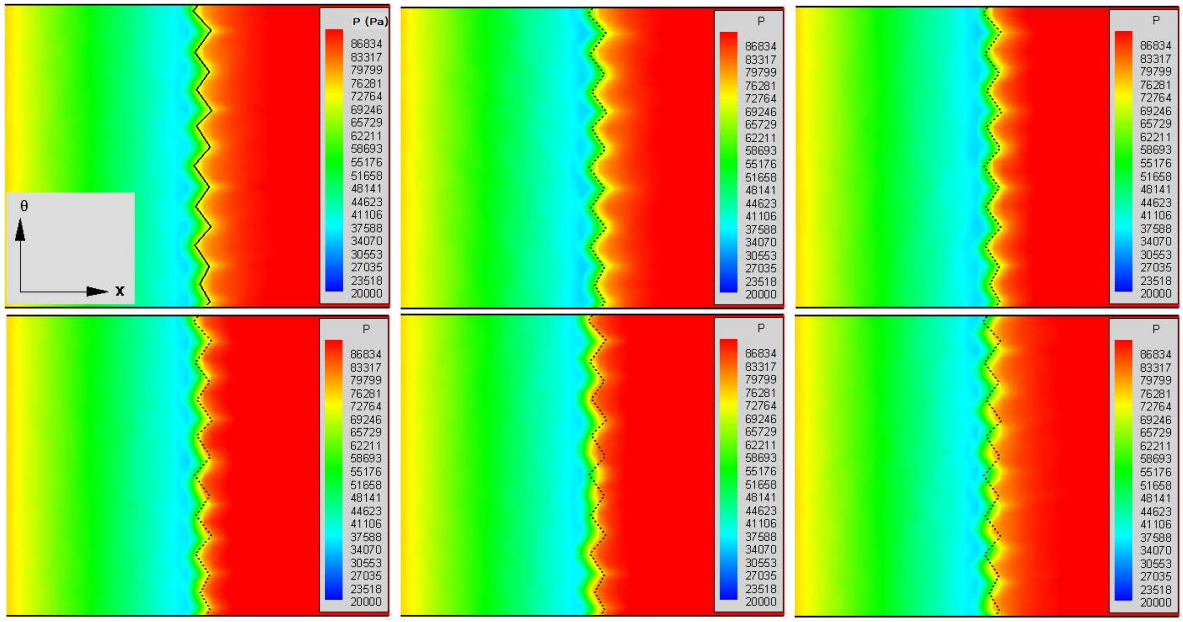

FIGURE 7.10 – Snapshots of iso-pressure (Pa) contours near the separation line along the nozzle wall, showing teepee like separation line at T=0.4, 8.7, 17.4, 26.1, 30.4 & 47.8 $*L_d/U_t$ (Left to Right - Top to Bottom, respectively) : NPR=15.5

The behaviour of conical shock shaped separation line is also numerically observed here from snapshots of iso-shock surfaces in Fig. 7.9. At this NPR, i.e. 15.5, the separation line location is far upstream of the nozzle exit, so that this conical type separation line can be observed all the time, and does not appear and disappear like in the aforementioned experimental observations in [98]. In order to visualize this separation line (at NPR=15.5) more clearly, a 2D slice of the nozzle wall pressure (axial (x) and azimuthal direction (θ)) is given in Fig. 7.10. The solid or dashed black line indicates the sketch of the separation line / teepees observed at the initial instant corresponding to Fig. 7.10 : Top-Left. We can notice that these teepees rotate

circumferentially in time. At various instants, completely opposite azimuthal and axial arrangement can be observed (see Fig. 7.10 at T=47.8*L_d/U_t). This indicates the unsteady and random behaviour of shock motion particularly in the azimuthal direction.

Since the formation of teepees is related to the location of the separation line, it varies as a function of NPR. Hence, the number of teepees at a particular NPR directly depends on the nozzle diameter at that very separation point location. The question arises to estimate whether this phenomenon also numerically depends on number of grid points in the azimuthal direction. At both NPR=15.5 and 19.0, the grid dependence in the azimuthal direction has been check by using two mesh configurations, i.e. with 72 & 144 point in the azimuthal direction. Figure 7.11 presents the numerical solution obtained by using mesh type CF, i.e. ((300*180)+(200*240))*144=14.7 million, with 144 grid points in the azimuthal direction. The mesh configuration contains 3.4 times the number of grid points used in the previous case, i.e. mesh type BE. In the case of FSS flow regime at NPR=15.5, the range of shock-excursion lies in between $x/L = 0.15 - 0.18$. The nozzle radius corresponding to these axial locations lies between $r = 30.7 - 33.9$ mm, that is $r/R_e = 0.41 - 0.45$. Finally the present grid configuration (CF) corresponding to this shock-excursion range gives the value of $\Delta z = 1.34 - 1.48$ mm. Figure 7.11, presents the separation line with the help of iso-pressure contour along the nozzle wall and illustrates the slight increase of the number of teepees obtained by comparison with the previous case (based on mesh type BE). The average wave length of these observed teepees, with the mesh type CF, is about 3.6 mm ($\frac{\lambda}{D} = 0.056$).

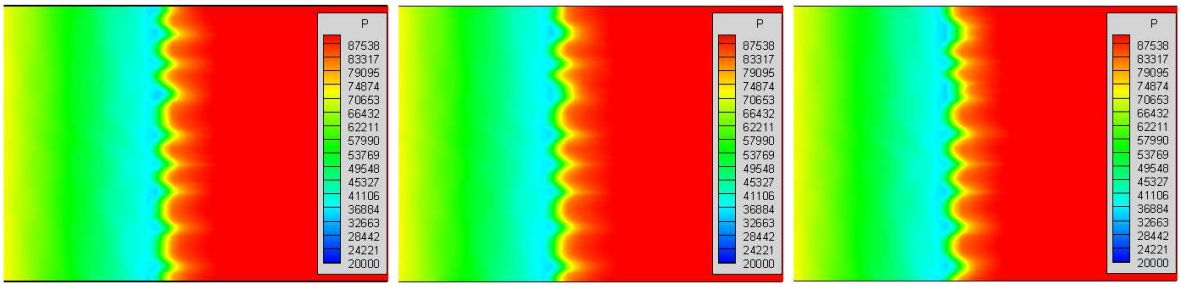

FIGURE 7.11 – Snapshots of iso-pressure (Pa) contours near the separation line nozzle wall with the evolution of time i.e. T=0.1, 1.0, & 2.6 *L_d/U_t : NPR=15.5, Mesh Type : (300*180+200*240)*144=14.7 Million

The numerical solution of the flow regime at NPR=19.0, presented in Fig. 7.12, is obtained with the grid configuration CF, i.e. 14.7 million ((300*180)+(200*240))*144), with 144 grid points in the azimuthal direction. In this case, the zone of the shock excursion ($x/L = 0.187 - 0.224$) and the corresponding nozzle radius ($r = 34.6 - 38.1$ mm) is slightly higher than in the case at NPR=15.5. However, the average wave length of the observed teepees is of the same order, i.e. about 3.5 mm ($\frac{\lambda}{D} = 0.048$). This suggests that the number of teepees increases both as a function of NPR and of the nozzle radius at which the flow separation takes place. This increase of the number of teepees (wavy separation line phenomenon) is directly linked with an increasing instability of the free shock-induced separated flow and of the resulting progressively increasing side-load activities.

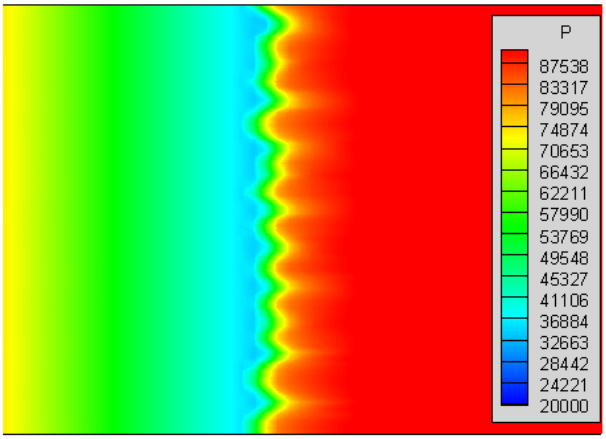

FIGURE 7.12 – Zoom of iso-pressure (Pa) contours near the separation line nozzle wall at T=1.2 $*L_d/U_t$ (Mesh Type : (300*180+200*240)*144=14.7 Million) : NPR=19.0

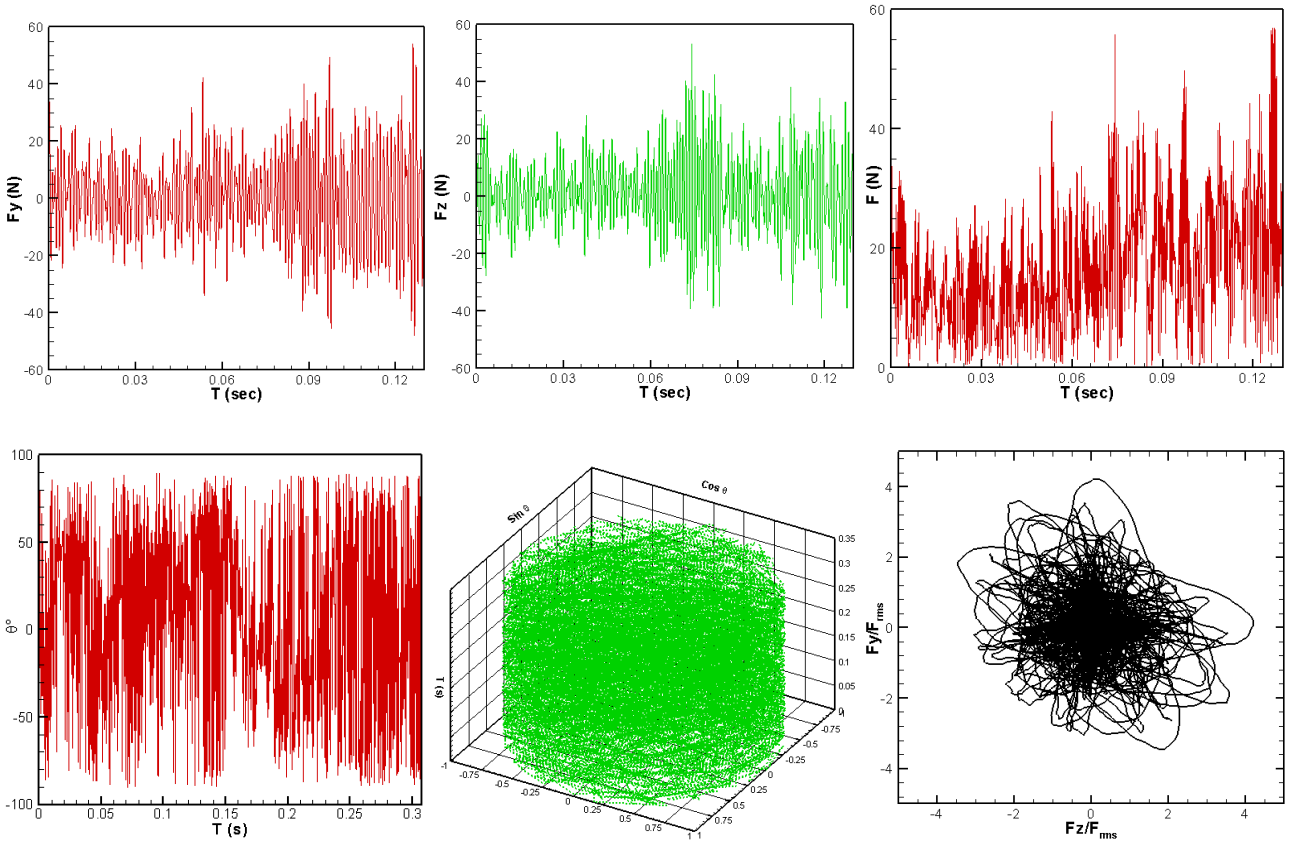

FIGURE 7.13 – Evolution of (Top) side-loads & (Bottom) its direction, Cosinus and Sinus of side-load direction : NPR=15.5, and its polar : NPR=19.0

The unsteady and three-dimensional pressure distribution on the inner wall of the nozzle induces unsteady asymmetrical loads. These loads can be obtained by integrating the unsteady wall pressure field on the nozzle extension during the calculation, and its components are given

as :

$$\begin{cases} F_y(t) = \int_0^L \int_0^{2\pi} p(x,\theta,t) r(x) \cos\theta \, d\theta \, dx \\ F_z(t) = \int_0^L \int_0^{2\pi} p(x,\theta,t) r(x) \sin\theta \, d\theta \, dx \end{cases}$$

The evolution of these computed lateral forces (and corresponding F_y and F_z components) for NPR=15.5 are given in Fig. 7.13, for a time period T≈0.13 s. We can notice a highly random behaviour of these side-loads. This behaviour can also be observed for NPR=19.0, see Annex B, Fig. B.13. However, the magnitude of these side-load activities is slightly higher than that at NPR=15.5. The computed RMS value of side-loads for these investigated NPR's, i.e. 5.0, 15.5 & 19.0, are 3, 12 & 19, respectively. The latter two are in fairly good agreement with the experimental data (see Fig. 6.4). However, the former one is slightly under-estimated, which could be due to a lack of time integration (i.e. 0.172 s only). The direction of these calculated side-loads for NPR=15.5 is given in Fig. 7.13 and shows a circular shape when we look at the evolution of sinus and cosinus part with respect of time. It indicates that this buffet load can be seen as a rotating vector uniformly distributed within the interval $[0, 2\pi]$ (i.e. no direction is privileged). This last result highlights the fact that the side-loads components are normally distributed.

Figure 7.13 : Bottom-Right, shows a typical polar plot of the calculated side-load components, $F_z(t)$ against $F_y(t)$, for NPR=19.0. One can notice the isotropic and random character of the fluctuating side loads. This side-load polar distribution is centered at zero (for an averaged axi-symmetrical flow, the side loads are absent). These side-load components F_y and F_z are in fact two independent random variables with zero mean and with the same variance. Thus, the side-loads have an isotropic behaviour. This isotropic and random character of the fluctuating side-loads is also observed in experiments (see Fig. 7.14.) and is numerically confirmed by Deck et al. [27].

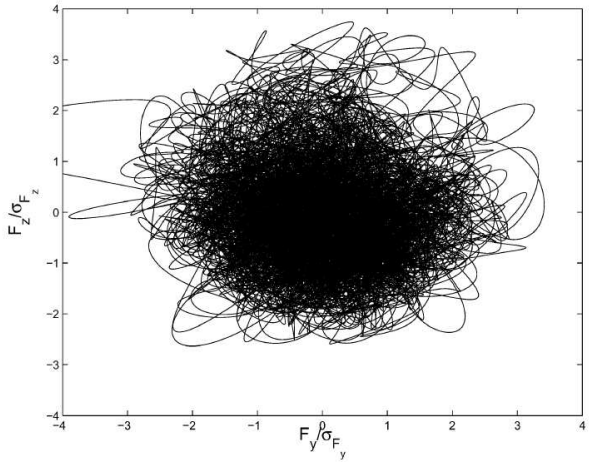

FIGURE 7.14 – Typical experimental polar plot of side-load activities (FSS : NPR=17.27) [27].

A statistical description is required in order to define the properties of magnitude and direction of the side-load activities caused by these random pressure fluctuations. The probability density function (PDF) of the computed side-loads is just considered. This computed side-force probability density function is compared with the Rayleigh distribution in Fig. 7.15. This indicates that the distribution of side-load amplitude follows a Rayleigh distribution (as suggested by Dumnov [40]). The obtained PDF of normally distributed side-load components could be

quite expected because the Rayleigh distribution is the particular case of a χ^2 distribution with two degrees of freedom, corresponding here to the side-load components. Figure 7.15 : Right, compares the computed PSD for the FSS regime with the experiments obtained at a slightly higher NPR (still corresponding to a FSS configuration [27]). The difference in the level of F_y and F_z components, for the case of simulation, is due to the lack of the time integration to obtain the statistical convergence for side-load activities. The present numerical results are in good agreement with the experiments and indicate that in this particular FSS regime the side loads are dominated by very low frequencies ($< 50Hz$). This aspect has also been observed for a truncated ideal contour (TIC) nozzle exhibiting only the FSS flow regime [58].

For each streamwise location, the flow has been expanded in Fourier modes in the azimuthal direction using the time samples. The PSD obtained in the azimuthal direction is given in Fig. 7.16 (only the initial 16 modes are shown).

$$p(x,\theta_j,t_n) = a_0(x_i,t_n) + \sum_{l=1}^{J/2-1} a_l(x_i,t_n)\cos(l\theta_j) + b_l(x_i,\theta_n)\sin(l\theta_j) \tag{7.1}$$

The time dependent coefficients $\mathbf{a}(x_i,t_n)$ and $\mathbf{b}(x_i,t_n)$ can be analyzed in time in order to determine the frequencies associated with each azimuthal mode along the nozzle wall. The results of this PSD analysis for the cosinus and sinus coefficients at NPR=15.5 are given in Annex B, Fig. B.3-B.5. Mode 0 corresponds to the axi-symmetric mode and departure from perfect axi-symmetry is analyzed by the expansion of the wall pressure field in azimuthal modes to check which mode contributing to side-load activities. In Fig. B.4-B.5, only 6 initial modes are shown and one can explicitly differentiate among them the dominant modes which contribute to the side-loads. One interesting point to note here is that all presented modes show some contribution in the separation line region. However, if we look in the region downstream of the separation line then only mode 1 is active in the whole separated region and is responsible for the side-load activities.

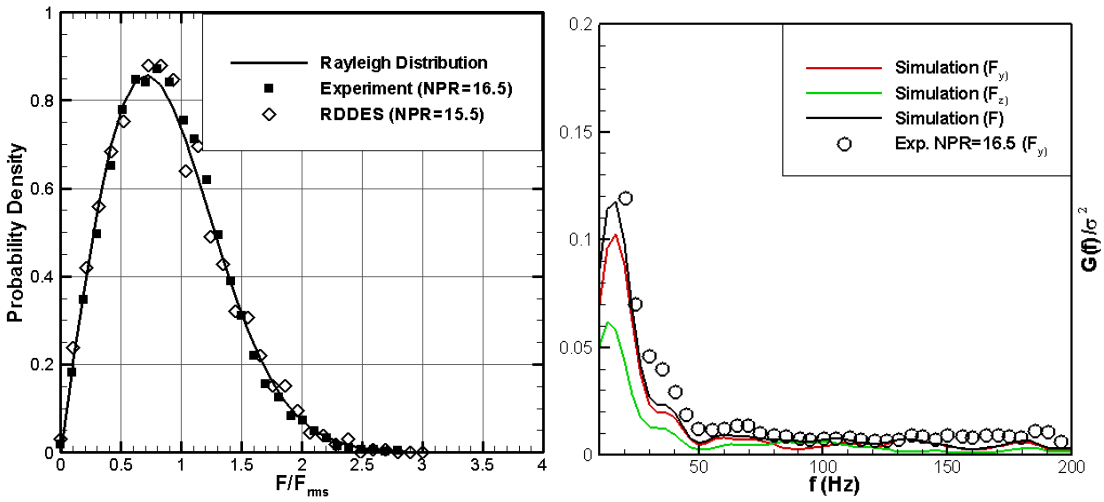

FIGURE 7.15 – PDF distribution (Left) and (PSD) spectra (Right) of side-loads : NPR=15.5

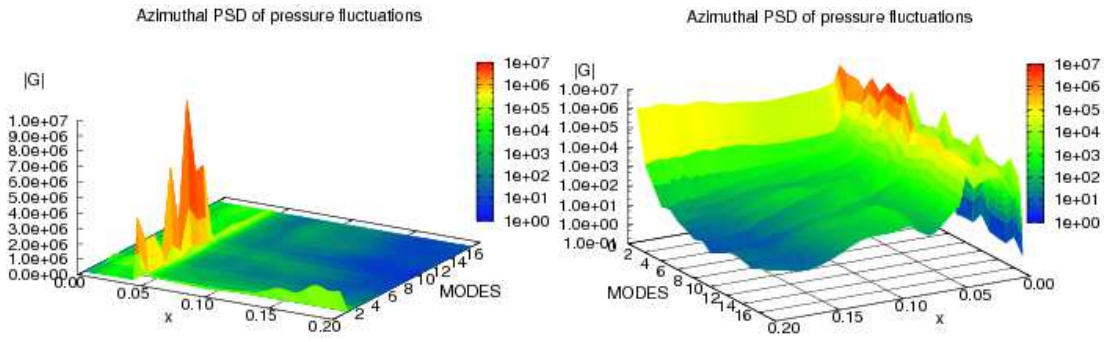

FIGURE 7.16 – Power spectral density of wall pressure fluctuations in the azimuthal direction along the nozzle wall : (Left) G(f), (Right) log(G(f)) : NPR=19.0

7.2 Epilogue

The FSS flow regime at three different NPR values has been investigated to analyse the flow unsteadiness and its increasing instability as a function of NPR. The wall pressure analysis has shown that the level of pressure fluctuations increases in the separation region (shock-excursion region). This increase in this level of fluctuations is due to the fact that the length of separation line increases with the nozzle radius accordingly, rather than to the direct effect of the pressure ratio. The flow-field analysis has revealed that a counter-current mixing layer forms between annular supersonic jet and the low speed flow around it. This separated shear layer interacts with the reflection shock. This interaction is highly unsteady and the resulting interaction surface (tip of the reflection shock) appears to be wavy and asymmetric in the azimuthal direction. Thus, the whole shock system moves. A careful examination of the wall pressure contours has shown the appearance of an asymmetric conical shock shaped (teepee) type separation line. This evolving asymmetry in the separation line seems to be related to unsteady and random interaction of separated shear layer with the oblique reflected shock. The number of teepees depends on nozzle radius, i.e. length of separation line, and directly linked with the increasing instability of the separated flow. The PSD analysis of the wall pressure field has shown that in the vicinity of the separation line, these pressure fluctuations are essentially dominated by low frequencies ($<$ 200 Hz), whose amplitude progressively increase with the increasing instability of the flow. This thus suggests that increase in RMS level of side-loads is mainly due to the increase of the low frequency contribution. Downstream of the shock excursion zone, the contribution of higher frequencies increases. However, the contribution of low frequencies ($<$ 1 kHz) remains significant. The computed side-loads increase as the instability of the flow grows and they are found to be in good agreement with the experiments. PSD analyses of pressure-field in the azimuthal direction along the nozzle wall also indicates that the side-load activities are mainly related to the first mode and are dominated by the low frequencies $<$50 Hz.

Chapitre 8

Towards Restricted Shock-Induced Separated Flow Regime

This chapter repots the analysis of the flow during the transition process from FSS to RSS configuration and the unsteady behaviour of the flow in restricted shock separation flow regime.

8.1 Flow Transition From (FSS $\rightarrow$ RSS)

In chapter 6, axi-symmetric URANS calculations performed on a wide range of NPR have shown that during the start-up process, the flow transition from FSS to RSS occurs at NPR=24.0, which is in agreement with the experimental data [101] for the case of LEATOC nozzle. It is important to recall that these aforementioned transition processes were observed by using stabilized inflow stagnation conditions, i.e. step by step increase of the NPR value. Experimental measurements [101] show a sudden decrease of the side-load activities during the forward transition (FSS to RSS) process. Following certain researchers ([54] & [106]), this transition process from FSS to RSS could be asymmetric (appearance of both FSS and RSS flow regimes at the same instant) in the azimuthal direction, which could be the main cause of high level of side-load activity [54], [105] & [106]. 3D simulations have been performed to ascertain this behaviour of side-load activities during the forward transition (FSS $\rightarrow$ RSS) process in LEATOC nozzle. The present simulations correspond to a low variation rate of the nozzle pressure ratio in the NPR range 10.0-25.0. The numerical parameters used to carry out this analysis are given in Table 8.1.

Simulation Parameters	
Mesh Type	BE
Number of grid points	$\approx$ 4.32 million
$\Delta\, T_{save}$	10 μ s
Number of samples	10500
Integration time	0.105 s
Physical sampling frequency	100 KHz

TABLE 8.1 – Simulation parameters for 3D simulation of FSS/RSS transition : NPR=10.0-25.0

The study of the flow transition FSS/RSS and RSS/FSS based on axi-symmetric calculations

has shown that the time duration of the transition process lies in the range 5-6.48 ms. Assuming that this time period would not change significantly for this new 3D simulation of the forward transition (FSS/RSS) process, the NPR increase rate has to be set to $d(p_i/p_a)/dt \approx 143s^{-1}$, which correspond to time periods at constant NPR equal to 7 ms. The transition process can thus be easily predicted whatever the NPR at which it occurs. Figure 8.1 (Left), presents time evolution of the computed RMS values of side-loads during this transition process. The solid red line indicates the FSS flow regime up to its limiting case, where the internal shock interacts with the Mach and makes "FTQP" (see Fig. 8.2).

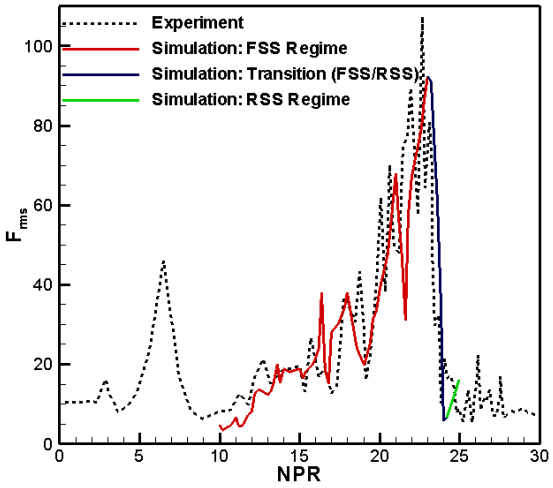

FIGURE 8.1 – Evolution of side-loads during the start-up process of LEATOC nozzle : Transition (FSS to RSS) regime with ramp increase in the NPR (P_0/P_a) in the range of 10-25.

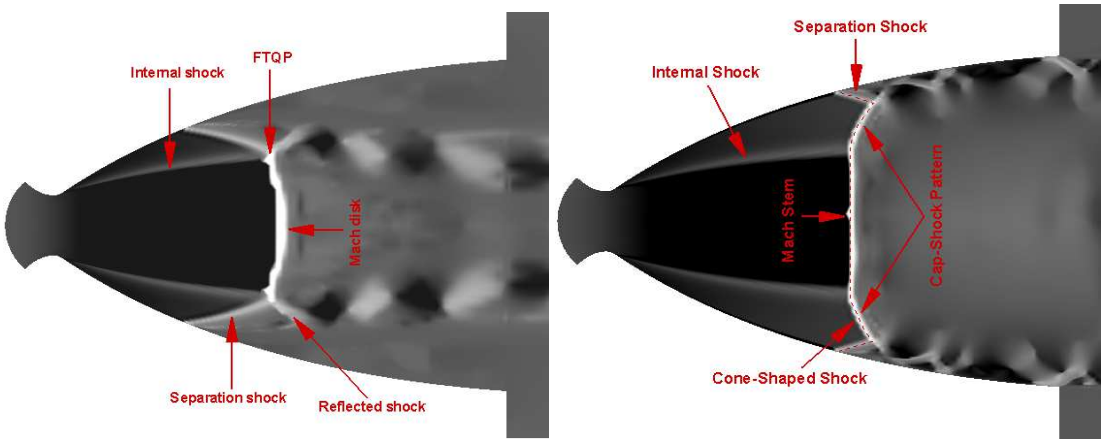

FIGURE 8.2 – (Left) Iso-contours of shock function at NPR=24.0 (T=0.096 s), FSS : flow transition quadruple point ; (Right) RSS flow regime at NPR=24.0.

The actual transition process is highlighted by the solid blue line and finally, the RSS flow regime corresponds to the green line. As expected, a high level of side-loads is detected when the NPR approaches to the CNPR and is followed by a sudden decrease. This phenomenon suggests that FSS/RSS transition is a process which starts from a strongly three dimensional unsteady flow and finishes in a much more quiet and less three dimensional state. The time

duration calculated for this flow transition is around 6 ms, which is of the same order of the value previously obtained in the case of axi-symmetric calculations. The global trend of the predicted time-evolution of side-loads is in agreement with experimental data, despite of the fact that the rate of change of NPR in the case of experiments of quite fast, i.e. $d(p_i/p_a)/dt \approx 32s^{-1}$ [101]. In fact, several distinct peaks of side-loads can be distinguished before reaching the actual transition phase. These predicted and experimental peaks do not perfectly coincide. However, their amplitude remains bounded in the same range. The exact level of unstationary reached at a given NPR might be strongly depend on the exact transition history of the inlet stagnation pressure. Accordingly, the results obtained appear to be rather well representative.

An important point to stress is that no sign of flow dissymmetry is observed during this reproduced transient transition (FSS to RSS) process. Thus, the increasing instability of flow in FSS regime is found to be the main source of increasing side-load activities before the FSS to RSS transition. This is in agreement with the experiments [101]. Of course, further numerical investigations would be required in order to ascertain this observation for different nozzle contours. In addition, this transient process started from NPR=10.0, which could be a possible factor of stabilization of the flow regime at the initial stages of its development.

8.2 Restricted Shock Separation (RSS)

A sudden decrease in the side-load activities is observed when the regime switches from FSS to RSS configuration (see Fig. 8.1). According to the side-load measurements made by Nguyen et al. [101], in LEATOC nozzle, two peaks are present when the flow is governed by RSS configuration (see Fig. 6.3 & 6.4). In order to analyse the physical mechanisms leading to the appearance of these side-loads activities, five different locations on the side-load chart (Fig. 6.4) have been selected to perform the numerical investigations presented in the following sections.

8.2.1 Simulation Parameters

Five NPR's (i.e. 25.5, 30.0, 38.0, 41.6 & 46) are selected on a wide range of side-load activities chart, as shown in Fig. 6.4. The objective is to understand the unsteady behaviour of RSS flow at different NPR levels which include in particular the NPR values corresponding to these two peaks in the side-load activities. The simulations parameters used to investigate these RSS flow regimes in LEATOC nozzle at above mentioned NPR's are given in Table. 8.2.

Simulation Parameters					
NPR	25.5	30.0	38.0	41.6	46.0
Mesh Type	BE	BE	BE	BE	BE
Number of grid points (million)	≈ 4.32	4.32	4.32	4.32	4.32
ΔT_{save} (μ s)	50	50	50	50	50
Number of samples	13000	8200	12800	15800	14000
Integration time (s)	0.65	0.41	0.64	0.79	0.7
Physical sampling frequency (KHz)	20	20	20	20	20
Range of min. possible frequency (Hz)	1.5	2.5	1.5	1.2	1.4
Blocks used for PSD	52	40	64	62	56

TABLE 8.2 – Simulation parameters for NPR=25.5, 30.0, 38.0, 41.6 & 46.0

8.2.2 Classification of RSS flow Regimes

The restricted shock separation is a complex flow regime and is characterized by a special cap-shock pattern along with a trapped vortex downstream of it along the nozzle axis. A small recirculation zone is also trapped due to the subsequent reattachment of the supersonic jet to the nozzle wall, see Fig. 8.3. The annular supersonic flow is subjected to expansion and compression waves reflected between the nozzle wall and the mixing layer separating the high speed region from the central trapped vortex, as shown in Fig. 8.3. These reflected waves give an oscillatory wall pressure distribution (see Fig. 8.4), which can lead in some cases to a secondary separation. This secondary separation bubble can be clearly visualized in Fig. 8.4, which shows the zoom of iso-Mach contours near the nozzle exit. The wall pressure distribution plotted against iso-shock contours indicates that the increase in wall pressure is related to the presence of compression shocks, while the plateau and decrease of pressure level between these shocks correspond to the presence of recirculation zones and expansion waves, respectively.

This particular RSS flow regime at NPR=38.0 still yields a secondary separation bubble close to the nozzle exit. Its unsteady behaviour may be related to its repeated opening to the ambient atmosphere. This suggests that RSS configurations which could be observed below this NPR can be classified into distinct flow regimes, following whether or not it exhibits two recirculation zones (primary and secondary) attached to the nozzle wall all the time. Above this NPR, the flow regime only contains a primary recirculation zone. We can further distinguish one flow regime for which this primary recirculation zone always remains inside the nozzle wall from another one which displays periodic opening of this recirculation zone to the ambient atmosphere. The latter RSS flow regime is commonly known as end-effects and is shown in Fig. 8.5. Therefore, the aforementioned flow regimes globally remain in RSS configuration. However, each regime behaves differently depending upon the appearance of recirculation zone near to the nozzle exit. In a much simple way, we may categorize them into three regimes, i.e.

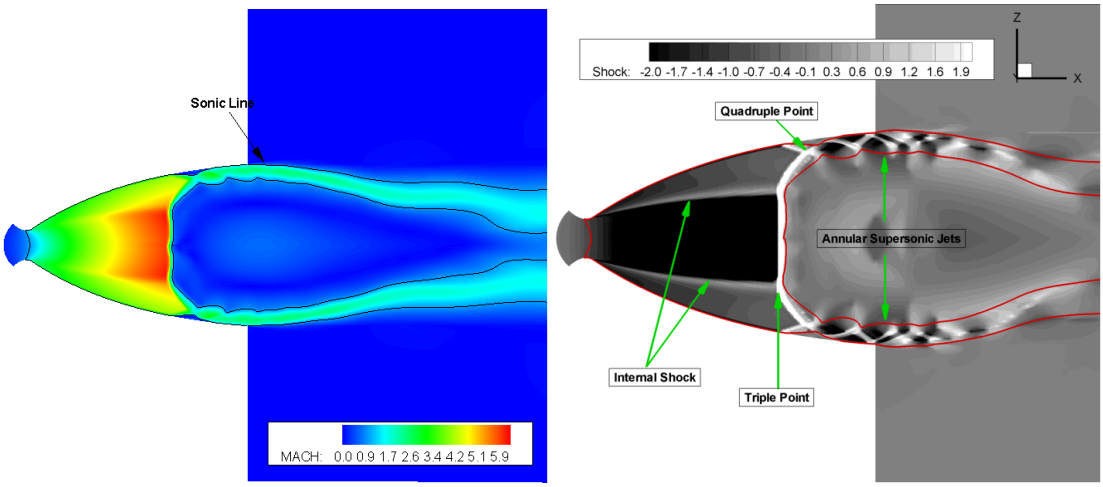

FIGURE 8.3 – (Left) Iso-Mach & (Right) shock contours of RSS flow regime at NPR=38.0, 2D slices at θ=0° & 180°.

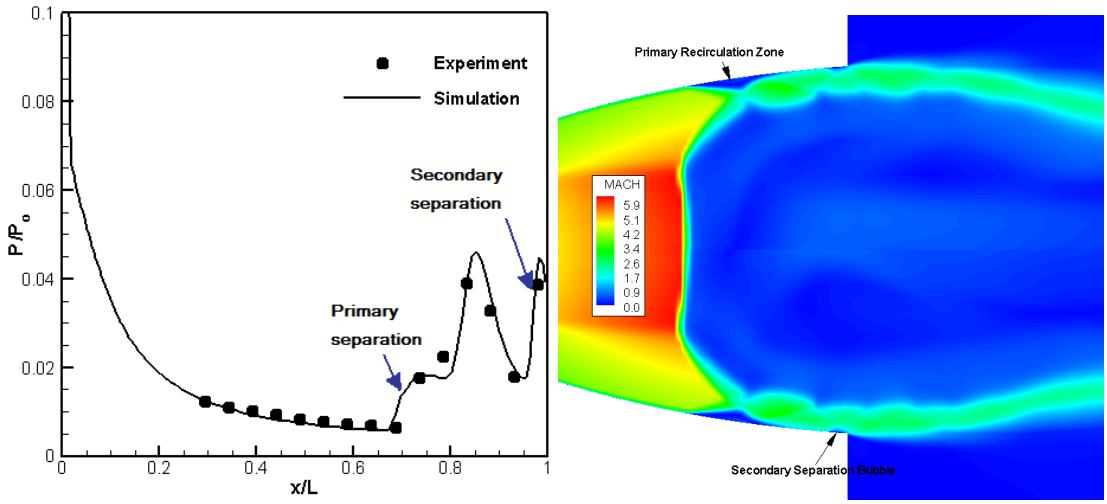

FIGURE 8.4 – (Left) Evolution of mean wall pressure & (Right) Zoom of iso-Mach contours near the nozzle exit at NPR=38.0, 2D slices at θ=0° & 180°.

– RSS flow regime without any opening of separation bubble/recirculation zone to the atmosphere, such as NPR=25.5, 30.0 and 41.6, which are considered for the present study.
– Flow regime, such as for NPR=38.0, for which a secondary separation bubble is close to the nozzle exit and is repeatedly evacuated to the ambient atmosphere. For this case, the primary recirculation zone remains attached inside the nozzle wall.
– End-effect flow regime, which is characterized by the quasi-periodic opening of the primary recirculation zone to the atmosphere. Here, we have selected the case at NPR=46.0 to reproduce this end-effect flow regime.

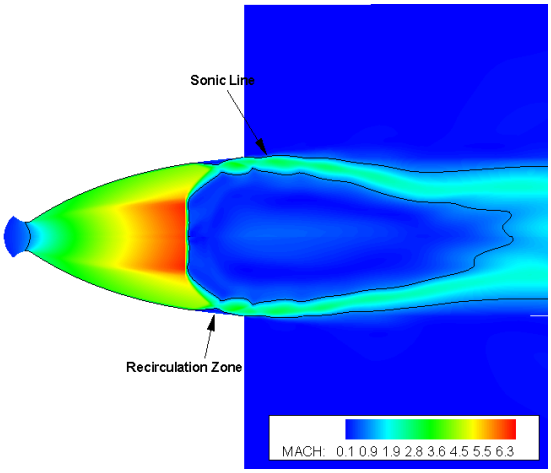

FIGURE 8.5 – End-effect flow regime at NPR=46.0 : iso-Mach contours, 2D slices at θ=0° & 180°.

8.2.3 Flow- and Wall Pressure-field Analysis

The distribution of mean pressure along the nozzle wall in the RSS flow regime is fairly complicated due to the reattachment of the supersonic jet. The adverse pressure gradient causes the boundary layer separation and the subsequent formation of the separation shock causes a sudden increase of the wall pressure. When the separated supersonic jet reattaches back to the nozzle wall, it induces a pressure increase even higher than the ambient pressure. Figure. 8.6 shows the computed wall pressure distributions for the five NPR and the available experimental results. The first two NPR values correspond to wall pressure distributions showing a second pressure peak corresponding to the impingement on the wall of a shock resulting from the reflexion of expansion waves on the nearly isobaric boundary separating the annular supersonic jet from the trapped vortex. The intermediate case at NPR=38 corresponds to a limit situation where the second peak occurs near the nozzle lip and the case at higher NPR=46.0 value shows only one peak, which occurs at position close to the nozzle exit.

Figure. 8.6 shows the computed RMS wall pressure fluctuations and the comparison with the available experimental results. These distributions are characterized by several peaks which correspond fairly well to regions of high absolute streamwise gradient on the mean wall pressure distribution.

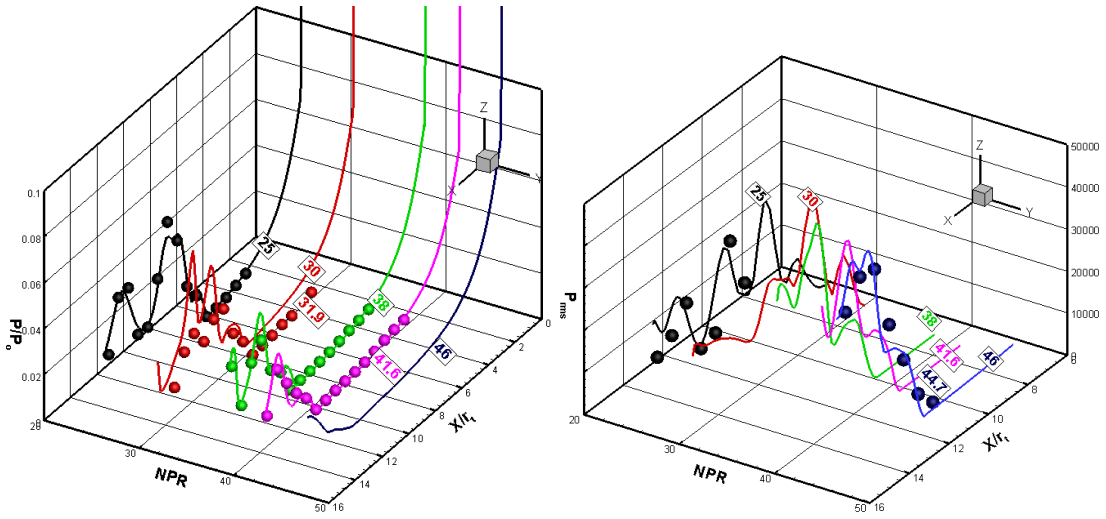

FIGURE 8.6 – (Left) Evolution of non-dimensionalized mean wall pressure (Right) and RMS wall pressure fluctuations (Pa) along nozzle axis •, Experiments & –, Simulations ; P_o=stagnation/chamber pressure, r_t(throat radius)=0.01362 m.

In order to analyse the distribution of pressure fluctuations along the nozzle for these RSS flow regimes, let us first consider the case of NPR=25.5, which exhibits both primary and secondary recirculation bubbles and three different shock-wave / boundary layer interaction zones. Mean wall pressure distribution is reproduced for this case and is annotated by the key elements corresponding to the flow structure.

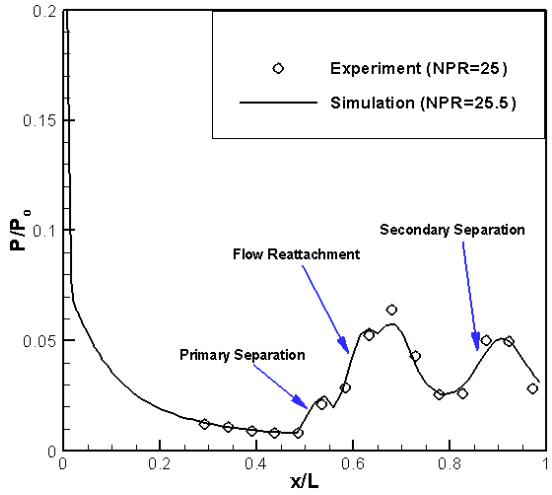

FIGURE 8.7 – Evolution of mean wall pressure along the nozzle axis at NPR=25.5, L(length of the divergent part=0.204 m).

Figure 8.8, presents the time history of the pressure fluctuation signals at different axial locations along the nozzle wall. Time is non-dimensionalized with the throat velocity (U_t) and the length of the computational domain (L_d). For the sake of clarity only the range of pressure signal history $T/(L_d/U_t)$=3 – 21 is reported here against the pressure fluctuation dimensionalized by the atmospheric pressure. The pressure fluctuations at different axial locations along

the nozzle wall, yield distinct characteristics depending upon their correspondence to the shock excursion regions, the attached flow upstream of it or to the recirculation zone.

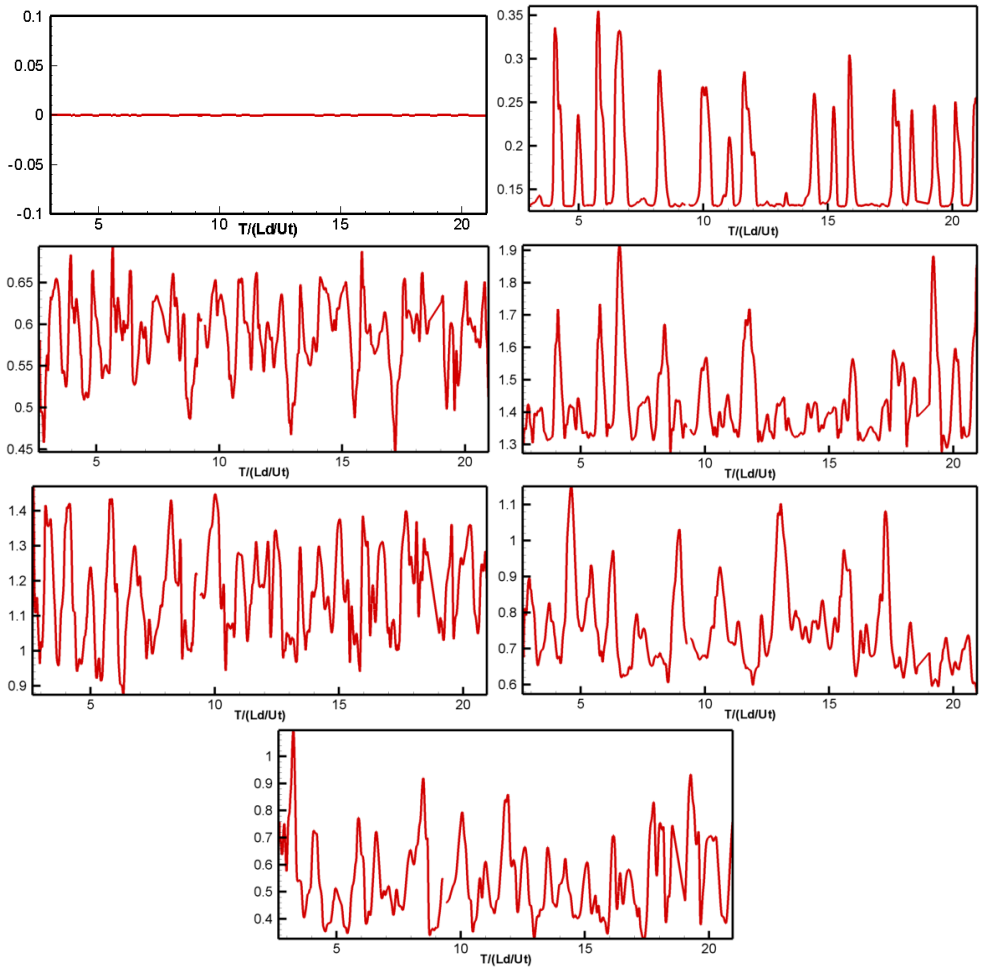

FIGURE 8.8 – Time history of pressure fluctuations ($P^{'}$(Pa)) along nozzle wall at x/L=0.44, 0.48, 0.53, 0.58, 0.68, 0.78 & 0.88, NPR=25.5.

In the attached zone (x/L=0.44), no significant pressure fluctuations are observed. The station x/L=0.48 is located at the beginning of the shock / wave boundary layer interaction zone. The unsteady separation shock randomly moves upstream, giving sudden increases of wall pressure superimposed on the quiet basic level corresponding to undisturbed nozzle flow. The positive spikes show the intermittency time of the separation shock presence in this quiet attached region. These pressure signals yield a more random behaviour when the separation line is nearly reached and in the recirculation region (x/L=0.53). Near the reattachment region, where the interaction of the viscous region and the reattachment shock takes place, the pressure signals indicate a behaviour similar to the one observed in the primary interaction (x/L=0.48), with distinct positive spikes. The only difference is that, these spikes now occur intermittently in addition to basic random signals found in the recirculation zone. Downstream of this secondary interaction, the pressure signal seem to be more random due to the successive interaction of shock and expansion waves in the annular supersonic jet attached to the nozzle wall (x/L=0.68). Interestingly, at x/L=0.78, which lies in the third interaction zone (before the secondary separation location) the same intermittent behaviour of pressure signals is observed. In this interaction

case, the level of upstream random pressure signals is relatively high and the presence of positive spikes seems to be less dominant as by comparison with the previous cases, x/L=0.48 & 0.58, respectively.

The probability density function of these pressure signals at different x/L locations is compared with the available experimental data in Fig. 8.9. The first point (x/L=0.68), which is located downstream of the flow reattachment, seems to have a quasi symmetric behaviour. The presence of positive peak in the PDF distribution for the downstream location (x/L=0.73). This location (x/L=0.73), corresponds to the decrease (negative pressure gradient) of the mean wall pressure caused by the presence of expansion fan. The locations x/L=0.78 & 0.83 are in the intermittent region of the third interaction zone, i.e. between the secondary separation shock and the attached annular supersonic jet. The probability density distributions in the intermittent region are highly skewed and indicate bimodal type distributions, which is a characteristic feature of an intermittent signal [35]. The wall pressure alternates between two different states, i.e. a state of basic fluctuations and a state of turbulent flow downstream of a relative strong shock-wave, spending a relative short time near the mean value. Thus there exist two maxima, positive and negative, in the probability distribution curves. In the evolution of the mean wall pressure, the last two x/L locations are expected to yield a statistical behaviour similar to the one observed at the locations x/L=0.73 & 0.83, because they are all located in the region of adverse pressure gradient (see Fig. 8.7). However, these last two axial locations (x/L=0.93 & 0.98) show a relatively low intensity and a significant shift of PDF on the negative side. This noticeable behaviour of PDF is in agreement with the experimental observations and arguments made by Dolling and Or [35], on the recorded pressure signals in a compression ramp flow configuration.

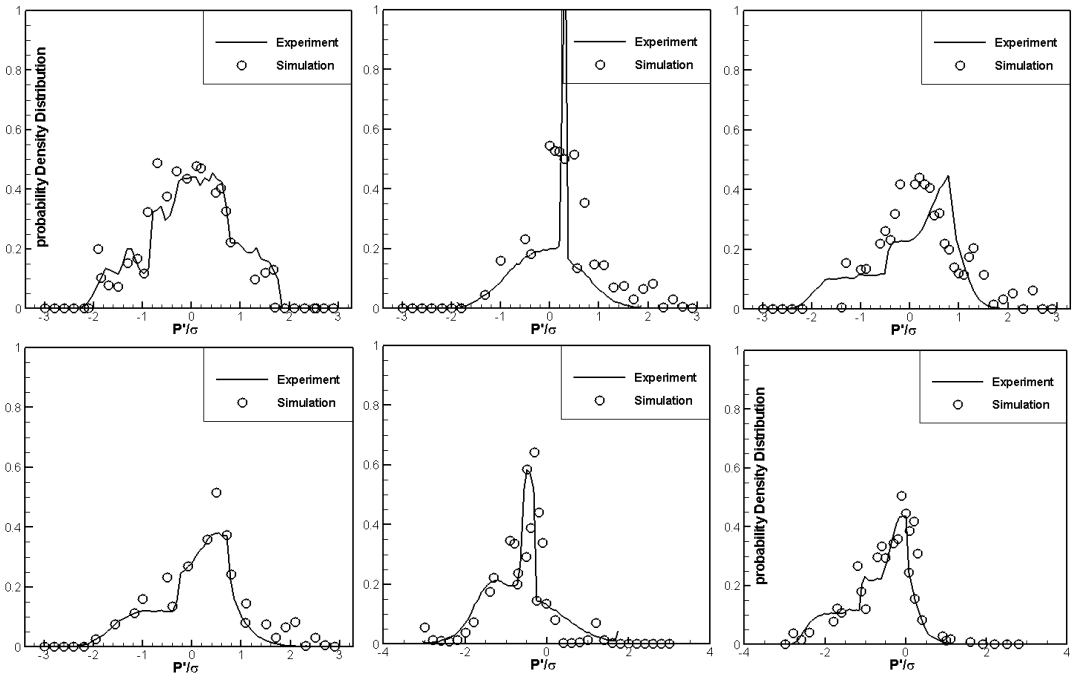

FIGURE 8.9 – Probability density function of pressure fluctuations (Left to Right - Top to Bottom) at x/L = 0.68, 0.73, 0.78, 0.83, 0.93 & 0.98, NPR=25.5.

The two point correlation $C(x_1, x_2)$ between these pressure fluctuations is given in Fig. 8.10 : Left. This map (for NPR=25.5) appears fairly complex but the important point is that, we have

large absolute correlations with several change of sign between separation at $x/L \simeq 0.5$ and at the nozzle exit. This two points correlation is also computed for NPR=38.0, which is an intermediate level for the investigated wall pressure distribution. This correlation map should be analysed in perspective of Fig. 8.22 : Top-Left, which shows a sequence of snapshots of the wall pressure distributions. Wall pressure fluctuations appear to result essentially from a fore and aft movement of the mean wall pressure distribution. This fore and aft movement of the pressure distribution generates positive or negative fluctuations with respect to the mean wall according to the sign of the local mean streamwise pressure gradient. This explains the change of sign in the correlation map in Fig. 8.10 : Right. We observe a weak correlation between the attached boundary layer and its interaction with the separation shock. Conversely, a high positive correlation is found between $0.68 \leq$ x/L < 0.9. In the present numerical investigations, this fore and aft movement is observed for the five NPR's. However, as shown by Fig. 8.11, the amplitude in the streamwise direction depends upon the NPR and the largest amplitude are observed at NPR=38.0 and NPR=46.0 in agreement with the peaks of side loads shown at the same NPR on Fig. 6.4.

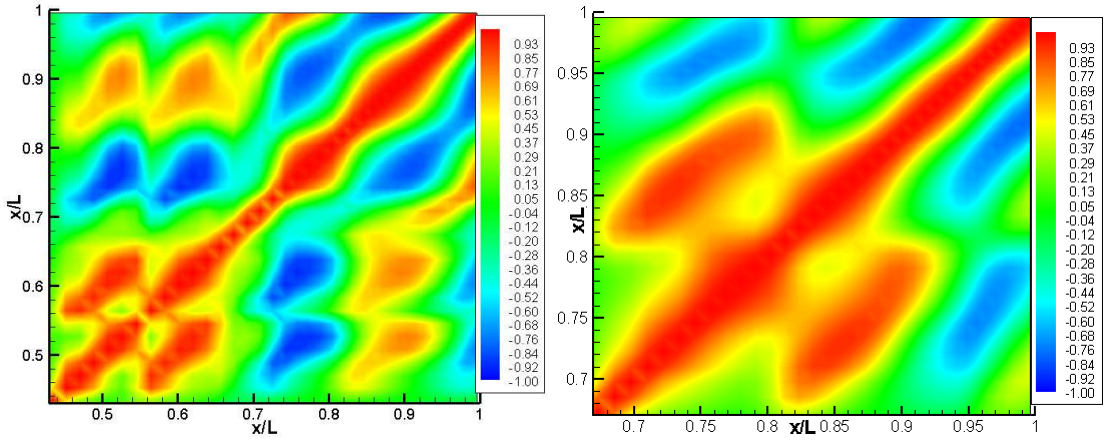

FIGURE 8.10 – Two point correlation map of pressure fluctuations along the nozzle wall at NPR= (Left) 25.5 & (Right) 38.0.

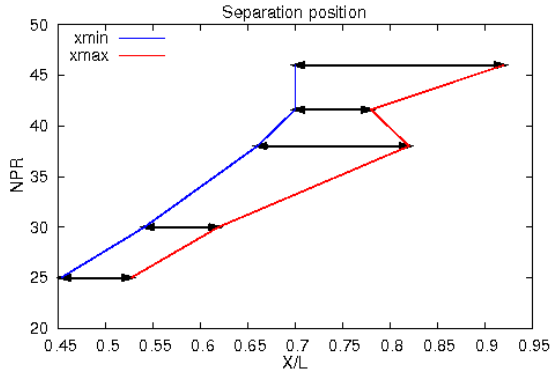

FIGURE 8.11 – Evolution of the minimum and maximum abscissa of separation with respect to NPR.

The distinct behaviour of RSS flow regimes for these investigated NPR's is more clearly

illustrated in Figure. 8.11. A flow regime which does not exhibit any recirculation zone near the nozzle exit leads to a relatively low level of amplitude in the fore and aft movement of the shock system in the streamwise direction. This makes them different from other two RSS regimes, i.e. at NPR=38.0 and 46.0, which display a relatively high level of amplitude, respectively.

Further analyses are now presented to better characterize the specific features of the unsteady behaviour corresponding to these flow regimes discussed above.

8.2.3.1 First Case, NPR=25.5, 30.0 and 41.6

The dimensionless analysis of LEATOC nozzle in the Chapter (6) suggests that the increase in NPR level increases the Reynolds number of the flow. For NPR=25.5, the relative Mach number of the shear layers around the supersonic jet at $x = 0.34$m (as in Fig. 8.14) is 0.96 & 1.26, respectively. At this M_r three dimensional disturbances are dominant, as it can be seen from iso-surface shown with the help of Q-criterion coloured with pressure (see Fig. 8.12). This is in agreement with the numerical observation made by Leep et al. [74]. The pressure distribution in the large trapped vortex is not constant and varies along the axial and radial directions. The unsteady and three dimensional shear layer on the inner side of the annular jet interacts with this trapped vortex. Therefore, the recirculation zone becomes three dimensional. This recirculation zone is subsonic and these induced pressure pulsations move upstream towards the cap-shock pattern and results in a change of the pressure level, downstream of the Mach disk (central part of the cap-shock).

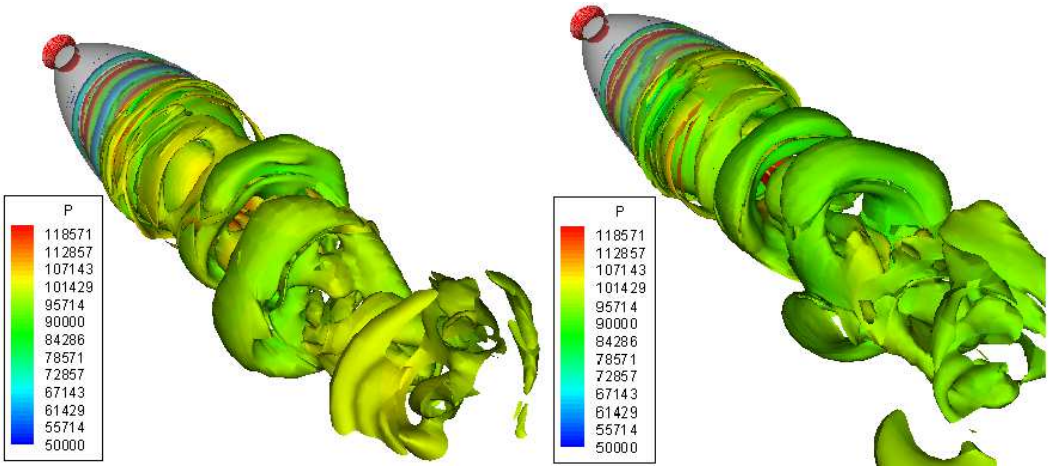

FIGURE 8.12 – Iso-surface of Q-criterion ($0.1 * U_t^2/D_e^2$) coloured with pressure (NPR=25.5) at T=$44.3 * L_d/U_t$ & $44.8 * L_d/U_t$, also see Fig. C.2.

It is worth to mention that the axial position of the Mach disk is adjusted according to the pressure jump across it. Let x_0 be the initial position of Mach disk for pressure jump $\Delta p_0(p_2/p_1)$ across it, as in Fig. 8.13. Now assume that, p_a and p_b are the change in the pressure that appear downstream of the Mach disk, such that $p_b > p_2$ and $p_a < p_2$. This means that among them pressure jump $\Delta p_b > \Delta p_o$, i.e. p_a/p_1 and $\Delta p_a < \Delta p_o$, i.e. p_a/p_1. As a result, the Mach disk moves upstream and downstream for Δp_b & Δp_a, respectively, as illustrated in Fig. 8.13.

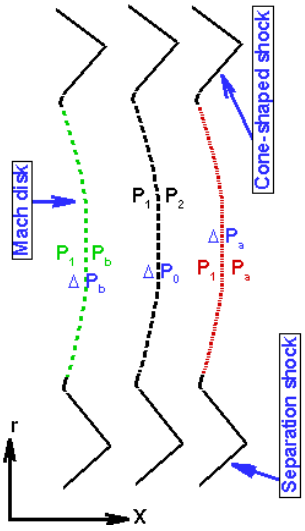

FIGURE 8.13 – Axial position of cap-shock pattern w.r.t pressure jump across it.

The upstream propagation of pressure pulsations in the trapped vortex causes the change in the initial pressure distribution. This change in pressure distribution is not symmetric. The axial position of Mach disk is thus adjusted with the pressure jump accordingly, and symmetry of the cap-shock pattern breaks-down, as shown in Fig. 8.14 : Right.

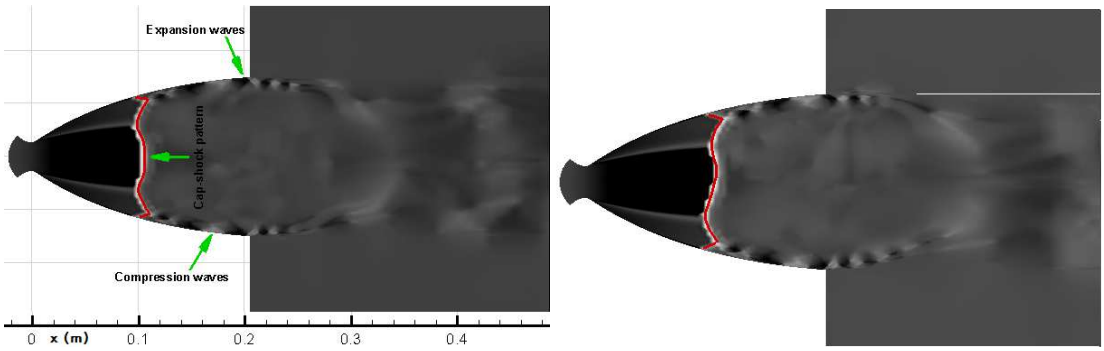

FIGURE 8.14 – Iso-contours of shock-function for NPR=25.5 at T=5.1&44.3$*L_d/U_t$, indicating "tilting" of cap-shock pattern, 2D slices at θ=0° & 180°.

This "tilting" effect of the cap-shock pattern (break of symmetry across nozzle axis) is much more enhanced in the case of NPR=38 and 46.0, which thus behave differently in comparison to present RSS configuration. As a consequence of this tilting effect of this cap-shock system, the separation line and the corresponding axial locations of compression and expansion waves become asymmetric in the azimuthal direction. This evolving asymmetry of the flow structures can be observed by looking at the wall pressure distribution in the azimuthal direction.

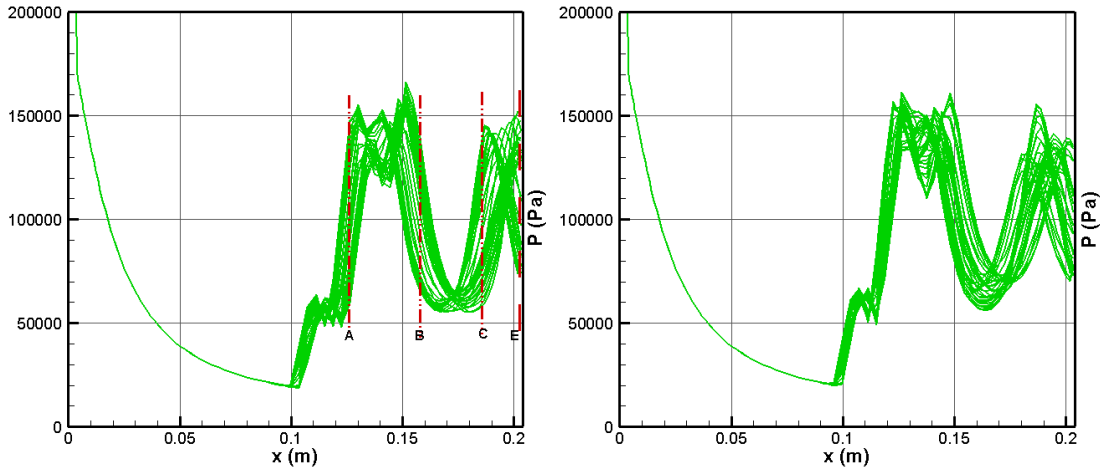

FIGURE 8.15 – Wall pressure distribution for all positions in azimuthal direction along the nozzle axis (NPR=25.5) at T=44.3&44.8 $*L_d/U_t$, respectively, also see Fig. C.3.

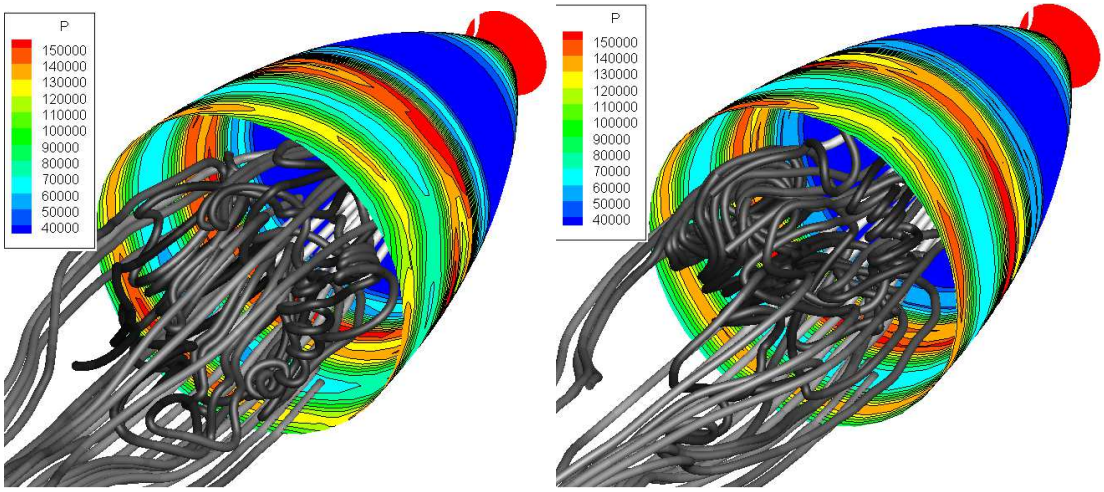

FIGURE 8.16 – Iso-pressure contours/lines on nozzle wall and streamlines (NPR=25.5) at T=44.8 & 47.4 $*L_d/U_t$, respectively, see also Fig. C.4.

Figure 8.15, presents the evolution of wall pressure along the nozzle axis for all computed positions in the azimuthal direction, which seems highly distorted. Moreover, these plots indicate that this departure from symmetry is more pronounced in the reattachment region and downstream of it, than in the separation line. This can also be noticed from the iso-pressure contours on the nozzle wall and the corresponding highly three dimensional trapped vortex (with the help of streamlines), see Fig. 8.16. Now let us take a look at the pressure distribution at nozzle exit, which indicate to high pressure jump (see line E in Fig. 8.15) in the azimuthal direction. For certain azimuthal positions, the pressure level decreases below the ambient pressure and at some locations it is higher. This increase and decrease in pressure level suggest the

presence of shock and expansion waves, respectively, in the azimuthal direction at the nozzle exit. Furthermore, this pressure jump (across ambient conditions) in the azimuthal direction can also be visualized from iso-pressure contours on a slice of the nozzle exit plane, see Fig. 8.17. For the sake of clarity, the pressure contours are kept in the range of 80000-150000 Pa. A highly asymmetric pressure distribution is observerable at the nozzle exit. It is worth mentioning that this evolving asymmetry in not only observed at the nozzle exit, but is also noticeable for axial positions corresponding to line A, B and C in Fig. 8.15.

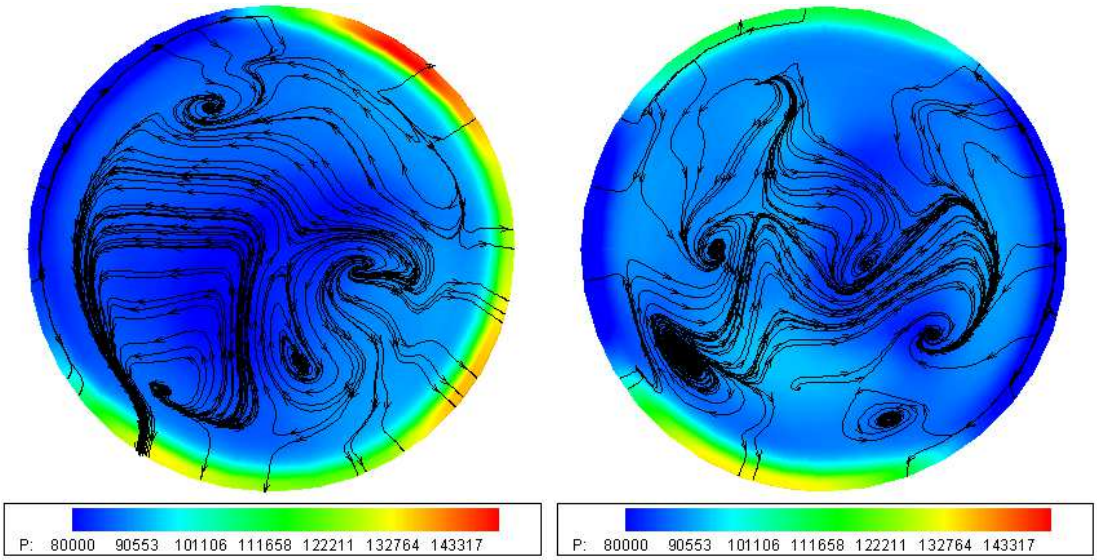

FIGURE 8.17 – 2D slice at nozzle exit : iso-pressure contours and streamlines (NPR=25.5) at T=44.3&44.8 $*L_d/U_t$, respectively, see also Fig. C.5.

A spectral analysis of computed pressure signals along the nozzle wall is shown in Fig. 8.18. The PSD distribution is dominated by the low frequency range (<1kHz) in the vicinity of the excursion of shock and/or their respective interactions. As mentioned earlier, in this particular RSS flow configuration, there are three interaction zones corresponding to the primary separation, reattachment and the secondary separation regions, see Fig. 8.18. The intensity of these interactions decreases as we move away from the primary interaction region. This has already been observed by analysing the PDF of the respective pressure fluctuations. The PSD of the computed pressure signals near the nozzle exit is performed for the case of NPR=25.5 & 41.6 and are shown in Fig. 8.19. A comparison with the available experimental data has been made and presents a fairly good agreement. Furthermore, the pressure spectra for both NPR display that pressure fluctuations are characterized by a significant contribution of low frequencies, i.e. $<$ 1kHz. However, the broad range distribution of these large-scale fluctuations suggests that the RSS regime at these NPR's exhibits a random behaviour.

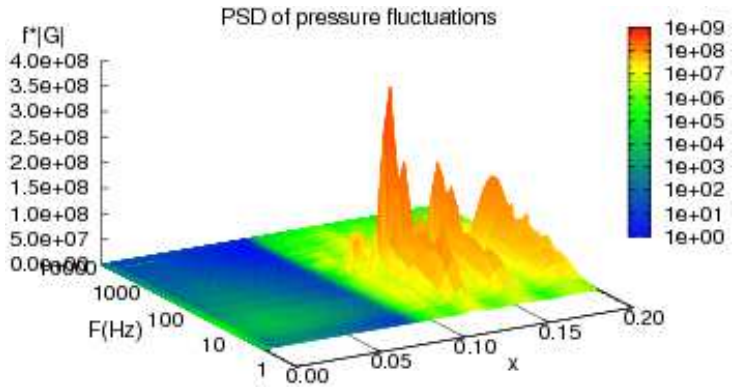

FIGURE 8.18 – Spectra of the wall pressure fluctuations along the nozzle wall (NPR=25.5) : f*G(f).

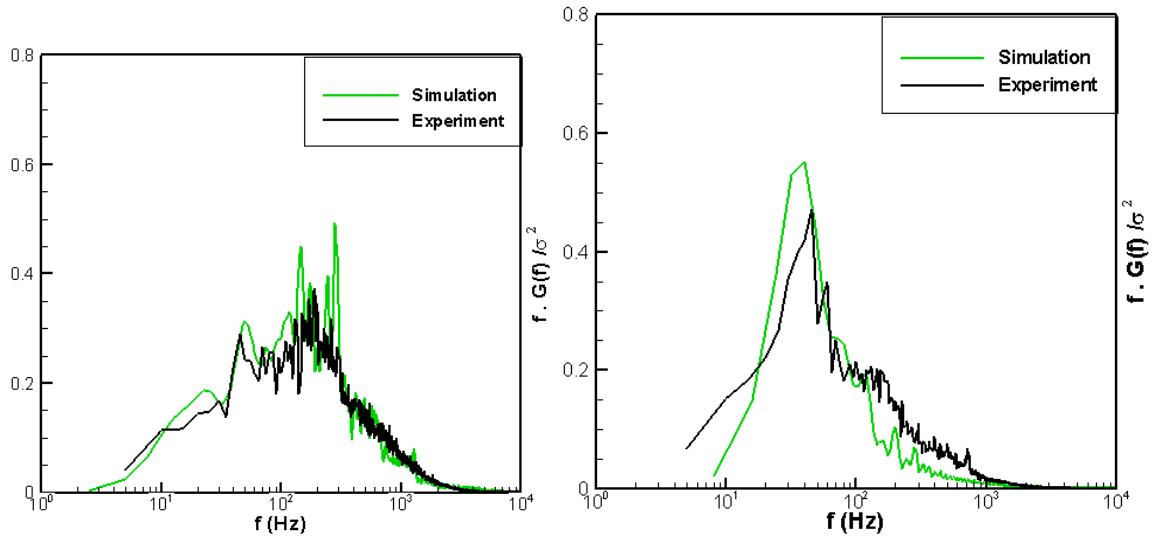

FIGURE 8.19 – Spectra of pressure fluctuations for NPR= (Left) 25.5 & (Right) 41.6, at x/L= 0.93.

8.2.3.2 Second Case, NPR=38.0

Previously we have noticed that at this NPR level, the secondary separation bubble appears very close to the nozzle exit. Following the same explanation given in the case of NPR=25.5, a variation in the radial pressure distribution downstream of the Mach disk breaks the symmetry of the cap-shock pattern. As a result, the separation line becomes asymmetric and so are the corresponding shock and the expansion waves in the azimuthal direction. Consequently, for some azimuthal position secondary separation bubble opens to the atmosphere, while at other location, it remains attached to the nozzle wall. This asymmetric evacuation of the separation bubble results in an enhanced tilting of the cap-shock pattern, in comparison with the case NPR=25.5. Series of snap-shots with the help iso-Mach contours and their zoom near the nozzle

exit are presented for the 2D meridian slices at θ=0^o & 180^o, in Fig. 8.20, to show this break of symmetry in this flow regime. Iso-contours of shock function corresponding to these snap-shots are shown to visualize the behaviour and position of the shock and expansion waves at that particular instant. The large trapped vortex downstream of the cap-shock pattern is shown with the help of instantaneous streamlines coloured by velocity contours. The solid black line on iso-Mach contours indicates the sonic line. Figure 8.20, display the three dimensional behaviour of the trapped vortex, asymmetric cap-shock pattern and the resulting evacuation of secondary separation bubble.

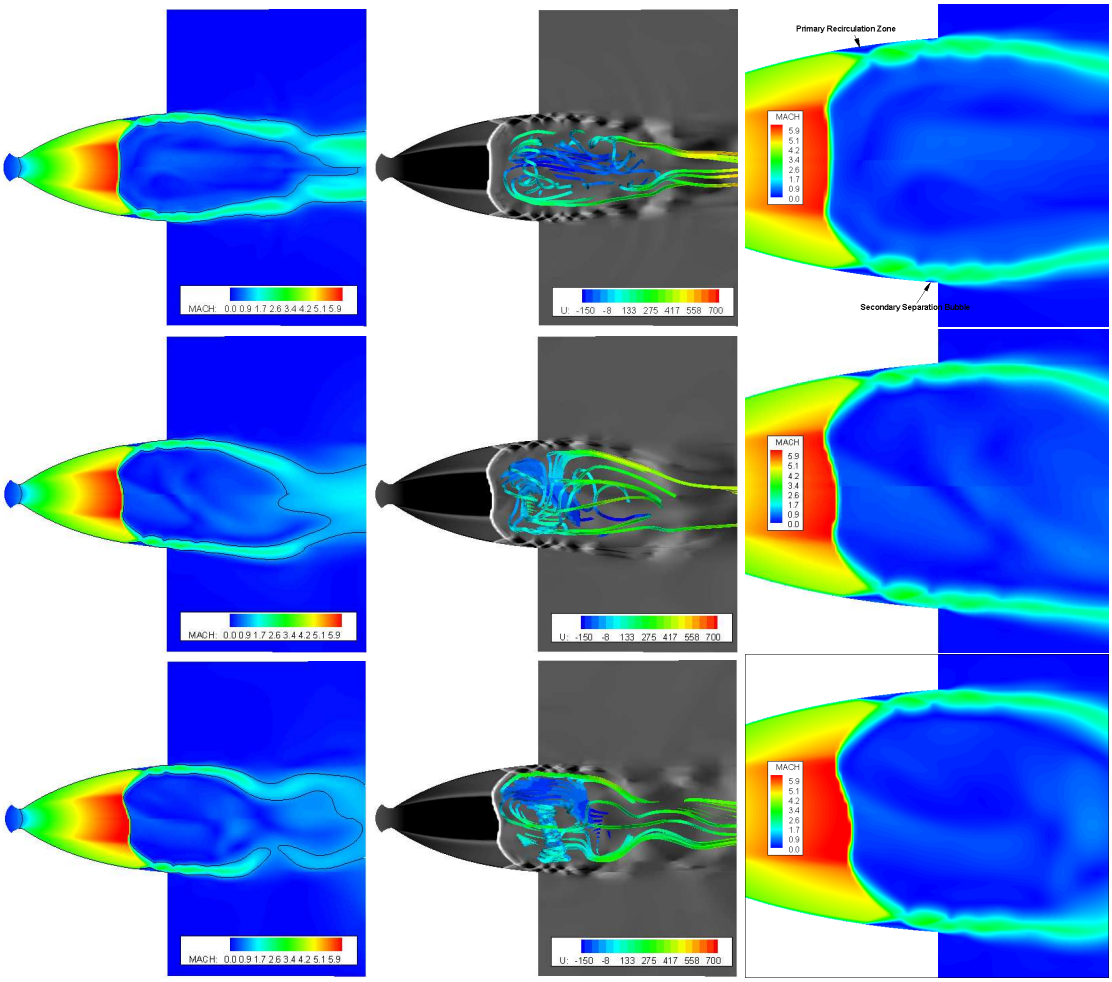

FIGURE 8.20 – 2D slices of (Top) Iso-Mach contours at θ = 0^o&180^o (Middle) Iso-contours of shock-function and streamlines coloured with velocity (Bottom) Zoom near the nozzle exit : iso-Mach contours at T=1.51, 2.81 & 3.40 $*L_d/U_t$ (Top-Bottom).

This downstream movement and the resulting tilting of the cap-shock can also be observed from Fig. 8.21. Solid black lines in this figure indicate the nozzle geometry while sonic lines at different instants are shown to highlight the positions of the cap-shock and the annular supersonic jet. Following the evacuation of the separation bubble to the ambient atmosphere, pressure level inside the trapped vortex slightly increases, but remains less than the ambient pressure. The

tilted cap-shock structure then moves upstream accordingly, which results in large-amplitude axial oscillations.

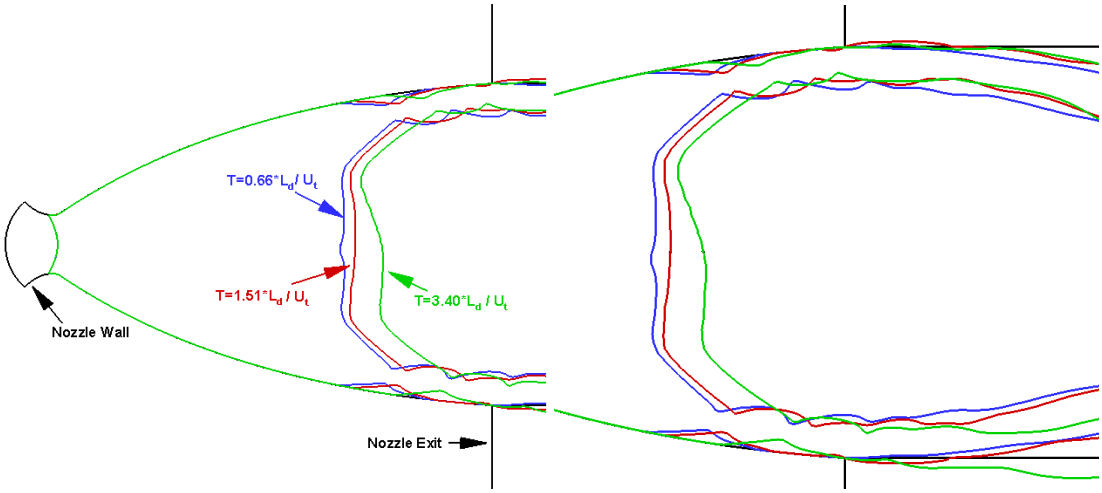

FIGURE 8.21 – Mechanism of shock tilting at NPR=38.0 : sonic lines (blue, red & green) at T=0.66, 1.51&3.4 $* L_d/U_t$ respectively

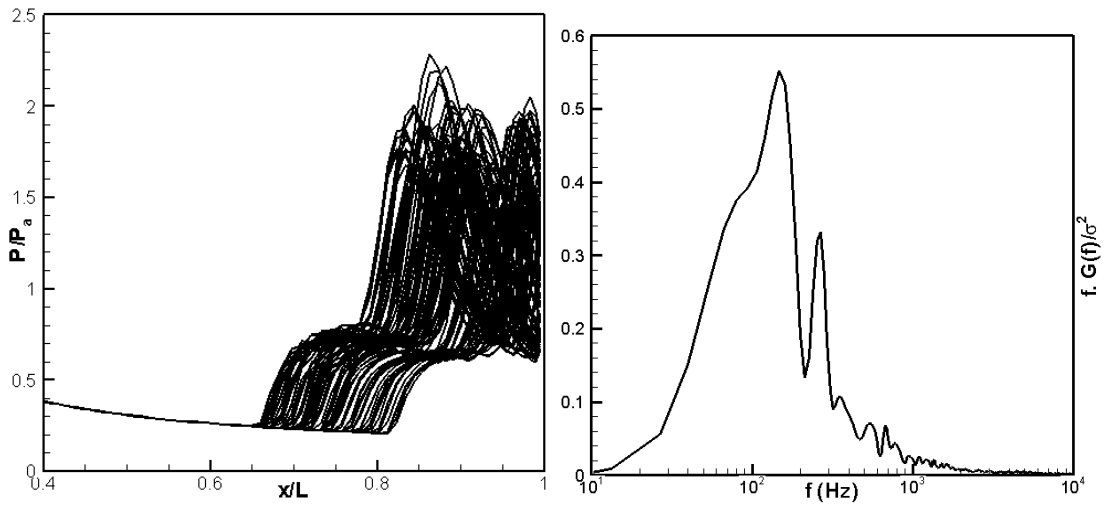

FIGURE 8.22 – (Left) Successive snapshots of wall pressure distributions near separation region, (Right) Spectra of wall pressure signals at x/L=0.69, NPR=38.0.

The instantaneous pressure distribution on the nozzle wall is displayed in Fig. 8.22 : Left. We can notice that the zone of shock excursion seems to be from x/L=0.65-0.82, which covers 17% of the nozzle divergent length. The pressure distribution corresponding to the most

upstream position of the cap-shock shows pressure levels higher than the ambient conditions at nozzle exit. This level suddenly decreases when the cap-shock reaches the central position of the excursion zone. At this instant, the secondary separation bubble opens to the atmosphere and the nozzle exit pressure is lower than the ambient conditions. This pressure difference at the nozzle exit causes a large axial oscillation and a time comes when we observed primary recirculation zone restricted by completely attached supersonic jet downstream of it, as shown in Fig. 8.20. This corresponds to the most downstream position of the cap-shock pattern for which the pressure at the nozzle exit increases at a level higher than the atmospheric pressure. These three positions are attributed to the (i) fully attached flow regime at nozzle exit (ii) opening of the secondary separation bubble to the atmosphere & (iii) again fully reattached condition without the presence of the secondary separation line.

Since the cap-shock pattern is not symmetric anymore, the resulting axial position of separation and reattachment lines are no longer the same in the azimuthal direction. This suggests that the RSS flow at this NPR is associated to high amplitude of axial-oscillations along with a random evolving asymmetry in the azimuthal direction. The spectrum of pressure signal at x/L=0.69 (i.e. shock (separation) excursion region) is computed and is given in Fig. 8.22 : Right. This PSD indicates that the shock motion is characterized by a broad range of low frequencies ($<$ 1 kHz). However, maximum of the energy is contained for the frequency range less than 200 Hz with a characteristic frequency peak at around 147 Hz. In addition, another peak appears near 260 Hz and contributes weakly to the shock motion. The broad range of frequency contributions in this pressure spectrum highlights that this oscillatory motion due to the repeated evacuation/formation of secondary separation bubble into the atmosphere is more a random process rather than a strictly periodic one.

8.2.3.3 Third Case, NPR=46.0

In order to analyse the high-amplitude axial oscillation in end-effect flow regime, instantaneous snap-shots of numerically reproduced flow-field are presented in Fig. 8.23-8.24. 2D slices at θ=0° & 180° with the help of iso-Mach contours illustrate the behaviour of flow field at several instants (see Fig. 8.23 : Left). In addition, the orientation (tilting) of cap-shock pattern and the three dimensional behaviour of trapped vortex downstream are shown with the help of iso-shock contours and instantaneous streamlines, respectively (see Fig.8.23 : Right). At initial stages (T=1.83 L_d/U_t) of this fully developed RSS configuration at NPR=46.0, the cap-shock is located at its most upstream position, and the flow regime seems quasi axi-symmetric. As soon as the symmetry of cap-shock pattern breaks down (according to the mechanism previously explained in the case of NPR=25.5 & 38.0), the reattachment line moves outside the nozzle and the trapped recirculation bubble (near the nozzle wall) opens to the atmosphere. A zoom near the nozzle exit displays more clearly the evacuation of this recirculation zone into the ambient atmosphere (see Fig. 8.24 : Left). Moreover, iso-shock surfaces are shown to visualize the tilting phenomenon of the three-dimensional cap-shock pattern in Fig. 8.23 : Right. One can depict completely asymmetric cap-shock along the nozzle axis corresponding to the snap-shots and the resulting asymmetry in the separation and reattachment lines.

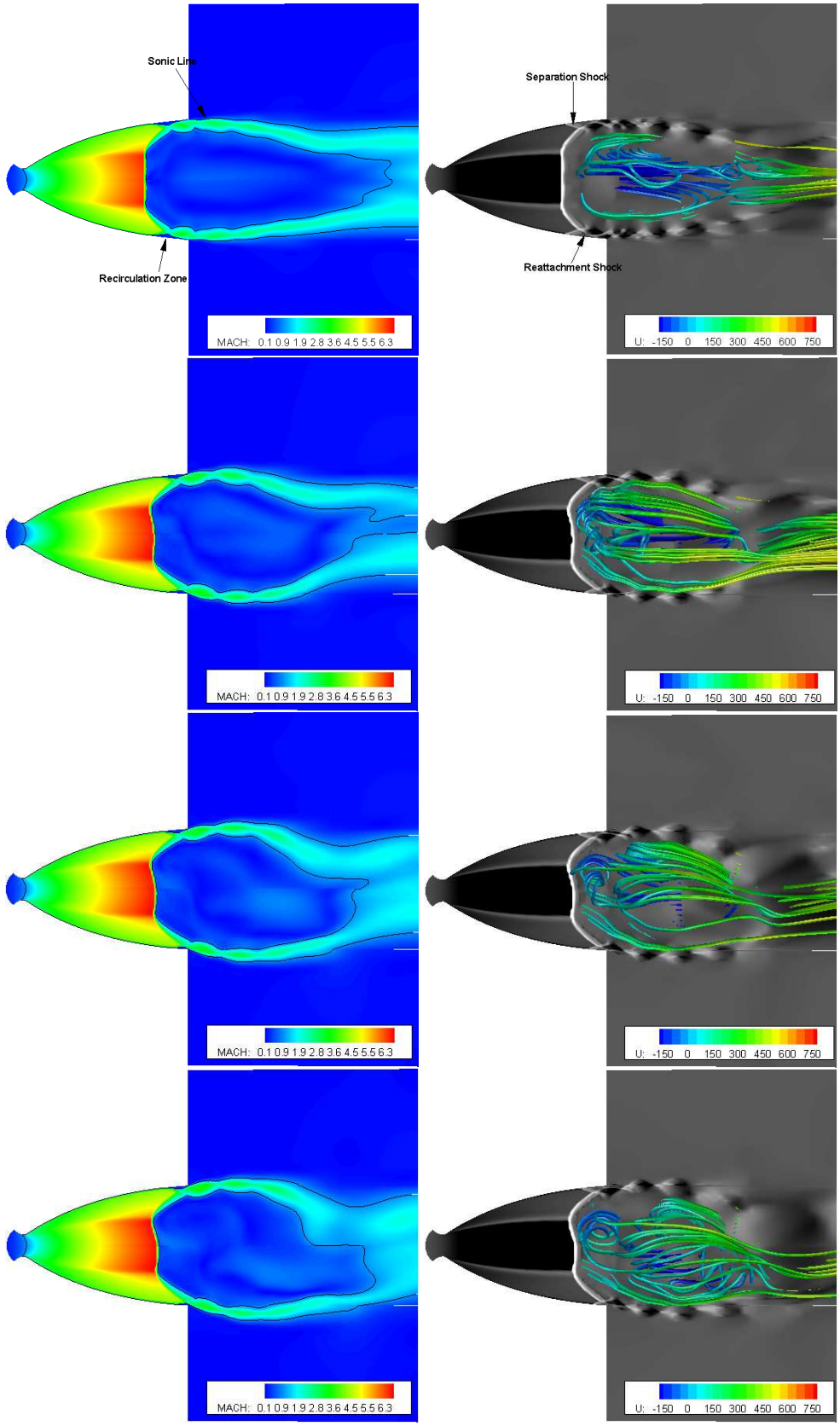

FIGURE 8.23 – Iso-contours of (Left) Mach number & (Right) shock-function at T=1.83, 1.89, 1.99 & 2.43 $*L_d/U_t$:Top to Bottom, 2D slices at θ=0° & 180°.

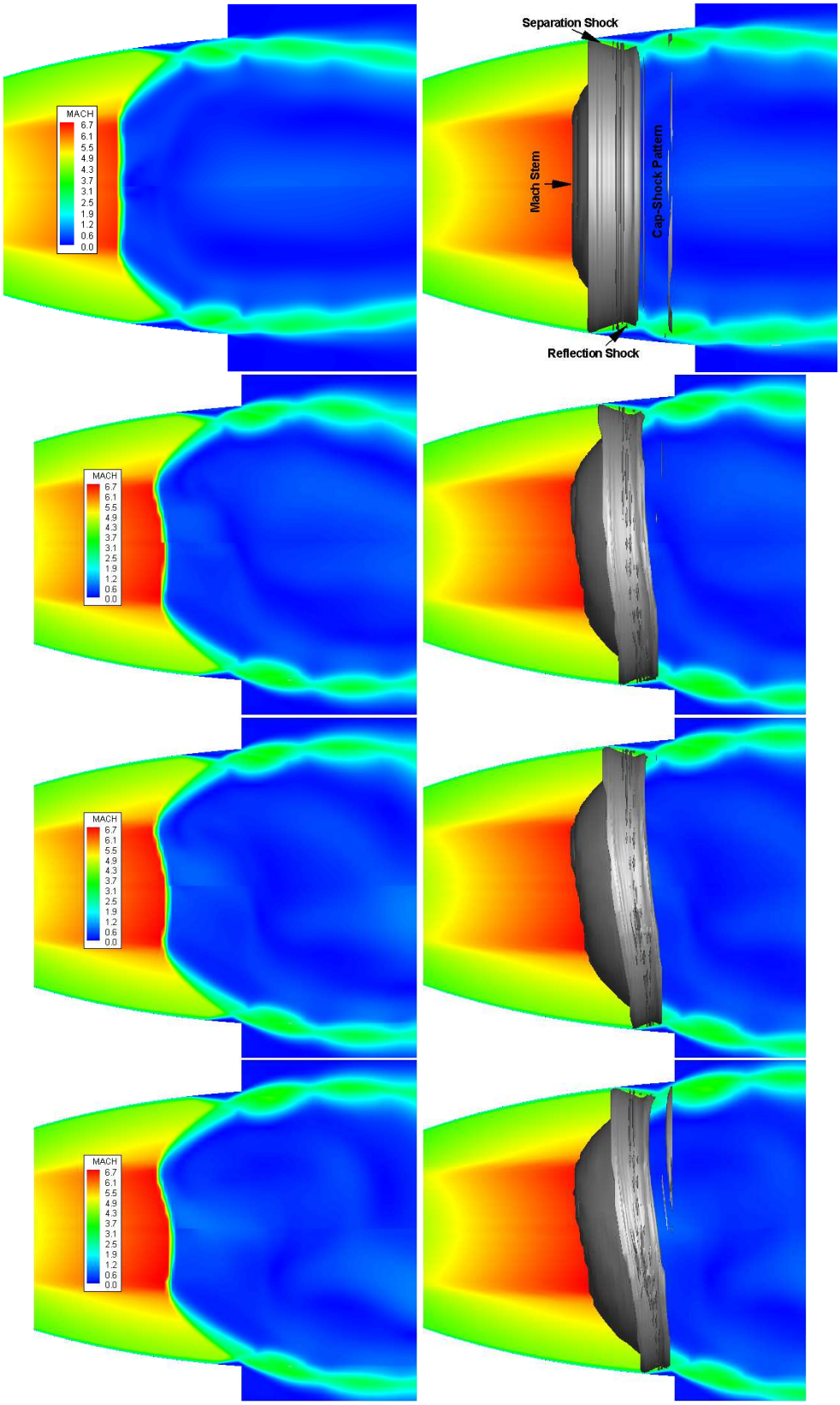

FIGURE 8.24 – Evolution of the recirculation zone in the end-effect regime (NPR=46.0) : zoom near the nozzle exit (Left) Iso-Mach contours & (Right) cap-shock pattern : iso-surfaces of shock-function at T=1.83, 1.89, 1.98 & 2.43 $*L_d/U_t$: Top to Bottom, 2D slices at θ=0° & 180°.

During the evacuation process of this recirculation zone, a purely separated regime appears, without any subsequent reattachment, as shown in Fig. 8.25. At this instant, the flow regime locally behaves like in FSS regime. In addition, the pressure level in the trapped vortex downstream of the cap-shock pattern increases and whole shock structure moves upstream. This induces the pulsatory process. However, during this reverse switch from locally FSS to RSS regime, the tilting of the cap-shock pattern produces a dissymmetric flow regime, as shown in Fig. 8.25. Iso-Mach contours in Fig. 8.25, suggest that for slice at $\theta = 0°$ flow is completely RSS, whereas, for $\theta = 180°$ it is opened to the ambient atmosphere. Although this dissymmetry appears during a very short instant, the pressure difference in the azimuthal direction produces a high level of impulsive lateral force.

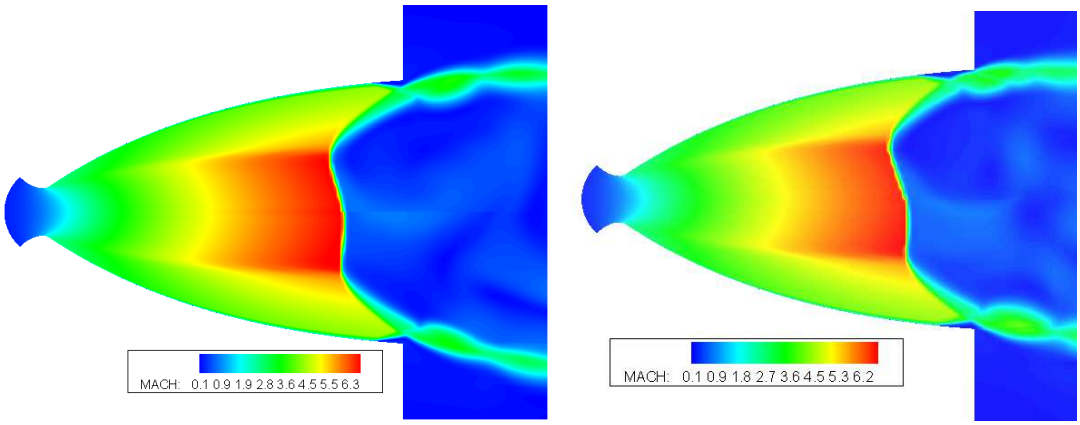

FIGURE 8.25 – Iso-Mach number of FSS flow configuration in end-effect regime at T=2.52 $*L_d/U_t$, 2D slices at θ=0° & 180°.

The cyclic back and forth transition from RSS to (locally) FSS flow configuration is characterized by the appearance of a tilted cap-shock and a large trapped vortex downstream of it, which is highly unsteady. This phenomenon is referred as cyclic RSS to FSS transition and implies the alternating bursting-formation of a recirculation zone/separation bubble at the nozzle wall. In the present case of end-effect regime, when the FSS configuration locally appears, as shown in Fig. 8.25, the wall pressure in the separated region is close to the ambient pressure. As a result, the separation line moves to adjust its location (determined by the level of the plateau pressure) by following the upstream location of the separation shock. Furthermore, this local FSS configuration causes the deflection of the annular supersonic jets and modifies its bending behind the large trapped vortex. These results in the pressure pulsations within the large vortex trapped by these annular supersonic jets around it. Nevertheless, iso-shock contours in the meridian plane indicate that the analysis is much more involved because shock and expansion waves reflect in the inner shear layer of the supersonic annular jet. Therefore, the wall pressure behind the separation line really results from the coupled response of the whole flow-field. The local appearance of the FSS flow regime at its upstream position exhibits the cap-shock pattern and a highly unsteady recirculation zone downstream of it. The pressure increase in this recirculation region favours the deflection of the surrounded annular supersonic jets towards the nozzle wall and results in a restricted shock separation. The fore and aft movement of this cap-shock pattern during this pulsatory regime shows higher amplitude of axial oscillation by comparison with the previous reported RSS regimes.

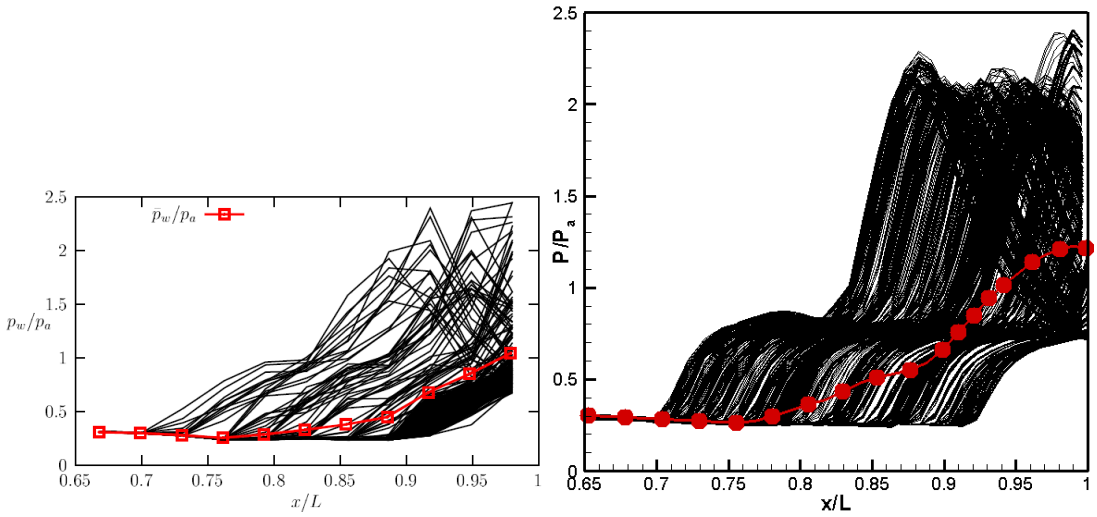

FIGURE 8.26 – Evolution of instantaneous wall pressure at (Left) Experiments : p_i/p_a=44.65 (Right) Simulation : $p_i/p_a = 46$.

Figure 8.26, presents the shock-excursion zone for this end-effect flow regime, which covers around 22% of the length of the nozzle divergent. The upstream limit of the wall pressure distribution is about $x/L = 0.7$ and the static wall pressure profile displays a peak with a level higher than the ambient pressure. This pressure peak confirms the reattachment of the flow and therefore the occurrence of the RSS configuration. When this separation line moves downstream towards its maximum limit, the level of the wall pressure remains less than the ambient pressure. The wall pressure fluctuations at two opposite points located in the same cross section at $x/L =$ 0.975 are now analyzed. The time history of the wall pressure at these two points and their difference are shown in Fig. 8.27.

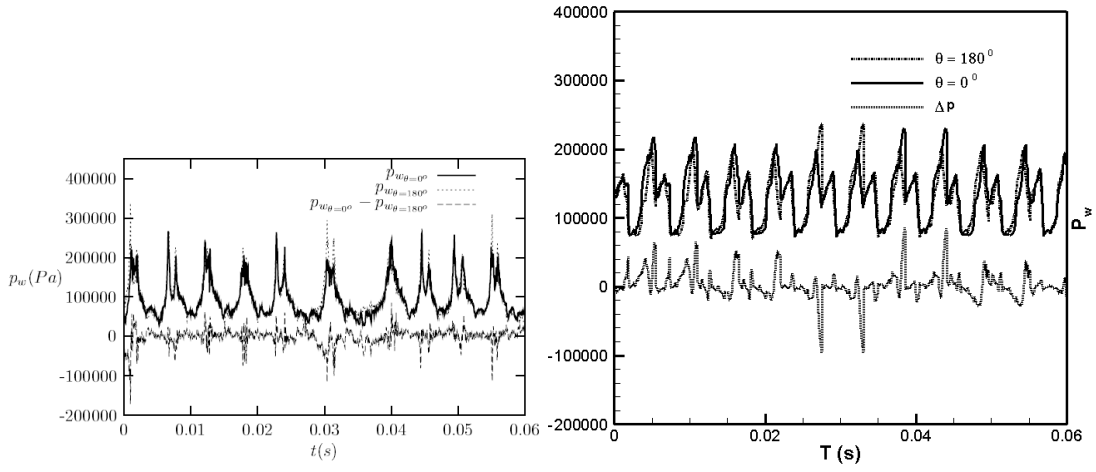

FIGURE 8.27 – Wall pressure fluctuations at two opposite points ($\theta = 0^o$&180^o)located in a cross section at x/L = 0.975, and their difference (Left) Experiments (NPR=42.63) & (Right) Simulation (NPR=46.0).

These impulse-like pressure signals clearly indicate that the flow is governed alternatively by the FSS and RSS regimes. In fact, these two pressure signals are only slightly different. The

maximum pressure difference is observed when the separated flow is governed by RSS configuration and/or flow dissymmetry. This quasi-periodic pulsation process is in good agreement with the experimental measurements for the end-effect flow regime at NPR=44.65, as shown in Fig. 8.27.

The computed pressure spectra at three different x/L stations nozzle wall are compared with the experimental data. The spectra display a large peak at low frequencies which corresponds to the characteristic frequencies of the large scale motion of the shock. In this case, the peak frequency is observed at 180 Hz. In addition, another peak is observed at 380 Hz, which is its first harmonic. The contribution of this peak is more significant near the separation line than near the reattachment line. However, in the recirculation region the whole frequency range $250Hz \geq f \leq 1kHz$ shows a significant contribution. The spectral analysis shows that this oscillatory motion is characterized by the sharp peak around 180 Hz and suggests that this end-effect phenomenon is quasi-periodic.

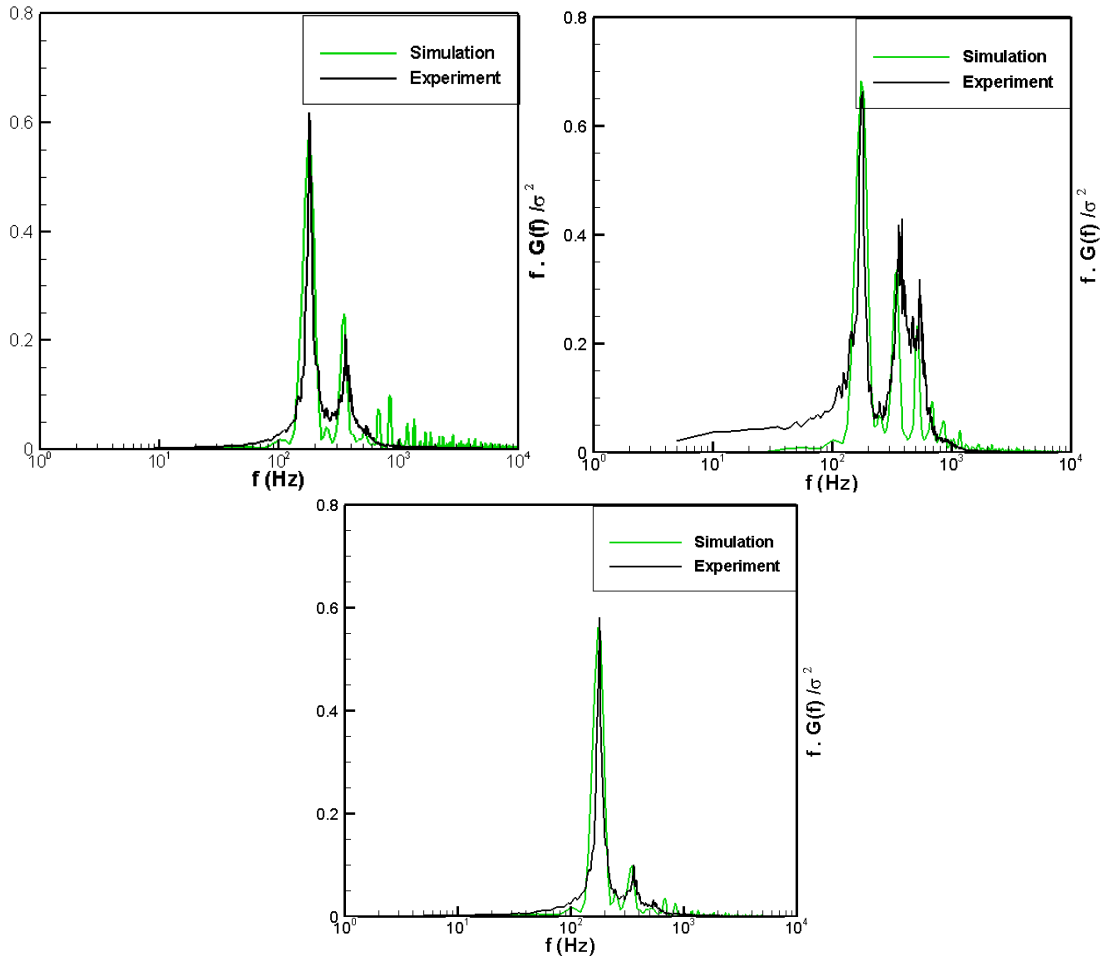

FIGURE 8.28 – Spectra of pressure signal at x/L= (Top) 0.88, (Middle) 0.93 & (Bottom) 0.98, Experiments (NPR=44.65) & Simulation (NPR=46.0)

This pressure field is expanded into Fourier modes in the azimuthal direction in order to analyse the spectral behaviour of modes 0 and 1 in this end-effect flow regime. Figure 8.29, displays the PSD of pressure fluctuations for mode 0, which is characterized by the sharp peak already observed for point spectra in Fig. 8.28. In addition, it is interesting to note that the PSD

contours for mode 1 displays a rather flat bump over 180 Hz indicating its random behaviour. As a conclusion, these results suggest that the flow can be interpreted as a random tilt of the whole cap-shock structure added to the basic axi-symmetric fore and aft movement of the separated flow.

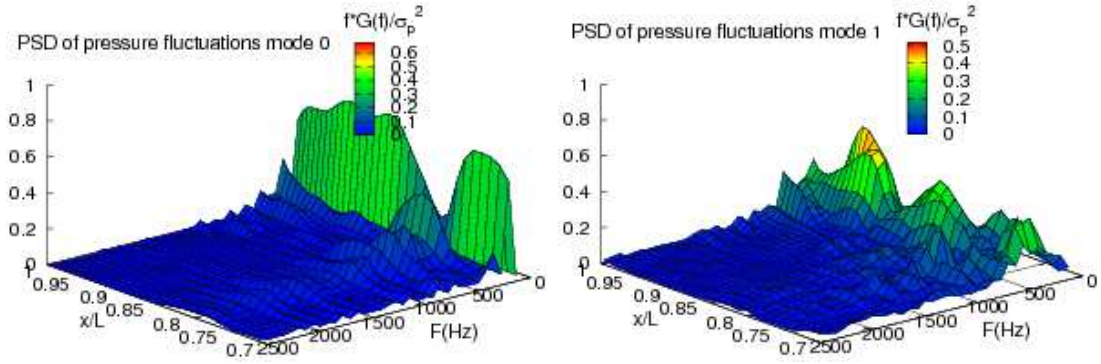

FIGURE 8.29 – PSD of azimuthal mode (Left) 0 & (Right) 1 of wall pressure fluctuations for NPR=46.0

8.2.4 Side-Loads

Figure 8.30, presents the trajectory of the polar plot for the force vector in (F_y, F_z) plane. As expected, there is no privileged direction and the force components have an isotropic and random character. This is confirmed by determination of the probability density function of the force modulus. As suggested by Dumnov [40] and confirmed by Deck [27] the distribution of side loads amplitude should be close to a Rayleigh distribution and Fig. 8.30 shows that the present computed results are also in close agreement with this prediction.

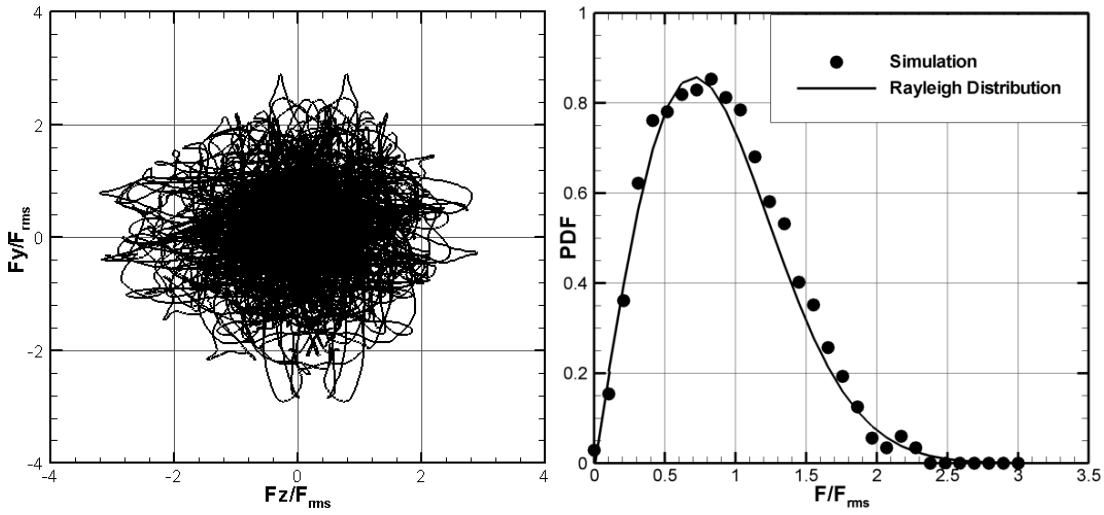

FIGURE 8.30 – (Left) Polar plot of side-loads at NPR=41.6 (Right) Probability density function of side-load components at NPR=30.0

The standard deviation of the side-loads modulus was computed for the five values of NPR and the results are compared on Fig. 8.31 : Left, with the experimental results of Nguyen et

al. [101]. The agreement is surprisingly good if one takes into account the fact that the experiment involves some amount of oxygen condensation and thus a rather large uncertainty of the effective NPR some inertia corrections, a severely limited frequency response of the measuring technique above 100 Hz.

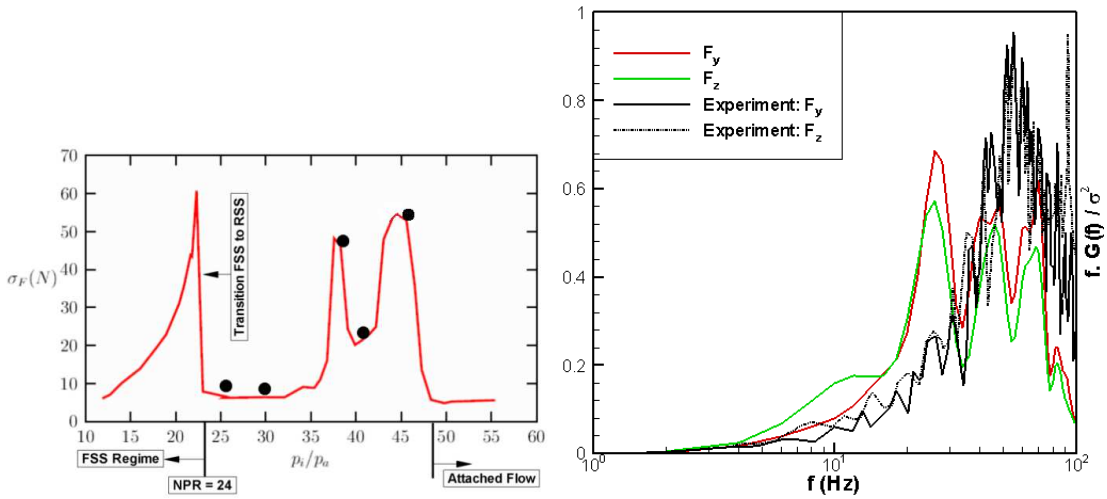

FIGURE 8.31 – (Left) Comparison of computed and measured RMS side-load levels with respect to NPR (Right) PSD of side-load components, computed at NPR=46.0 & experiments at NPR=42.23.

The power spectral density of side loads components was also determined by using Welch method. Figure 8.31 : Right, allows to compare the numerical results at NPR=46 with the measurements of Nguyen et al. at NPR=42.23. Although not perfect the agreement can be consider as reasonable if one takes into account the difficulty of the measurements on the experimental side and the uncertainty in the determination of the power spectral density from a rather short sample on the numerical side. Both results are characterized by a rather low dominant frequency range below 100 Hz. A similar type of behaviour has been observed for other NPR's and is given in Annex C.

8.2.5 Generation of side loads

Let $\phi(t) = tan^{-1}(F_z/F_y)$ be the direction of the side force F(t). Assuming that we have computed $F(t)$ and therefore that we know the direction $\phi(t)$, we can project the radial elementary force $p(x,\theta,t)r(x)\,d\theta\,dx$ on direction ϕ defining directly the force modulus :

$$|F(t)| = \int_0^L \int_0^{2\pi} p(x,\theta,t)r(x)\cos(\theta-\phi(t))\,d\theta\,dx$$

We introduce the time dependent force modulus density $F_{mod}(x,t)$ given by :

$$F_{mod}(x,t) = \int_0^{2\pi} p(x,\theta,t)r(x)\cos(\theta-\phi(t))\,d\theta$$

and such that :

$$|F(t)| = \int_0^L F_{mod}(x,t)\,dx$$

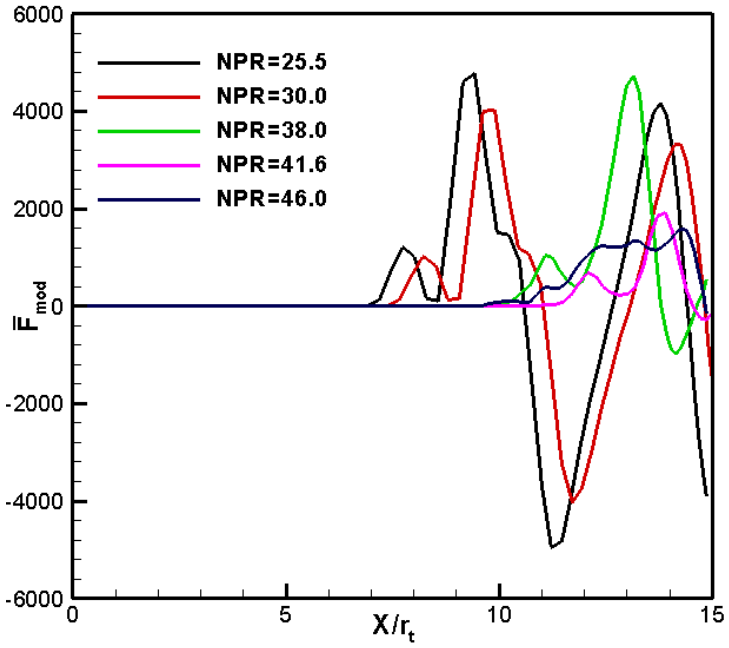

FIGURE 8.32 – Averaged force modulus density for the five NPR

Averaging in time we define an averaged force modulus density :

$$\overline{F_{mod}}(x) = \frac{1}{T}\int_t^{t+T} F_{mod}(x,t)\,dt$$

which allows to recover the averaged side loads modulus by :

$$\overline{|F|} = \int_0^L \overline{F_{mod}}(x)\,dx$$

The examination of $\overline{F_{mod}}(x)$ allow to identify where the side loads are generated along the nozzle. The integral with respect to x of this density is always greater or equal to zero but the local value can be positive or negative. It is therefore possible to observe, on the average, a low level of side loads due to a near balance between positive and negative contributions. One should notice that in such a situation it remains possible to have, on average, a significant moment of the side loads and this should perhaps be taken into account because, in several experiments, one measures in fact only the moment of the side loads with respect to a given point. As shown by Fig. 8.32, the results for NPR 25.5, 30.0 and 41.6 show a near balance between large positive and negative contributions. In contrast, the peak values of side loads observed for NPR=38.0 and 46.0 result essentially from imbalance between the negative and positive contributions.

8.2.6 Epilogue

The numerical analysis of the RSS flow regime shows that, for all investigated five NPR, the flow is dominated by large amplitude fluctuations. An attempt has been made to understand the origin to unsteadiness in this particular flow. It has been observed that the pressure variation in highly three dimensional trapped vortex downstream of the cap-shock pattern breaks the flow symmetry. Furthermore, results suggest that the flow can be interpreted as a random tilt

of the whole cap-shock structure added to the basic axi-symmetric fore and aft movement of the separated flow. The movement generates pressure fluctuations whose sign depends upon the local mean pressure gradient. Pressure fluctuations generate local side forces and integration along the nozzle wall give the resulting side loads. It appears that this integration process can, for some particular NPR values, lead to a rather small resulting force due to a near balance between negative or positive contributions to the final side load modulus. This balance or imbalance of the local contribution depends upon the location of the nozzle exit with respect to the mean wall pressure distribution which involves large amplitude variations associated with reflexion of shocks and expansion wave between the nozzle wall and the central quasi-isobaric trapped vortex. This mechanism explains the occurrence of two peaks of RMS values of side loads observed by Nguyen et al. [101] when either the secondary or the primary recirculation bubble opens to the ambient atmosphere.

Chapitre 9

Conclusions

Shock-induced separated flows play a fundamental role in the design and operation of high-speed aerospace vehicles and propulsion systems, in both internal and external aerodynamics configurations. They involve complex interactions between shock or expansion waves with both boundary and shear layers which can lead to dramatic modifications of their global topology, depending on the inflow or outflow conditions. They yield a low-frequency unsteady behaviour which can induce dangerous pressure and thermal loads. Despite such flows have been areas of interest since several decades, the physical mechanisms which drive this unsteadiness still remain an issue while a fully reliable prediction of their unsteady features still escapes the research community.

The research work reported in this thesis, is a contribution to the numerical simulation of these shock-induced separated flows. The targeted objectives have been twofold : i/ improving our understanding of the physical mechanisms which drive the flow unsteadiness for the various flow regimes and ii/ suggesting an appropriate numerical strategy in order to predict them satisfactorily. This study focuses more particularly on shock-induced separated flows occurring in a thrust optimized contour (TOC) nozzle operating under over-expanded conditions. This TOC type nozzle has been experimentally investigated at the Laboratoire d'Etudes Aérodynamiques LEA (Poitiers, France), and denoted as LEATOC nozzle. The flow configurations found in this nozzle significantly vary as a function of the nozzle pressure ratio (NPR). During the initial stage of a transient start-up, the shock-induced separation occurring within the nozzle leads to the formation of a massive recirculation zone and thus to mixing layers surrounding the separated annular shocked jet and undergoing compression and expansion zones. As the NPR grows, this flow Free Shock Separation (FSS) configuration switches into a Restricted Shock Separation (RSS) regime, characterized by the jet flow reattachment at the wall upstream of the nozzle exit. The main motivation of this work has been to better understand the flow unsteadiness of these flow regimes and the key mechanisms which drive this flow transition and which lead to the particular evolution of side-loads as a function of the flow regime.

In order to carry out reliable and workable numerical simulations of these separated flows, some challenging numerical and modelling issues have first been addressed. They are related to the requirements to consider both spatial and temporal accuracy and sufficiently long integration times to simulate the low-frequency motion of complex interactions between shocks and wall or free shear layers. Accordingly, the numerical strategy proposed in this study, and which has been implemented into the code TGNS3D developed at CEAT/LEA, relies on the combination of a high-order spatial (MPWENO) schemes, accurate implicit time integration (DDADI) with a

realizable extension of the Delayed Detached Eddy Simulation approach, called RDDES. This approach has first been validated on various flow configurations. It has then been applied to investigate separated flows in LEATOC nozzle flows in both FSS and RSS regimes, as well as during their respective switching process (FSS $\Leftrightarrow$ RSS). A wide range of NPR has been considered in order to analyse, for each specific regime, the unsteady physical mechanisms leading to the dangerous lateral fluctuating loads.

The key conclusions of this study are summarized as follows :

– Numerical Methods and Turbulence Modelling

The relative performances of second order MUSCL and fifth order MPWENO schemes combined with an implicit time integration algorithm (DDADI) have been assessed by preliminary tests in order to address accurate long time prediction of FSS and RSS flow regimes. The results suggest that, due to their high numerical diffusion across the shock, low-order schemes used on reasonably refined grids are insufficient. They can lead to the appearance of non-physical vortical structures downstream of the Mach stem which are thus likely to inhibit a correct prediction of the unsteady developpement of the downstream flow structure. Conversely, the fifth order MPWENO scheme is found to constitute a satisfying compromise to better control the numerical diffusion across flow discontinuities while representing a reasonable computational cost. In addition, the evolution of the numerical dissipation as a function of the CFL number, evaluated on a vortex advection test case, indicates that the numerical prediction remains satisfying as long as the CFL remains less than 25.0. This constraint has thus been taken into account for this study.

A comparative study of classical RANS models ($k-\varepsilon$ Chien, $k-\omega$, SST,...), implemented in the code TGNS3D has been carried out to evaluate their respective performance in over-expanded nozzle flows. These models lead in fact to unrealistic high values of turbulent kinetic energy (TKE) produced across the shock, which sometimes produce misleading numerical solution at a given NPR. It was shown that the realizability correction not only overcomes this problem, but also improves the prediction of the separation point, in comparison with more classical limiters used for the production term of TKE. Various hybrid RANS/LES techniques have been implemented and tested in the framework of shock-induced separated flows. This approach aims at switching progressively from a RANS evaluation in near-wall attached flow regions to a Large-Eddy Simulation (LES) like computation in detached zones, by modifying the characteristic turbulent length-scale into the transport equations in function of the local grid resolution. In this framework, the models sensitivity to the grid resolution was carefully checked and a satisfactory compromise has been found for the azimuthal direction in order to handle workable computations. It was observed that LNS and DDES-SST models suffer from problems of modelled stress depletion (MSD) and unrealistic increase of TKE, respectively, in the shock interaction region. This problem was overcome by reintroducing both the realizability correction and the shielding function in a $k-\omega$ based DDES model. In addition, it was found that the introduction of an additional DES length scale in the expression of the turbulent eddy viscosity term (for RDDES-II) improves the prediction of the developpement of instabilities within the shear layers, which is obtained when this DES length scale is only substituted in the production term. This point appears to be critical to correctly capture the jet flapping downstream of the shock structure and thus the induced wall-pressure fluctuations in both FSS and RSS regimes. Accordingly, the numerical and modelling strategy retained to investigate the LEATOC flows is based on the combination of fifth-order MPWENO,

second order implicit integration algorithm and the RDDES II formulation.

– Free Shock Separation flow regime
  In LEATOC nozzle, starting from a relatively low NPR, the free shock separation regime is characterized by an increasing unsteadiness when the NPR approaches to the critical NPR at which the flow regime bifurcates towards the RSS regime. In order to analyse this phenomenon, a detailed observation of the flow dynamics has been carried out for three particular fixed NPR's covering the range at which this FSS regime is found. The expected flow features corresponding to this regime have been qualitatively well reproduced and the levels of pressure fluctuations obtained are in good agreement with the available experimental data. In this regime, the separation shock interacts with the Mach disk and forms a triple point with the reflected oblique shock, which is inclined towards the nozzle wall. The separated shear layer, evolving between the recirculation region and the central jet region, interacts with the reflection shock. The results obtained have shown that this interaction is highly unsteady while the resulting interaction surface (tip of the reflection shock) appears to be wavy and asymmetric in the azimuthal direction, which induces an asymmetric motion of the whole shock system. A rapid growth of instabilities has been observed within the counter-current mixing layer which forms between the annular supersonic jet and the surrounding low speed flow. They lead to the formation of large coherent structures which yield a random behaviour in the azimuthal direction downstream of the nozzle and are associated to an intense flapping of the separated jet. This instability of the flow is found in fact to increase significantly as a function of the NPR and seems to directly drive the increasing wall-pressure fluctuations. However, this increase of the level of pressure fluctuations, in particular in the shock-excursion and separation regions, seems to be more related to the increase of the length of the separation line, which increases as a function of the nozzle radius when NPR increases, rather than to the direct effect of this pressure ratio. The examination of the wall pressure contours has confirmed the appearance of an asymmetric conical shock shaped separation line in the shape of teepees. This evolving asymmetry of the separation line seems to be related to the asymmetric non-stationary interaction of the separated shear layer with the reflected oblique shock. The asymmetric form of the separation line (number of teepee patterns) seems in fact to depend on its length (function of the local nozzle radius), and thus to its receptivity to the instabilities propagated through the separated flow. In the vicinity of the separation line, the pressure fluctuations are found to be essentially dominated by the contribution of low frequencies (< 200 Hz) which progressively increases with the increasing flow instability. Downstream of the shock excursion zone, the contribution of higher frequencies increases while the contribution of low frequencies (< 1 kHz) remains significant. This contribution of higher frequencies seems to be mainly associated to the flapping of the separated jet while the low-frequency range corresponds to the motion of the shock system. The computed lateral forces, in good agreement with the experiments, are found to increase as the global flow unsteadiness grows. The PSD analysis of the wall-pressure fluctuations has revealed that the first azimuthal mode is dominant. Although all the initial azimuthal modes of the wall-pressure fluctuations are also active in the shock-excursion zone, only the first mode survives throughout the separated region. In addition, as expected, these side-loads are dominated by the low frequencies <50 Hz.

– Flow Transition FSS $\Leftrightarrow$ RSS regimes
  A complex flow transition from FSS to RSS regimes occurs in LEATOC nozzle. The re-

verse process has also been observed, at a different NPR, so that a complex hysteresis cycle exists. One of the motivations of this work has been to address the fundamental question to know which key event triggers this process and how the flow structure effectively evolves during this transition. Accordingly, the simulation of this hysteresis cycle of the flow transition has been addressed, in both axi-symmetric and three-dimensional configuration. For that purpose, the transient increase of has been artificially reproduced by using stabilized inflow conditions following a piecewise constant evolution law of the stagnation pressure. Both forward and reverse transition processes have been successfully reproduced and the critical NPR (CNPR) numerically observed in each case is in good agreement with the experimental value (NPR=24 and 14 for forward and reverse transition respectively). The obtained RMS levels of side-loads (lateral forces) are also in good agreement with the experimental data, which give confidence in the representativity of the process simulated by the approach retained. It has been found that, for both the forward and reverse transition process, the transition occurs in a quite short time period (of the order of 5-6 ms), as soon as a common interaction point is reached. The point corresponds to the direct interaction of both the internal shock emanating from the near-throat region, the separation shock and the Mach stem. This common interaction point has been called 'Flow Transition Quadruple Point (FTQP)'. This critical point was found to correspond to a radical modification of the distribution of radial and axial momentum and thus to the appearance or disappearance of the cap-shock pattern found in RSS regime and the subsequent flow attachment at the wall. It was also found that the flow morphology observed during this transition seems to highly depend on the transient inlet condition, and so is the time required to switch from one regime to the other. In particular, an inversion of the curvature of the Mach disk has been observed with a large impulsive increase of the NPR. However, no strong asymmetry has been detected during the transition. This clearly contradicts the hypothesis of a possible coexistence of both FSS and RSS regimes to explain the peak of side-loads observed during the transition process. Therefore, this peak of side-loads observed just before the forward transition appears to be mainly attributed to the increasing instability of the separation line and of the subsequent downstream jet structure at the very end of the FSS regime, and to a stabilization of this separation line when the flow reattaches at the wall at the beginning of the RSS regime.

– Restrited Shock Separation flow regime
The shock-induced separation with a subsequent reattachment of the annular supersonic jet in RSS flow regime is characterized by the formation of a special shock-system (cap-shock), followed by a large recirculation zone and successive interactions between compression or expansion waves, the boundary layer and the internal shear layer. In this regime, after a stabilizing effect of the jet flow reattachment at the wall, the evolution of the side-load activities as a function of NPR shows the appearance of two distinct peaks. In order to analyse the various mechanisms leading to these peaks, this RSS regime has been simulated at five characteristic NPR values, with established inflow conditions. For all these investigated NPR, the flow appears in fact to be dominated by large amplitude fluctuations. Due to its interaction with the highly unsteady and three dimensional mixing layer, the subsonic trapped vortex downstream of the Mach stem becomes three-dimensional and propagates the pressure variations produced downstream of the cap-shock pattern. The increase of side-load activities is found to be associated with the increasing occurrence of the opening of either the secondary, or the primary (end-effect

regime) recirculation bubble to the ambient atmosphere. Like in FSS regime, only the first azimuthal mode of the expansion of the wall-pressure fluctuations really contributes to the side-loads in RSS regime. The PSD analysis leads to interpret the flow as a random tilt of the whole cap-shock structure superimposed to a basic axi-symmetric fore and aft movement of the separated flow. This movement generates pressure fluctuations whose sign depends on the local mean pressure gradient. By decomposing the integration process of the local side forces as a function of axial contributions, it was found that, as long as the flow remains attached, a near balance between negative and positive contributions is found, which results in a relatively low level of side-loads. Conversely, this distribution becomes unbalanced in case of a recirculation zone reaches the nozzle exit. This balance or imbalance of the local contributions depends upon the location of the nozzle exit with respect to the mean wall pressure distribution resulting from the successive shock and expansion waves reflections between the nozzle wall and the central trapped vortex.

The numerical and turbulence modelling strategy retained in this research work has enabled the investigation of the unsteady features of various flow configurations of shock induced separated flows occurring in the LEATOC nozzle. In spite of a necessary compromise made in terms of azimuthal resolution to obtain reasonable grids and address a wide range of flow cases, the results obtained have been found to be in good agreement with the available experimental data. These encouraging results suggest that, at first order, the evolution of side-loads is driven by a closed loop involving mainly large-scale events and that the effects of the details of the downstream turbulent events remain of secondary importance. Accordingly, the present approach appears to be suited for further studies in order to address both fundamental and more applied issues. Firstly, the exact influence of the azimuthal grid refinement needs to be checked. We suspect in fact a direct influence of this resolution on the sensitivity of the separation line to the flow disturbances that would require a more careful examination. In addition, the compressibility effects on the turbulence might have a non-negligible influence on the privileged oscillation modes, so that new modelling developments would help to clarify this point. The results obtained in this study seem however sufficiently representative of the large-scale dynamics of the flow to be used in a perspective of low-order dynamical modelling. From a more practical point of view, new nozzle geometries could be investigated to assess the universality of the mechanisms which have been identified in this study. In particular, the flow behaviour during the transition process in LEATOC was typically associated to the presence of the incident shock issued from the throat region. The time-varying flow morphology of the overall shock structure is likely to be different in case of another nozzle geometry. Then, it has been highlighted that this transition mechanism depends on the features of the transient inflow conditions. An important issue that could be addressed would be the influence of taking into account a more realistic transient start-up process on the evolution of the flow structure and its related unsteadiness. The numerical/ turbulence modelling strategy retained represents a fairly good compromise between accuracy and computational cost. Therefore, we might imagine to implement quite easily various control strategies in order to limit as far as possible the occurrence of dangerous side loads. This could be done on this reference configuration of LEATOC nozzle for example by blowing at the nozzle lip. Finally, it should be recalled that the LEATOC nozzle facility was initially designed with external walls, parallel to the nozzle exit plane, in order to better control the sources of external perturbations. It might be expected that removing these walls might influence the preferential modes of unsteadiness causing the flapping of the jet and maybe reveal other typical behaviours occurring within the nozzle (coexistence of FSS and RSS

flow regimes in contrast with the present calculation ?).

Bibliographie

[1] Adams, N., Direct simulation of the turbulent boundary layer along a compression ramp at M=3 and Re_θ=1685 : J. Fluid Mech. 420 : 47-83, 2000.

[2] Andreopoulos, J., Muck, K., Some new aspects of the shock wave boundary layer interaction in compression-ramp flows. J. Fluid Mech. 180 : 405-28, 1987.

[3] Alziary de Roquefort, T., Unsteadiness and side loads in over-expanded supersonic nozzles, in : Proc. 4th European Symp. Aerothermodynamics for Space Vehicles, ESA SP-487, Capua, Italy, 2001.

[4] Alziary de Roquefort, T., Low frequency fluctuations in separated turbulent compressible flows. Symposium on Advanced Fluid Information, Tokyo, Japan, 2002.

[5] Arens, M., Spiegler, E., Shock-induced boundary layer separation in overexpanded conical exhaust nozzles. AIAA J., 1(3), 578, 1963.

[6] Arnal, D., Délery, J., Laminar-Turbulent Transition and Shock-Wave / Boundary layer Interaction, RTO AVT Lecture Series, von Kármán Institute, Rhode-St-Genśe, Belgium, 10-14 May, 2004.

[7] Balaras, E., Benocci, C., Piomelli, U., Finite-difference computations of high Reynolds number flows using the dynamic sub grid scale model. Theoretical Computational Fluid Dynamics, 7 : 207-216, 1995.

[8] Balsara, D. S., and Shu, C. W., Monotonicity preserving weighted essentially non-oscillatory schemes with increasing high order of accuracy. J. of Computational Physics, Vol. 160, 2000, pp. 405-452.

[9] Batten, P., Goldberg, U., Chakarvarthy, S., LNS - An approach towards embedded LE. AIAA paper, 2002-0427, 2002.

[10] Bibko, V., Efimtsov, B., Korkach, B., Kuznetsov, V., About the fluctuations of shockwave induced by the boundary layer separation. J. Fluid Mech., 4 : 168-70, 1990.

[11] Bloomer, H. E., Antl, R. J., Renas, P. E., Experimental study of the effects of the geometric variables on performance of conical rocket engine exhaust nozzles. NASA TN D-846, 1961.

[12] Boussinesq, J., Essai sur la théorie des eaux courantes. Mem. Pres. Acad. Sci., XXIII, 46, Paris, 1877.

[13] Boussinesq, J., Théorie de lécoulement tourbillonant et tumubteur des liquides dans les lits rectiligues. Comptes Rendus de 1'Acad. des Sciences, CXXII, pp. 1293, 1896.

[14] Brazhko, V., Periodical structure of flow and heat transfer in the region of attachment of supersonic flows. Uchenie Zapiski TSAGI (Scientific Notes of TSAGI), 10 : 113-8, 1979.

[15] Breuer, M., Lakehal, D., Rodi, W., Flow around a surface mounted cubical obstacle : Comparison of LES and RANS results. In M. Deville, S. Gavrilakis, and I.L. Ryming, editors, Computation of 3D Complex flows, volume 53 of Notes on Numerical Fluid Mechanics, pages 22-30. Vieweg Verlag, 1996.

[16] Cabot, W., Large eddy simulations with wall models. In Annual Research Briefs-1995. Center for Turbulence Research. Stanford University, 1995.

[17] Casey, M., Wintergerste, T., Best Practice Guidelines. ERCOFTAC, 2000.

[18] Chapman, D., Huehn, D., Larson, H., Investigation of Separated Flows in Supersonic and Subsonic Streams with Emphasis on the Effect of Transition, NACA Report 1536, Ames Aeronautical Laboratory, Moffet Field, 1958.

[19] Chapman, D. R., Computational aerodynamics, development and outlook. AIAA J., 17 : 1293-313, 1979.

[20] Charwat, A., Supersonic flows with imbedded separated regions. Adv. Heat Transfer, 6 : 1-132, 1970.

[21] Chen, C. L., Chakravarthy, S. R., Hung, C. M., Numerical investigation of separated nozzle flows. AIAA J., Vol. 32, 1836-43, 1994.

[22] Chien, Y., Predictions of channel and boundary layer flows with a low-Reynolds number Turbulence model, AIAA J., Vol. 20, No. 1, 33-38, 1982.

[23] Coakley, T. J., Huang, P. G., Turbulence modelling for high speed flows. AIAA Paper 92-0436, 1992.

[24] Deardorff, J. W., A numerical study of three-dimensional turbulent channel flow at large Reynolds numbers. J. Fluid Mech., 41 : 453-480, 1970.

[25] Deck, S., Simulation Numériques des charges latérale instationaires sur des configuration de lanceurs. Ph.D Thesis, Université d'Orléans, 2002.

[26] Deck, S., Garnier, E., Guillen, P., Turbulence modelling applied to space launcher configurations. Journal of Turbulence, 3 (2002) 057, 2002.

[27] Deck, S., Nguyen, A. T., Unsteady side loads in a thrust-optimized contour nozzle at hysteresis regime, J. Propulsion and Power, 42 (9) 1878-1888, 2004.

[28] Deck, S., Delayed detached eddy-simulation of the end-effect regime and side-loads in an over expanded nozzle flow. Shock Waves, 19 (3) 239-249, 2009.

[29] Délery, J., Marvin J., In : Reshotko, E., editor. Turbulent shock-wave/boundary layer interaction. AGARDograph No. 280, February 1986.

[30] Délery, J., Shock interaction phenomena in hypersonic flows. Part II : Physical features of shock wave/boundary layer interaction in hypersonic flows. In AGARD Conference on Future Aerospace Technology in the Service of the Alliance, 14-16 April 1997, Ecole Polytechnique, Palaiseau, France.

[31] Délery, J., Shock phenomena in high speed aerodynamics : still a source of major concern. The Aeronautical Journal of the Royal Aeronautical Society, pp. 19-34, Jan. 1999.

[32] Délery, J., Handbook of Shock Wave, Vol. 2, Academic Press, New York, 2001.

[33] Délery, J., and Dussauge, J.-P., Some physical aspects of shock wave/boundary layer interactions, Shock Waves, 19 : 453-468, 2009.

[34] Dolling, D., Murphy, M., Unsteadiness of the separation shockwave structure in a supersonic compression ramp flowfield. AIAA J., 12 : 1628-34, 1983.

[35] Dolling, D., Or, C., Unsteadiness of the shockwave structure in attached and separated compression ramp flows. Exp. Fluids, 3 : 24-32, 1985.

[36] Dolling, D. S., Brusniak, L., Separation shock motion in fin, cylinder, and compression ramp-induced turbulent interactions, AIAA J., 27 (6), 1989.

[37] Dolling, D., Fluctuating loads in shockwave turbulent boundary layer interaction : tutorial and update. AIAA Paper, 93-0284, 1993.

[38] Dolling, D., High-speed turbulent separated flows : consistency of mathematical models and flow physics. AIAA J., 36 : 725-32, 1998.

[39] Dolling, D., Fifty years of shockwave boundary layer interaction research : what next ? AIAA J., 39 : 1517-31, 2001.

[40] Dumnov, G. E., Unsteady side-loads acting on the nozzle with developed separation zone. AIAA Paper, 98-3619, 1996.

[41] Dussauge, J. -P., Dupont, P., Debiève, J. -F., Unsteadiness in shock wave boundary layer interactions with separation. Aerospace Science and Technology, 10, 85-91, 2006.

[42] Dussauge, J. -P., Why do shock waves move in separated flows ?, IUTAM Symposium on Unsteady Separated Flows and their Control, June 18-22, Corfu, Greece, 2007.

[43] Dussauge, J. -P, Piponniau, S., Shock / boundary layer interactions : possible sources of unsteadiness. J. Fluids Structure, 24, 1166-1175, 2008.

[44] Emanuel, G., Gas dynamics : Theory and Applications, AIAA Education Series, AIAA New York, 1986.

[45] Erengil, M., Dolling, D., Unsteady shockwave structure near separation in a Mach 5 compression ramp interaction. AIAA J., 29 : 728-35, 1991.

[46] Erengil, M., Dolling, D., Correlation of shock motion with pressure fluctuations in the incoming boundary layer. AIAA J., 29 : 1868-77, 1991.

[47] Fage, A. and Sargent, R. F., Effect on aerofoil drag of boundary layer suction behind a shock wave, ARC R & M N° 1913, 1943.

[48] Farley, J. M., Campbell, C. E., Performance of several methods of characteristic exhaust nozzles. NASA TN D-293, 1960.

[49] Favre, A., Equations des gaz turbulents compressibles, part 1 : formes générales. J. de Mécanique 4, pp. 361-390, 1965.

[50] Favre, A., Equations des gaz turbulents compressibles, part 2 : méthode des vitesses moyennes ; méthode des vitesses moyennes pondérés par la masse volumique. J. de Mécanique 4, pp. 391-421, 1965.

[51] Floryan, J. M.,On the Gortler instability of boundary layers. Prog. Aerospace Sci., 28, 235-271, 1991.

[52] Forsythe, J., Hoffman, K., Damevin, H. M., An assessment of several turbulence models for supersonic compression ramp flow. AIAA Paper 98-2648, 1998.

[53] Frey, M., Hagemann, G., Status of Flow separation Prediction in Rocket Nozzles. 34^{th} Joint Propulsion Conference & Exhibit. AIAA Paper, 98-3619, 1998.

[54] Frey, M., Hagemann, G., Flow separation and side-loads in rocket nozzles, AIAA Paper, 99-2815, 1999.

[55] Frey, M., Hagemann, G., Restricted Shock Separation in rocket nozzles. J. of Propulsion and Power, Vol. 16, No. 3, May-June, 2000.

[56] Froehlich, J., Large Eddy Simulation turbulenter Stromungen. Teubner Verlag, 2006.

[57] Ganapathisubramani, B., Clemens, N. T., and Dolling, D. S., Effects of upstream boundary layer on the unsteadiness of shock-induced separation, J. Fluid Mech., Vol. 585, pp. 369-394, 2007.

[58] Girard, S., Etude des charges latérales dans une tuyère supersonique surdétendue. PhD Thesis, Université de Poitiers, 1999.

[59] Girard, S., Deniau, H., Nguyen, A. T., Alziary de Roquefort T., Etude de l'écoulement dans une tuyére propulsive à contour parabolique en régime surdétendu. 37^{eme} Colloque d'Aérodynamique Appliquée de l'AAAF : Aérodynamique et Propulsion des Véhicules à grande vitesse., Aracachon, France, 2001.

[60] Glotov, G., The features of incipiency and development of the re-circulated zones in the supersonic layers of supersonic flows. Appl Mech Tech Phys., 36(5) : 30-9, 1998.

[61] Green, J., Interactions between shockwaves and turbulent boundary layers. Prog Aerosp Sci., 11 : 235-341, 1970.

[62] Hagemann, G., Frey, M., Koschel, W., Appearance of restricted shock separation in rocket nozzles. J. of Propulsion and Power, Vol. 18, No. 3, May-June, 2002.

[63] Hagemann, G., Frey, M., Shock pattern in the plume of rocket nozzles : needs for design consideration. Shock Waves, 17 : 387-395, 2008.

[64] Ho, C. M., Huang, L. S., Subharmonics and vortex merging in mixing layers, Journal of Fluid Mechanics, 119, 443, 1982.

[65] Ho, C. M., Huerre, P., Perturbed free shear layers, Annual Review of Fluid Mechanics. 16, 365, 1984.

[66] Inger, G. R., Three-dimensional heat- and mass- transfer effects across high-speed reattaching flows. AIAA J., 15, 383-389, 1977.

[67] Keanini, R. G., Brown, A. M., Scale analysis and experimental observations of shock-induced turbulent boundary layer separation in nozzles. European J. of Mechanics B/Fluids, 26, 494-510, 2007.

[68] Knight, D., Yan, H., Panaras, A. G., and Zheltovodov, A., Advances in CFD prediction of shock wave turbulent boundary layer interactions. Progress in Aerospace Sciences, 39, 121-184, 2003.

[69] Kok, J. C., Harmen van der Ven, Destabilizing free shear layers in X-LES using a stochastic subgrid-scale model, Third Symposium on Hybrid RANS-LES Methods, 10-12 June, Gdansk, Poland, 2009.

[70] Kuehn, D., Experimental investigation of the pressure rise required for incipient separation of turbulent boundary layers in two-dimensional supersonic flow. NASA TM 1-21-59A, 1959.

[71] Kwan, W., Stark, R., Flow separation phenomena in sub-scale rocket nozzles. AIAA Paper 2002-4229, 2002.

[72] Laufer, J., Investigation of turbulent flow in a two-dimensional channel. NACA TN 1053. Washington, DC : Natl. Advis. Comm. Aeronaut, 1950.

[73] Lawrence, R. A., Symmetrical and unsymmetrical separation in supersonic nozzles. Research Repy. 67-1, Southern Methodist University, 1967.

[74] Leep, L. J., Dutton, J. C., Burr, R. E., Three-Dimensional Simulations of Compressible Mixing Layers : Visualizations and Statistical Analysis, AIAA Journal, 0001-1452 vol.31 no.11 : 2039-2046, 1993.

[75] Leer, Van. B., Towards the ultimate conservation difference scheme I : The quest of Monotonicity. Lecture notes in Physics. Pages 163-168, 1973.

[76] Leer, Van. B., Towards the ultimate conservation difference scheme II : Monotonicity and conservation combined in a second order scheme. J. of Computational Physics, 14 : 361-370, 1974.

[77] Leer, Van. B., Towards the ultimate conservation difference scheme III : Upstream-centered finite difference schemes for ideal compressible flow. J. of Computational Physics. 23 : 263-275, 1977.

[78] Leer, Van. B., Flux vector splitting for the Euler equations. In the preceedings of the $8th$ International Conference on numerical Methods in Fluid Dynamics. pages, Berlin, Lecture Notes in Physics, Vol. 170, Springer Verlag, 1982.

[79] Leer, Van. B., Progress in multi-dimensional upwind differencing. ICASE Report, 92-43, 1992.

[80] Lengrand, J. C., Dynamique des gaz raréfiés. Cours de l'Ecole Supérieure de l'Energie et des Matériaux, DEA Energétique, Université d'Orléans, France, 1999.

[81] Liepmann, D., Gharib, M., The role of streamwise vorticity in the near-field entrainment of round jets, Journal of Fluid Mechanics, 245, 643, 1992.

[82] Liou, W. W., Huang, G., Shih, T. H., Turbulence model assessment for shock wave / turbulent boundary layer interaction in transonic and supersonic flows. Computers and Fluids, Vol. 29, No. 3, 275-299, 2000.

[83] Lovely, D., Haimes, R., Shock detection function from computational fluid dynamics results. AIAA paper 99-3285, 1999.

[84] Ludeke, H., Radespiel, R., Schulein, E., Simulation of streamwise vortices at the flaps of re-entry vehicles. Aerospace Science and Technology, 8, 703-714, 2004.

[85] Lumley, J. L., Computational Modeling of Turbulent Flows. Advances in Applied Mechanics, 18, pp. 123-176, 1978.

[86] Menter, F. R., Two-equation eddy-viscosity turbulence models for engineering applications. AIAA J., 32(8), 1598-1605, 1994.

[87] Menter, F. R., Kuntz, M., Adaptation of eddy-viscosity turbulence models to unsteady separated flows behind vehicles. The aerodynamics of heavy vehicles : Trucks, busses and trains, Springer, Asilomer, Ca, 2002.

[88] Menter, F. R., Kuntz, M., Langtry, R., Ten years of industrial experience with the SST turbulence model. Turbulence, Heat and Mass Transfer, 2003.

[89] Meyer, M., Buter, T., Bowerson, R., Compressible turbulence measurements in a supersonic boundary layer with impinging shock wave interaction. AIAA Paper, 97-0427, 1997.

[90] Mikulla, V., Horstman, C., Turbulence measurements in hypersonic shock-wave boundary layer interaction flows. AIAA J., 14(5) : 568-75, 1976.

[91] Modarress, D., Johnson, D., Investigation of turbulent boundary-layer separation using laser velocimetry. AIAA J., 17(7) : 747-52, 1979.

[92] Moore, J. G., Moore, J., Realizability in two equation models. 30^{th} Fluid Dynamics Conference, AIAA Paper, 99-3779, 1999.

[93] Moríñigo, J. A., Salvá, J. J., Three-dimensional simulation of the self-oscillating flow and side-loads in an over-expanded subscale rocket nozzle. Proc. IMechE Vol. 220 Part G : J. Aerospace Engineering, 507-523, 2006

[94] Moríñigo, J. A., Salvá, J. J., Numerical study of the start-up process in an optimized rocket nozzle, Journal of aerospace science and Technology, Vol. 12, pp. 485-489, 2008.

[95] Morkovin, M.V., Effects of Compressibility on Turbulent Flow. The Mechanics of Turbulence, Favre, A. (ed.), Gordon and Breach, New York, 1964.

[96] Nasuti, F., Onofri, M., Viscous and inviscid vortex generation during startup of rocket nozzles, AIAA J., 36 (5) 809-815, 1998.

[97] Nasuti, F., Onofri, M., Shock structure in separated nozzle flows, Shock Waves, 19 : 229-237, 2009.

[98] Nave, L. H., and Coffey, G. A., Sea-Level Side-Loads in High Area Ratio Rocket Engines, AIAA J., 73-1284, 1973

[99] Nebbache, A., Pilinski, C., Pulsatory phenomenon in a thrust optimized contour nozzle, Aerospace Science and Technology, 10(2006), 295-308, 2006.

[100] Nguyen, A. T., Découlement instationaire et charges latérales dans les tuyéres propulsives. Ph.D Thesis, Université de Poitiers, 2003.

[101] Nguyen, A. T., Deniau, H., Girard, S., Alziary de Roquefort T., Unsteadiness of flow separation and end-effects regime in a thrust-optimized contour rocket nozzle. Flow, Turbulence and Combustion, 71 : 161-181, 2003.

[102] Onofri, M., Nasuti, F., Bongiorno, M., Shock generated vortices and pressure fluctuations in propulsive nozzles. AIAA Paper, 98-0777, 1998.

[103] Onofri, M., Nasuti, F., The physical origins of side loads in rocket nozzles, AIAA Paper, 99-2587, 1999.

[104] Mattsson, J., Högman, U., Torngren, L., A Sub-Scale Test Programme on Investigation of Flow Separation and Side-Loads in Rocket Nozzles, Proceedings of the 3rd European Symposium on Aerothermodynamics of Space Vehicles, ESA-ESTEC, Netherlands, November 24-26, 1998.

[105] Östlund, J., Jaran, M., Assessment of turbulence models in over expanded rocket nozzle flow simulations. 35^{th} Joint Propulsion Conference & Exhibit. AIAA Paper, 99-2583, 1999.

[106] Östlund, J., Flow Processes In Rocket Engine Nozzles With Focus On Flow Separation And Side-Loads, Licentiate Thesis, KTH Stockholm, 2002.

[107] Pao, Y. H., Structure of turbulent velocity and scalar fields at largewave numbers. Physics of Fluids, 8 : 1063-75, 1965.

[108] Pekkari, L.-O., Aeroelastic Stability of Supersonic Nozzles with Separated Flow, AIAA Paper, 93-2588, June 1993.

[109] Pekkari, L.-O., Aeroelastic Analysis of Side-Loads in Supersonic Nozzles with Separated Flow, AIAA Paper, 94-3377, June 1994.

[110] Pilinski, C., Etude numérique du decollément en tuyére supérsonique. Ph.D Thesis, INSA de Rouen, 2002.

[111] Pilinski, C., Abderrahmane, N., Flow separation in truncated ideal contour nozzle. Journal of turbulence, Vol ; 5, No. 1, 2004.

[112] Piomelli, U., Moin, P., Ferziger, J. H., Kim, J., Newapproximate boundary conditions for large-eddy simulations of wall-bounded flows. Physics of Fluids, 1 : 1061-68, 1989.

[113] Piomelli, U., Chasnov, J. R., Large-Eddy Simulations : theory and applications. In M. Hallback, D.S. Henningson, A.V. Johansson, and P.H. Alfredson, editors, Turbulence and Transition Modelling, pages 269-331. Kluwer Academic, 1996.

[114] Piomelli, U., Balaras, E., Pasinato, H., Squires, K. D., Spalart, P. R., The inner-outer layer interface in large eddy simulations with wall-layer models. Int. J. Heat and Fluid flow, 24 : 538-550, 2003.

[115] Piponniau, S., Dussauge, J. -P., Debiève J. F., and Dupont P., A simple model for low-frequency unsteadiness in shock-induce separation, J. of Fluid Mechanics, Vol. 629, pp. 87-108, 2009.

[116] Pirozzoli, S., and Grasso, F., Direct numerical simulation of impinging shock wave / boundary layer interaction at M=2.25, Physics of Fluides, Vol. 18, No. 065113, 2006.

[117] Poinsot, T. J., Lele, S. K., Boundary conditions for direct simulations of compressible viscous flows J. Computational Physics 101, 104-129,(1992)

[118] Radhakrishnan, S., Piomelli, U., Keating, A., Silva, L. A., Reynolds-averaged and large-eddy simulations of turbulent non-equilibrium flows. J. of Turbulence, 7(63) : 1-30, 2006.

[119] Rao, G. V. R., Recent Developments in Rocket Nozzle Configurations, ARS Journal, Vol. 31, No. 11, pp. 1488-1494, November 1961.

[120] Reda, D., Murphy, J., Shock-Wave turbulent boundary layer interactions in rectangular channels. AIAA Paper, No. 72-715, 1975.

[121] Reijasse, P., Bouvier, F., Servel, P., Experimental and numerical investigation of the cap-shock structure in over-expanded thrust-optimized nozzles. West-East High Speed Flow Field Conference Marseille, France, 2002.

[122] Reijasse, P., Aérodynamique des tuyères propulsives en sur-détente : décollement libre et charges latérales en régime stabilisé, PhD Thesis, Université de Paris VI, 2005.

[123] Reijasse, P., Coponet, D, Luyssen, J.,-M., Bar, V., Palerm, S., Oswald, J., Amouroux, F., Robinet, J.,-C., Kuszla, P., Wall pressure and thrust of a dual bell nozzle in a cold gas facility, Third EUCASS conference, Paris, 2009.

[124] Reynolds, O., On the Dynamical Theory of Incompressible Viscous Fluid and the Determination of the Criterion, Phil. Tran. Ro. Soc. Lon., Series A, Vol. 186, 123-161, 1874.

[125] Reynolds, W. C., The potential and limitations of direct- and large-eddy simulations. In Whither Turbulence Turbulence at the Crossroads, ed. J L Lumley, pp. 313-42. Heidelberg : Springer, 1990.

[126] Robinson, S. K., Coherent motions in the turbulent boundary layer. Annual Review of Fluid Mechanics, 23 : 601-39, 1991.

[127] Roe, P. L., Approximate Riemann solvers, parameter vectors, and difference schemes. J. of Computational Physics. 43 : 357-372, 1981.

[128] Rose, W., Johnson, D., Turbulence in a shock wave boundary layer interaction. AIAA J., 13(7) : 884-9, 1975.

[129] Rudy, D. H., Strikwerda, J. C. A non-reflecting outflow boundary condition for subsonic Navier-Stokes calculations, J. Computational Physics, 36, 55-70, 1981.

[130] Sagaut, P., Large Eddy Simulation of Incompressible Flows. Springer, 3 edition, 2006.

[131] Schmucker, R., Flow Processes in Over expanding Nozzles of Chemical Rocket Engines (published in German), Report TB-7,-10,-14, Technical University Munich, 1973.

[132] Schumann, U., Subgrid-scale model for finite difference simulation of turbulent flows in plane channels and annuli. J. Computational Physics, 18 : 376-404, 1975.

[133] Schumann, U., Realizability of Reynolds stress turbulence models, Physics of Fluids, 20, 721-725, 1977.

[134] Shimizu, T., Hiroshi, M., & Masatoshi K., Numerical study of restricted shock separation in a compressed truncated perfect nozzle. AIAA J., Vol. 44, No. 3., 2006.

[135] Smits, A., Dussauge, J. -P., Turbulent shear layers in supersonic flow. Woodbury, NY : American Institute of Physics, 1996.

[136] Spalart, P. R., Allmaras, S. R., A One-Equation Turbulence Model for Aerodynamic Flows. AIAA Paper 92-0439, 1992.

[137] Spalart, P. R., Jou, W. -H., Strelets, M., Allmaras, S. R., Comments on the feasibility of LES for wings, and on a hybrid RANS/LES approach. In C. Liu and Z. Liu, editors, Advances in DNS/LES. Greyden Press, 1997.

[138] Spalart, P. R., Deck, S., Shur, M. L., Squires, K. D., Strelets, M., Travin, A., A new version pf detached-eddy simulation, resistant to ambiguous grid densities. Theoretical Computational Fluid Dynamics, Vol. 20, Issue 3, pp. 181-195, 2006.

[139] Stanewsky, E., Shock-boundary layer interaction in transonic and supersonic flows. In : Transonic flows in turbomachinery. Von Karman Institute, Rhodes Saint-Genese, Belgium, Lecture Series No. 59, May 1973.

[140] Stark, R., Kwan, W., Quessard, F., Hagemann, G. and Terhardt, M., Rocket nozzle cold gas test campaigns for plume investigations. Paper presented at Fourth European Symposium on Aerothermodynamics for Space Vehicles, 2001.

[141] Strykowski, P. J., Krothapalli, A., Jendoubi, S., The effect of counterflow on the development of compressible shear layers. J. Fluid Mech, 308, pp. 63-96, 1996.

[142] Summerfield, M., Foster, C., and swan, W., Flow Separation in Overexpanded superonic Exhaust Nozzles, Jet Propulsion, pp. 319 ff., September-October, 1954.

[143] Takahashi, M., Ueda, S., Tomita, T., Tamura, H., Aoki, K., Transient flow simulation of a compressed truncated perfect nozzle, AIAA Paper, 2001-3681, 2001.

[144] Tenaud, C., Garnier, E., Sagaut, P., Evaluation of some high-order shock capturing schemes for direct numerical simulation of unsteady two-dimensional free flows, International J. for Numerical Methods in Fluids, Vol. 33, pp. 249-278, 2000.

[145] Terhardt, M., Hagemann, G., Frey, M., Flow Separation and Side-Load Behaviour of the Vulcain Engine, AIAA Paper, 99-2762, 1999

[146] Thivet, F., Knight, D. D., Zheltovodov, A. A., Maksimov, A. I., Some insights in turbulence modeling for crossing shock-wave/boundary-layer interactions, 38th Aerospace Science Meeting & Exhibit, AIAA Paper, 2000-0131, 2000.

[147] Travin, A., Shur, M ;, Strelets, M., Spalart, P. R., Physical and numerical upgrades in the detached-eddy simulation of complex turbulent flows. In : Friederich, R. and Rodi, W. (eds.), Advances in LES of Complex Flows, Proceedings of EUROMECH Colloquium 412, Kluwer Academic Publishers, Dordrecht/Boston/London. Fluid Mech. Applic. 65, 239-254, 2002.

[148] Verzicco, R., Mohd-Yusof, J., Orlandi, P., Haworth, D., Large-eddy simulation in complex geometric configurations using boundarybody forces. AIAA J., 38 : 427-33, 2000.

[149] Wallin, S., An efficient explicit algebraic Reynolds stress k-ω model (EARSM) for aeronautical applications. The Aeronautical Research Institute of Sweden (FFA), Bromma, Sweden, 1999.

[150] Wang, M., Moin, P., Computation of trailing-edge flow and noise using Large-Eddy Simulation. AIAA J., 38 : 2201-2209, 2000.

[151] Wang, M., Moin, P., Dynamic wall modeling for Large-Eddy Simulation of complex turbulent flows. Physics of Fluids, 14 : 2043-2051, 2002.

[152] Wang, T,-S., Transient three-dimensional startup side load analysis of a regeneratively cooled nozzle, Shock Waves, 19 : 251-264, 2009.

[153] Welch, P. D, The Use of Fast Fourier Transform for the Estimation of Power Spectra : A Method Based on Time Averaging Over Short, Modified Periodograms, IEEE Trans. Audio Electroacoustics, Vol. AU-15, pp.70-73, June 1967.

[154] Werner, H., Wengle, H., Large Eddy Simulation of turbulent flow over and around a cube in a plane channel. In F. Durst, R. Friedrich, B.E. Launder, F.W. Schmidt, U. Schumann, and J.H. Whitelaw, editors, Selected Papers from the 8th Symposium on Turbulent Shear Flows, pp. 155-168. Springer, 1993.

[155] Wilcox, D. C., Reassessment of the scale deterring equation for advanced turbulence models. AIAA J., 26, 1299-1310, 1988.

[156] Wilcox, D. C., Turbulence Modeling for CFD. DCW Industries, Inc. 1993.

[157] Wilcox, D., Turbulence modeling : an overview. AIAA Paper No. 2001-0724. Washington, DC : Am. Inst. Aeronaut. Astronaut, 2001.

[158] Yan, J., Mockett, C., Thiele, F., Investigation of Alternative Length Scale Substitutions in Detached-Eddy Simulation. Flow, Turbulence and Combustion, 74, pp. 85-102, 2005.

[159] Yule, A. J., Large structures in the mixing layer of a round jet, J. of Fluid Mechanics. 89, 413, 1978.

[160] Zheltovodov, A. A., Schulein, E., Yakovlev, V. N., Development of turbulent boundary layer under conditions of mixed interaction with shock and expansion waves. Preprint 28-83 ITAM, USSR Academy of Sciences, Siberian Branch, Novosibirsk, (in Russian), 1983.

[161] Zheltovodov, A., Pavlov, A., Schülein, E., Yakovlev, V., Interconnectionship between the flow separation and the direct and inverse transition at supersonic speed conditions. In :

Kozlov V, editor. Laminar-turbulent transition, IUTAM Symposium Novosibirsk/USSR 1984, Berlin, Heidelberg : Springer, pp. 503-8, 1985.

[162] Zheltovodov, A. A., Yakovlev, V. N., Stages of development, flowfield structure and turbulence characteristics of compressible separated flows in the vicinity of 2-D obstacles. Preprint 27-86 ITAM, USSR Academy of Sciences, Siberian Branch, Novosibirsk, (in Russian), 1986.

[163] Zheltovodov, A., Peculiarities of development and modeling possibilities of supersonic turbulent separated flows. In : Kozlov V, Dovgal A, editors. Separated flows and jets, IUTAM Symposium, Novosibirsk, USSR. Berlin : Springer, pp. 225-36, July 1990.

[164] Zheltovodov, A., Trofimov, V., Schülein, E., Yakovlev, V., An experimental documentation of supersonic turbulent flows in the vicinity of forward- and backward-facing ramps. Report No. 2030, Institute of Theoretical and Applied Mechanics, USSR Academy of Sciences, 1990.

[165] Zheltovodov, A., Trofimov, V., Filippova, E., Yakovlev, Y., Influence of turbulence change on the heat exchange under the conditions of supersonic separated flows. In : Abstracts : IUTAM Symposium on Separated Flows and Jets, USSR Academy of Sciences, Siberian Division, Novosibirsk, pp. 273-4, 1990.

Annexe A

Numerical Methods and Turbulence Modelling

A.1 Navier-Stokes Equations in General Coordinate System

The unsteady compressible, three dimensional Navier-Sokes equation in Cartesion coordinate system can be written as :

$$(U)_t + \underbrace{(E_i - E_v)_x}_{(E_t)_x} + \underbrace{(F_i - F_v)_y}_{(F_t)_y} + \underbrace{(G_i - G_v)_z}_{(G_t)_z} = 0 \tag{A.1}$$

where E_i, F_i, G_i are the convective fluxes and E_v, F_v, G_v are the viscous fluxes. The indices x, y, z and t indicates the partial derivatives in space and time respectively. The expressions for the convectives fluxes in x, y and z directions are given as follows :

$$E_i = \begin{bmatrix} \rho u \\ \rho u^2 + p \\ \rho uv \\ \rho uw \\ (E+p)u \end{bmatrix} \tag{A.2}$$

$$F_i = \begin{bmatrix} \rho v \\ \rho uv \\ \rho v^2 + p \\ \rho vw \\ (E+p)v \end{bmatrix} \tag{A.3}$$

$$G_i = \begin{bmatrix} \rho w \\ \rho uw \\ \rho vw \\ \rho w^2 + p \\ (E+p)w \end{bmatrix} \tag{A.4}$$

Similarly the expressions for the viscous fluxes are :

$$E_v = \begin{bmatrix} 0 \\ \tau_{xx} \\ \tau_{xy} \\ \tau_{xz} \\ u\tau_{xx} + v\tau_{xy} + w\tau_{xz} - q_x \end{bmatrix} \tag{A.5}$$

$$F_v = \begin{bmatrix} 0 \\ \tau_{xy} \\ \tau_{yy} \\ \tau_{yz} \\ u\tau_{xy} + v\tau_{yy} + w\tau_{yz} - q_y \end{bmatrix} \tag{A.6}$$

$$G_v = \begin{bmatrix} 0 \\ \tau_{xz} \\ \tau_{yz} \\ \tau_{zz} \\ u\tau_{xz} + v\tau_{yz} + w\tau_{zz} - q_z \end{bmatrix} \tag{A.7}$$

The viscous stresses are evaluated with the help of Newton's Law :

$$\begin{aligned} \tau_{xx} &= \frac{2}{3}\mu(2u_x - v_y - w_z) \quad ; \quad \tau_{xy} = \mu(u_y + v_x) \quad ; \\ \tau_{yy} &= \frac{2}{3}\mu(2v_y - u_x - w_z) \quad ; \quad \tau_{xz} = \mu(u_z + w_x) \quad ; \\ \tau_{zz} &= \frac{2}{3}\mu(2w_z - v_y - u_x) \quad ; \quad \tau_{yz} = \mu(u_z + w_y)\,. \end{aligned} \tag{A.8}$$

and the heat flux obey the Fourier law :

$$\begin{aligned} q_x &= -\lambda\frac{\partial T}{\partial x} \\ q_y &= -\lambda\frac{\partial T}{\partial y} \\ q_z &= -\lambda\frac{\partial T}{\partial z} \end{aligned} \tag{A.9}$$

The co-efficient of heat conductivity λ is expressed as :

$$\lambda = \frac{C_\mu \mu}{P_r} \tag{A.10}$$

$$\mu = T^{\frac{3}{2}}\left(\frac{1 + \frac{110.4}{T}}{T + \frac{110.4}{T}}\right) \tag{A.11}$$

At last, the viscosity coefficient μ is given by the Sutherland law and we suppose the air as a perfect gas. The expression for total specific energy is give as :

$$\rho E = \frac{p}{\gamma - 1} + \frac{1}{2}\rho\left(u^2 + v^2 + w^2\right) \tag{A.12}$$

Finallly the vector for the conservative variable U is defined by :

$$U = \begin{bmatrix} \rho \\ \rho u \\ \rho v \\ \rho w \\ \rho E \end{bmatrix} \tag{A.13}$$

A.2 Coordinate Transformation

Since the present research work is in the frame work of curvilinear coordinate system and the equations expressed in the previous section must be transformed for the discretization on the curvilinear mesh. To do this the following curvilinear coordinate system is used :

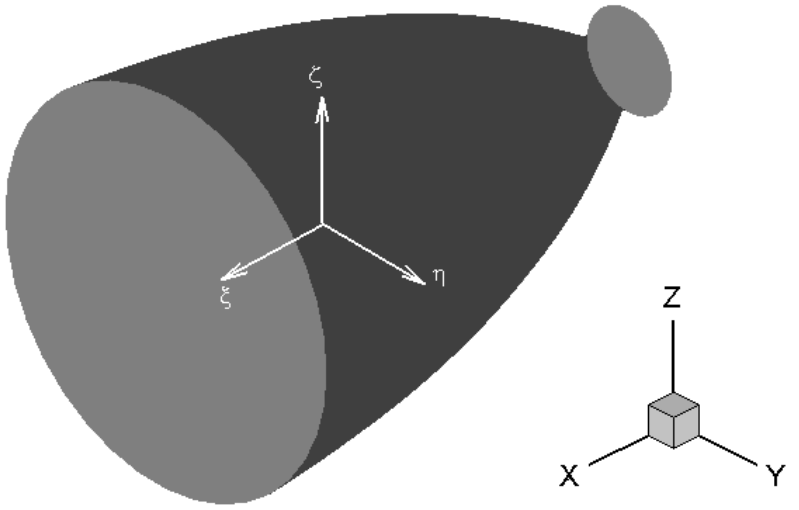

FIGURE A.1 – Co-ordinate transformation for the case of nozzle.

$$\begin{cases} \xi = \xi(x,y,z) \\ \eta = \eta(x,y,z) \\ \zeta = \zeta(x,y,z) \end{cases} \tag{A.14}$$

where ξ represents the longitudinal direction, whereas η and ζ are the transversal directions.

Then the Navier-Stokes equation becomes :

$$(U/J)_t + (\widehat{E}_t)_\xi + (\widehat{F}_t)_\eta + (\widehat{G}_t)_\zeta = 0 \tag{A.15}$$

With,

$$\begin{cases} \widehat{E}_t = \widehat{E}_i - \widehat{E}_v = E_t\frac{\xi_x}{J} + F_t\frac{\xi_y}{J} + G_t\frac{\xi_z}{J} \\ \widehat{F}_t = \widehat{F}_i - \widehat{F}_v = E_t\frac{\eta_x}{J} + F_t\frac{\eta_y}{J} + G_t\frac{\eta_z}{J} \\ \widehat{G}_t = \widehat{G}_i - \widehat{G}_v = E_t\frac{\zeta_x}{J} + F_t\frac{\zeta_y}{J} + G_t\frac{\zeta_z}{J} \end{cases} \tag{A.16}$$

where J is the Jacobian to change the variables :

$$J = \begin{vmatrix} \xi_x & \xi_y & \xi_z \\ \eta_x & \eta_y & \eta_z \\ \zeta_x & \zeta_y & \zeta_z \end{vmatrix} \tag{A.17}$$

Remarks :

when there is a source term S, the equation in the Cartesian coordinate system can be written as :

$$(U/J)_t + (\widehat{E}_t)_x + (\widehat{F}_t)_y + (\widehat{G}_t)_z = S \tag{A.18}$$

and after changing the variables, we have :

$$(U)_t + (\widehat{E}_t)_\xi + (\widehat{F}_t)_\eta + (\widehat{G}_t)_\zeta = \frac{S}{J} \tag{A.19}$$

A.2.1 Expression for Convective Flux

The convective fluxes of the Navier-Stokes equations in the curvilinear coordinate system are given as :

$$\widehat{E}_i = \begin{bmatrix} \rho\widehat{U} \\ \rho\widehat{U}u + \frac{\xi_x}{J}p \\ \rho\widehat{U}v + \frac{\xi_y}{J}p \\ \rho\widehat{U}w + \frac{\xi_z}{J}p \\ (E+p)\widehat{U} \end{bmatrix} \tag{A.20}$$

$$\widehat{F}_i = \begin{bmatrix} \rho\widehat{V} \\ \rho\widehat{V}u + \frac{\eta_x}{J}p \\ \rho\widehat{V}v + \frac{\eta_y}{J}p \\ \rho\widehat{V}w + \frac{\eta_z}{J}p \\ (E+p)\widehat{V} \end{bmatrix} \tag{A.21}$$

$$\widehat{G_i} = \begin{bmatrix} \rho\widehat{W} \\ \rho\widehat{W}u + \frac{\zeta_x}{J}p \\ \rho\widehat{W}v + \frac{\zeta_y}{J}p \\ \rho\widehat{W}w + \frac{\zeta_z}{J}p \\ (E+p)\widehat{W} \end{bmatrix} \tag{A.22}$$

where in the above expression $\widehat{U}$, $\widehat{V}$ & $\widehat{W}$ are the velocities in $\vec{\xi}$, $\vec{\eta}$ & $\vec{\zeta}$ directions, and are given as :

$$\begin{cases} \widehat{U} = u\frac{\xi_x}{J} + v\frac{\xi_y}{J} + w\frac{\xi_z}{J} \\ \widehat{V_t} = u\frac{\eta_x}{J} + v\frac{\eta_y}{J} + w\frac{\eta_z}{J} \\ \widehat{W_t} = u\frac{\zeta_x}{J} + v\frac{\zeta_y}{J} + w\frac{\zeta_z}{J} \end{cases} \tag{A.23}$$

A.3 Finite Volume Method

Unsteady Navier - Stokes equations are descretized according to the finite volume method.

$$\frac{\partial}{\partial t}\int\int\int_V U d\tau + \int\int\int_V div\left(\overline{\overline{H}}d\tau\right) = 0 \tag{A.24}$$

$$\int_\Omega \frac{\partial U}{\partial t}d\Omega + \int_\Omega \vec{div}\overline{\overline{H}}d\Omega = 0 \tag{A.25}$$

where $\overline{\overline{H}}$ is the tensor of components $\widehat{E_i} - \widehat{E_v}$; $\widehat{F_i} - \widehat{F_v}$; $\widehat{G_i} - \widehat{G_v}$ and V is the control volume. With the Gauss divergence theorem.

$$\frac{\partial}{\partial t}\int\int\int_V U d\tau + \int\int_S \overline{\overline{H}}.\vec{n}dS = 0 \tag{A.26}$$

$$\int_\Omega \frac{\partial U}{\partial t}d\Omega + \oint_\Omega \overline{\overline{H}}.\vec{n}dS = 0 \tag{A.27}$$

where $\vec{n}$ is the vector normal to the surface S and Ω is the computational domain, $d\Omega$ is the frontier, and $\vec{n}$ is the normal to the exterior, shown in the Fig. A.2.

Now let suppose that the computational domain is consist of hexahedral cell Ω_{ijk} of the surface $d\Omega_{ijk} = \sum_{l=1}^{6} s_l$. By applying this formulation to the control volume in the Fig. A.3, and we suppose that $\overline{\overline{H}}$ is constant at each face of the volume, we obtain the following discretization :

$$V(U^*)_t + \sum_{6}^{l=1} \overline{\overline{H}}_l \overline{S}_l = 0 \tag{A.28}$$

$$\frac{d}{dt}(\overline{\Omega}\vec{U}_{ijk}) + \vec{R}_{ijk} = 0 \tag{A.29}$$

where :

$$\vec{R}_{ijk} = (\widehat{E_t})^{n+1}_{j,k} - (\widehat{E_t})^{n}_{j,k} + (\widehat{F_t})^{n+1/2}_{j+1/2,k} - (\widehat{F_t})^{n+1/2}_{j-1/2,k} + (\widehat{G_t})^{n+1/2}_{j,k+1/2} - (\widehat{G_t})^{n+1/2}_{j,k-1/2} \tag{A.30}$$

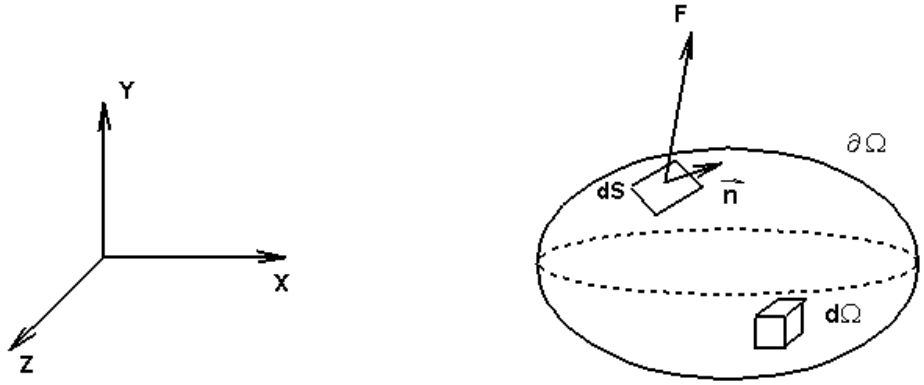

FIGURE A.2 – Computation Domain.

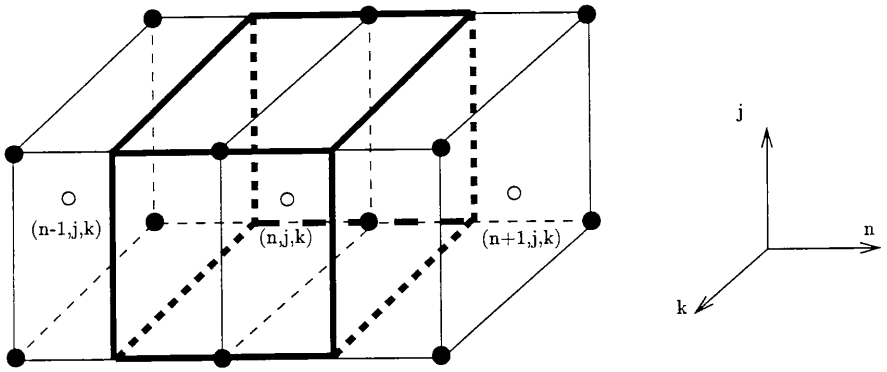

FIGURE A.3 – □ control volume ; ○ computation point ; and • mesh point.

Here V is the volume of the control volume and U^* is the averaged value of the state vector U on that control volume. The average value of the stat vector at the center of it. By performing the temporal discretization of first order the equation becomes :

$$V\frac{U_{j,k}^{t+\Delta t,n}-U_{j,k}^{t,n}}{\Delta t}(U^*)_t+\left(\widehat{E_t}\right)_{j,k}^{n+1/2}-\left(\widehat{F_t}\right)_{j,k}^{n-1/2}+\left(\widehat{F_t}\right)_{j+1/2}^{n}-\left(\widehat{F_t}\right)_{j-1/2}^{n}+\left(\widehat{G_t}\right)_{k+1/2}^{n}-\left(\widehat{G_t}\right)_{k-1/2}^{n}=0 \tag{A.31}$$

To describe the mesh in the longitudinal direction ξ, we prefer the usual notation with an index i, by using n.

A.3.1 Evolution of Matrix

The matrix is determined by the same manner as that employed for the equations of Navier-Stokes. If the vectors of the surfaces of the control volume are defined by :

$$S_{j,k}^{n+1/2} = \left| \begin{array}{c} s_1 \\ s_2 \\ s_3 \end{array} \right. \tag{A.32}$$

$$S_{j+1/2,k}^{n} = \left| \begin{array}{c} s_4 \\ s_5 \\ s_6 \end{array} \right. \tag{A.33}$$

$$S_{j,k+1/2}^{n} = \left| \begin{array}{c} s_7 \\ s_8 \\ s_9 \end{array} \right. \tag{A.34}$$

where $\vec{R}_{ijk} = \sum_6^{l=1} \overline{\overline{H}}_l \overline{S}_l$ we obtain :

$$\begin{array}{c} \frac{\xi_x}{J} = s_1; \frac{\xi_y}{J} = s_2; \frac{\xi_z}{J} = s_3 \\ \frac{\eta_x}{J} = s_4; \frac{\eta_y}{J} = s_5; \frac{\eta_z}{J} = s_6 \\ \frac{\zeta_x}{J} = s_7; \frac{\zeta_y}{J} = s_8; \frac{\zeta_z}{J} = s_9 \end{array} \tag{A.35}$$

J can be interpreted as the inverse of the control volume. However, this relatively simple calculation of matrix elements and Jacobien poses a problem in the case of mesh having discontinuity in the slope. This case is found, for example, in the case of nozzle has a slope discontinuity. The throat region of the nozzle we have big curvature and in that region the computation point C_1 does not correspond to the center of the control volume (see Fig. A.4).

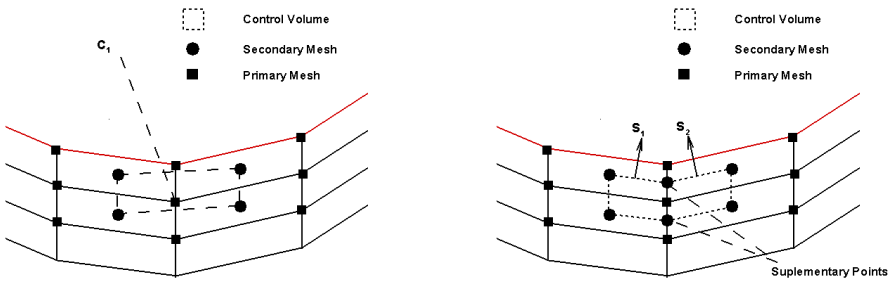

FIGURE A.4 – Mesh correction in the nozzle throat region.

But when we modify the definition of control volume for the point C_1 we are forced to include two supplementary points. Now the computation point C_1 correspond to the center of the control volume. Note that this cell is in fact associated with the two cells in the first case, the surface vector here is the sum of the two surface vectors S_1 and S_1.

A.4 Discretization of Navier-Stokes Equations

The computational domain is discretized by using the finite volume method, which means we are interested in the average value of the stat vectors U on the control volume. The average value of the stat vector on the volume control is taken equal to the value of the vector in the center of it.

The mesh is structured, and one can compute the three indices (i, j, k) of the directions (ξ, η, ζ) respectively . Again considering the first order discretization in time the equations cas be written as :

$$J_{i,j,k}\frac{U^{n+1}_{i,j,k}-U^{n}_{i,j,k}}{\Delta t}+(\widehat{E}_t)^{n+\alpha}_{i+\frac{1}{2},j,k}-(\widehat{E}_t)^{n+\alpha}_{i-\frac{1}{2},j,k}+(\widehat{F}_t)^{n+\alpha}_{i,j+\frac{1}{2},k}-(\widehat{F}_t)^{n+\alpha}_{i,j-\frac{1}{2},k} +(\widehat{G}_t)^{n+\alpha}_{i,j,k+\frac{1}{2}}-(\widehat{G}_t)^{n+\alpha}_{i,j,k-\frac{1}{2}}+J_{i,j,k}S^{n}_{i,j,k}=0 \tag{A.36}$$

If the system is written in explicit form then $\alpha = 0$. In the case where $\alpha = 1$ the system can be written in the implicit form and is given as follows :

$$J_{i,j,k}\frac{U^{n+1}_{i,j,k}-U^{n}_{i,j,k}}{\Delta t}+(\widehat{E}_t)^{n+1}_{i+\frac{1}{2},j,k}-(\widehat{E}_t)^{n+1}_{i-\frac{1}{2},j,k}+(\widehat{F}_t)^{n+1}_{i,j+\frac{1}{2},k}-(\widehat{F}_t)^{n+1}_{i,j-\frac{1}{2},k} +(\widehat{G}_t)^{n+1}_{i,j,k+\frac{1}{2}}-(\widehat{G}_t)^{n+1}_{i,j,k-\frac{1}{2}}+J_{i,j,k}S^{n}_{i,j,k}=0 \tag{A.37}$$

A.4.1 Linearization of Flux

Not knowing the expression of fluxes at time step $n+1$ we will linearize the flux by using first order Taylor decomposition. For the flux in the direction η, it is given as follows :

$$(\widehat{F}_t)^{n+1}_{i,j+\frac{1}{2},k}=(\widehat{F}_t)^{n}_{i,j+\frac{1}{2},k}+\left[\frac{\partial(\widehat{F}_t)_{i,j+\frac{1}{2},k}}{\partial U_{i,j,k}}\right]^{n}\delta^{n+1}U_{i,j,k}+\left[\frac{\partial(\widehat{F}_t)_{i,j+\frac{1}{2},k}}{\partial U_{i,j+1,k}}\right]^{n}\delta^{n+1}U_{i,j+1,k} \tag{A.38}$$

that, $\delta^{n+1}U_{i,j,k}=U^{n+1}_{i,j,k}-U^{n}_{i,j,k}$

Now for the explicit expression of the linearization of flux, now onwards we will determine the expression for the convective flux.

A.4.2 Roe Scheme

Here we are presenting the Roe scheme [26] for the resolution of scalar law of conservation and then the extension of this scheme in the case of mono-dimensional Euler equation.

$$\frac{\partial w}{\partial t}+\frac{\partial f(w)}{\partial x}=0 \tag{A.39}$$

with the initial condition at time t is given below :

$$w^t(x)=\begin{cases} w^t_j & x<x_{j+1/2} \\ w^t_{j+1} & x>x_{j+1/2}\end{cases} \tag{A.40}$$

This problem of Riemann then linearized by :

$$\frac{\partial w}{\partial t} + \lambda(x_{j+1}, x_j)\frac{\partial w}{\partial x} = 0 \tag{A.41}$$

where $\lambda(x_{j+1}, x_j)$ is a function of two variables defined by :

$$\lambda(x,y) = \begin{cases} \frac{f(x)-f(y)}{x-y} & if \ \ x \neq y \\ \frac{df}{dx}(x) & if \ \ x = y \end{cases} \tag{A.42}$$

The solution of the equation (A.41) is a discontinuity which propagate with the speed $\lambda(x_{j+1}, x_j)$. The Roe scheme is obtained for choosing the numerical flux $h_{j+1/2}$ an upwind value following the sign of the velocity of the wave propagation $\lambda(x_{j+1}, x_j$. More precisely if this velocity is positive, we will choose $h_{j+1/2} = f(w_j)$, compatible choice with the fact that the physical information propagate from upstream to downstream ; conversely, for the negative speed, we take the upwind of downwind, either : $h_{j+1/2} = f(w_{j+1})$. The numerical flux at the interface $j+1/2$ can be expressed under the following form :

$$h_{j+1/2} = \frac{1}{2}\left[f(w^t_{j+1}) + f(w^t_j) - |\lambda(x_{j+1}, x_j)|(w^t_{j+1} - w^t_j)\right] \tag{A.43}$$

A.4.3 One Dimensional Euler Equation

Like in the case of scalar conservative law, the problem of Riemann is linearized under the form [26] :

$$U_t + \widetilde{A}(U^t_j, U^t_{j+1})U_x = 0 \tag{A.44}$$

The properties and the determination of the Roe matrix $\widetilde{A}$ under the framework of unsteady Euler Equation will not be discussed here. Roe [26] showed that this matrix identify a Jacobien matrix $\frac{\partial F}{\partial U}$ calculated on a point called as Roe average point. As one of the properties of the Roe matrix is to be diagonisable, it is possible to replace the linearized problem by P independent differential equations for the P components of the characteristic variables W. The system (A.44) is therefore equivalent to :

$$W_t + \widetilde{\Lambda} W_x = 0 \tag{A.45}$$

where $\widetilde{\Lambda}$ represente la diagonal matrix of Eigen values of $\widetilde{A}$. By assinging the matices of left and right Eigen values by $\widetilde{R}$ and $\widetilde{R}^{-1}$ respectively, we have the following relation :

$$\widetilde{A} = \widetilde{R}\widetilde{\Lambda}\widetilde{R}^{-1} \ \ at \ \ W = \widetilde{\Lambda}^{-1}U \tag{A.46}$$

We note that the w_i components of vector W and the $\widetilde{\lambda}_i$ Eigen values of the matrix $\widetilde{A}$, we obtain P scalar equations similar to the equation (A.41).

$$\frac{\partial w_i}{\partial t} + \widetilde{\Lambda}_i \frac{\partial w_i}{\partial x} = 0 \tag{A.47}$$

Applying the Roe scheme for each component of the characteristic variables, we construct an expression of the numerical flux $h_{j+1/2}$ in the Eigen space of the Roe matrix. This flux verifies the relationship :

$$\widetilde{R}^{-1} h_{j+1/2} = \frac{1}{2}\left[\widetilde{\Lambda} W_{j+1} + \widetilde{\Lambda} W_j - |\widetilde{\Lambda}|(W_{j+1} - W_j)\right] \tag{A.48}$$

Now looking back to the conservative variables by multiplying this equation by $\widetilde{R}$, which gives :

$$h_{j+1/2} = \frac{1}{2}\left[\widetilde{A} U^t_{j+1} + \widetilde{A} U^t_j - |\widetilde{A}_{j+1/2}|(U^t_{j+1} - W^t_j)\right] \tag{A.49}$$

By re-arranging the terms that comes in the difference of two fluxes $h_{j+1/2}$ and $h_{j-1/2}$ and using the following property of the Roe linearization.

$$E_t(U) - E_i(V) = \widetilde{A}(U - V) \tag{A.50}$$

We easily show that the flux at the interface $j + 1/2$ can be written under the form :

$$h_{j+1/2} = \frac{1}{2}\left[F(U^t_{j+1}) + F(U^t_j) - |\widetilde{A}_{j+1/2}|(U^t_{j+1} - F(U^t_j))\right] \tag{A.51}$$

The absolute value of the Roe matrix is defined by :

$$|\widetilde{A}_{j+1/2}| = \widetilde{R}_{j+1/2} |\widetilde{\Lambda}_{j+1/2}| \widetilde{R}^{-1}_{j+1/2} \tag{A.52}$$

This scheme allows capturing the shock wave very well and it is more economical in computing time that that of Osher's or Gudunov's scheme. It also allows good resolution of slip line and therefore the boundary layers. Unfortunately, this pattern can lead to non-physical solutions when the one Eigen value of the Roe matrix canceled [8]. Various techniques exist to cope with this problem.

A.4.4 Explicit Discretization of Convective Flux of First Order in Space

After having justified the extension of the Roe scheme adopted in the case of multi-dimensional systems, we will present the crucial issue involved in such scheme namely "Entropy Correction".

A.4.5 Application of Roe Scheme

The purpose of this paragraph is to present the methodology adopted to implement the Roe scheme to unsteady three-dimensional Euler equations. The presentation of different space using that the data Eigen vector matrix is essential to show that the choice of this is not indifferent and to expose three modes of calculations parameters which involved in the Harten entropy correction.

A.4.6 Multi-dimensional System

Euler equation in generalized co-ordinate system can be written as :

$$(U/J)_t + (\widehat{E}_i)_\xi + (\widehat{F}_i)_\eta + (\widehat{G}_i)_\zeta = 0 \tag{A.53}$$

For the multi-dimensional hyperbolic system the theory analogue to the one described in previous paragraph for hyperbolic system mono-dimensional is used. It is formally extended to the previous scheme by considering each direction of the space separately. This decomposition however introduces a dependence viz a viz the mesh [10]. More precisely, in the case where the discontinuity is aligned with the grid lines, the decomposition on two mono-dimensional problems is satisfied. Such schemes, which are based on the resolution of Riemann problem has been especially developed by Roe [27] and van-Leer [16]. As the mesh used is not suitable to capture the form of shock, we will face the numerical problems for capturing shock waves which are slanted compared with respect to the mesh. The three directions are being resolved separately and in an equivalent manner, we present exclusively the formulation of the numerical flux $\widehat{E}_i$ according to ξ direction described by the exponent n.

A.4.7 Expression of the Numerical Flux

We note that the vector $\widehat{U}$ is defined by : $\widehat{U} = U/J$ and $\widehat{A}$ the jacobian matrix $\frac{\partial \widehat{E}_i}{\partial \widehat{U}}$. Then we apply the Roe scheme to the equation :

$$(\widehat{U})_t + (\widehat{E}_i)_\xi \tag{A.54}$$

We define the curvilinear co-ordinate system (ξ, η, ζ), locally orthogonal in space. The transformation $E_i^{'}, F_i^{'}, G_i^{'}$ of fluxes are $\widehat{E}_i, \widehat{F}_i, \widehat{G}_i$ is the same as one in the expressions of the Cartesian co-ordinate system by replacing Cartesian velocity components u, v, w by the components $u^{'}, v^{'}, w^{'}$ in the local Cartesian co-ordinate system. Here $A^{'}$ is the Jacobian matrix $\frac{\partial E_i^{'}}{\partial U^{'}}$, $U^{'}$ represent the transformation of the stat vector U. The Eigen values and vectors of the matrix $A^{'}$ are the same as that we have obtained in the Cartesian system. If we assign $\widehat{\lambda}_{\xi l}$ the Eigen values of the matrix $\widehat{A}$, we obtain the following relations by using the transformation T :

$$(\widehat{\lambda}_{\xi l})_{l=1,5} = \sqrt{\xi_x^2 + \xi_y^2 + \xi_z^2}(u^{'} - c, u^{'}, u^{'}, u^{'}, u^{'} + c) \tag{A.55}$$

The matrix R_ξ of the right Eigen vectors of the matrix $\widehat{A}$ can be written as :

$$R_\xi = \begin{pmatrix} 1 & 0 & 0 & 1 & 1 \\ u - s_1^{'} c & s_4^{'} & s_7^{'} & u & u + s_1^{'} c \\ v - s_2^{'} c & s_5^{'} & s_8^{'} & v & v + s_2^{'} c \\ w - s_3^{'} c & s_6^{'} & s_9^{'} & w & w + s_3^{'} c \\ h_t - u^{'} c & u^{'} & w^{'} & 1/2q^2 & h_t + u^{'} c \end{pmatrix} \tag{A.56}$$

where $\frac{1}{2}q^2$ represents the kinetic energy $1/2(u^2+v^2+w^2)$. The expression of the upwind flux in the directions ξ at the interface $n+1/2$ can be written as :

$$\Phi_\xi = R_\xi \left| Diag(\widehat{\lambda}_{\xi l}) \right| R_\xi^{-1} \left(\widehat{U}^{n+1} j,k - \widehat{U}^n j,k \right) \tag{A.57}$$

In the same way, in the direction η, the upwind flux at the interface $j+1/2$ is written as :

$$\Phi_\eta = R_\eta \left| Diag(\widehat{\lambda}_{\eta l}) \right| R_\eta^{-1} \left(\widehat{U}^{n+1} j,k - \widehat{U}^n j,k \right) \tag{A.58}$$

The matrices used to calculate the flux at the interface $n+1/2$ are evaluated effectively at that interface. The vectors $\widehat{U}_{j,k}^{n+1}$ and $\widehat{U}_{j,k}^{n}$ are respectively given by $\widehat{U}_{j,k}^{n+1}/J_{j,k}^{n+1/2}$ and $\widehat{U}_{j,k}^{n}/J_{j,k}^{n+1/2}$. It is than possible that it does not come explicitly the vector $\widehat{U}$ by dividing the Eigen values $(\widehat{\lambda_{\xi l}}_{l=1,5})$ by the jacobian of the transformed co-ordinate. Later we will note that the $\lambda_{\xi l}$ is the value of fraction $\widehat{\lambda}_{\xi l}/J$. Then the upwind flux cen be simply written as :

$$\Phi_\xi = R_\xi \left| Diag(\widehat{\lambda}_{\xi l}) \right| R_\xi^{-1} \left(\widehat{U}^{n+1} j,k - \widehat{U}^n j,k \right) \tag{A.59}$$

A.4.8 Entropy Correction

In this section, the formulation for the entropy correction proposed by Harten [8] is given.

A.4.9 Principle of This Correction

Lets us consider the following two scalar equations :

$$(U)_t + (E_i)_x = 0 \tag{A.60}$$

$$(U)_t + (E_i)_x = \nu U_{xx} \tag{A.61}$$

In the case of equation (A.61), which is time parabolic, there are mathematical results that assure the existence and uniqueness of a regular solution. However, no result is similar to the first equation (A.60). It shows, that the solution limit of the equation (A.61), when the viscosity ν tends to zero corresponds to a solution also called unique physical solution, also called the entropic solution of equation (A.60). As the upwind flux is treated as a dissipation term, the use of the upwind scheme allows us to get the physical solution of the equation [10]. However, as the upwind flux cancelled with the Eigen value of the Roe matrix, Harten [8] proposed modify to the expression of upwind fluxes to prevent them from cancellation. He suggested that replace the modulus of Eigen values of Roe matrix by a function called Harten function and is noted as Ψ. Harten function is defined by :

$$\Psi_\xi = \begin{cases} |x| \;\; si \;\; |x| \geq \delta \\ \frac{x^2+\delta^2}{2\delta} \;\; si \;\; |x| \leq \delta \end{cases} \tag{A.62}$$

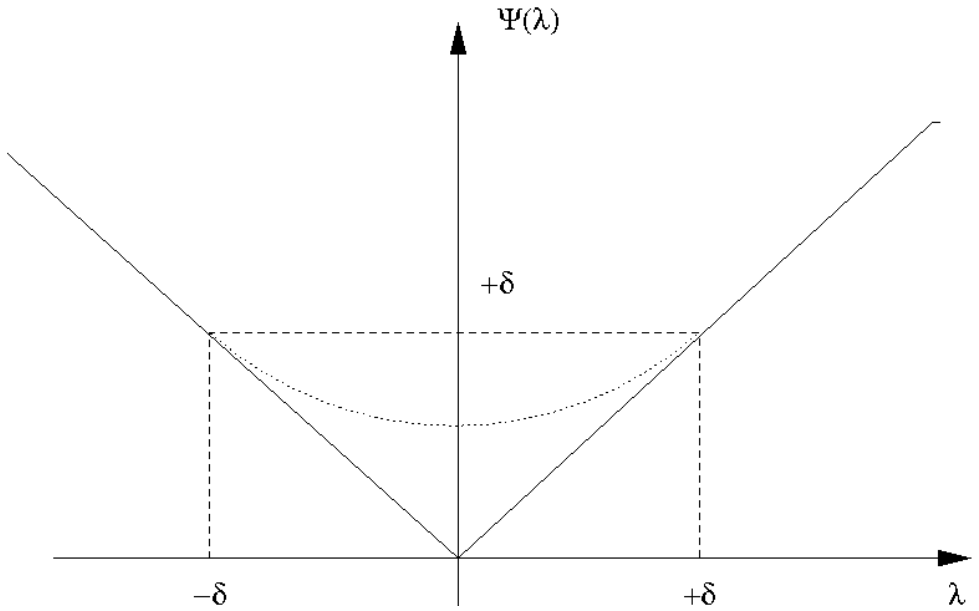

FIGURE A.5 – Correction Module of Eigen values by Harten's Correction.

where δ is a positive parameter, it is designated in the following as the Harten correction. Then the expression of the upwind flux at the interface $n+1/2\Psi_\xi$ becomes :

$$\Phi_\xi = R_\xi Diag(\Psi(\lambda_{\xi l}))|R_\xi^{-1}\left(U^{n+1}j,k - U^n j,k\right) \tag{A.63}$$

Another possible interpretation of the entropy correction based on the following observations : the equation (A.61), in general does not gives regular solution in time even if the initial condition are regular. In effect, because of non-linear flux E_i, there is a development of discontinuity after a finite time. Among the different type of solutions of the discontinuity equation, only some are physically acceptable. If we consider for example a discontinuity propagate with the speed s, one can see from the theory of characteristics [18] that from characteristic speed of both sides of the discontinuity, we obtain an expansion converging the characteristic lines. A solution of such "compression shock" is acceptable while a solution of type "expansion fan" is not. Definitely, the entropy correction permits us to select the discontinuity having a physical sense. As the solution of shock or expansion fan are associated to the Eigen values $u+c$ and $u-c$, the correction of Harten does not involve full certainty that these two Eigen values. The third presentation of the possible correction of entropy uses are mathematical arguments. The solution denoted V of the equation is called entropic solution, if it verifies :

$$\frac{\partial \Theta}{\partial t}(V) + \frac{\partial F}{\partial x}(V) \leq 0 \tag{A.64}$$

For all convex function Θ of U equally called entropy function. F is called entropy flux and verify :

$$\frac{\partial \Theta}{\partial U}\frac{\partial E_i}{\partial U} = \frac{\partial F}{\partial U} \tag{A.65}$$

The definition justify the so-called "Entropic solution" since the entropy in the thermodynamic sense consist of an entropy function (Θ) according to the definition given above.

A.4.10 Determination of Parameters for Harten's Correction

The first tricky point is the choice of the Eigen values for which this correction should be applied. It was shown in the preceding paragraph only Eigen values $u \pm c$ are affected by this correction. However, if the velocity component u is cancelled, the upwind flux is also cancelled so that the scheme is a locally reduced to the center scheme. The application of the Harten correction of the Eigen value u seems interesting to avoid this degeneration of upwind scheme. The cancellation of this Eigen value u occurs predominantly at the frontier of the axis of symmetry on the wall. However, the addition of artificial dissipation is not mandatory for all cases of calculation. Gaitonde [6] and Muller [19] applied the Harten correction exclusively to these Eigen values $u \pm c$ to calculate the flux on a compression ramp, but they applied to the three Eigen values for the calculation of blunt bodies. The addition of this correction for Eigen value u is essential to properly calculate the flux in the vicinity of symmetry axis in the case of a three-dimensional flow (phenomena of "Carbuncle") [24]. The second difficulty of Harten correction reside in the determination of parameter δ. The calculation of the boundary layer is very sensitive to the level of dissipation of the numerical scheme, so the choice of the high value of Harten correction leads to the loss of precision in the resolution of the scheme. In contrast, a too low value of this parameter leads the appearance of the expansion shock and oscillations. Initially, Harten chooses a constant value of this parameter. This choice is sufficient for the calculation of boundary layer of flat plate or compression with attached shock. However, the presence of strong shock wave obliges us to use a high value of this parameter. The formulations of parameter Harten are divided into two categories according to whether the expression of this parameter is the same for all directions or not.

A.5 Second Order TVD Scheme

The numerical schemes of the first order in space are generally too dissipative to calculate the boundary layers and have tendency to spread out the discontinuities. However, the direct use of the scheme of the second order leads to the generation of oscillations. The study of the formulation of these parasitic oscillations highlighted that existence is related to them to the stressing of extrema or with the local creation of new extrema of the function U. This phenomenon results in an increase in the total variation of U according to time. However, as we know that the entropic solution of a scalar law of conservation has Total Variation Diminishing (TVD). So that property TVD is respected by the discrete solution, a new class of scheme was developed Van-Leer [12],[13], [14] & [15] , Sweby [33] and by Osher and Chakravarthy [22], [21] & [23]. These schemes are particularly robust and make it possible to capture strong discontinuities without developing parasitic oscillations. However, the respect of property TVD imposes that the scheme is of first order at the extrema of the function U. The Total variation TV of the variable u solution of a law of non linear scalar hyperbolic conservation of type :

$$u_t + f(u)_x = 0 \tag{A.66}$$

is defined as :

$$TV = \int \left| \frac{\partial u}{\partial x} \right| dx \tag{A.67}$$

We show that the total variation of this solution never increases. We define the total variation of the discrete solution of a numerical calculation by :

$$TV(u) = \sum_j \left| u_{j+1} - u_j \right| \tag{A.68}$$

The numerical scheme is called total variation diminishing of the solution at instant $t + \delta t$ is inferior to that at the instant t :

$$TV(u^{t+\delta t} \leq TV(u^t) \tag{A.69}$$

The scheme of second order in that study is constructed to satisfy that property. To achieve the second order of the Roe scheme, two methods are possible as was very well given in Yee [35] : the method MUSCL and the method non MUSCL. In the method MUSCL (Monotone), we change the values of states U_{j+1} et U_j to calculate the flux at the interface $j+1/2$. In the other case, corresponding to the technical implemented in the code TGNS3D, the flux at the interfaces is directly modified. Thus, in the direction η, the convective flux at the interface $j+1/2$ is written as :

$$(\widehat{F_i})_{j+1/2} = (\widehat{F_i})^I_{j+1/2} + (\widehat{F_i})^{II}_{j+1/2} \tag{A.70}$$

ou $(\widehat{F_i})^I_{j+1/2}$ represent the flux given by the scheme of first order. Two formulation of the second $(\widehat{F_i})^{II}_{j+1/2}$ have been coded in TGNS3D.

A.5.1 Slope Limiter, TVD Property

The role of this function has cancelled the correction of the second order in presence of the oscillations. The limiters used here are the real functions of two variables x & y, such that :

$$\Gamma(\lambda x, \lambda y) = \lambda \Gamma(x, y)$$

It is possible to write this limiter in the ratio $r = y/x$

$$\Gamma(x, y) = x\Gamma(1, r) = x\gamma(r)$$

We use the relation, on can show that :

$$\gamma(\frac{1}{r}) = \frac{\gamma r}{r}$$

The properties of the Osher-Chakarvarthy schemes are presented in the frame of the resolution of the scalar equation :

$$u_t + cu_x = 0$$

The numerical flux at the interface $j+1/2$ can be written un the form :

$$h_{j+1/2} = cu_j + \frac{1+\Phi}{4}(\widetilde{dF_2^+}) + \frac{1-\Phi}{4}(\widetilde{dF_1^+})$$

We show that the sufficient conditions for the scheme to be TVD are :

$$1 + \frac{1}{2}\frac{q(r_j)}{r_j} - \frac{1}{2}q(r_{j-1}) \geq 0$$

where $r_j = \frac{u_j - u_{j-1}}{u_{j+1} - u_j}$ and the function q is defined by :

$$q(r) = \frac{1+\Phi}{2}\Gamma(1,br) + \frac{1-\Phi}{2}r\Gamma(1,\frac{b}{r})$$

The sufficient conditions are equally translated by :

$$\forall r,\ \frac{q(r)}{r} \leq 2 \ et \ q(r) \leq 2$$

In the case whee the parameter of compression is equal to 1, the function q can be written as :

$$q(r) = \frac{1+\Phi}{2}\gamma(r) + \frac{1-\Phi}{2}r\gamma(\frac{1}{r})$$

The function $q(r)$ reduces to $\gamma(r)$. It is shown in the theory of TVD scheme for the resolution of the scalar conservation law, a sufficient condition for the property of TVD scheme is only the graph of the slope limiters $\gamma(r)$ which includes in the grey area of the Fig. A.6.

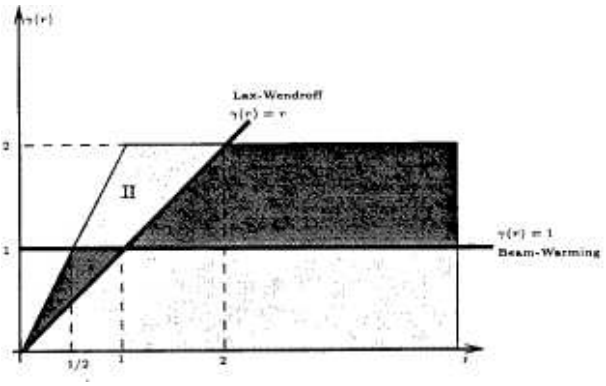

FIGURE A.6 – TVD Domain

One can notice that the slopes are of opposite sign ($r \leq 0$), the limiter is zero so the scheme becomes first order. Also note that the extremum is characterized by a change of sign of the slope, therefore scheme is degenerated to first order in vicinity of extremum. A slope limiter which is a part of the graph is located in the area, II, also a total variation decreasing (TVD), it is too much compressed in the sense that the extrema will spread. Sweby numerically found that a sinusoidal wave will transform into a square signal with this type of slope limiter. In this study has been used, i.e., van Albada & minmod. These limiters are defined by :

Minmod

$$\gamma(r) = max(0, min(1, r))$$

van Albada

$$\gamma(r) = \frac{r+|r|}{1+|r|}$$

In the Fig. A.6, the graphs of these limiters are presented. The limits of TVD domain are achieved for the minmod limiter (most dissipative). In the cases where the compression parameter is different from 1, the sufficient condition for the Chakarvarthy-Osher scheme is carried by

TVD on the slop limiter and to the compression factor. In case where we use the slope limiter minmod, the conditions lead to a existence of a superior b_{max} of variations of b as a function Φ.

$$b_{max} = \frac{3-\Phi}{1-\Phi}$$

A.6 Extension of Conservation Laws

Three-dimensional Euler equations in the conservative form are given as :

$$\frac{\partial U}{\partial t} = \frac{\partial F}{\partial x} + \frac{\partial G}{\partial y} + \frac{\partial H}{\partial z} = 0$$

with :

$$U = \begin{bmatrix} \rho \\ \rho u \\ \rho v \\ \rho w \\ \rho E \end{bmatrix} \; E_i = \begin{bmatrix} \rho u \\ \rho u^2 + p \\ \rho uv \\ \rho uw \\ (E+p)u \end{bmatrix} \quad F_i = \begin{bmatrix} \rho v \\ \rho uv \\ \rho v^2 + p \\ \rho vw \\ (E+p)v \end{bmatrix} \quad G_i = \begin{bmatrix} \rho w \\ \rho uw \\ \rho vw \\ \rho w^2 + p \\ (E+p)w \end{bmatrix}$$

The above equation can be written in the non-conservative form :

$$\frac{\partial U}{\partial t} = A\frac{\partial U}{\partial x} + B\frac{\partial U}{\partial y} + C\frac{\partial U}{\partial z} = 0$$

where the Jacobian of the fluxes A, B and C are defined as :

$$A = \frac{\partial F}{\partial U} \;\; B = \frac{\partial G}{\partial U} \;\; A = \frac{\partial H}{\partial U}$$

The three terms are the matrices 5×5 :

$$A = \begin{vmatrix} 0 & 1 & 0 & 0 & 0 \\ -u^2 + \frac{\gamma-1}{2}\vec{u}^2 & (3-\gamma)u & -(\gamma-1)v & (\gamma-1)w & \gamma-1 \\ -uv & v & u & 0 & 0 \\ -uw & w & 0 & u & 0 \\ -\gamma uE + (\gamma-1)u\vec{u}^2 & \gamma E - \frac{\gamma-1}{2}(\vec{v}^2 + 2u^2) & -(\gamma-1)uv & (\gamma-1)uw & \gamma u \end{vmatrix}$$

$$B = \begin{vmatrix} 0 & 0 & 1 & 0 & 0 \\ -uv & v & u & 0 & 0 \\ -v^2 + \frac{\gamma-1}{2}\vec{v}^2 & -(\gamma-1)u & (3-\gamma)v & -(\gamma-1)w & \gamma-1 \\ -vw & 0 & w & v & 0 \\ -\gamma vE + (\gamma-1)v\vec{v}^2 & -(\gamma-1)uv & \gamma E - \frac{\gamma-1}{2}(\vec{v}^2 + 2v^2) & -(\gamma-1)vw & \gamma v \end{vmatrix}$$

$$C = \begin{vmatrix} 0 & 0 & 0 & 1 & 0 \\ -uw & w & 0 & u & 0 \\ -vw & 0 & w & v & 0 \\ -w^2 + \frac{\gamma-1}{2}\vec{v}^2 & -(\gamma-1)u & -(\gamma-1)v & (3-\gamma)w & \gamma-1 \\ -\gamma wE + (\gamma-1)w\vec{v}^2 & -(\gamma-1)uw & -(\gamma-1)vw & \gamma E - \frac{\gamma-1}{2}(\vec{v}^2 + 2w^2) & \gamma w \end{vmatrix}$$

These matrices are diagonisable, and their Eigen values can be written respetively as below :

$$\Lambda_A = L_x A R_x \quad \Lambda_B = L_y B R_y \quad \Lambda_C = L_z C R_Z$$

with :

$$\Lambda_A = \begin{vmatrix} u & & & & \\ & u & & & \\ & & u & & \\ & & & u+c & \\ & & & & u-c \end{vmatrix}$$

$$\Lambda_B = \begin{vmatrix} v & & & & \\ & v & & & \\ & & v & & \\ & & & v+c & \\ & & & & v-c \end{vmatrix}$$

$$\Lambda_C = \begin{vmatrix} w & & & & \\ & w & & & \\ & & w & & \\ & & & w+c & \\ & & & & w-c \end{vmatrix}$$

$$R_x = \begin{vmatrix} 1 & 0 & 0 & \frac{\rho}{2c} & \frac{\rho}{2c} \\ u & 0 & 0 & \frac{\rho}{2c}(u+c) & \frac{\rho}{2c}(u-c) \\ v & 0 & -\rho & \frac{\rho v}{2c} & \frac{\rho v}{2c} \\ w & \rho & 0 & \frac{\rho w}{2c} & \frac{\rho w}{2c} \\ \frac{\vec{v}^2}{2} & \rho w & -\rho v & \frac{\rho}{2c}(H+cu) & \frac{\rho}{2c}(H-cu) \end{vmatrix}$$

$$R_y = \begin{vmatrix} 0 & 1 & 0 & \frac{\rho}{2c} & \frac{\rho}{2c} \\ 0 & u & \rho & \frac{\rho u}{2c} & \frac{\rho u}{2c} \\ 0 & v & 0 & \frac{\rho}{2c}(v+c) & \frac{\rho}{2c}(v-c) \\ -\rho & w & 0 & \frac{\rho w}{2c} & \frac{\rho w}{2c} \\ -\rho w & \frac{\vec{v}^2}{2} & \rho u & \frac{\rho}{2c}(H+vc) & \frac{\rho}{2c}(H-vc) \end{vmatrix}$$

$$R_z = \begin{vmatrix} 0 & 0 & 1 & \frac{\rho}{2c} & \frac{\rho}{2c} \\ 0 & -\rho & u & \frac{\rho u}{2c} & \frac{\rho u}{2c} \\ \rho & 0 & v & \frac{\rho v}{2c} & \frac{\rho v}{2c} \\ 0 & 0 & w & \frac{\rho}{2c}(w+c) & \frac{\rho}{2c}(w-c) \\ \rho v & -\rho u & \frac{\vec{v}^2}{2} & \frac{\rho}{2c}(H+wc) & \frac{\rho}{2c}(H-wc) \end{vmatrix}$$

$$L_x = \begin{vmatrix} 1-\frac{\gamma-1}{2}M^2 & (\gamma-1)\frac{u}{c^2} & (\gamma-1)\frac{v}{c^2} & (\gamma-1)\frac{w}{c^2} & -\frac{\gamma-1}{c^2} \\ -\frac{w}{\rho} & 0 & 0 & \frac{1}{\rho} & 0 \\ \frac{v}{\rho} & 0 & -\frac{1}{\rho} & 0 & 0 \\ \frac{c}{\rho}(\frac{\gamma-1}{2}M^2-\frac{u}{c}) & \frac{1}{\rho}(1-(\gamma-1)\frac{u}{c}) & -\frac{(\gamma-1)v}{\rho c} & -\frac{(\gamma-1)w}{\rho c} & \frac{\gamma-1}{\rho c} \\ \frac{c}{\rho}(\frac{\gamma-1}{2}M^2+\frac{u}{c}) & \frac{-1}{\rho}(1-(\gamma-1)\frac{u}{c}) & -\frac{(\gamma-1)v}{\rho c} & -\frac{(\gamma-1)w}{\rho c} & \frac{\gamma-1}{\rho c} \end{vmatrix}$$

$$L_y = \begin{vmatrix} \frac{w}{\rho} & 0 & 0 & \frac{-1}{\rho} & 0 \\ 1-\frac{\gamma-1}{2}M^2 & (\gamma-1)\frac{u}{c^2} & (\gamma-1)\frac{v}{c^2} & (\gamma-1)\frac{w}{c^2} & -\frac{\gamma-1}{c^2} \\ \frac{-u}{\rho} & \frac{1}{\rho} & 0 & 0 & 0 \\ \frac{c}{\rho}(\frac{\gamma-1}{2}M^2-\frac{v}{c}) & -\frac{(\gamma-1)u}{\rho c} & \frac{1}{\rho}(1-(\gamma-1)\frac{v}{c}) & -\frac{(\gamma-1)w}{\rho c} & \frac{\gamma-1}{\rho c} \\ \frac{c}{\rho}(\frac{\gamma+1}{2}M^2-\frac{v}{c}) & -\frac{(\gamma-1)u}{\rho c} & \frac{1}{\rho}(1+(\gamma-1)\frac{v}{c}) & -\frac{(\gamma-1)w}{\rho c} & \frac{\gamma-1}{\rho c} \end{vmatrix}$$

$$L_z = \begin{vmatrix} -\frac{v}{\rho} & 0 & 0 & \frac{1}{\rho} & 0 \\ \frac{u}{\rho} & \frac{-1}{\rho} & 0 & 0 & 0 \\ 1-\frac{\gamma-1}{2}M^2 & (\gamma-1)\frac{u}{c^2} & (\gamma-1)\frac{v}{c^2} & (\gamma-1)\frac{w}{c^2} & -\frac{\gamma-1}{c^2} \\ \frac{c}{\rho}(\frac{\gamma-1}{2}M^2-\frac{w}{c}) & -\frac{(\gamma-1)u}{\rho c} & -\frac{(\gamma-1)v}{\rho c} & \frac{1}{\rho}(1-(\gamma-1)\frac{w}{c}) & \frac{\gamma-1}{\rho c} \\ \frac{c}{\rho}(\frac{\gamma-1}{2}M^2+\frac{w}{c}) & -\frac{(\gamma-1)u}{\rho c} & -\frac{(\gamma-1)v}{\rho c} & \frac{1}{\rho}(1+(\gamma-1)\frac{w}{c}) & \frac{\gamma-1}{\rho c} \end{vmatrix}$$

A.7 Weighted Essentially Non-Oscillatory (WENO) Scheme

WENO schemes are based on ENO (essentially non-oscillatory) schemes, which were first introduced by Harten, Osher, Engquist, and Chakravarthy [9] in the form of cell averages. The key idea of ENO schemes is to use the "smoothest" stencil among several candidates to approximate the fluxes at cell boundaries to a high order accuracy and at the same time to avoid spurious oscillations near shocks.

The cell-averaged version of ENO schemes involves a procedure of reconstructing point values from cell averages and could become complicated and costly for multi-dimensional problems. Later, Shu and Osher [28] & [28] developed the flux version of ENO schemes which do not require such a reconstruction procedure. Here the WENO schemes based on this flux version of ENO schemes is formulated. The WENO schemes of Liu et al. [17] are based on the cell-averaged version of ENO schemes. For applications involving shocks, second-order schemes are usually adequate if only relatively simple structures are present in the smooth part of the solution (e.g., the shock tube problem).

However, if a problem contains rich structures as well as shocks (e.g., the shock entropy wave interaction problem, high order shock capturing schemes (order of at least three) are more efficient than low order schemes in terms of CPU time and memory requirements. ENO schemes are uniformly high order accurate right up to the shock and are very robust to use. However, they also have certain drawbacks. One problem is with the freely adaptive stencil, which could change even by a round-off perturbation near zeroes of the solution and its derivatives. Also, this free adaptation of stencils is not necessary in regions where the solution is smooth.

Consider the one-dimensional hyperbolic system in conservation form given by

$$U_t + divF(U) = 0 \tag{A.71}$$

Here $U = (u_1, ..., u_m)$ is the vector of conserved variables, $F(U) = (F_1, ..., F_d)$ is a collection of vectors of fluxes. Let us descritize the space into uniform intervals of size Δx. The spatial operator of the WENO scheme will take the following conservative form

$$\frac{dU}{dt} = L(U) \tag{A.72}$$

and

$$L(U_j) = -\frac{1}{\Delta x}(\widehat{F}_{j+1/2} - \widehat{F}_{j-1/2}) \tag{A.73}$$

where the numerical flux $\widehat{F}_{j+1/2}$ approximates $h_{j+1/2} = h(x_{j+1/2})$ to high order with $h(x)$ implicitly defined by :

$$F(u(x)) = \frac{1}{\Delta x}\int_{x-\Delta x/2}^{x+\Delta x/2} h(\xi)d\xi \tag{A.74}$$

A.7.1 Roe Flux Splitting

For the flux splitting with entropy fix (RF) (for detail see [9]) let $\widehat{F}^{j+1/2}$ and $\widehat{F}^{j-1/2}$ be respectively the numerical fluxes obtained from the positive and negative parts of $f(u)$, given as :

$$\widehat{F}_{j+1/2} = \widehat{F}^{+}_{j+1/2} + \widehat{F}^{-}_{j+1/2} \tag{A.75}$$

As in the essentially non-oscillatory scheme (ENO) each of the stencils can render an approximation of $h_{j+1/2}$. If the stencil is smooth, this approximation is rth-order accurate ; otherwise it is less accurate or even not accurate at all if the stencil contains a discontinuity. One could assign a weight ω_k to each candidate stencil S_k, $k = 0, 1, ..., r-1$, and use these weights to combine the r different approximations to obtain the final approximation of $h_j + 1/2$ as :

$$\widehat{f}_{j+1/2} = \sum_{k=0}^{r-1} \omega_k q_k^r(f_{j+k-r+1}, ..., f_{j+k}) \tag{A.76}$$

To achieve essentially non-oscillatory property, one then requires the weight to adapt to the relative smoothness of f on each candidate stencil such that any discontinuous stencil is effectively assigned a zero weight.

Simple algebra gives the coefficients C_k^r such that

$$q_{r-1}^{2r-1}(f_{j-r+1}, ..., f_{j+r-1}) = \sum_{k=0}^{r-1} C_k^r q_k^r(f_{j+k-r+1}, ..., f_{j+k}) \tag{A.77}$$

where ω_k is the weight function and q_k^r is the ENO reconstruction on the kth stencil. The consitancy of the scheme impose $\sum_{k=0}^{r-1} \omega_k = 1$.

The weight coefficients ω_k are defined by the following way :

$$\omega_k = \frac{\beta_k}{\beta_0 + ... + \beta_{r-1}} \tag{A.78}$$

where

$$\alpha_k = \frac{C_k^r}{(\varepsilon + IS_k)^P} \quad k = 0, 1, ..., r-1. \tag{A.79}$$

Here ε is a positive real number which is introduced to avoid the denominator becoming zero, we will take $\varepsilon = 10^{-6}$. The exponent p is chosen as 2.

As we know, an ENO scheme chooses the smoothest ENO stencil by comparing a hierarchy of undivided differences. This is because these undivided differences can be used to measure the smoothness of the numerical flux on a stencil. IS_k is defined as :

$$IS_k = \sum_{l=1}^{r-1} \sum_{l=1}^{r-1} \frac{(f[j+k+i-r, l])^2}{r-l} \tag{A.80}$$

When r=2, we have

$$IS_k = (f[j+k-1, 1])^2, \quad k = 0, 1 \tag{A.81}$$

and when r=3, we get

$$IS_k = \frac{1}{2}((f[j+k-2, 1])^2 + (f[j+k-1, 1])^2) + (f[j+k-2, 2])^2, \quad k = 0, 1, 2. \tag{A.82}$$

when r=3, Taylor expansion of the above function gives

$$IS_0 = \frac{1}{2}((f^{'}h - \frac{3}{2}f^{''}h^2)^2 + ((f^{'}h - \frac{1}{2}f^{''}h^2)^2) + (f^{''}h^2)^2 + O(h^5) \tag{A.83}$$

$$IS_1 = \frac{1}{2}((f^{'}h - \frac{1}{2}f^{''}h^2)^2 + ((f^{'}h + \frac{1}{2}f^{''}h^2)^2) + (f^{''}h^2)^2 + O(h^5) \tag{A.84}$$

$$IS_2 = \frac{1}{2}((f^{'}h + \frac{1}{2}f^{''}h^2)^2 + ((f^{'}h + \frac{3}{2}f^{''}h^2)^2) + (f^{''}h^2)^2 + O(h^5) \tag{A.85}$$

A.7.2 Smoothness Measurement

Jiang and Shu [11] presented a new way of measuring the smoothness of the numerical solution on a stencil which can be used to replace (IS-k equation above) to form a new weight. This is given as :

$$IS_k = \sum_{l=1}^{r-1} \int_{x_{j-1/2}}^{x_{j+1/2}} h^{2l-1} (q_k^{(l)})^2 dx \tag{A.86}$$

where $q^{(l)}k$ is the lth-derivative. When r=2, this smoothness function gives the same results as by Liu et al. [17]. However, they become different for $r \geq 0$. For r = 3, the smoothness function gives :

$$IS_0 = \frac{13}{12}(f_{j-2} - 2f_{j-1} + f_j)^2 + \frac{1}{4}(f_{j-2} - 4f_{j-1} + 3f_j)^2 \tag{A.87}$$

$$IS_1 = \frac{13}{12}(f_{j-1} - 2f_j + f_{j+1})^2 + \frac{1}{4}(f_{j-1} - f_{j+1})^2 \tag{A.88}$$

$$IS_2 = \frac{13}{12}(f_j - 2f_{j+1} + f_{j+2})^2 + \frac{1}{4}(f_j - 4f_{j+1} + f_{j+2})^2 \tag{A.89}$$

In smooth regions, Taylor expansion of above equations gives, respectively.

$$IS_0 = \frac{13}{12}(f^{''}h^2)^2 + \frac{1}{4}(2f^{'}h - \frac{2}{3}f^{'''}h^3)^2 + O(h^6) \tag{A.90}$$

$$IS_1 = \frac{13}{12}(f^{''}h^2)^2 + \frac{1}{4}(2f^{'}h + \frac{1}{3}f^{'''}h^3)^2 + O(h^6) \tag{A.91}$$

$$IS_2 = \frac{13}{12}(f^{''}h^2)^2 + \frac{1}{4}(2f^{'}h - \frac{2}{3}f^{'''}h^3)^2 + O(h^6) \tag{A.92}$$

where $f^{'''} = f^{'''}(u_j)$. If $f^{'} \neq 0$, then

$$IS_k = (f^{'}h)^2(1 + O(h^2)), \quad k = 0, 1, 2. \tag{A.93}$$

which means the weights resulting from this measurement satisfy the condition for $r = 3$; thus we obtain a fifth-order (the optimal order for r = 3) accurate WENO scheme.

Moreover, this measurement is also more accurate at critical points of $f(u(x))$. When $f^{'} = 0$, we have

$$IS_k = \frac{13}{12}(f^{''}h^2)^2(1 + O(h^2)), \quad k = 0, 1, 2. \tag{A.94}$$

which implies that the weights resulting from the measurement is also fifth-order accurate at critical points.

A.7.3 Monotonicity Preserving WENO (MPWENO)

The monotonicity preserving weighted essentially non-oscillatory (MPWENO) schemes have high phase accuracy and high order of accuracy. The high-order members of this family are almost spectrally accurate for smooth problems. Nevertheless, they have robust shock capturing ability. They are also efficient and do not have a computational complexity makes them viable competitors to lower-order schemes, for problem containing both discontinuities and rich smooth region structure. The tables for the coefficients and the equations for the smoothness estimator, and optimal weights in order to design MPWENO schemes for increasingly high of accuracy. Co-efficients for r = 3 are presented in the previous section.

A.7.4 Monotonicity Preserving Bounds

Suresh and Huynh [32] found a general way of bounding the value $u^L_{j+1/2}$ so that the bounded value is monotonicity preserving. The key idea was that one must distinguish between smooth local extrema and a genuine $O(1)$ discontinuity.

Following Suresh and Huynh [32] they focused on the local measures of curvature. In order to utilize them in a numerical code we need to define the minmod and median functions as

$$minmod(x, y) = \frac{1}{2}(sgn(x) + sgn(y))min(|x|, |y|) \tag{A.95}$$

$$median(x,y,z) = x + minmod(y-x, z-x) \tag{A.96}$$

It then become useful to define the curvature measures at the zone centers as

$$d_j = u_{j+1} - 2u_j + u_{j-1} \tag{A.97}$$

The above expressions are used to define the curvature at the zone boundary. This is where a variety of definitions become possible. The definition of the curvature at the zone boundary which is least restrictive in that it provides maximal space for local extrema to develop is given by

$$d^{MM}_{j+1/2} = minmod(d_j, d_{j+1}) \tag{A.98}$$

The superscript MM in equation indicates the use of the minmod function. Suresh and Huynh [32] recommend using a measure of the curvature at the zone boundary that is somewhat more restrictive in that it reduces the space for local extrema to develop when the ratio d_{j+1}/d_j is larger than 4 or smaller than 1=4 (hence the use of the superscript M4 in the ensuing equation). It is given by

$$d^{M4}_{j+1/2} = minmod(4d_j - d_{j+1}, 4d_{j+1} - d_j, d_j, d_{j+1}) \tag{A.99}$$

Without damaging the monotonicity preserving character of the interpolation strategy one can write this measure of the curvature with extended

$$d^{M4X}_{j+1/2} = minmod(4d_j - d_{j+1}, 4d_{j+1} - d_j, d_j, d_{j+1}, d_{j-1}, d_{j+2}) \tag{A.100}$$

The left-sided upper limit (denoted by superscript UL) to the solution at $x_{j+1/2}$ is given by

$$u^{UL} j+1/2 = u_j + \alpha(u_j - u_{j-1}) \tag{A.101}$$

The median (denoted by superscript MD) value of the solution at $x_{j+1/2}$ is given by

$$u^{MD} j+1/2 = \frac{1}{2}(u_j + u_{j+1}) - \frac{1}{2} d^{MD}_{j+1/2} \tag{A.102}$$

The left-sided value with allowance made for a large curvature (denoted by superscript LC) in the solution at $x_{j+1/2}$ is given by

$$u^{LC} j+1/2 = u_j + \frac{1}{2}(u_j - u_{j-1}) - \frac{\beta}{3} d^{LC}_{j-1/2} \tag{A.103}$$

The value of β determines the amount of freedom available from utilizing a large value for the local curvature. Expressions for $u^{L,min}_{j+1/2}$ and $u^{L,max}_{j+1/2}$ are given as :

$$u^{L,min} j+1/2 = max[min(u_j, u_{j+1}, u^{MD}_{j+1}, min(u_j, u^{UL}_{j+1/2}, u^{LC}_{j+1/2} \tag{A.104}$$

$$u^{L,max} j+1/2 = max[min(u_j, u_{j+1}, u^{MD}_{j+1}, max(u_j, u^{UL}_{j+1/2}, u^{LC}_{j+1/2} \tag{A.105}$$

The monotonicity preserving value for $u^{L}_{j+1/2}$ can be obtained by using the following equation

$$u^{L} j+1/2 = median(u^{L}_{j+1/2}, u^{L,min}_{j+1/2}, u^{L,max}_{j+1/2}) \tag{A.106}$$

A.8 Time Integration

In practice, a scheme such that the Roe scheme is subjected to rather constraining stability conditions which generalize the condition of Courant Friedrich Lewy :

$$\frac{(|u|+c)\Delta t}{\Delta x} \leq 1 \tag{A.107}$$

One cures this problem by adopting an implicit scheme, which is generally subjected to a limitation much less severe on the step of time (One can manage to use time step corresponding to values of Current-Friedrich-Lewy (CFL) number of about a 10 to 1000 and even higher) [1]. For time integration, the equations can be written under the form :

$$\frac{\partial U}{\partial t} + \mathcal{L}(U) = 0 \tag{A.108}$$

where $U = [\rho, \rho u, \rho v, \rho E, \rho k, \rho\chi]^T$ (with following the model of turbulence used $\chi = \varepsilon$ or ω).

The time derivative is approximated by backward scheme on three (3) points and the operator $\mathcal{L}$ is linearized around the time $n\Delta t$:

$$\begin{cases} \left[\frac{3}{2}I - \Delta t \frac{\partial \mathcal{L}}{\partial U}\right] \Delta U = -\Delta t\, \mathcal{L}(U^n) - \frac{1}{2}\left(U^n - U^{n-1}\right) \\ \\ U^{n+1} = U^n + \Delta U \end{cases} \tag{A.109}$$

This scheme is second order in time provided that $\frac{\partial \mathcal{L}}{\partial U}$ is the exact Jacobian of $\mathcal{L}(U)$.

A.9 Limited Numerical Scales (LNS) : 2000

Inspired by the original proposal of Speziale, Batten et al.[4],[4]&[5] developed a variant of this approach which they called Limited Numerical Scales (LNS) setting

$$\tau_{ij}^{model} = \alpha \tau_{ij}^{RANS} \tag{A.110}$$

and using a cubic $k-\varepsilon$ model for τ_{ij}^{RANS}. Aware of the consistency issue, the authors proposed to use τ_{ij}^{model} instead of τ_{ij}^{RANS} in the transport equations for k and ε. As a consequence, these quantities become k_τ and ε_τ since they are determined as solutions of some sort of subgrid-scale transport equations. Hence τ_{ij}^{RANS} computed with k_τ and ε_τ is turned into a subgrid stress model. Damping this model again results in a "double-damped" τ_{ij}^{model}. To compensate for this, Batten et al. adjusted the contribution function signifcantly. They termed it latency factor and used

$$\alpha =_f racmin[\nu_t^{LES}; \nu_t^{RANS}]\nu_t^{RANS} \tag{A.111}$$

Hence

$$0 \leq \frac{\nu_t^{LES}}{\nu_t^{RANS}} \leq \alpha \leq 1$$

. Here, ν_t^{RANS} is the RANS-equivalent eddy-viscosity obtained by using k_τ and ε_τ in the original RANS definition, while ν_t^{LES} is the eddy viscosity of an LES model of choice. The Smagorinsky model with

$$\nu_t^{LES} = C_s \Delta^2 S \tag{A.112}$$

where $C_s = 0.05$ and

$$\Delta = 2max\Delta_x;\Delta_y;\Delta_z \tag{A.113}$$

Bibliographie

[1] Alziary de Roquefort, T., Cours sur les écoulements supersoniques, ENSMA, Poitiers, France. 2006.

[2] Dubois, F., Mehlman, G., A non-parameterized entropy correction of Roe's approximate Riemann solver. SIAM Journal of Numerical Analysis, 1991.

[3] Batten, P., Goldberg, U., Chakravarthy, S., Sub-Grid turbulence modeling for unsteady flow with acoustic resonance. AIAA Paper 00-0473, 38th AIAA Aerospace Sciences Meeting and Exhibit, Reno, Nevada, 2000.

[4] Batten, P., Goldberg, U., Chakravarthy, S., LNS-An Approach Towards Embedded LES. AIAA Paper 02-0427, 40th AIAA Aerospace Sciences Meeting and Exhibit, Reno, Nevada, 2002.

[5] Batten, P., Goldberg, U., Chakravarthy, S., Interfacing statistical turbulence closures with large-eddy simulation. AIAA J., 42(3) : 485-492, 2004.

[6] Gaitonde, D., Shang, J. S., Accuracy of flux-split algorithms in high-speed viscous flows. AIAA Journal, 31 (7) : 1215-1221, July 1993.

[7] Godunov, S. K., A finite difference method for the numerical computation of discontinuous solutions of the equations of fluid dynamics. Math. Sbornik, 47 : 271-290, 1959. Translated as U. S Dept. of Commerce JPRS 7225, 1960.

[8] Harten, A., High resolution schemes for hyperbolic conservation laws. Journal of Computational Physics. 49 : 357-393, 1983.

[9] Harten, A., Engquist, B., Osher, S., Chakarvarthy, S. R., Uniformly high order accurate essentially non-oscillatory schemes III. Journal of Computational Physics. 71(2) : 231-303, 1987.

[10] Hirsch, C., Numerical Computation of Internal and External Flows, Volume 2 : Computational Methods for Inviscid and Viscous Flows. Wiley-Interscience Series : Numerical Methods in Engineering. John Wiley & Sons, Chichester, New York, Second Edition, 1990.

[11] Jiang, G. S., Shu, C. H., Efficient implementation of weighted ENO schemes. Journal of Computational Physics, 126 : 202-228, 1996.

[12] Leer, Van. B., Towards the ultimate conservation difference scheme I : The quest of Monotonicity. Lecture notes in Physics. Pages 163-168, 1973.

[13] Leer, Van. B., Towards the ultimate conservation difference scheme II : Monotonicity and conservation combined in a second order scheme. Journal of Computational Physics. 14 : 361-370, 1974.

[14] Leer, Van. B., Towards the ultimate conservation difference scheme III : Upstream-centered finite difference schemes for ideal compressible flow. Journal of Computational Physics. 23 : 263-275, 1977.

[15] Leer, Van. B., Flux vector splitting for the Euler equations. In the preceedings of the 8th International Conference on numerical Methods in Fluid Dynamics. pages, Berlin, Lecture Notes in Physics, Volume 170, Springer Verlag, 1982.

[16] Leer, Van. B., Progress in multi-dimensional upwind differencing. ICASE Report, 92-43, 1992.

[17] Liu, X. -D., Osher, S., Chen, T., Weighted essentially non-oscillatory schemes, Journal of Computational Physics, 115 : 200-212, 1994.

[18] Luneau, J., Bonnet, A., Aérodynamique-Thérie de la dynamique des fluides. Collection La Chevéche. Cepadues Editions, Toulouse, Premiére édition, ISBN 2-85428-218-3, 1989.

[19] Muller, B., Simple improvements of an upwind TVD scheme for hyperbolic flow. AIAA-paper 89-1977, June 1989.

[20] Osher, S., Solomon, F., Upwind Difference Schemes for Hyperbolic Systems of Conservation Laws. Mathematical Computation, 1982.

[21] Osher, S., Chakarvarthy, S. R., High resolution schemes and the entropy condition. SIAM Journal of Numerical Analysis. 21(5) : 955-984, October 1984.

[22] Chakarvarthy, S. R., Osher, S., A new class of high accuracy TVD schemes for hyperbolic conservation laws. AIAA Paper. 85-0363, January 1985.

[23] Osher, S., Chakarvarthy, S. R., Very high order accurate TVD schemes. The IMA volumes in mathematical computation. 49 : 105-121, 1987.

[24] Quirk, J. J., A contribution to the great Riemann solver debate. International Journal for Numerical Method in Fluids, 18 : 555-574, 1994.

[25] Riedelbauch, S., Brenner, G., Numerical simulation of laminar hypersonic flow past blunt bodies including high temperature effects. AIAA-paper 90-1492, June 1990.

[26] Roe, P. L., Approximate Riemann solvers, parameter vectors, and difference schemes. Journal of Computational Physics. 43 : 357-372, 1981.

[27] Roe, P. L., Discrete methods for numerical analysis of time dependent multi-dimensional gas dynamics. Journal of computational physics, 63 : 458-476, 1986.

[28] Shu, C.-W., Osher, S., Efficient implementation of Essentially Non-Oscillatory shock capturing schemes I. Journal of Computational Physics. 77 : 439-471, 1988.

[29] Shu, C. -W., Osher, S., Efficient implementation of Essentially Non-Oscillatory shock capturing schemes I. Journal of Computational Physics. 83 : 32-78, 1989.

[30] Shu, C. -W., Essentially Non-Oscillatory and Weighted Essentially Non-Oscillatory Schemes for Hyperbolic Conservative Laws, NASA/CR-97-206253 and ICASE Report 97-65, 1997.

[31] Steger, J. L., Warming, R. F., Flux vector splitting for the inviscid gas dynamics equation with applications to finite difference methods, Journal of Computational Physics, 40 : 236-293, 1981.

[32] Suresh, A., Huynh, H. T., Accurate monotonicity preserving scheme with Runge-kutta time-stepping, J. Comput. Phys. 136, 83, 1997.

[33] Sweby, P. K., High Resolution Schemes Using Flux Limiters for Hyperbolic Conservation Laws. SIAM Journal of Numerical Analysis, 21 (5) : 995-1011, October 1984.

[34] Yang, J. Y., Hsu, C. A., High resolution non oscillatory schemes for unsteady compressible flows. AIAA Journal. 30 : 1570-1575, 1992.

[35] Yee, H. C., Upwind and symmetric shock capturing schemes, NASA Technical Memorandum 89464, NASA Ames Research Center, Moffet Field, California 94035, May 1987.

Annexe B

Results of Free Shock Separation

B.1 NPR=5.0

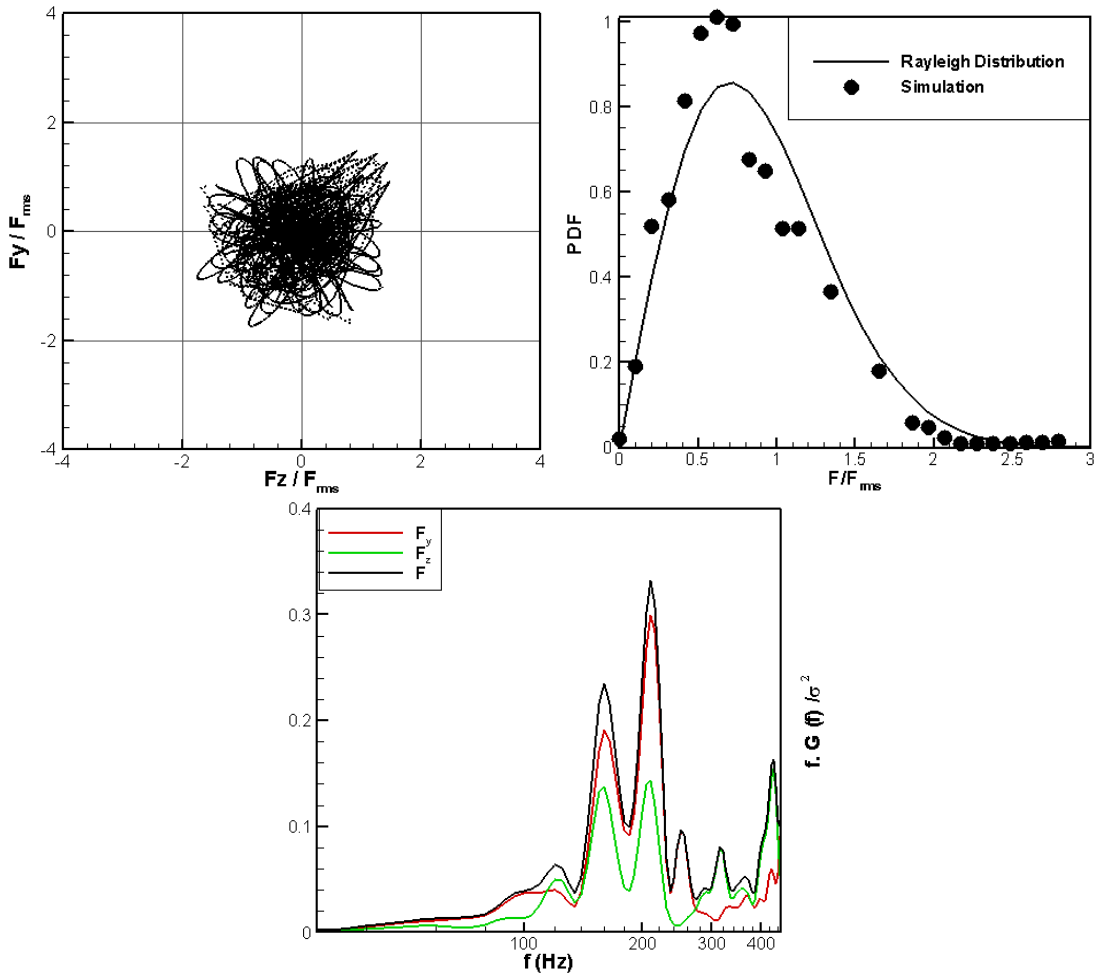

FIGURE B.1 – (Top) Polar of side-load components and its PDF distribution ; (Bottom) PSD of computed side-loads.

B.2 Results : NPR=15.5

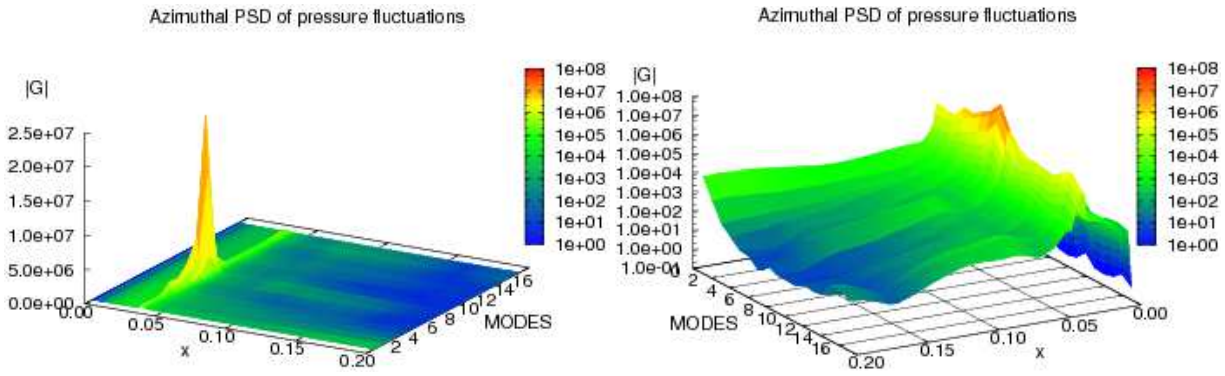

FIGURE B.2 – Power spectral density in the azimuthal direction : (Left) G(f), (Right) log(G(f)).

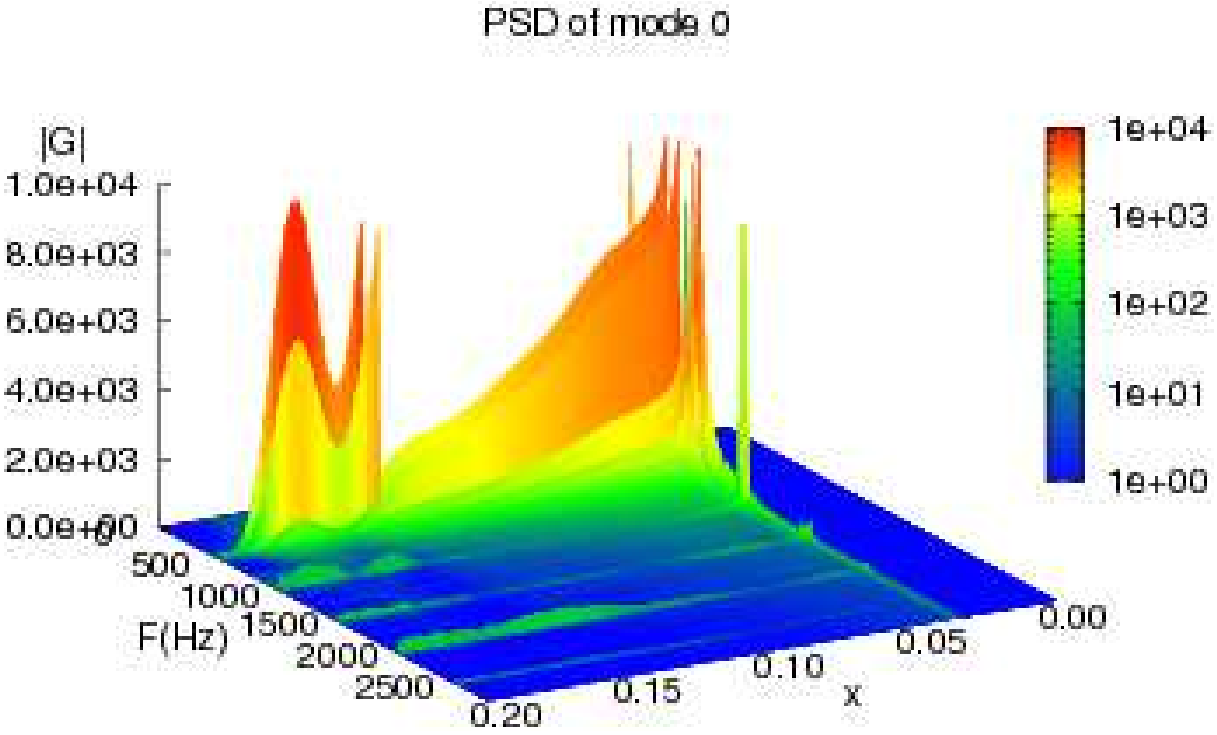

FIGURE B.3 – PSD analysis of coefficient a_0

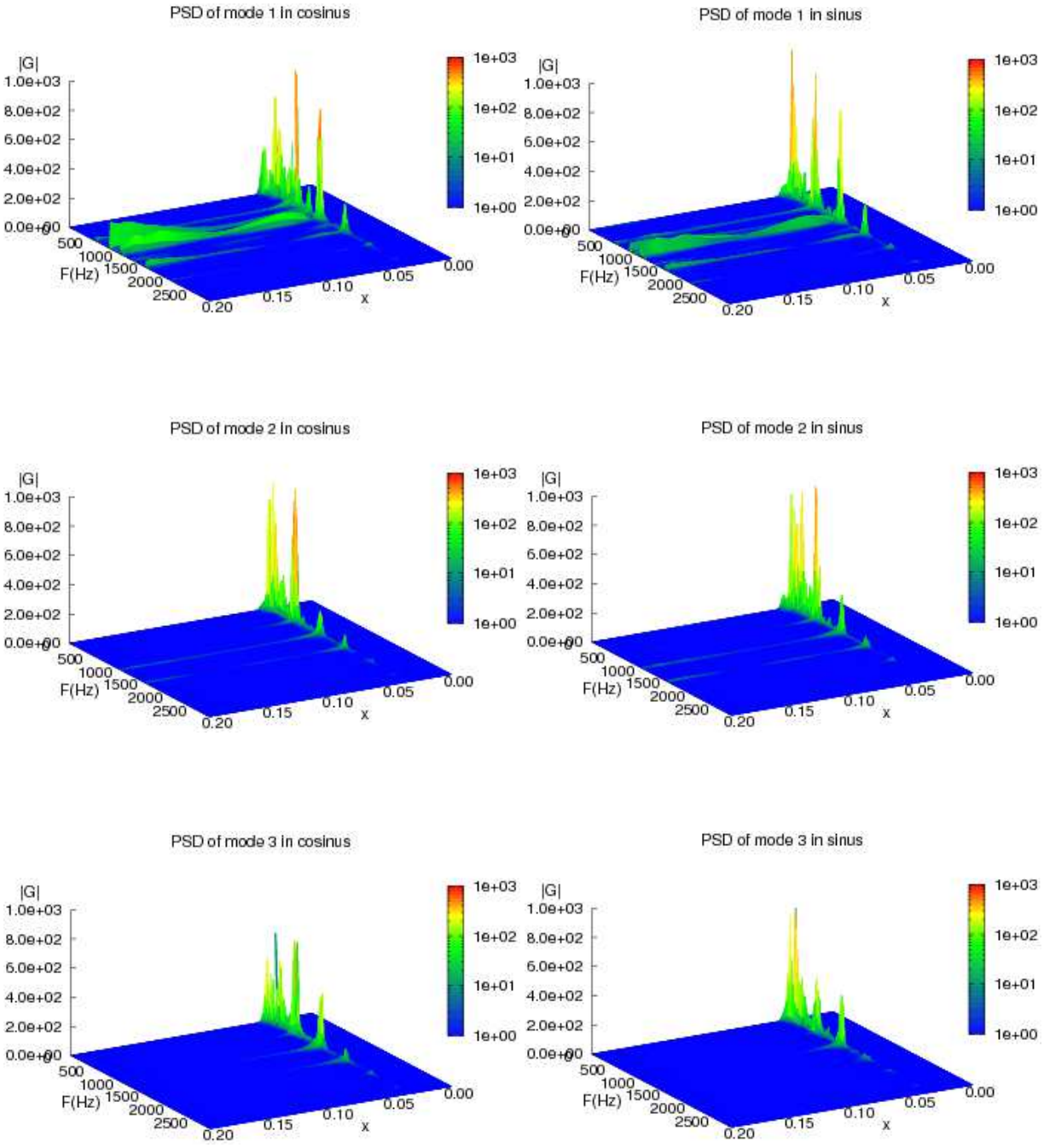

FIGURE B.4 – PSD analysis of coefficients (Top) a_1 and b_1, (Middle) a_2 and b_2 & (Bottom) a_3 and b_3

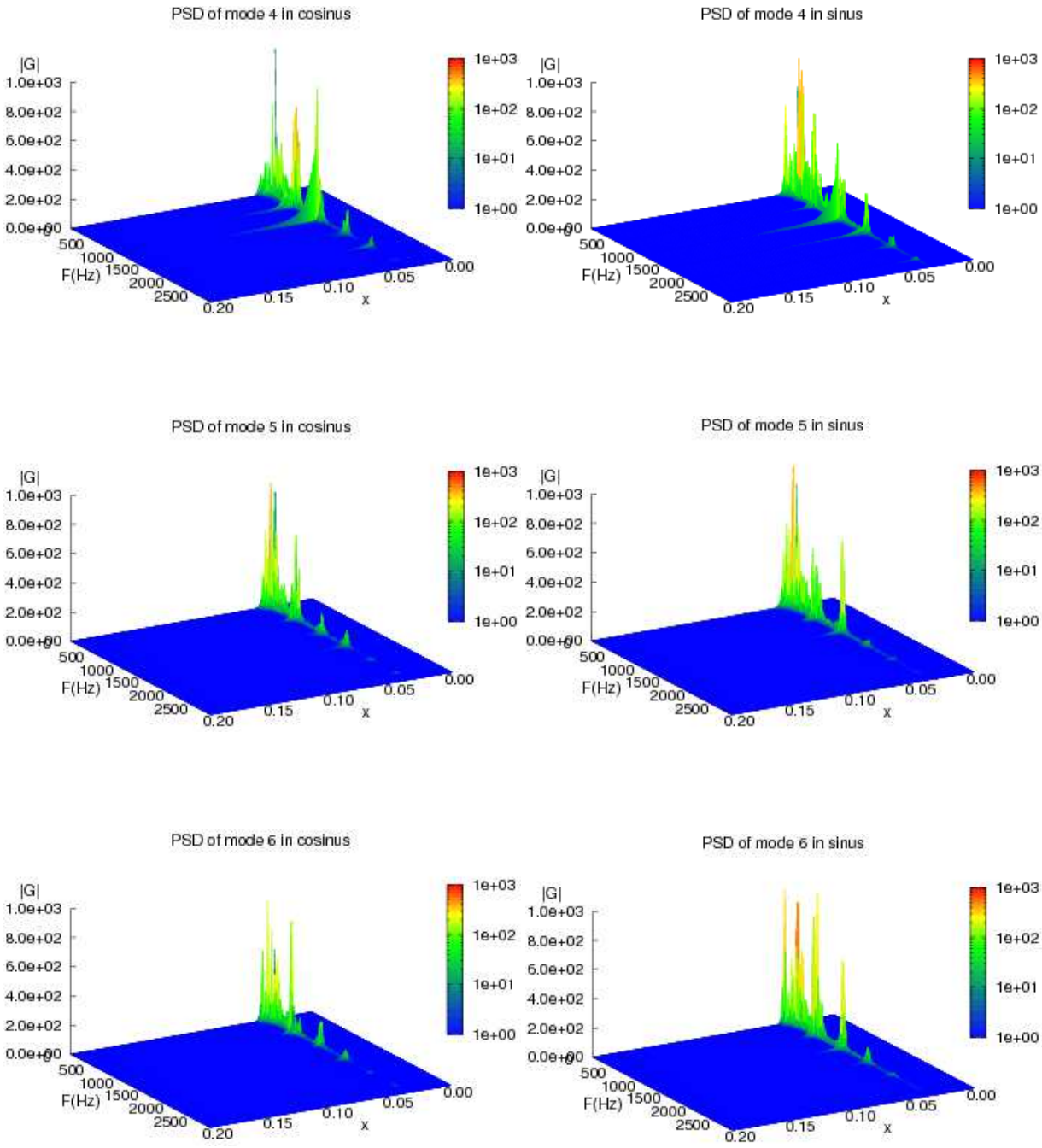

FIGURE B.5 – PSD analysis of coefficients (Top) a_4 and b_4, (Middle) a_5 and b_5 & (Bottom) a_6 and b_6

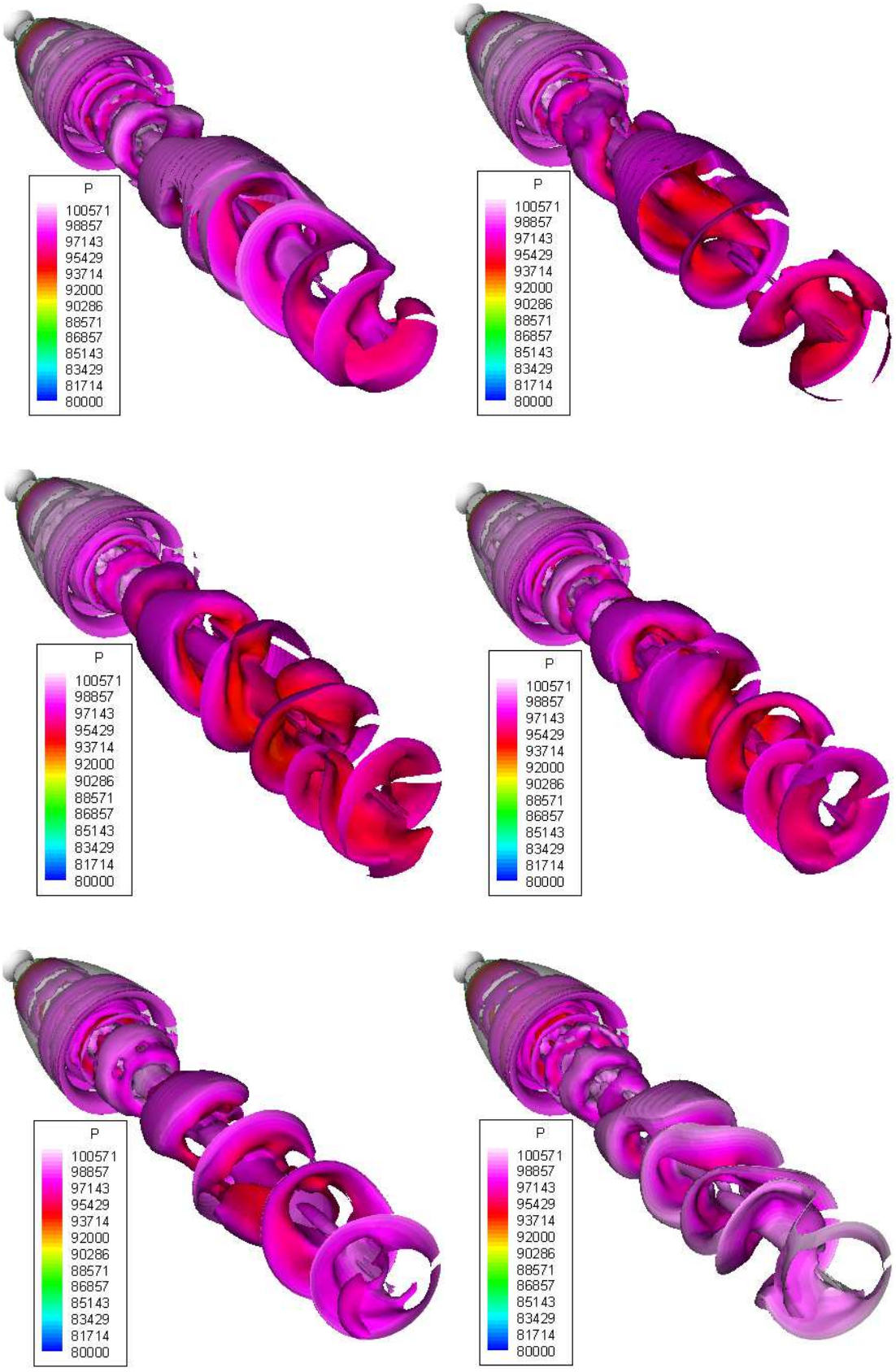

FIGURE B.6 – Iso-surface of Q-criterion ($0.1 * U_t^2/D_e^2$) coloured with pressure at T= 8.7, 13.0, 17.4, 21.7, 26.1 & 30.4 $*L_d/U_t$: Left to Right ; Top to Bottom, respectively.

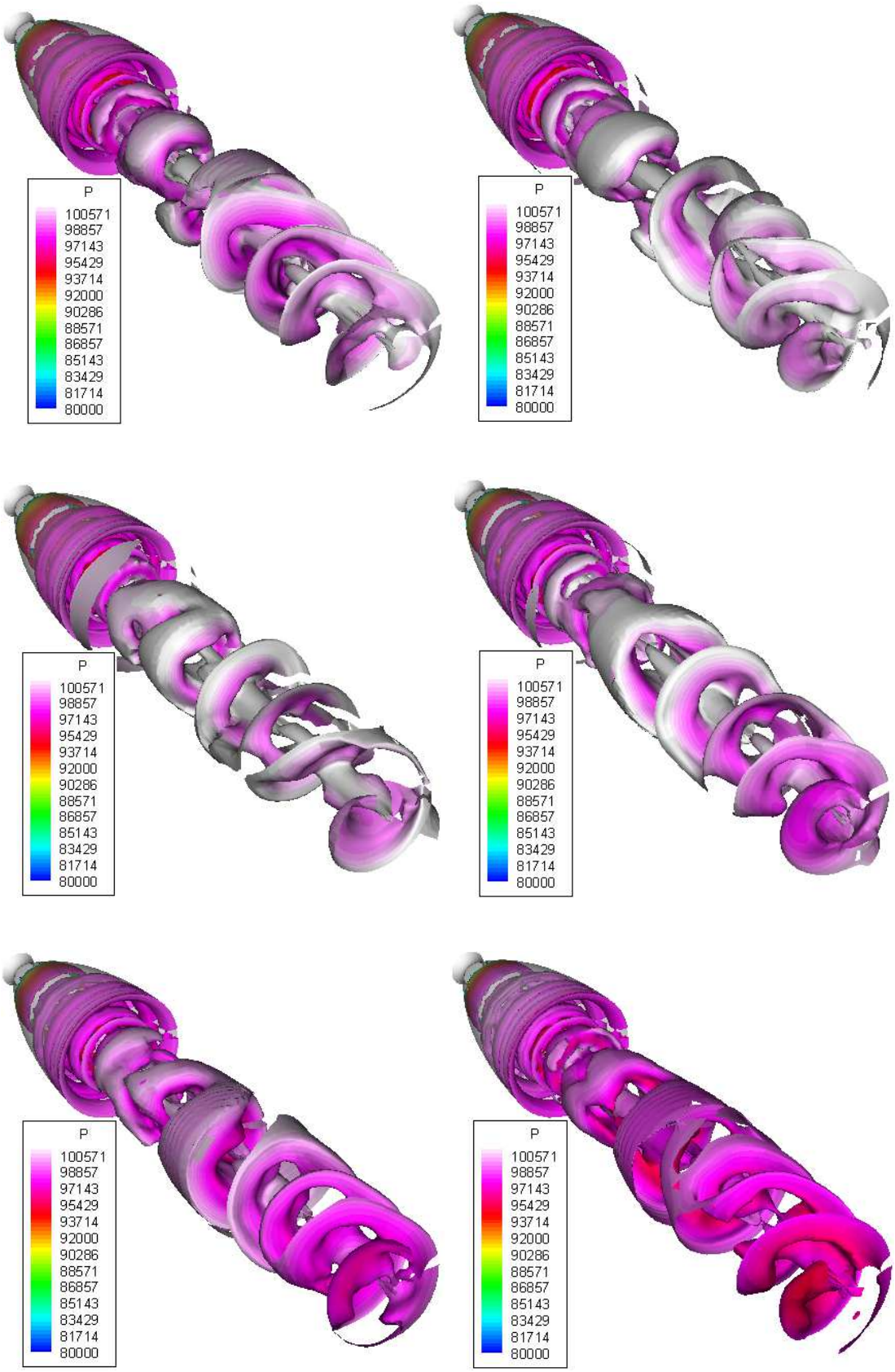

FIGURE B.7 – Iso-surface of Q-criterion ($0.1 * U_t^2/D_e^2$) coloured with pressure at T= 34.8, 39.1, 43.5, 47.8, 52.2 & 56.5 $*L_d/U_t$: Left to Right ; Top to Bottom, respectively.

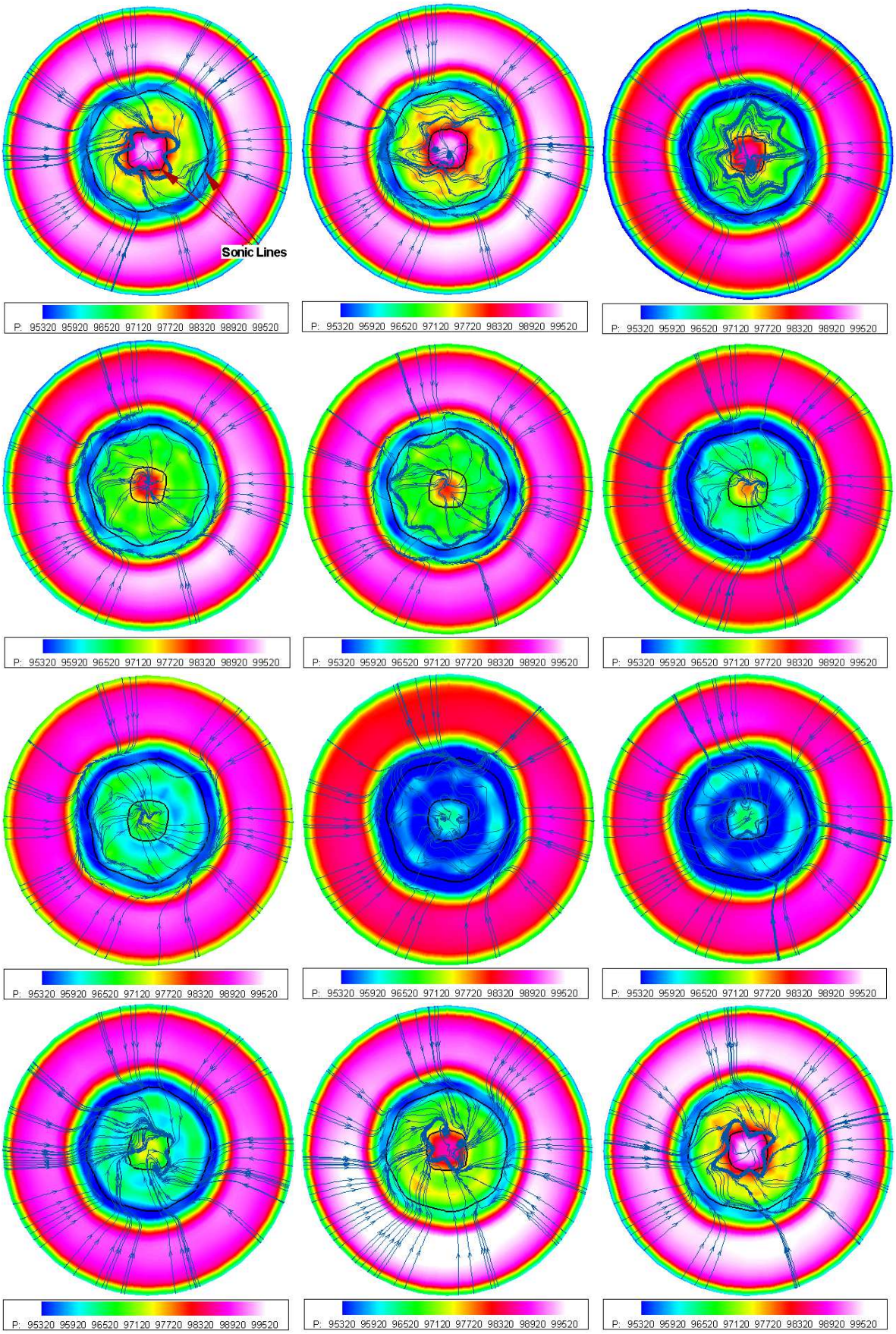

FIGURE B.8 – 2D slice at nozzle exit : iso-pressure contours, streamlines and sonic lines (solid black line) at T=0.4, 4.3, 8.7, 13.0, 17.4, 21.7, 26.1, 30.4, 34.8, 39.1, 43.5 & 47.8 $*L_d/U_t$: Left to Right ; Top to Bottom, respectively.

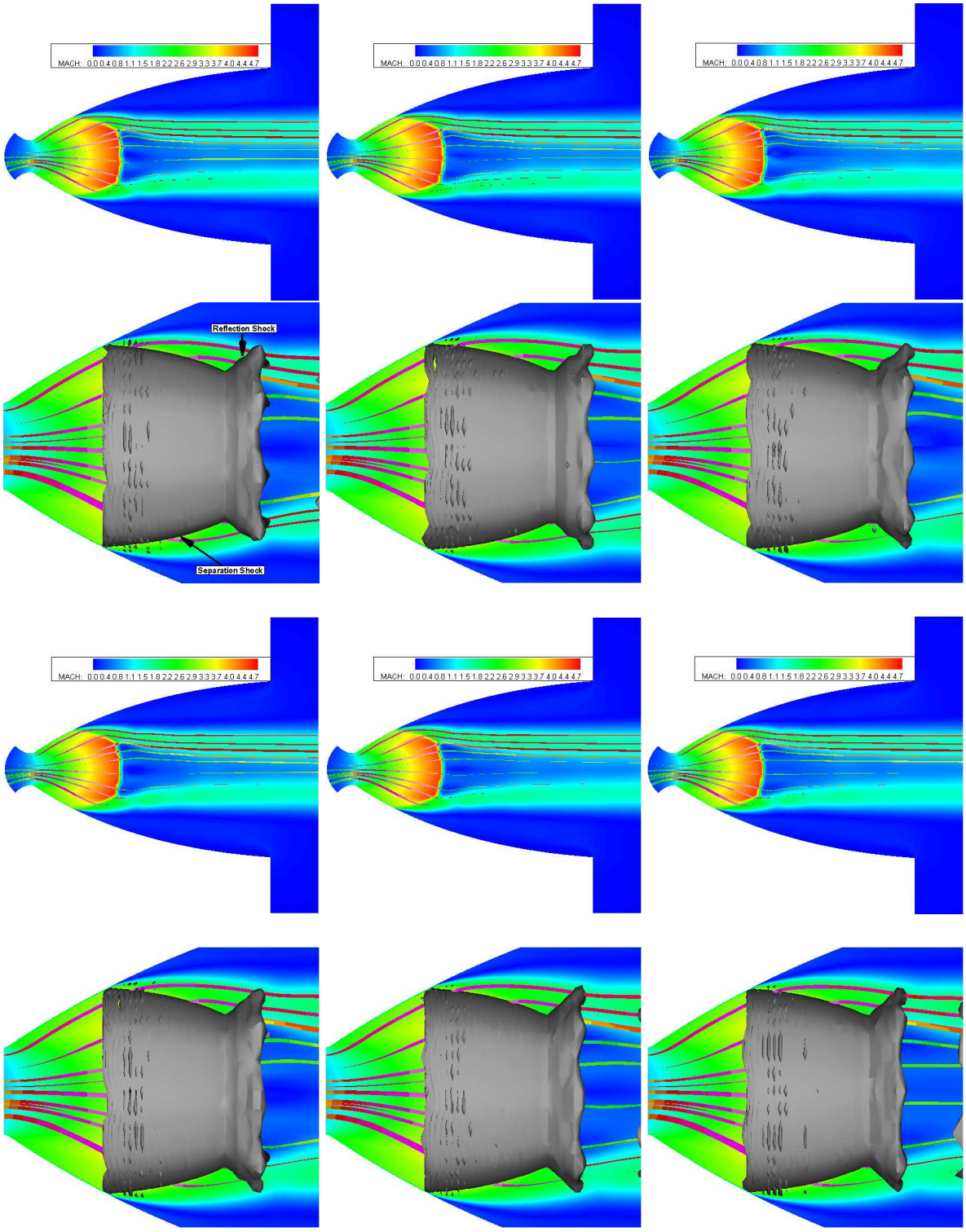

FIGURE B.9 – Iso-contours of Mach number and streamlines & Zoom near the Mach reflection : iso-surface of shock function (separation line, separation shock and reflected shock) at T= 0.4, 4.3, 8.7, 13.5, 17.4 & 21.7*L_d/U_t : Left to Right ; Top to Bottom, respectively.

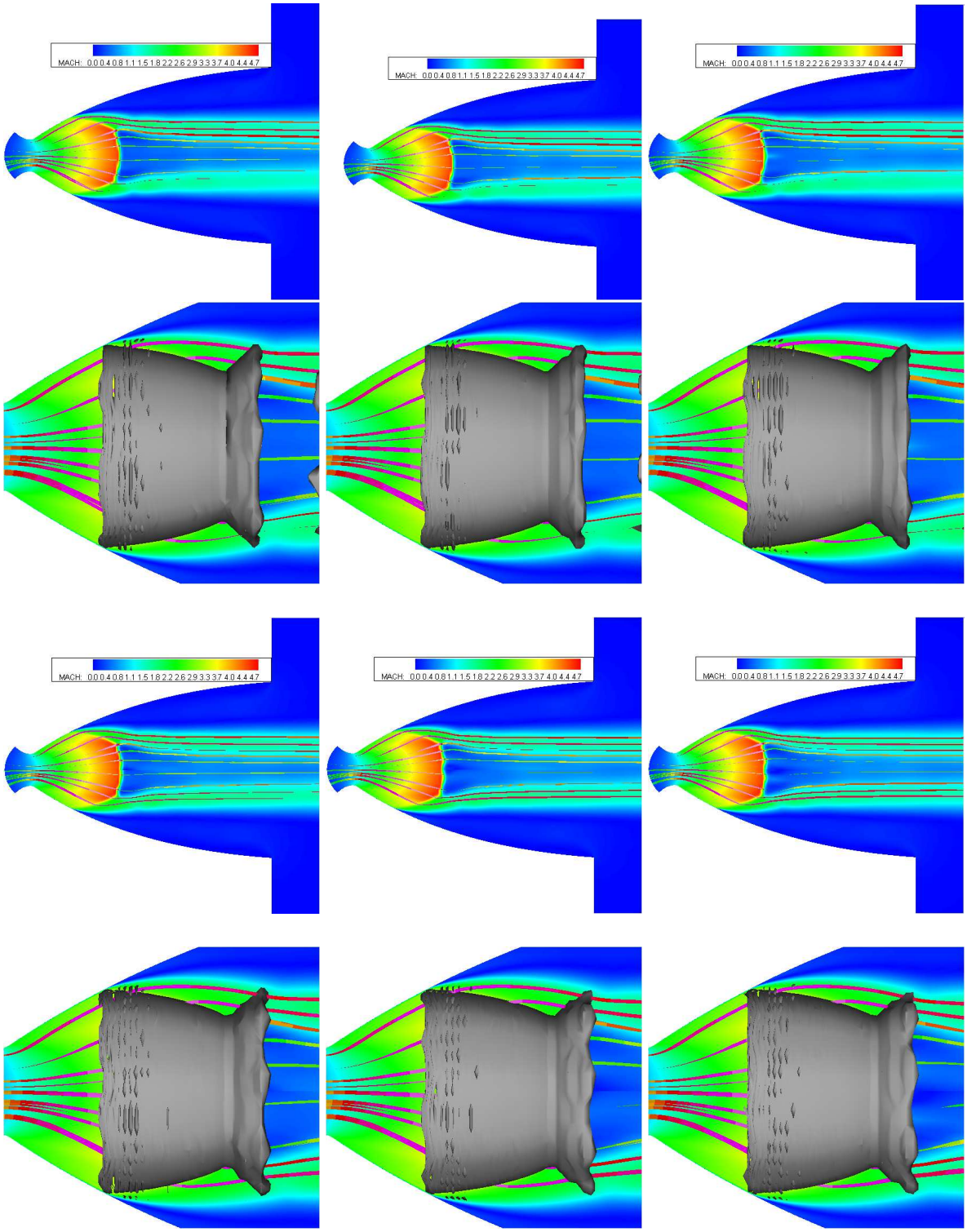

FIGURE B.10 – Iso-contours of Mach number and streamlines & Zoom near the Mach reflection : iso-surface of shock function (separation line, separation shock and reflected shock) at T= 26.1, 30.4, 34.8, 39.1, 43.5 & 47.8*L_d/U_t : Left to Right ; Top to Bottom, respectively.

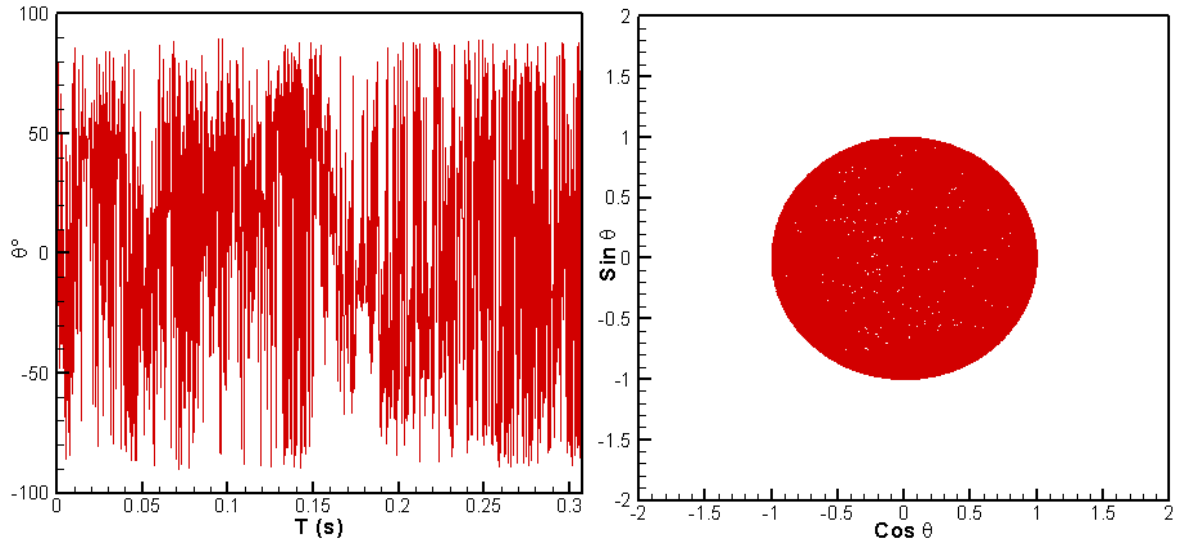

FIGURE B.11 – (Left) Direction of side-loads with the evolution of time & (Right) and its polar

B.3 Results : NPR=19.0

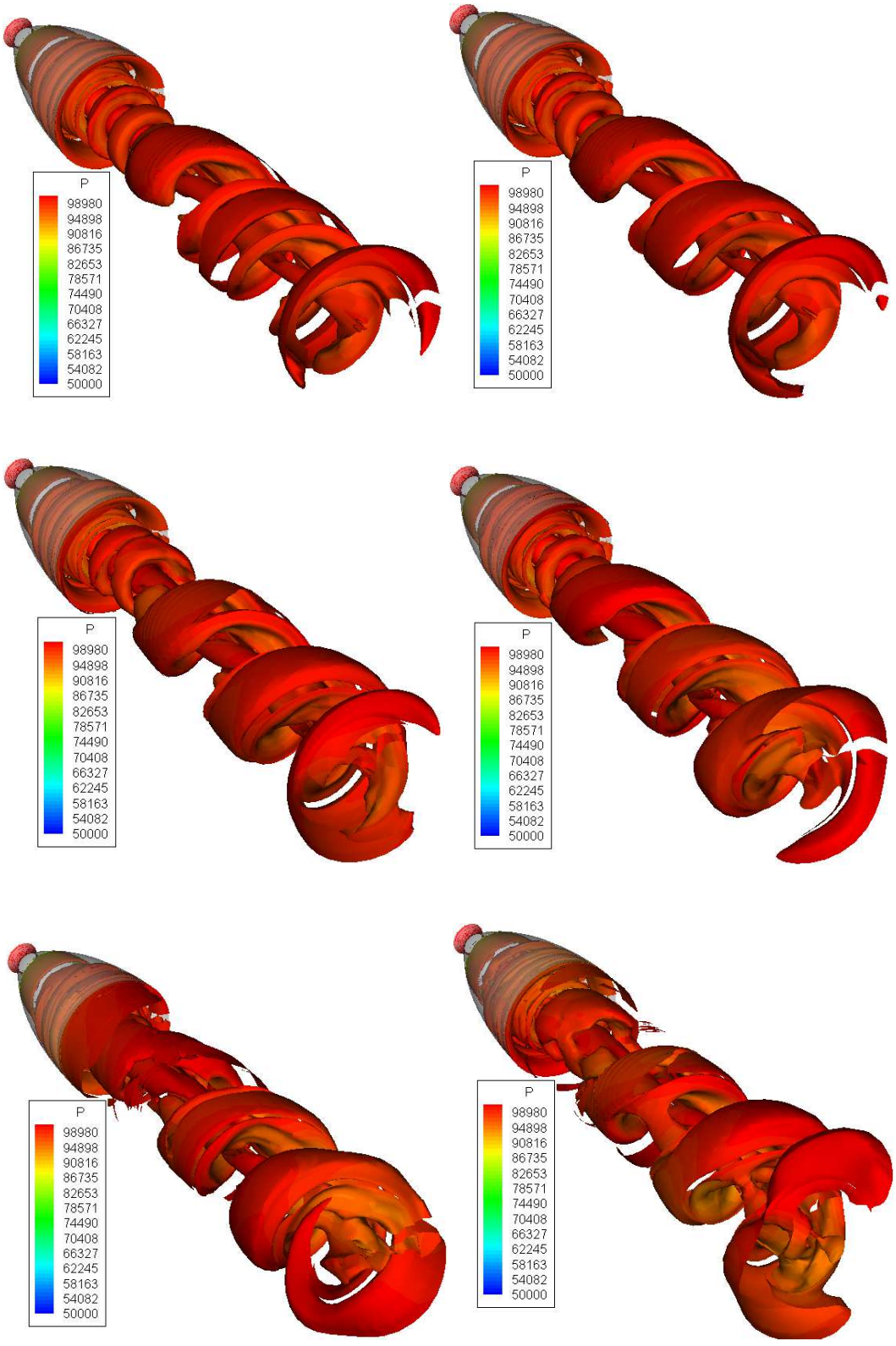

FIGURE B.12 – Iso-surface of Q-criterion ($0.1 * U_t^2/D_e^2$) coloured with pressure at T= 18.3, 23.7, 34.6, 47.6, 62.8 & 84.6* L_d/U_t : Left to Right ; Top to Bottom, respectively.

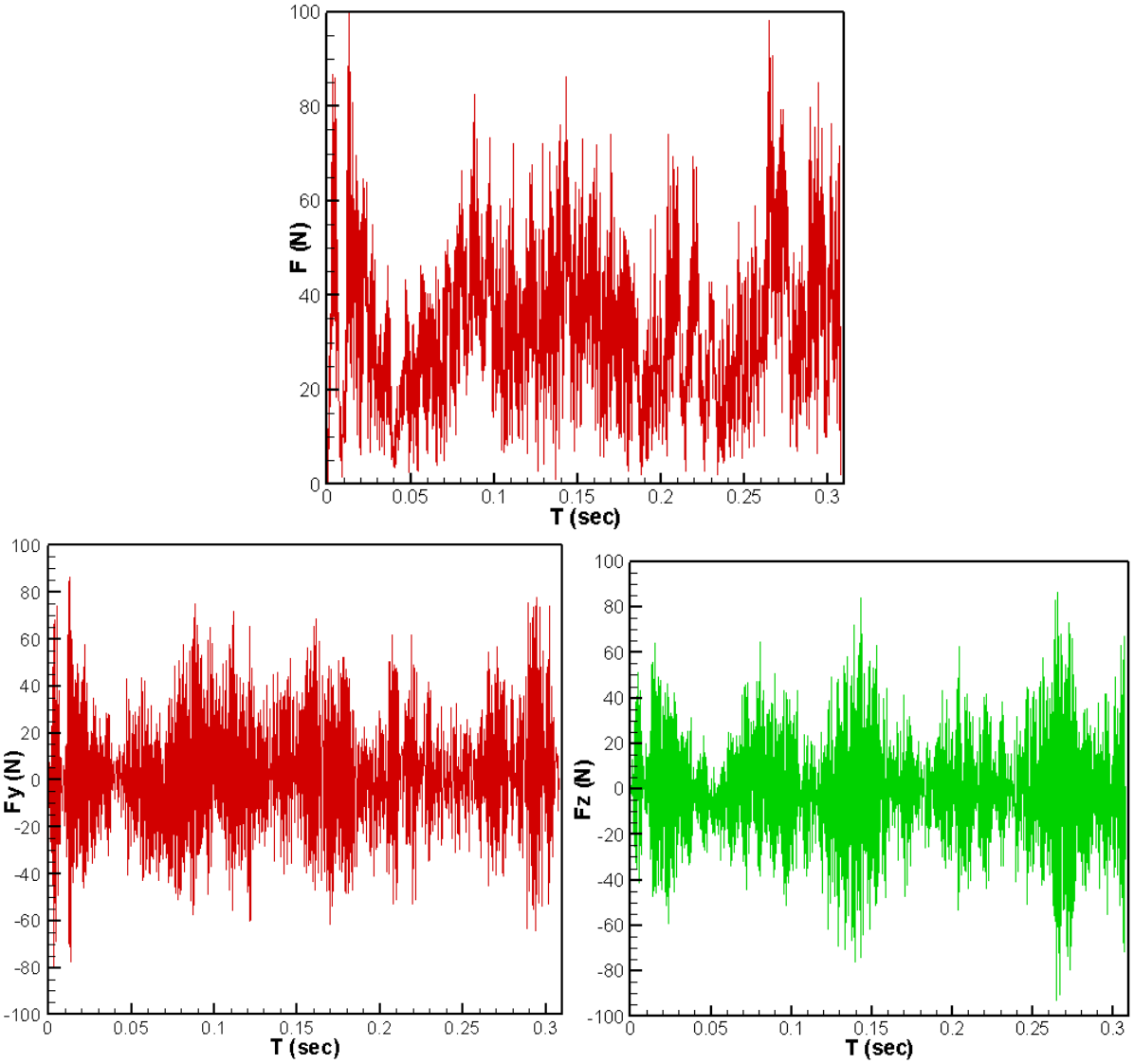

FIGURE B.13 – (Top) Evolution of side-load & (Bottom) its components .

Annexe C

Results of Restricted Shock Separation

C.1 Results : NPR=25.5

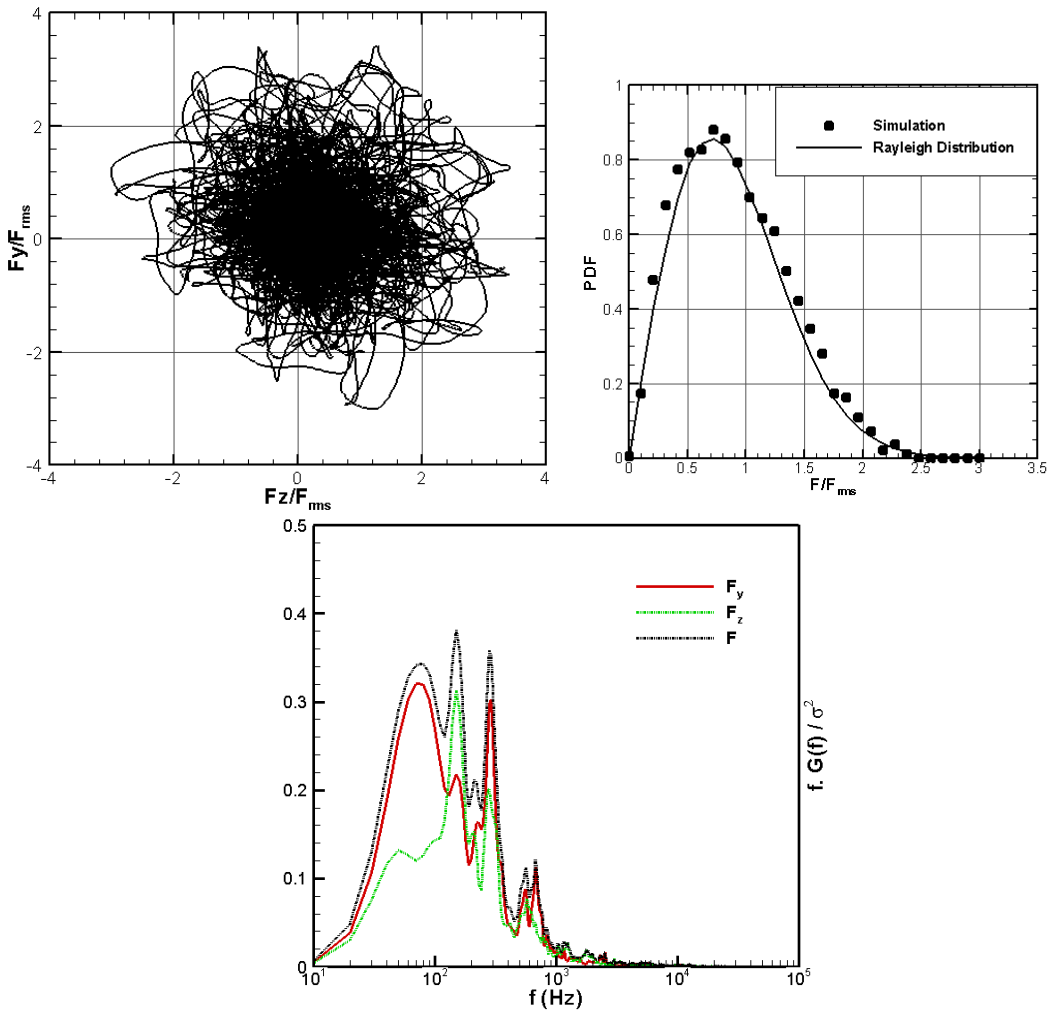

FIGURE C.1 – (Top) Polar plot & PDF distribution (Bottom) PSD of side-load and their components.

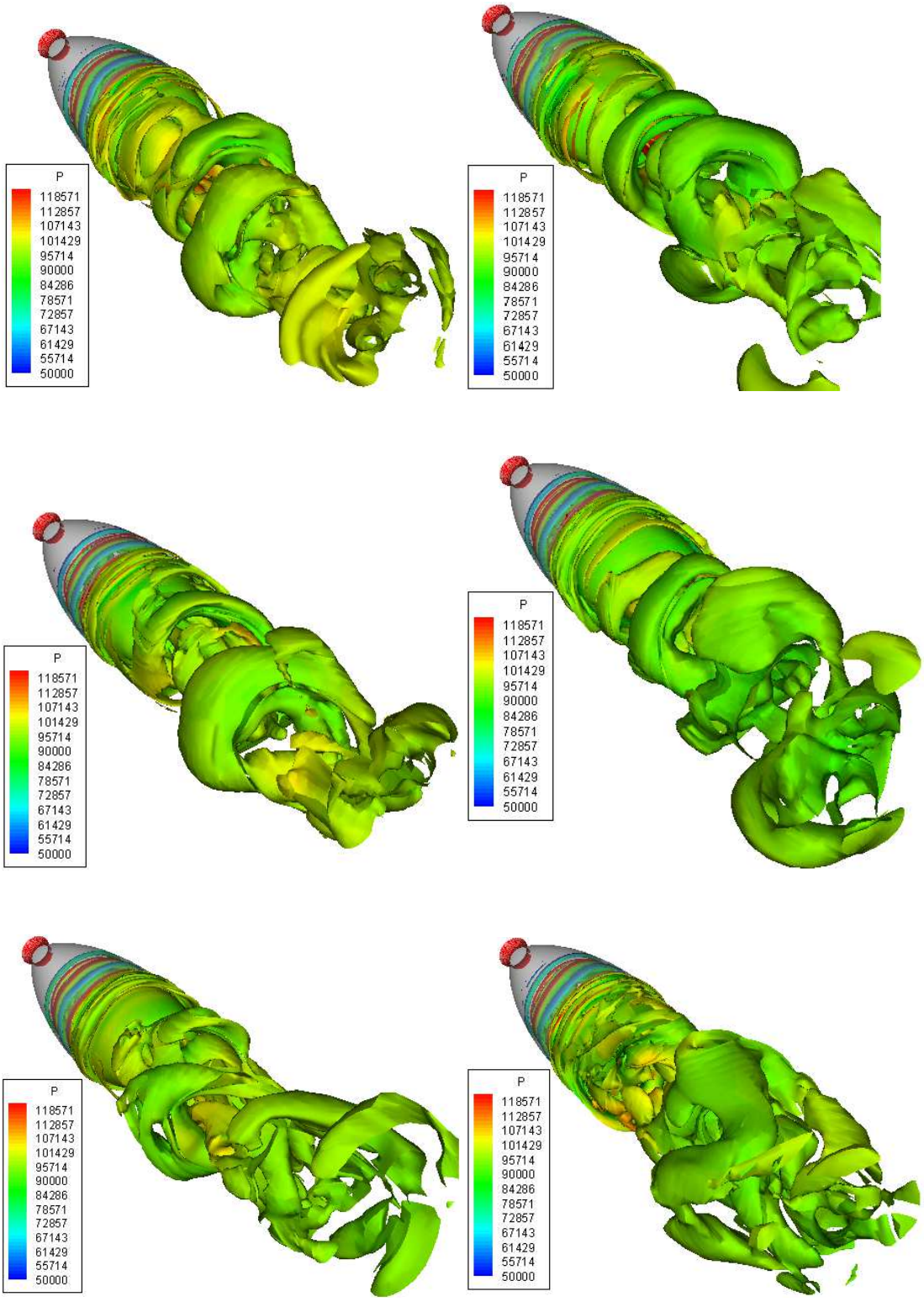

FIGURE C.2 – Iso-surface of Q-criterion ($0.1 * U_t^2/D_e^2$) coloured with pressure at T=48.2, 44.8, 45.6, 47.4, 48.2 & 49.1 * L_d/U_t : Left to Right ; Top to Bottom, respectively.

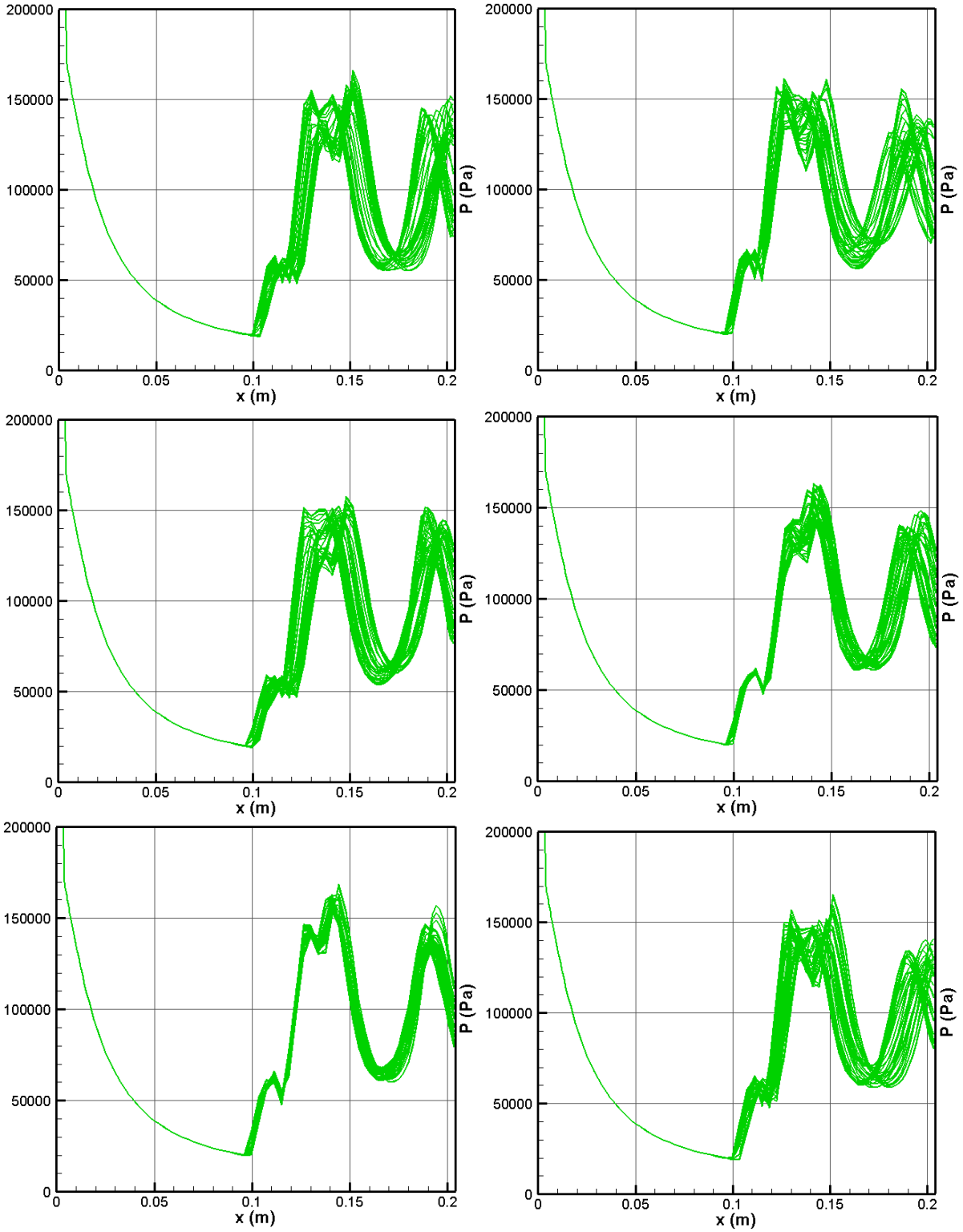

FIGURE C.3 – Evolution of wall pressure for each azimuthal direction along nozzle axis at T=44.3, 44.8, 45.6, 47.4, 48.2, & 49.1 $*L_d/U_t$: Left to Right ; Top to Bottom, respectively.

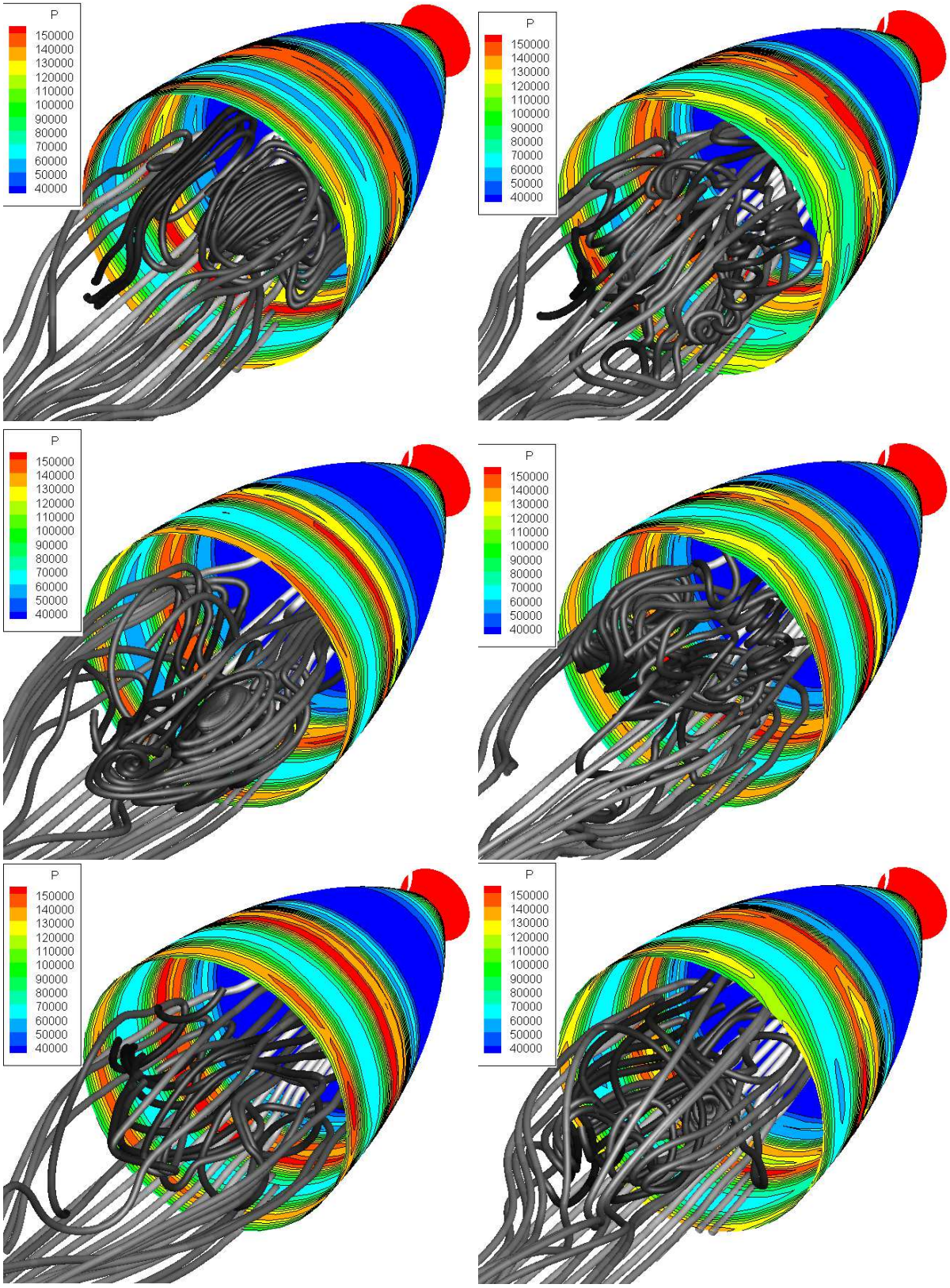

FIGURE C.4 – Iso-pressure contours/lines on nozzle wall (Left to Right - Top to Bottom) at T=44.3, 44.8, 45.6, 47.4, 48.2, & 49.1 $*L_d/U_t$: Left to Right ; Top to Bottom, respectively.

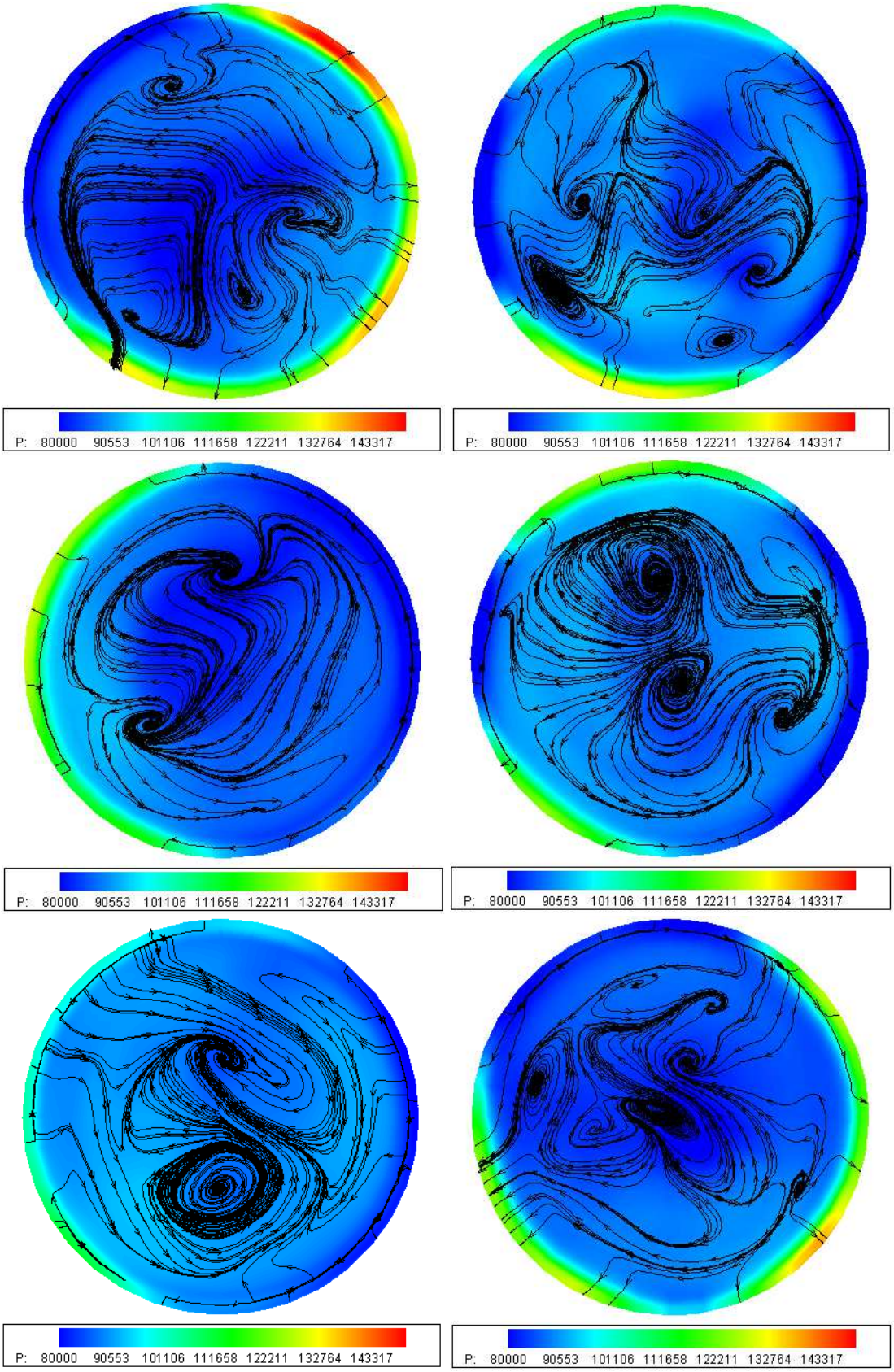

FIGURE C.5 – 2D slice at nozzle exit : iso-pressure contours and streamlines (Left to Right - Top to Bottom) at T=44.3, 44.8, 45.6, 47.4, 48.2, & 49.1 $* L_d/U_t$: Left to Right ; Top to Bottom, respectively.

C.2 Results : NPR=38.0

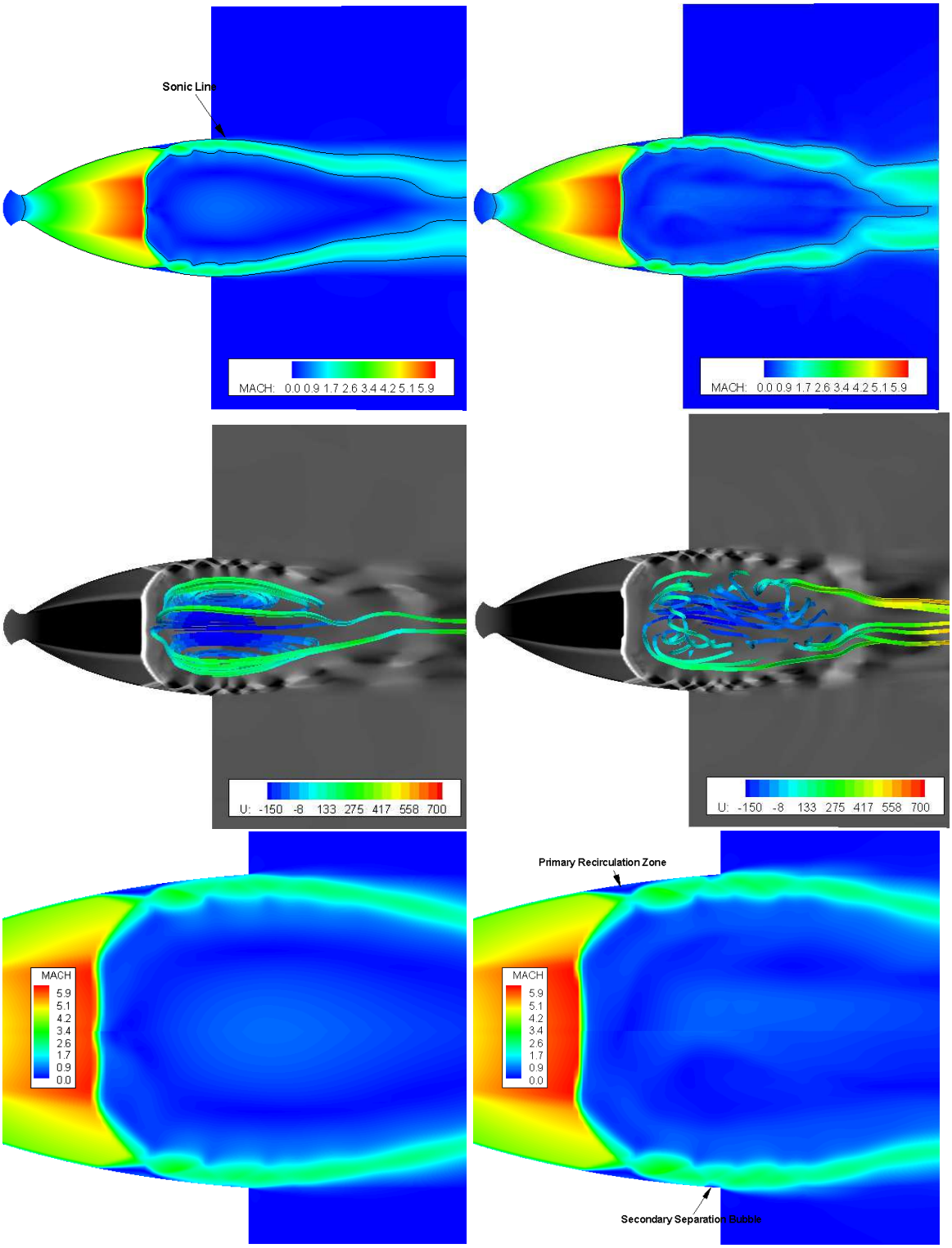

FIGURE C.6 – (Top) Iso-Mach contours of 2D slices at $\theta = 0^o \& 180^o$ (Middle) Iso-contours of shock-function and streamlines coloured with velocity (Bottom) Zoom near the nozzle exit : iso-Mach contours at T=0.66 & 1.51 $*L_d/U_t$: Left-Right.

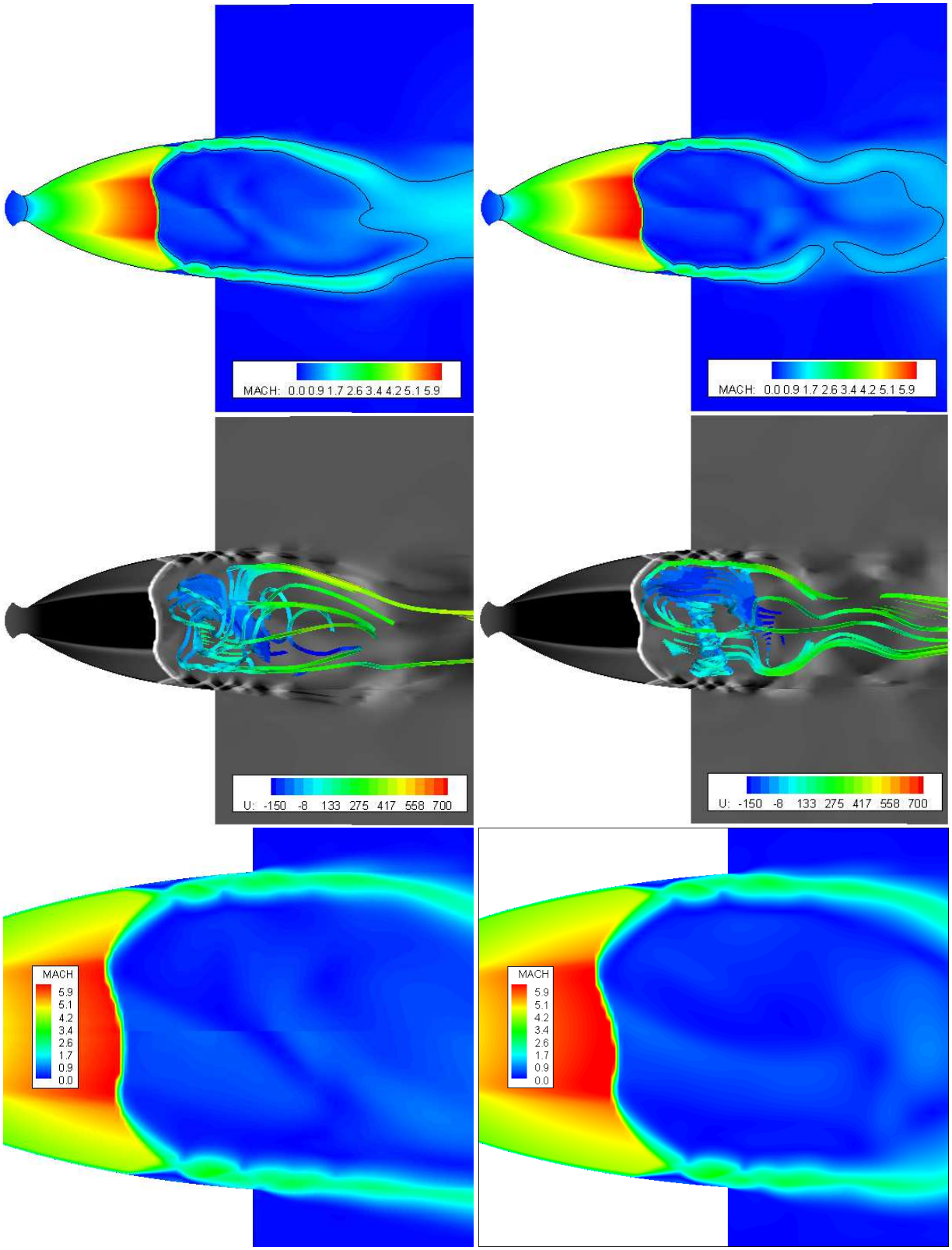

FIGURE C.7 – (Top) Iso-Mach contours of 2D slices at $\theta = 0^o \& 180^o$ (Middle) Iso-contours of shock-function and streamlines coloured with velocity (Bottom) Zoom near the nozzle exit : iso-Mach contours at T=2.81 & 3.40 $*L_d/U_t$: Left-Right.

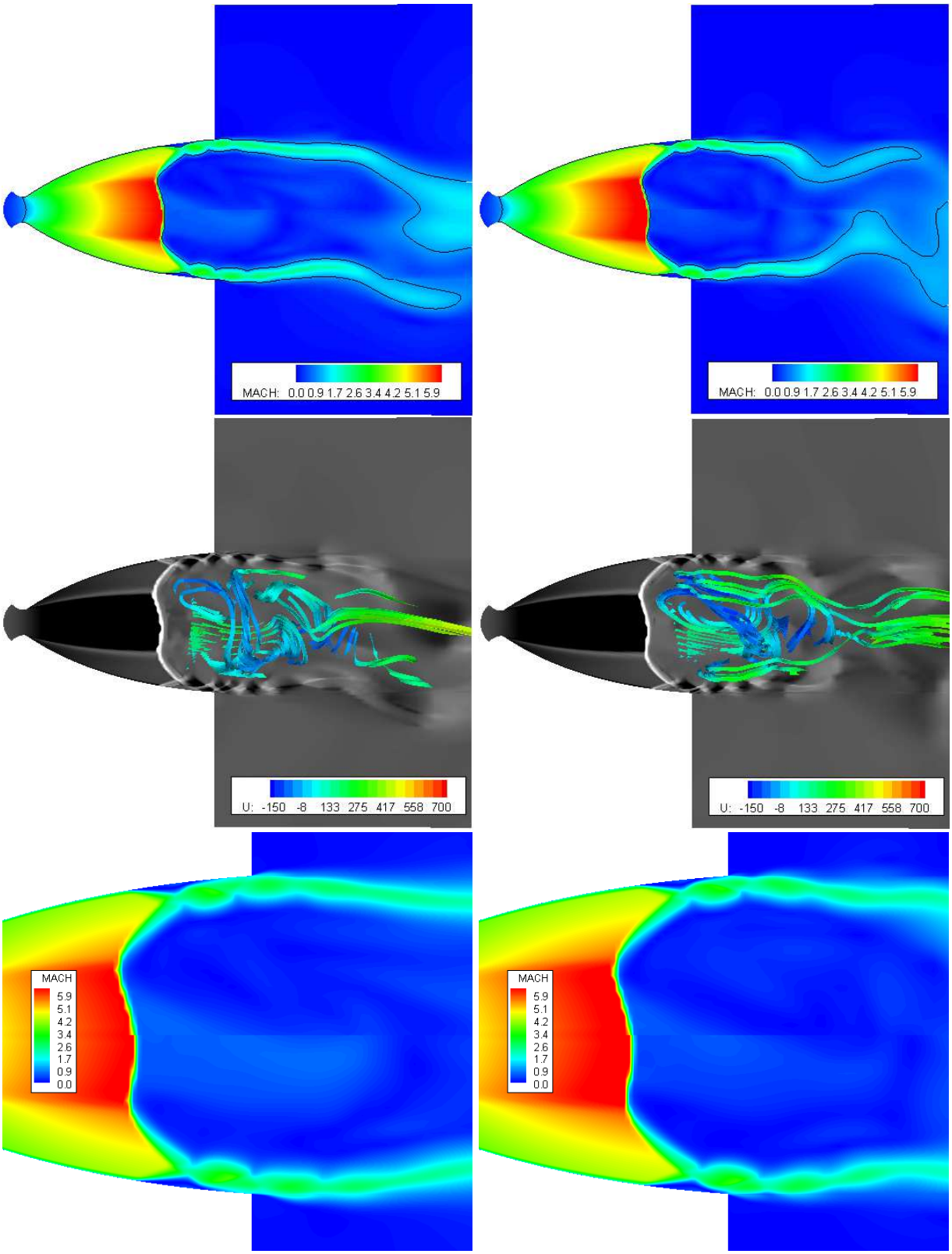

FIGURE C.8 – (Top) Iso-Mach contours of 2D slices at $\theta = 0^o \& 180^o$ (Middle) Iso-contours of shock-function and streamlines coloured with velocity (Bottom) Zoom near the nozzle exit : iso-Mach contours at T=3.03 & 3.21 $*L_d/U_t$: Left-Right.

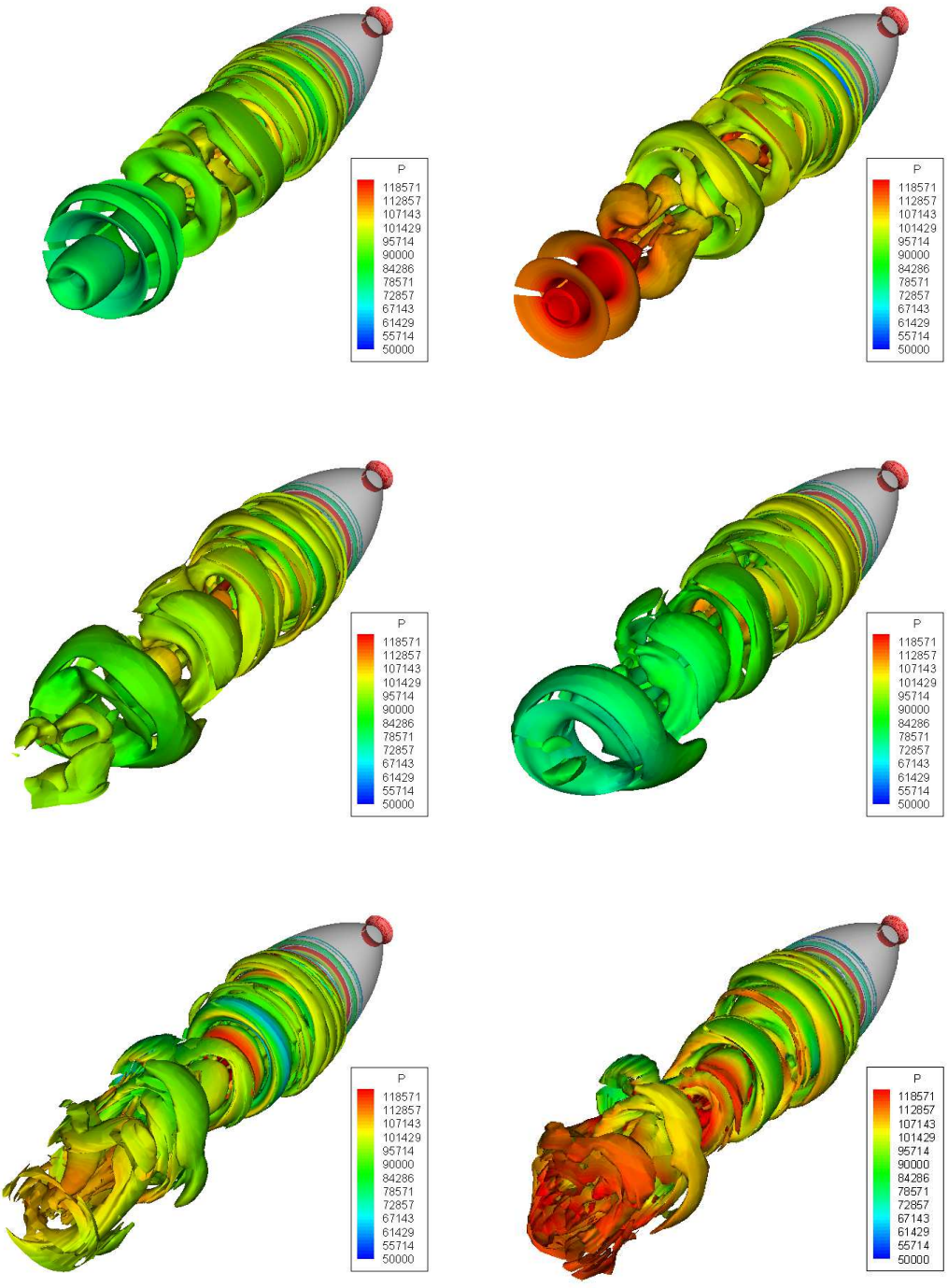

FIGURE C.9 – Iso-surface of Q-criterion ($0.1 * U_t^2/D_e^2$) coloured with pressure at T=0.66, 0.85, 1.16, 1.30, 1.51 & 1.64 * L_d/U_t : Left to Right ; Top to Bottom, respectively.

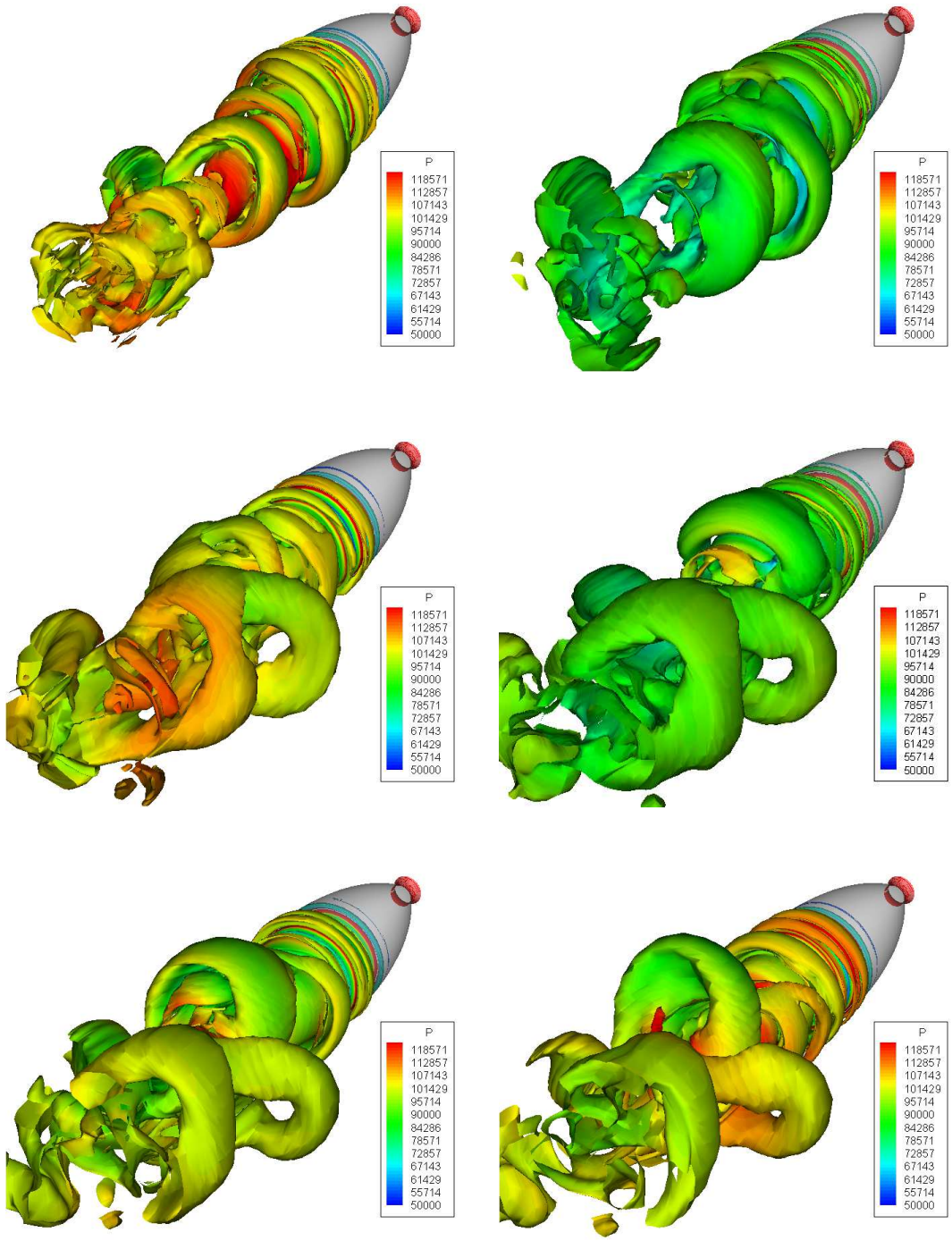

FIGURE C.10 – Iso-surface of Q-criterion ($0.1 * U_t^2/D_e^2$) coloured with pressure at T= 1.83, 2.10, 2.36, 2.81, 3.03 & 3.20 * L_d/U_t : Left to Right ; Top to Bottom, respectively.

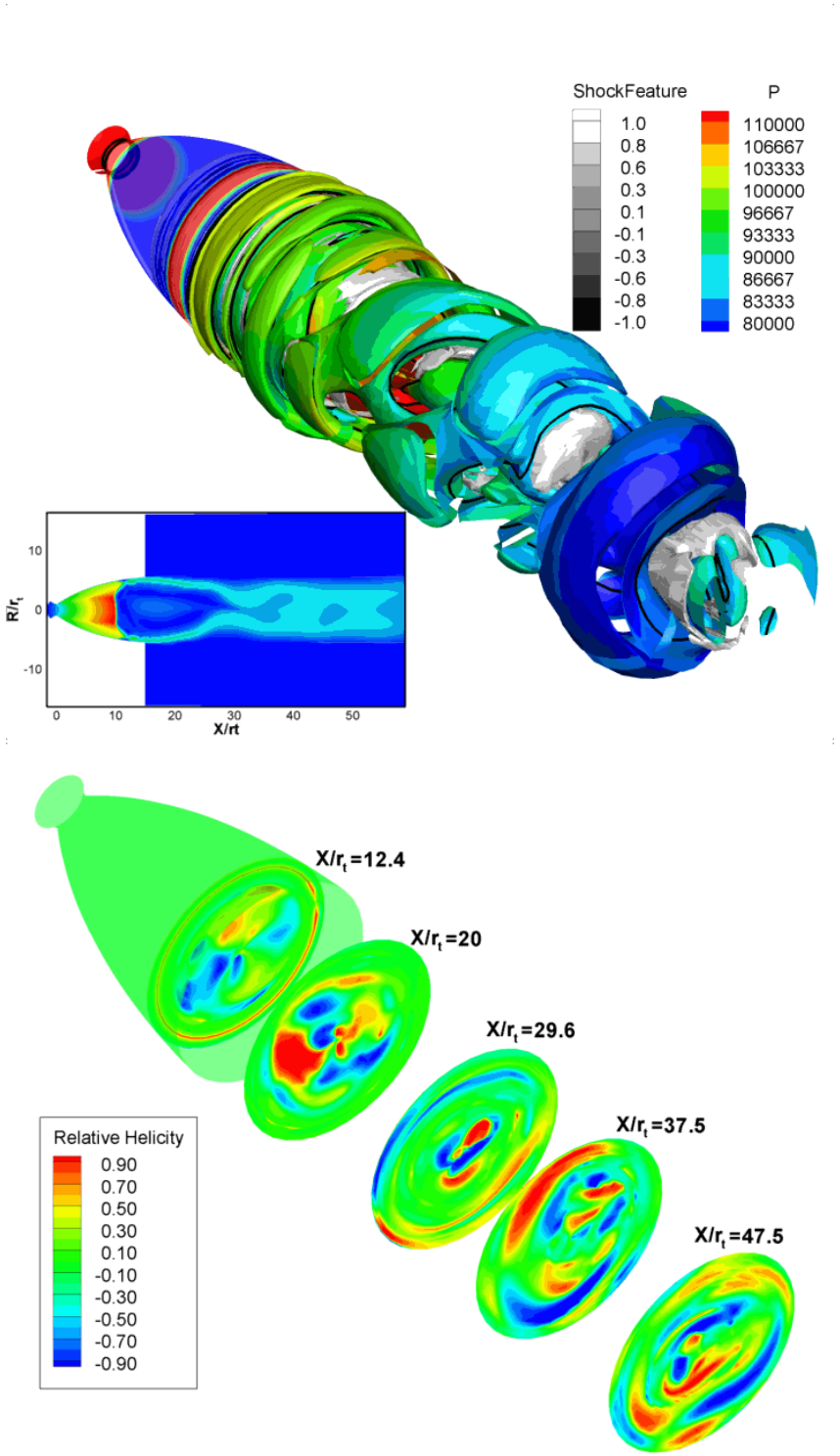

FIGURE C.11 – (Top) Iso-surface of Q-criterion coloured with iso-pressure and shock function contours (Bottom) Iso-helicity contours on 2d slice along the streamwise direction

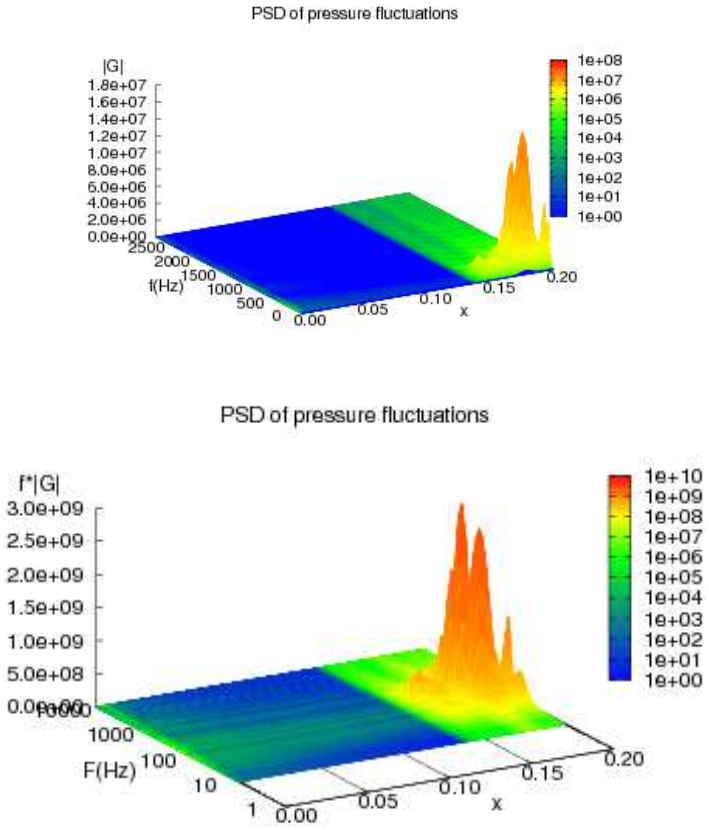

FIGURE C.12 – Spectra of the wall pressure fluctuations : (Top) G(f) & (Bottom) f*G(f).

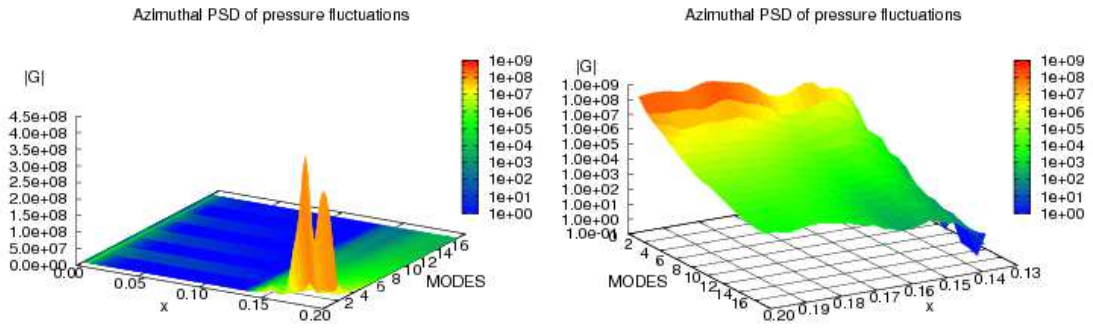

FIGURE C.13 – Power spectral density in the azimuthal direction : (Left) G(f), (Right) log(G(f)).

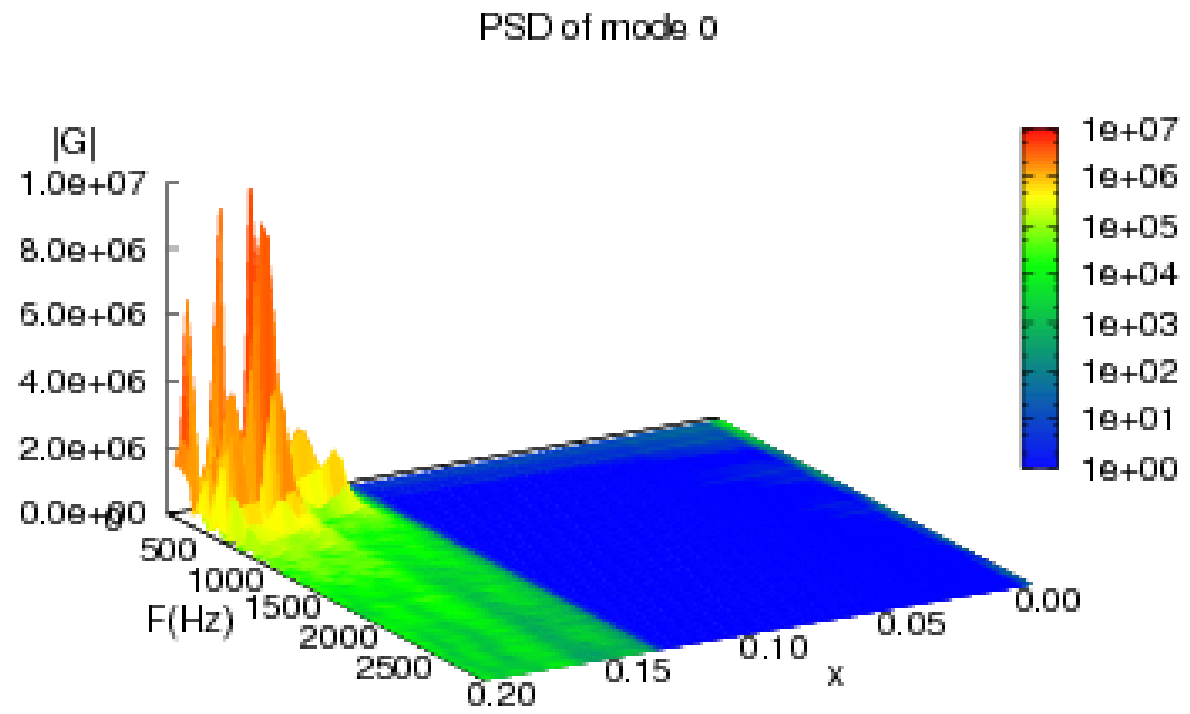

FIGURE C.14 – PSD analysis of coefficient a_0

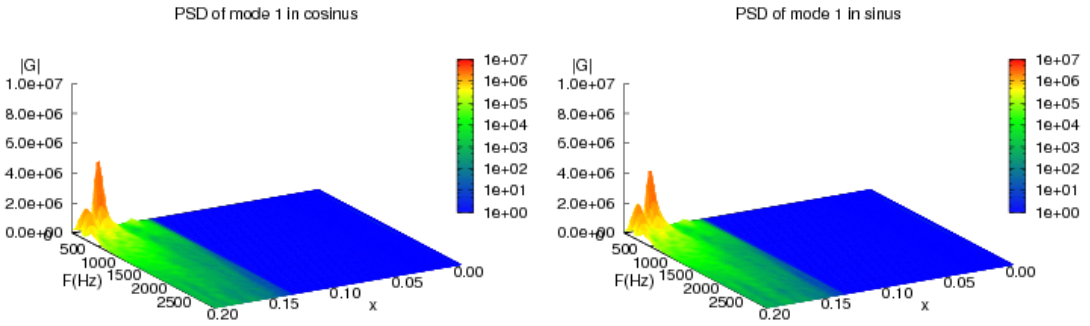

FIGURE C.15 – PSD analysis of coefficients a_1 and b_1

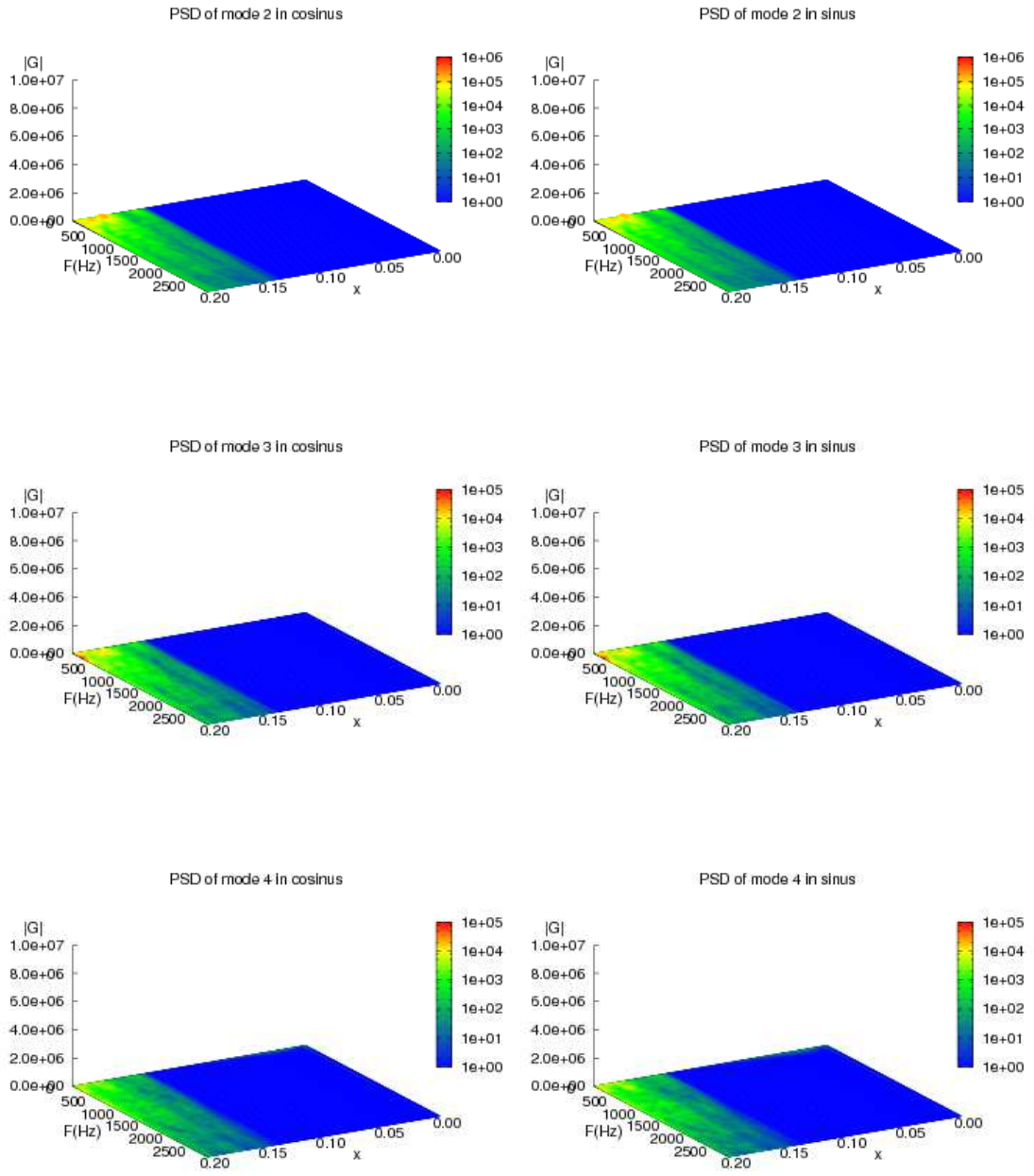

FIGURE C.16 – PSD analysis of coefficients (Top) a_2 and b_2, (Middle) a_3 and b_3 & (Bottom) a_4 and b_4

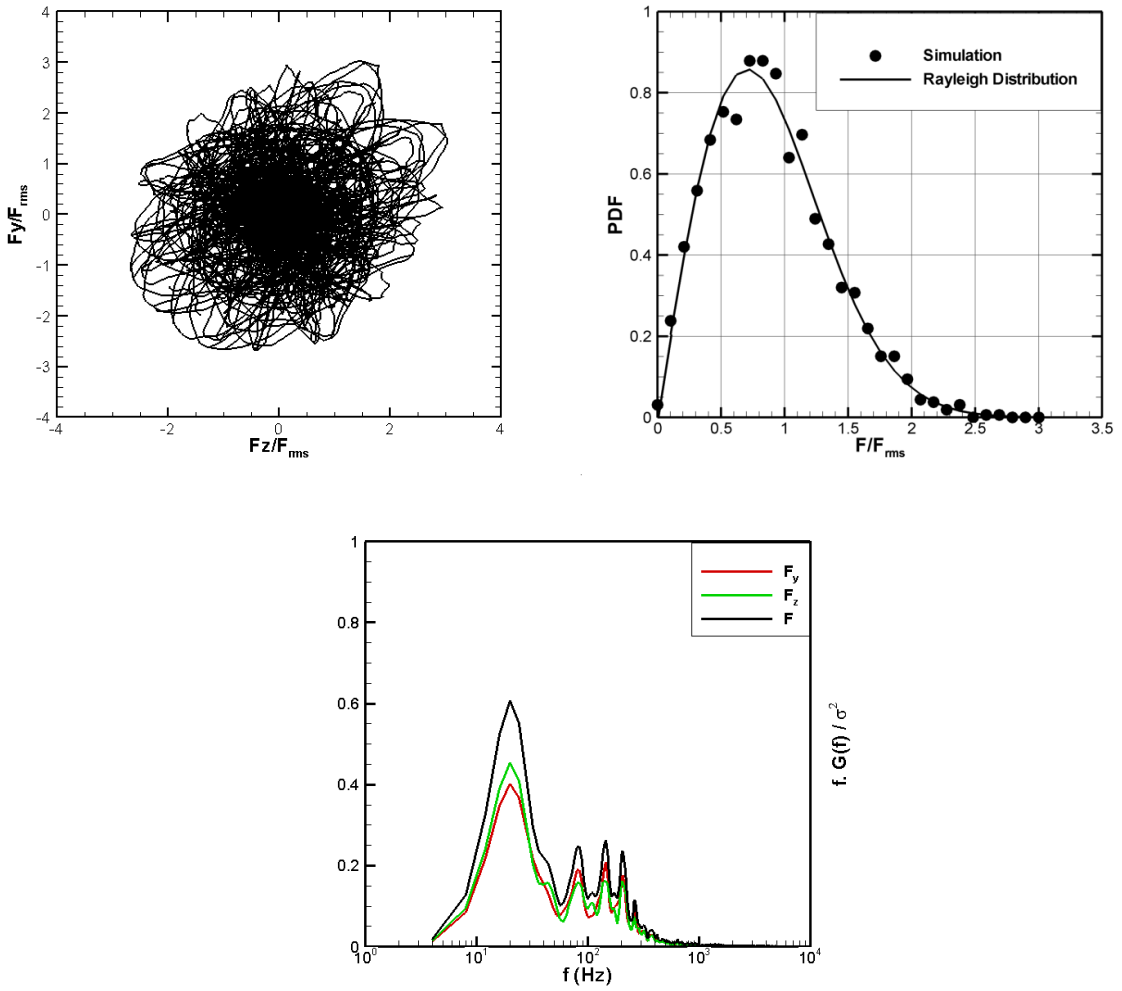

FIGURE C.17 – (Top) Polar plot and PDF distribution (Bottom) PSD of side-load and its components

C.3 Results : NPR=41.6

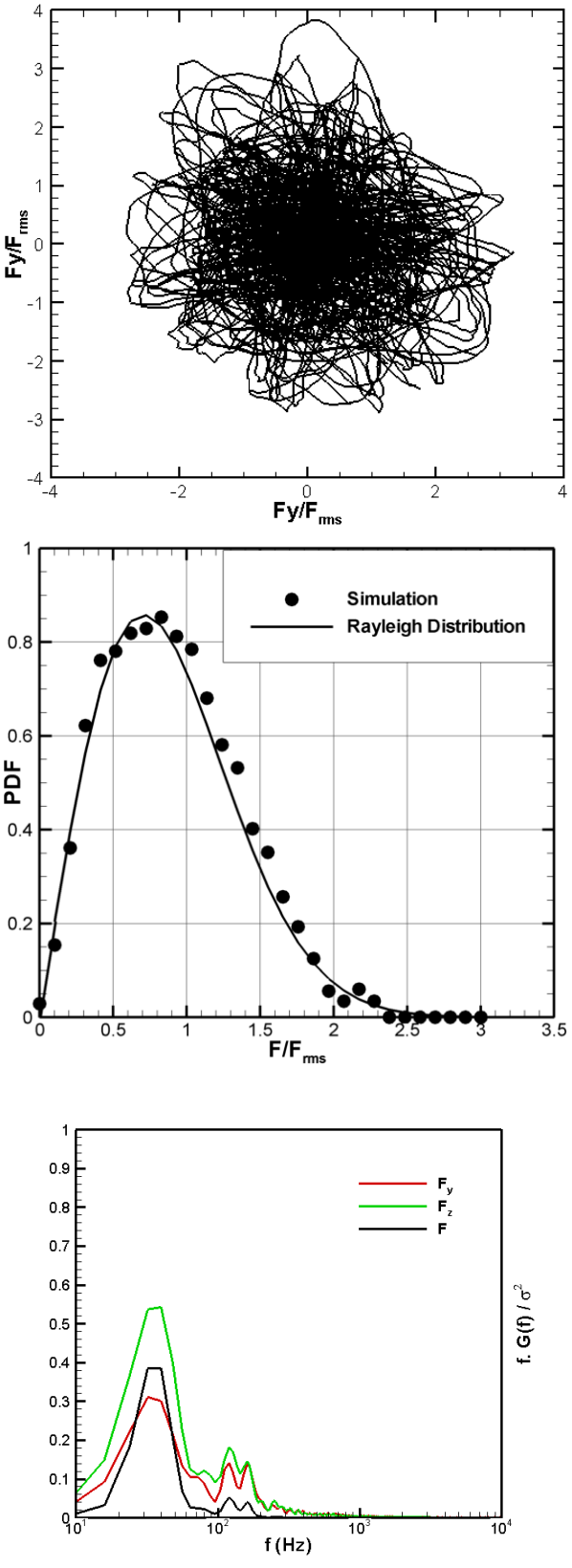

FIGURE C.18 – (Top) Polar plot (Middle) PDF distribution (Bottom) PSD of side-load and its components.

Annexe D

Spectral Analysis and Side-Load Calculations

D.1 Spectral Analysis

Signal processing, and more specifically digital signal processing, is an essential tool in experimental data analysis. It is also becomes more and more important to analyze numerical results as unsteady phenomena are now simulated. Spectral analysis is used to obtain information about the frequencies contained in a data set, to analyze the spectral components shared by several signals or to determine the transfer function of a system. Classical spectral analysis generally uses Fast Fourier transformation (FFT) which is a common tool in practical applications.

D.1.1 Spectral Analysis of One Signal

If $x(t)$ is a signal with a finite energy, i.e :

$$E = \int_{-\infty}^{+\infty} x^2(t)dt < +\infty \tag{D.1}$$

The Fourier transform $\widehat{x}(f)$ of this signal exists and is defined by :

$$\widehat{x}(f) = \int_{-\infty}^{+\infty} x(t)exp(-2\pi ft)dt \tag{D.2}$$

where i is the complex number such as $i = \sqrt{-1}$ and $\widehat{x}(f)$ are generally complex, but, in practical applications, the signal $x(t)$ is real. The Parseval theorem expresses the energy in terms of the time and frequency domain descriptions of the signal :

$$E = \int_{-\infty}^{+\infty} x^2(t)dt = \int_{-\infty}^{+\infty} |\widehat{x}(f)|df \tag{D.3}$$

From this theorem, $|\widehat{x}(f)|^2$ may be viewed as the energy spectral density of the signal $x(t)$. Accordingly, $|\widehat{x}(f)|^2 df$ is the energy contained in the bandwidth $[f, f+df]$. One may also define autocorrelation function :

$$\tilde{R}_{xx} = E[x^*(t)x(t+\tau)] \tag{D.4}$$

In analogy with previous definitions, the power spectral density of this process may be determined as the Fourier transformation of this function :

$$S_{xx}(f) = \int_{-\infty}^{+\infty} \tilde{R}_{xx}(\tau) exp(-2i\pi f\tau) d\tau \tag{D.5}$$

This relation is known as the Wiener-Khinchin theorem, because it may be derived defining the power spectral density in terms of the Fourier transform to the truncated function $x_T(t)$:

$$S_{xx}(f) = \lim_{T\to+\infty} \frac{E[|\widehat{x}_T(f)|^2]}{T} \tag{D.6}$$

where

$$\widehat{x}_T(f) = \int_{-T/2}^{+T/2} x(t) exp(-2i_p ift) dt \tag{D.7}$$

The two definitions of the power spectral are equivalent. It is worth noticing that the last expression contains an ensemble average operation. Indeed, statistically stable estimates of the power spectral density cannot be obtained without taking this ensemble average. In practical applications, the ensemble average is replaced by a time averaging operation.

D.1.2 Cross-Spectral Density and Coherence Function

The previous analysis may be extended to the case of two random signals $x(t)$ and $y(t)$. The common frequency components of these two signals may be determined by calculating the cross-spectral density which may be defined as :

$$S_{xy}(f) = \lim_{T\to+\infty} \frac{1}{T} E[\widehat{x}_T^*(f)\widehat{Y}_T(f)] \tag{D.8}$$

where the Fourier transforms of truncated signals are defined as before :

$$\widehat{x}_T(f) = \int_{-T/2}^{+T/2} x(t) exp(-2i\pi ft) dt \tag{D.9}$$

and

$$\widehat{y}_T(f) = \int_{-T/2}^{+T/2} y(t) exp(-2i\pi ft) dt \tag{D.10}$$

As easily shown, the cross-spectral density is the Fourier transform of the cross-correlation function :

$$S_{xy}(f) = \int_{-\infty}^{+\infty} \tilde{R}_{xy}(\tau)(-2i\pi f\tau) d\tau \tag{D.11}$$

where the cross-correlation function is given by :

$$\tilde{R}_{xy}(\tau) = \lim_{T\to+\infty} \frac{1}{T} \int_{-T/2}^{+T/2} x^*(t) y(t+\tau) dt \tag{D.12}$$

The cross-correlation function may be computed from the cross spectral density :

$$\tilde{R}_{xy}(\tau) = \int_{-\infty}^{+\infty} S_{xy}(f) exp(2i\pi f\tau) df \tag{D.13}$$

The *coherencefunction* is another useful quantity in evaluating the degree of similarity of two signals. It is defined by the following ratio :

$$\gamma_{xy}(f) = \frac{|S_{xy}(f)|}{\sqrt{S_{xx}(f)S_{yy}(f)}} \tag{D.14}$$

The Schwartz inequality indicates that, this coherence function is always greater or equal to zero and lower or equal to 1 :

$$0 \leq \gamma_{xy}(f) \leq 1 \tag{D.15}$$

and the phase angle is given as :

$$\theta_{xy}(f) = tan^{-1}\left[\frac{\Im_{xy}(f)}{\Re_{xy}(f)}\right] \tag{D.16}$$

where $\Im_{xy}(f)$ & $\Re_{xy}(f)$ are the real and imaginary parts of $S_{xy}(f)$ respectively.

For the frequency components which are shared by both signals the coherence function is close to unity. This function is close to zero if the corresponding frequency components are not common to the two signals. It is worth noting that the coherence function is a real number while the cross spectral function takes value close to 1, the phase difference determined with the cross-spectral density describes the phase relation of the frequency component shared by the two signals.

D.1.3 Spectral Estimation

To compute the power spectral density of a signal is based on the following expression :

$$S_{xx}(f) = \lim_{T\to+\infty} \frac{E[|\widehat{x}_T(f)|^2]}{T} \tag{D.17}$$

The application of this expression is considered in the case of sampled signal. Consider the signal $x(t)$ and let : $x(t) = x(n\Delta t)$, with $n = 0, 1, .., Q$, designate the sequence of Q samples obtained by sampling this sample periodically with a sampling period Δt. The data set is first subdivided into M segments of N samples each $(MN = Q)$. The time duration of each segment is $N\Delta t$. If $x_j(n)$ is the n^{th} sample of the j^{th} segment, the discrete Fourier transform of this segment is :

$$\widehat{x}_j(k) = \sum_{n=0}^{N-1} x_j(n) exp(-2i\pi k\frac{n}{M}) \tag{D.18}$$

The k_{th}, sample of this discrete Fourier transform corresponds to the frequency $f = k\Delta f$ where the frequency step is given by $\Delta f = 1/N\Delta t$. Accordingly :

$$\widehat{x}_T(k\Delta f) = \Delta t\widehat{x}(k) = \Delta t \sum_{n=0}^{N-1} x_j(n) exp(-2i\pi k\frac{n}{N}) \tag{D.19}$$

Then the power spectral density may be estimated by first forming the periodgorem :

$$\frac{|\widehat{x}_T(k\Delta f)|^2}{T} = \frac{(\Delta t)^2}{T}|\widehat{x}_j(k)|^2 = \frac{\Delta t}{N}|\widehat{x}_j(k)|^2 \tag{D.20}$$

The ensemble average is then evaluated from the M available periodogram and real to an estimate of the power spectral density

$$S_{xx}(f_k) = \frac{\Delta t}{MN}\sum_{j=1}^{M}|\widehat{x}_j(k)|^2 \quad with \quad f_k = k\Delta f \quad and \quad \Delta f = \frac{1}{N\Delta t} \tag{D.21}$$

Detailed description of analyzing random data based on this periodogram approach is given in [1] & [2].

D.1.4 Probability Distribution Functions

There are several theoretical distribution functions but the most important of these distribution functions from the applied statistics point of view is the Gaussian (normal) distribution.

Besides there are three different distribution functions associated with the normal distribution. Among them χ^2 distribution is of pure interest and has been discussed here.

D.1.5 Normal Distribution

The probability density and distribution functions of a normally distributed random variable x are defined as :

– the normal probability density function

$$p(x) = (\sigma\sqrt{2\pi})^{-1} exp\left[-\frac{(x-\bar{x})^2}{2\sigma^2}\right] \tag{D.22}$$

– the normal probability distribution function

$$P(x) = (\sigma\sqrt{2\pi})^{-1}\int_{-\infty}^{x} exp\left[-\frac{(\xi-\bar{x})^2}{2\sigma^2}\right] d\xi \tag{D.23}$$

a more convenient form of the normal distribution in terms of standardized variable z which is given by :

$$z = \frac{x-\bar{x}}{\sigma} \tag{D.24}$$

When this expression is substituted in the above equations, standardized normal density and distribution functions with zero mean and unit variance ($\bar{z} = 0$;$\sigma_z{}^2 = 1$) are obtained as follows :

$$p(z) = (\sigma\sqrt{2\pi})^{-1} e^{-z^2/2} \tag{D.25}$$

$$P(z) = (\sigma\sqrt{2\pi})^{-1}\int_{-\infty}^{z} e^{-\xi^2/2} d\xi \tag{D.26}$$

The density function $p(z)$ is uni-modal, monotonic about the mode, and symmetric with the inflection point at ± 1.

D.1.6 Chi-Square Distribution

Let $z_1, z_2, z_3, ..., z_n$ be n independent random variables, each of which has a normal distribution with zero mean and unit variance. Let a new random variable be defined as :

$$\chi_n{}^2 = z_1{}^2 + z_2{}^2 + z_3{}^2 + ... + z_n{}^2 \tag{D.27}$$

The random variable $\chi_n{}^2$ is the chi-square variable with n degrees of freedom. The number of degrees of freedom n represents the number of independent or "free" squares entering into the expression. The probability density function of $\chi_n{}^2$ is given by

$$p(\chi^2) = [2^{n/2}\Gamma(n/2)] - 1(\chi^2)^{((n/2)-1)}e^{-\chi^2/2} \qquad \chi^2 \geq 0 \tag{D.28}$$

where $\Gamma(n/2)$ is the gamma function. The corresponding distribution function of $\chi_n{}^2$, given by the integral of the above equation from minus infinity to a specific value of $\chi_n{}^2$, is called the chi-square distribution with n degrees of freedom.

D.2 Evolution of Side-Loads From Wall Pressure Measurements

To understand the direct estimation of side loads from the unsteady wall pressure measurements, let us consider an axi-symmetric convergent-divergent nozzle. Consider x be the coordinate along the nozzle axis, θ the azimuthal angle and r is the radial coordinate. The nozzle wall contour is defined by $r(x)$. One thing to remind here is that by $side - loads$ we means the global forces acting on the nozzle wall, which does not means that one should discard the higher order modes giving the distribution of the side-loads in the azimuthal direction.

D.2.1 Theoretical Evolution From Azimuthal Fourier Decomposition

Consider a pressure field, which is off course the function of $x, theta$ & time (t). Now we expand the pressure field in Fourier modes with the respect to θ :

$$p(x,\theta,t) = P_{a0}(x,t) + \sum_{k=1}^{\infty}[P_{ak}(x,t)cos(k\theta) + P_{bk}(x,t)sin(k\theta)] \tag{D.29}$$

To check out the force acting on a 2D slice of length dx. Let $\vec{dF}(x,t)$ be the instantaneous force on a slice od length dx. Then the respective components of the for $\vec{dF}$ are given by :

$$dF_y(x,t) = \left[\int_0^{2\pi} p(x,\theta,t)cos\theta d\theta\right] r(x)dx \tag{D.30}$$

$$dF_z(x,t) = \left[\int_0^{2\pi} p(x,\theta,t)sin\theta d\theta\right] r(x)dx \tag{D.31}$$

By using the Fourier decomposition eq. D.29 we get :

$$dF_y(x,t) = \pi P_{a1}(x,t)r(x)dx \tag{D.32}$$

$$dF_z(x,t) = \pi P_{b1}(x,t) r(x) dx \tag{D.33}$$

These above mentioned components of the side-loads depend only upon the first mode of the azimuthal Fourier decomposition.

D.2.2 Practical Evaluation From Discrete Pressure Measurements

we assume that the wall pressure field $p(x,\theta,t)$ is known at given x=constant cross-section by measuring the pressure at J equidistant locations $\theta_j = (j-1)\frac{2\pi}{J}$ with $j = 1,2,..,J$.

Then the truncated Fourier expansion can be determined as :

$$p(x,\theta,t) = P_{a0}(x,t) + \sum_{k=1}^{\frac{J}{2}-1} [P_{ak}(x,t)cos(k\theta) + P_{bk}sin(k\theta)] + P_{a\frac{J}{2}}(x,t)cos(\frac{J}{2}\theta) \tag{D.34}$$

The coefficients are determined by using the J measured values $p(x,\theta,t)$ for $j = 1,2,...J$. It is well known (according to Shannon theorem) that the coefficients of the truncated Fourier expansion eq. D.34 are identical to those of the full expansion eq. D.29 provided that the coefficients of the exact expansion are equal to 0 for $k \geq \frac{J}{2}$. In fact, for the purpose of the coefficients P_{a1} and P_{b1} and it is sufficient that coefficient of the exact expansion be 0 for $k > J-2$ as shown in Fig. D.1 (J-1 is an alias for 1).

Direct Summation of the Force Components :

Instead of performing the Fourier expansion of the pressure field and the using the Fourier decomposition of the force components, one can also attempt to compute directly the force components from the relationships of the instantaneous force components using the J measured values. Integrating in the azimuthal direction with the trapezoidal rule one gets :

$$dF_y(x,t) = \sum_{j=1}^{J} p(x,\theta_j) cos\theta_j \Delta\theta_j r(x) dx \tag{D.35}$$

$$dF_z(x,t) = \sum_{j=1}^{J} p(x,\theta_j) sin\theta_j \Delta\theta_j r(x) dx \tag{D.36}$$

For equidistant locations $\theta_j = (j-1)\frac{2\pi}{J}$ and due to the discrete orthogonality the above relations eq. D.32, D.33 & eq. D.35, D.36 like :

$$\sum_{j=1}^{J} cos\left(k(j-1)\frac{2\pi}{J}\right) cos\left((j-1)\frac{2\pi}{J}\right) = \begin{cases} 0 & if \quad k \neq 1 \\ \pi & if \quad k = 1 \end{cases} \tag{D.37}$$

we see that eq. (D.35) & (D.36) given exactly the same results than eq. (D.32) & (D.33) i.e. we don't need to perform really the Fourier decomposition eq. D.34.

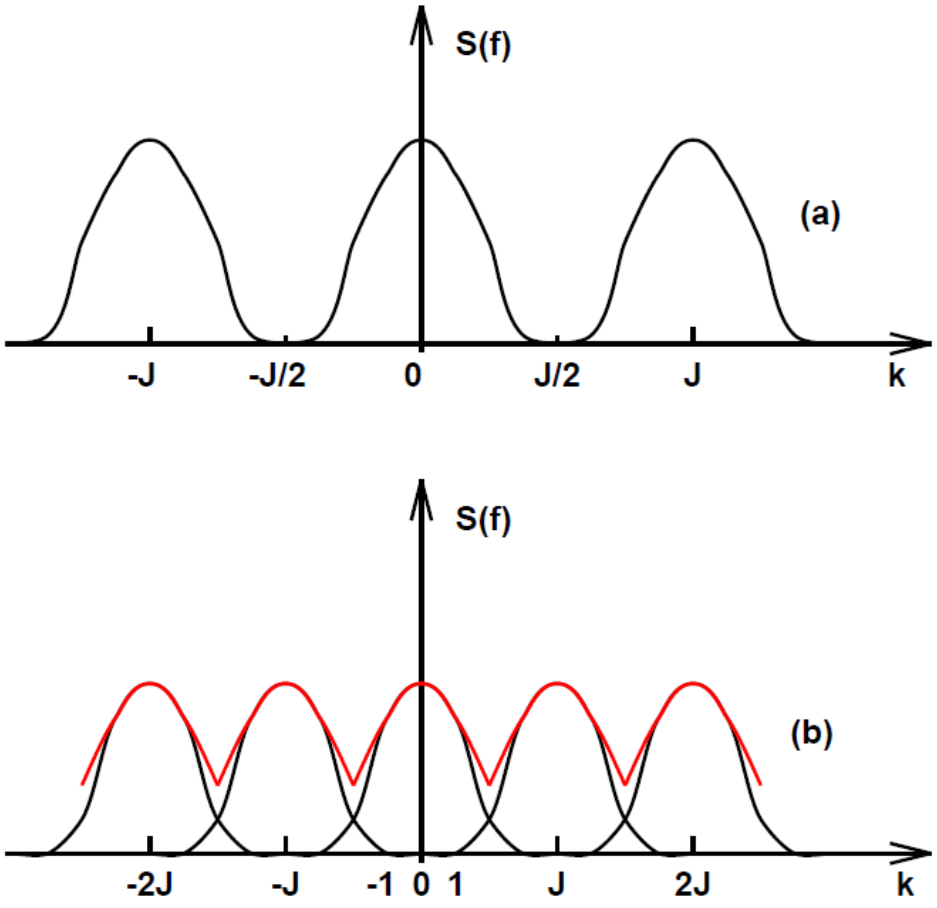

FIGURE D.1 – Application of the sampling theorem in the azimuthal direction

Bibliographie

[1] Bendat, J. S., and Piersol, A. G., Random data, Analysis and measurement procedures, 3rd Edition, 2000.

[2] Veynante, D., Survey of signal processing techniques, von Karman Institute for Fluid Dynamics, Lecture series 2002-04, Post-processing of experimental and numerical data, April 22-26, 2002.

CONTRIBUTION A LA SIMULATION NUMERIQUE DES DECOLLEMENTS D'ECOULEMENTS TURBULENTS INDUITS PAR CHOC : APPLICATION A L'ECOULEMENT DE LA TUYERE SUPERSONIQUE SUR-DETENDU

Les décollements d'écoulement induits par choc et leur éventuel réattachement sur paroi sont observés dans de nombreuses configurations d'intérêt pratique, incluant les entrées d'air, les profils transsoniques ou les tuyères de lanceurs spatiaux. Ces phénomènes mettent en jeu des interactions complexes entre couches limites et ondes de choc ou de détente conduisant à des instationnarités à basses fréquences dont l'origine reste aujourd'hui à élucider. Cette étude vise d'une part à proposer une stratégie numérique permettant de prévoir plus précisément ces phénomènes de décollement et d'autre part d'identifier les principaux mécanismes physiques qui pilotent l'évolution de leur structure globale.

L'étude porte plus particulièrement sur les configurations de décollements libres ou séparés apparaissant en tuyère optimisée en poussée opérant en régime surdétendu. Différents modèles phénoménologiques sont ainsi testées pour décrire l'évolution du champ de pression instationnaire et dissymétrique en fonction du niveau de surdétente. La stratégie numérique proposée repose sur la combinaison de schémas à capture de choc d'ordre élevé (WENO 5), d'algorithmes d'intégration implicite en temps et d'une modélisation de la turbulence étendant l'approche Detached Eddy Simulation via l'ajout de corrections de réalisabilité. Une large plage de niveaux de surdétente est considérée, à la fois en condition d'entrée stabilisée et transitoire, afin de clarifier les conditions d'existence des différents régimes de décollements libres et restreints, ainsi que l'évolution temporelle de la morphologie globale de l'écoulement transitant entre ces deux régimes. L'évolution instationnaire de l'écoulement est simulée sur des temps suffisamment longs pour permettre une analyse spectrale des contributions des premiers modes azimutaux à la dynamique basse fréquence du champ de pression pariétale.

Mots clés : Ondes de choc, Tuyères supersoniques, Décollement des écoulements, Aérodynamique supersonique, Simulation numérique, Ecoulements turbulents, Méthodes hybrides.

CONTRIBUTION TO THE NUMERICAL SIMULATION OF TURBULENT SHOCK-INDUCED SEPARATED FLOWS : APPLICATION TO SUPERSONIC OVER-EXPANDED NOZZLE FLOWS

Shock-induced flow separation and reattachment are encountered in many configurations, such as supersonic inlets, transonic airfoils or rocket nozzles. These phenomena involve complex interactions of boundary layers with compression or expansion waves and exhibit a low-frequency unsteady behaviour which still requires a clear explanation. This study aims at better identifying the physical mechanisms which drive the global structure of these flows and suggesting improved numerical tools in order to predict these more accurately. The appearance of free and restricted separations in supersonic annular jets occuring in thrust optimised contour nozzles operating in over-expanded conditions is more particularly investigated while various hypothesis are tested to explain the evolution of the associated unsteady asymmetric wall pressure field in function of the nozzle pressure ratio. The numerical strategy proposed relies on a realizable extension of the Detached Eddy Simulation, combined with high order shock capturing schemes and an implicit time integration algorithm. This methodology is applied for a wide range of both constant or transient inflow conditions and leads to identify more accurately the appearance of free and restricted separations and the time-varying morphology of the flow during the transition process. For both regimes, the simulation is carried out for long-enough time to perform reliable statistical analysis and azimuthal expansion of the wall pressure field and thus investigate extensively the possible origins of the side-load activities.

Keywords : Shock wave, Supersonic nozzle, Flow separation, Supersonic aerodynamic, Numerical simulation, Turbulent flows, Hybrid methods.

Institut PPRIME
CNRS UPR 3346 - ENSMA - Université de Poitiers
Département Fluides, Thermique, Combustion
Branche Fluides
Téléport 2- 1, avenue Clément Ader, BP 40109,
86961 Futuroscope Chasseneuil Cedex